# The Effects of Titanium Ti-6Al-4V Powders Manufactured Using Electron Beam Melting (EBM) - Additive Manufacturing on Metallurgical Evaluation.


By

EMMANUEL MUZANGAZA


A thesis submitted to the University of Birmingham for the degree of Masters by Research in Materials and Metallurgy Programme


School of Metallurgy and Materials

College of Engineering and Physical Sciences

University of Birmingham


29 October 2018

## ABSTRACT

Multiple methods of manufacturing Ti-6Al-4V powders for Additive Manufacturing (AM) are available. The effects of the powder quality, properties and post-processing conditions on microstructure and mechanical properties in Electron Beam Melting (EBM) process are investigated in this work. Two powders manufactured using Plasma (PA) and Gas (GA) Atomisation were fully characterised. Test specimens were built using default manufacturer's (Arcam) parameters and mechanically tensile tested in different post-processing conditions: as built (near net-shape), heat treated using Hot Isostatic Pressing (HIP), and on surface machined .

Each build specimen was cut and polished to analyse for porosity, defects, and microstructure. The microstructure of as-built samples was found to be of very fine and acicular morphology due to high-solidification rate. HIP heat treatment has been observed to homogenise as-built anisotropic grain microstructure, with reduction and elimination of gas pores and defects for as-built EBM samples. However, this (HIP) also resulted in coarser grain microstructure. Both GA and PA specimens yield strength (YS) and ultimate tensile strength (UTS) measured, with PA found to have higher values in comparison to GA. The study found that lack of fusion/un-melted particles caused lower elongation for as-built PA samples due to un-optimised parameters and process instability. Spherical gas pores (argon trapped) in GA powders and parts were predominately found due to atomisation process thus inherited in as-built parts.

Nonetheless, all samples had better and some above the minimum ASTM F294-14 titanium tensile requirement. The PA yield strength and tensile strength of the EBM as-built specimens were 850 and 925 MPa irrespectively, while GA yield strength and tensile strengths were 810 and 887 MPa irrespectively.

ACKNOWLEDGEMENTS

Firstly, I would like to thank my thesis academic supervisor, Professor Moataz Attalah; industrial supervisor, Professor David Wimpenny of University of Birmingham (UoB), and The Manufacturing Technology (MTC) Centre Ltd irrespectively. Without their input, intense supervision, and expertise in Metallurgy and AM, I would have struggled through the process of researching.

I would also like to thank the following for their passionate support and guidance in the experimental characterisation of this thesis: Dr. Yijun Liu (Chief Metallurgist, MTC), Riccardo Tosi (EngD UoB/MTC), The National Centre for AM equipment's at MTC and UoB Metallurgy lab for the manufacturing and characterisation of specimens in this project

Finally, I must express my profound gratitude to my parents, family, and my wife for being there to provide unfailing support throughout the years, even though they all struggled and still try to understand this fascination - AM technology.

Publications:

During the study of this thesis I have had the following journals and conference presentations published:

1. Title: Optimising the Dynamic Process Parameters in EBM to Achieve Internal Defect Quality Control.
   Publisher: EPMA Metal AM Seminar 2017.
2. Title: EBM- Effect of Low-Cost Alternative Ti-6Al-4V Powder Feedstocks on Mechanical Properties of AM.
   Publisher: IOM3 (second Additive Manufactured Metallic Materials Properties & Structures (AM3PS), 24 May 2017.
3. EBM Adaptronic build chamber development**
   Publisher: EBAM Seminar 2016.

**Being Contributing author

CONTENTS

NOMENCLATURE

| | |
|---|---|
| AM | Additive Manufacturing |
| ASTM | American Society for Testing of Materials |
| BCC | Body-Centered Cubic |
| CCT | Continuous Cooling Transformation |
| EBM | Electron Beam Melting |
| GA | Gas Atomisation |
| HCP | Hexagonal Close-Packed |
| HDH | Hydride De-Hydride |
| HIP | Hot Isostatics Pressing |
| IP | Intellectual Property |
| L-PBF | Laser Powder Bed Fusion |
| PA | Plasma Atomisation |
| PREP | Plasma Rotating Electrode Process |
| PS | Plasma Spheroidised |
| PSD | Particle Size Distribution |
| SEM | Scanning Electron Microscope |
| Ti | Titanium |
| UTS | Ultimate Tensile Strength |
| Wt. % | Weight Percentage |
| YS | Yield Strength |
| %El | percentage externstion |

# 1.0 INTRODUCTION

## Background

The cost of titanium powder for AM is driven mainly by the specialist production methods required to deal with the high reactivity of Titanium melts, and the need for free-flowing powders, resulting in the desire for highly spherical particles. Several methods exist for the manufacture of spherical titanium powders, including variations of Gas Atomisation (GA), Plasma Atomisation (PA), and the Plasma Rotating Electrode Process (PREP) [1]. Currently, GA methods allow for the highest throughput at the lowest cost per mass. However, this process typically leads to a high degree of 'satellite' (small powder particles) formation in comparison to the PA or PREP atomised methods, which are capable of producing highly spherical powders at the cost of reduced yield in the 45-106 µm particle size range typically used in EBM process.

The quality of manufactured powder has a significant impact on the mechanical properties of additively manufactured parts, acting as a Key Process Input Variable (KPIV) alongside build parameters. Process induced defects during melting have a particularly detrimental effect on mechanical performance such as tensile static strength and dynamic fatigue life and can be caused both by existing porosity in powder or poor consolidation during the build process.

This work investigates the effect of powder(s) properties on mechanical properties in parts built by EBM under different post-processing conditions. Powders manufactured by Electrode Induction GA (EIGA) and PA have been subjected to a suite of characterisation tests. Test specimens have then been built with each powder and mechanically tested in the following three different postconditions: as-built, HiPed, and machined. The resulting mechanical and microstructural properties of the test specimens are compared, and a correlation with powder properties and defects is discussed.

## Projects objectives

The primary aims of this research study are to:

- Explore the feasibility of using alternative different TI6Al4V powder in the EBM (EBM) process, i.e., plasma atomised, pa & gas atomised, EIGA powder.
- Evaluate the role of thermal post-processing (HiPing), as-built and machined of AM parts on mechanical properties and microstructure.
- Understand Ti6Al4V material and evaluate metallurgy of test specimens manufactured using EBM AM Process.
- U understand AM powder sensitivity and the impact of powder variables in the EBM process, microstructure, and defects.

## Industrial applications

With Titanium being the ninth abundant element on earth, the production method of extracting/mining the ingot and wrought has very high natural cost in comparison to other materials such as iron and aluminium [2] - [3]. Other associated elements such as carbon, hydrogen, nitrogen, and oxygen increase the cost of material as result of energy input required to separate and purify such elements [5].

Titanium alloys are currently and commonly utilised in different industrial applications such as in the aerospace, energy sectors, nuclear, gas turbines, chemical, medical, sports and automotive. [4]. Below Figure 1 shows an example of an aero engine with different sections of the engine parts using titanium alloys.

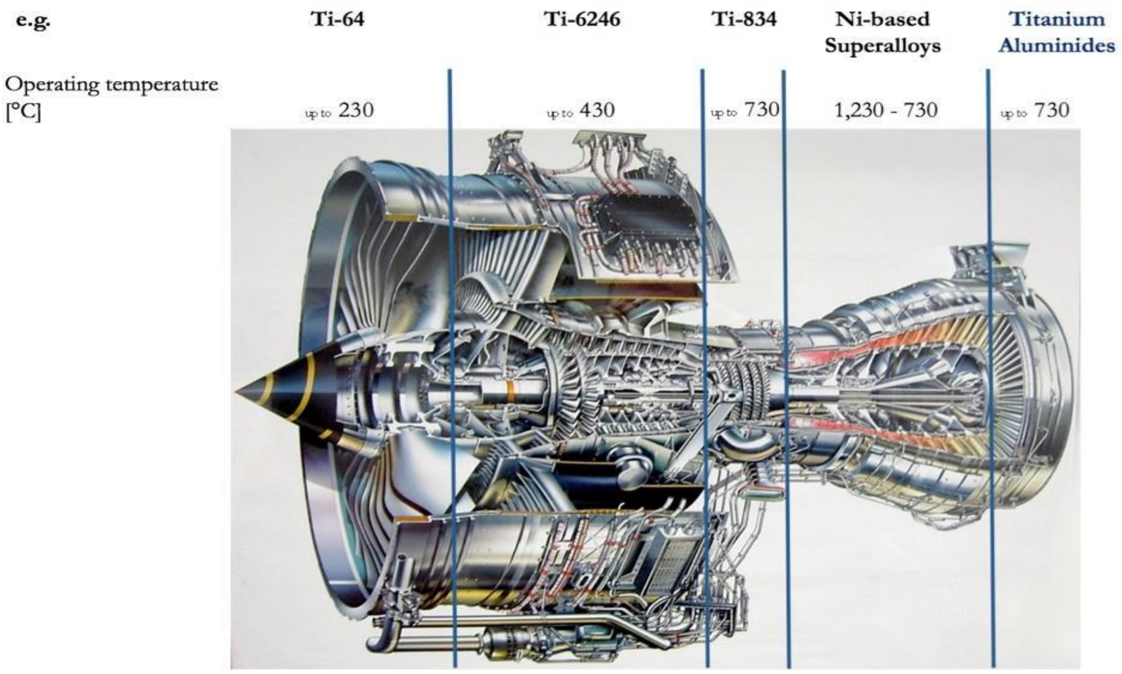


*Figure 1 an engine casing with titanium parts [2]*

The alloy's excellent corrosion resistance, low density, and high strength make it more attractive in different sectors of the industry [5] [2]. Donachie and Matthew J, 2000 [2] reported industrial applications such as petrochemical and marine environments where there is the tendency of corrosion-related failure; titanium alloys have been found to be highly resistant to corrosion in such condition [4] [6].

Noneless, the biocompatibility of these alloys has also been appreciated significantly in medical and orthopaedic industrial applications. Orthopaedics use titanium material for replacing and repairing patients' or animals' broken bones, knees, surgical instruments, external prostheses, dental implants, bone and joint replacement, to name a few. [2] [7].

Bikramjit Basu, 2016, [7] [8]states that 'more than 1000 tonnes (2.2 million pounds) of titanium devices of every description and function are implanted in patients worldwide every year.  Figure 2shows examples of medical parts currently being manufactured and commercialised using additive manufacturing. Titanium is particularly important in medical applications due to the natural properties, low-level toxicity and high resistance to corrosive liquids and substances found in human bodies [4][3].

*Figure 2 Medical replacements parts manufactured using Additive [9].*

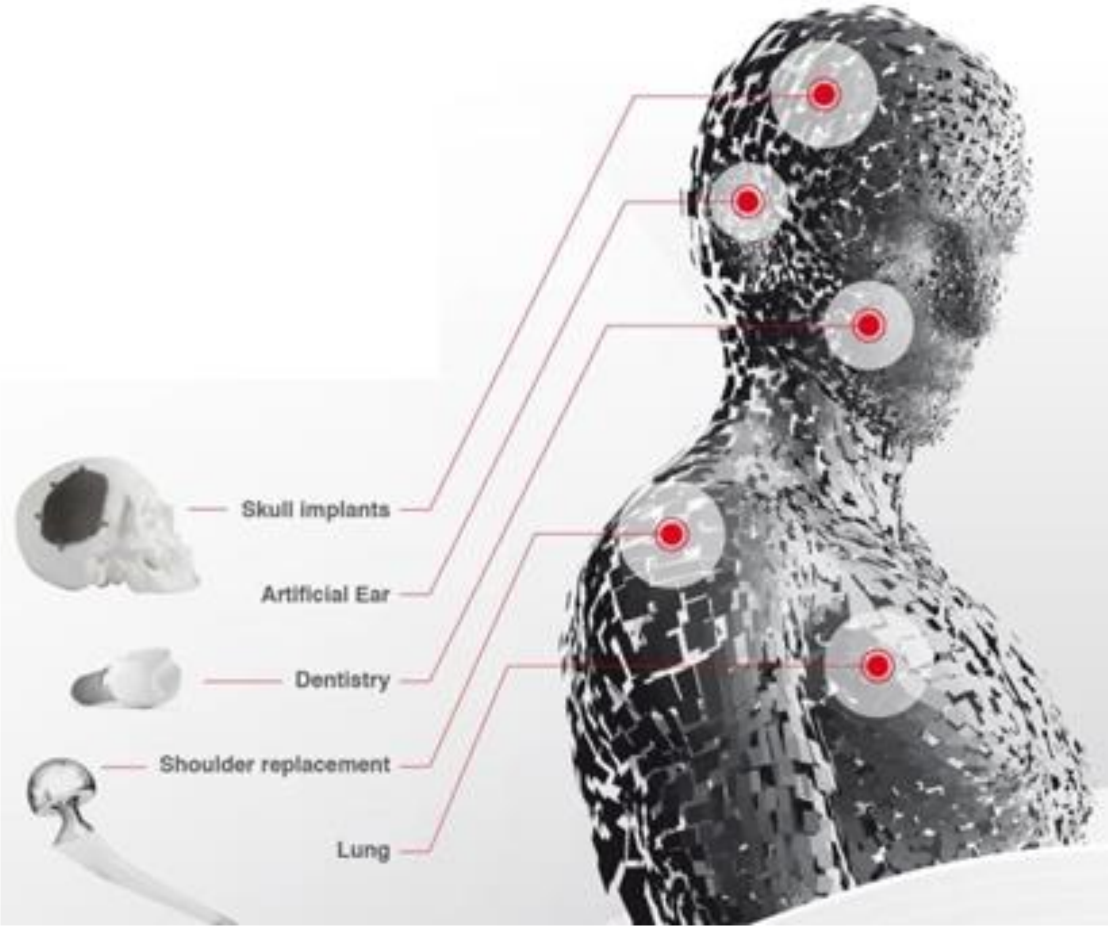

2.0 Literature Review

Metallurgy of Titanium Alloys

This section aims to give a background of Titanium (Ti) alloys and a review of different classifications of alloys. Finally, a more detailed discussion on Ti α-β, phase transformation, microstructure and mechanical properties which is the main subject of this thesis is discussed.

## 2.1 Titanium Alloys review

Titanium (Ti) alloys vary a lot with their composition, manufacturing method, and condition. The tensile strength of these alloys lies between 200 MPa and 1400 MPa [6]. The Ti-6Al-4V alloy material has thermal conductivity which varies from 5.5 W/mK to 25 W/mK for the operating temperature ranging from 35$^{o}$C to 200$^{o}$C. The crystallographic metallurgy of Ti is altered predominately when in the pure metals at 882‘C. Donachie and Matthew J, 2000 [2] reports that below this transformation temperature, the alloy has hexagonal close-packed (HCP) structure known as alpha (α); while when above it, the structure exhibits a body-centered cubic (BCC) known as beta (β). [2]

Alloying elements such as oxygen, nitrogen, aluminium, and vanadium are some of the stabilisers that are added to titanium alloy. The addition of these elements governs and influence the β-transus temperature and thereby influencing microstructure solidification transformation. [1], [7], [8][9]. These stabilising elements can be grouped into the two main categories:

Ti Stabilisers

<u>α - stabilisers:</u> these are elements that form with less than four bounds with atoms to dissolve in the α-phase thus an increase β-transus temperature. The most common elements added to Titanium alloy are, e.g., oxygen and aluminium. It has been reported that an increase of more than >8% Al, can result in brittle formation in Ti alloys [[1], 10], [11]

<u>β - stabilisers:</u> these elements, such as the vanadium, chromium, decrease the transformation temperature and are known to exhibit lower alpha phase solubility. These elements can further be sub-categories into either beta-isomorphous or beta-eutectoid elements [10]. Elements are also added to increase the solubility of different materials. Such stabilisers also lower the alpha type characteristics

within a titanium alloy. Apart from this, the resistance of titanium alloys is also reduced because of the addition of such beta stabiliser's due to which they could be deformed conveniently. Figure 3 shows the effects of stabilise elements in the influence of microstructure formation in Titanium alloys

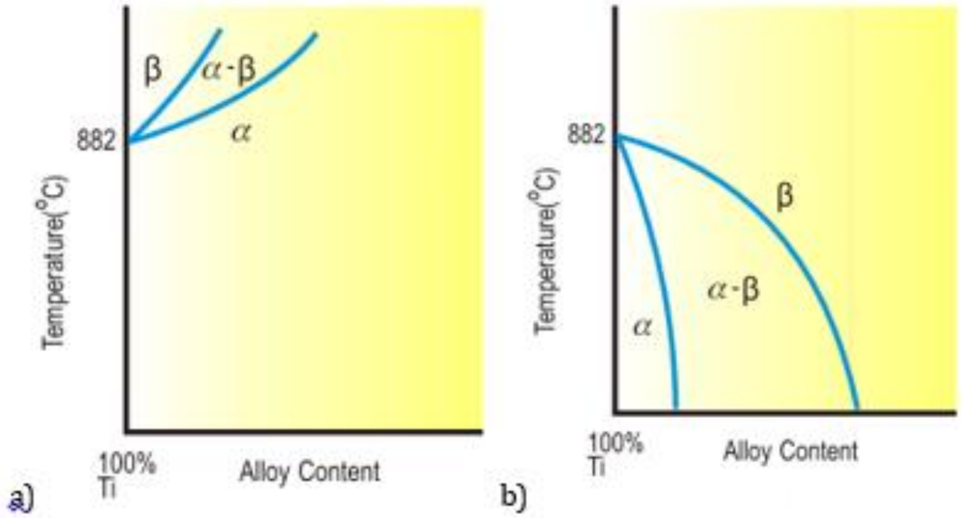


*Figure 3 effect of stabiliser elements TI with a) Alpha stabiliser, e.g., Al, Oxygen, Nitrogen and (b) Beta stabilisers such as Vanadium [6].*

Table 1 shows titanium alloys with different composition as result of alloying elements wt. % for tailoring materials strength and ductility. That being discussed, it also means three Ti alloys can be formed, and these are alpha, alpha-beta and beta alloys. All of these alloys have different properties since in each of them has different stabiliser elements added to ensure that the properties of titanium crystal structure are transformed. Therefore, with the addition of the stabilisers above, the titanium crystal structure could withstand from even cold to high temperatures above [12][1], [13] Thus, improving the mechanical performance of a part or strength of alloys.

| **Alloy** | **Stability factor of β-phase** | **Alloying elements content, wt.%** | | | | | | | |
|---|---|---|---|---|---|---|---|---|---|
| | $K_\beta$ | Al | Mo | V | Cr | Fe | C | Si | Ti |
| Ti-6Al-4V | 0.3 | 6.1 | – | 4.3 | – | 0.16 | 0.01 | – | bal. |
| Ti-6Al-2Mo-2Cr | 0.6 | 6.3 | 2.6 | – | 2.1 | 0.40 | 0.05 | 0.2 | bal. |
| Ti-6Al-5Mo-5V-1Cr-1Fe | 1.2 | 5.8 | 5.3 | 5.1 | 0.9 | 0.8 | 0.05 | 0.15 | bal. |

*Table 1 Titanium alloys with different alloying composition stabilisers*

### 2.1.1 Titanium Microstructure

As aforementioned, three Ti main forms as discussed from the stabilisers above are Alpha phase (HCP), Beta phase (BCC), and Aplha+Beta phase (mixed).

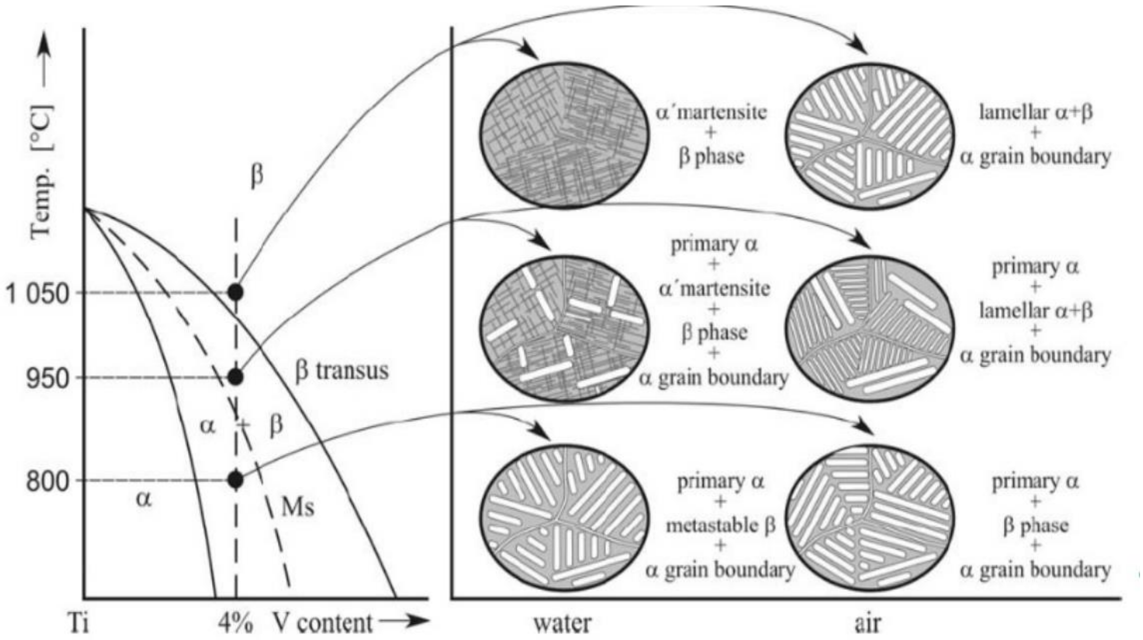


*Figure 4 diagram showing the formation of microstructure influenced by water and air for Ti6Al4V [14].*

**Alpha Alloys (HCP):** This group of alloy is commercial pure titanium with iron (Fe) and oxygen (O) are the main primary alloying elements. The material has creep resistance and have low to medium quality, excellent strength;and have magnificent qualities at the temperature of cryogenic [2], [10].

**Beta Alloys (BCC):** Beta Alloys are known to possess a BCC crystal structure; Alloy such as Ti-ll.SMo-6Zr-4.5Sn (also known as Beta III) , Ti-3AI-8V-6Cr-4Mo-4Zr are some of the most commonly used alloys [11] [6]. The alloys are heat treatable and for the most part weldable. Although these materials are higher cost. A report by Chattoraj 2014 [12] suggest these alloys are more used in medical or orthopaedics applications due to no vanadium or aluminium present so alloys such Timetal 21S, Beta C, Ti-10-2-3, BT 22 and Ti 17 are commonly used instead [12] [6].

.

**Alpha - Beta Alloys:** In these two phase α+β the TI alloy has three main different types of microstructure that can form as a result of thermal mechanical process. Thus, formation of a lamellar structure, equaiaxed structure and duplex microstructure [13]. These are the most commonly used Ti alloys. The material properties are a right balance in their mechanical plasticity, castability, weldability, and thermal conductivity [5], [14] [6]. The combination of α and β stabilisers at different ratio has typical alloy such as Ti-6Al-4V, Ti-6Al-2Sn-4Zr-6Mo and Ti-6Al-2Sn among the most common commercial material [10]. The materials are commonly used at elevated temperature of 315 °C - 400 °C [3]. The addition of Aluminium strengthens the α phase, while also increase α+β↔β but can result in reduction of the density. However, the addition of Vanadium – β- stabiliser reduces transformation temperature. In pure metals, change from the alpha to the beta stage transforms above 883 °C, yet most alloying components either balance out the alpha stage to higher temperatures or balance out the beta stage to lower temperatures. [3],[10], [15], [13].

**Phase Transformation**

During this phase transformation, the molecules within one crystal of titanium alloy changes completely. Due to such change, the boiling point, as well as melting point, changes [17]. The physical characteristics such as hardness and strength of such alloys can improve and change microsture during the diffusion.. Such processes are usually reversible which means that beta crystal can be changed back into the alpha crystal by applying thermal heat and changing the cooling solidification rate. Such pressure would bring the molecules together due to which the crystal would regain its physical and metallic strength. Typically, when a beta crystal is transformed, or an alpha crystal is changed into some other form, its metallic properties are affected [17].

**HCP and BCC**

The BCC crystal refers to the unit cell with one variant of the densily packed {110} lattice planes [17]. titanium alloy arrange in a cubic manner due to which the molecules do not arrange in the form of compact packages as happen in the HCP structure. [[1], [8], [9], [17]. One molecule is present at each corner of the cubic structure while one is present at the centre of the cube. However, there are large empty spaces in between the molecules due to which the crystal could be deformed very easily. As far as HCP crystal is concerned, such a form of crystal comprises of layers of molecules packed tightly together in a manner that all the layers of molecules lie adjacent to each other. The behaviour of crystal structure of the alpha phase plays a fundamental role in the elastic and plasticity physical properties. This increases the strength of titanium alloys [1], [8], [9], [17].

In summary, beta-ti alloys form and exhibit E-moduli at room temperature in the range of 70 – 90 GPa, while alpha+ beta ti alloys will have properties above >100 GPa [8], [9].

**Ti-6Al-4V**

The most commonly used Titanium (Ti) material grade in the industries is Ti-6Al-4V. It contains 90% titanium, 6% aluminium, and 4% vanadium as evident from its name, although the material can contain small amounts of other components, such as of oxygen, hydrogen, nitrogen, and iron [16]. This material has been extensively studied due to its exceptional properties, which include corrosion resistant, higher strength to weight ratio, and bio-compatibility among the key benefits [2], [6]. All these studies over the last three decades have helped manufacturers to enhance its qualities. [2], [6], [7].

Noneless, it should be noted that there are some disadvantages of using Ti-6Al-4V. These are, for example, higher reactivity, non-eco-friendly mining or extraction of the material, and the high production cost, making it one the most expensive materials. [3]. It's been reported [3] that the energy required for sponge extraction for Ti is 16 times more than that for steels hence the high cost. The material has been found to lose its strength when operating at elevated temperatures of above 350 – 400 °C. Nickel-based alloys are well suited to the operator at the conditions above. [5] [6]

BCC Transformation of Ti-6Al-4V to HCP in Phase

Both HCP and BCC have very different structures as far as the orientation of molecules is concerned. Therefore, these forms could be achieved by either heating or cooling. Study carried out by Campbell et al 2005 [16] found Ti transforms the HCP phase to the BCC phase at 1156K .Both structures have different coordination numbers. Apart from that, they have different packaging factors owing to the different alignment of molecules within their structure. Upon heating, the alpha phase changes into beta phase while when cooling to room temperature , the beta phase changes into alpha phase [2]. When cooling, Ti-6Al-4V changes into HCP structure and expand when cooled and contract when they are heated [5].The atoms of titanium alloy become distant from each other and do not remain in the form of tight packets as in BCC. In HCP, the atoms are located far from each other and are packed together in the form of cubes. This sudden change in shape occurs due to change in temperature [6] [3] [10].

Microstructure and Phase Transformation of Ti-6Al-4V

Ti-6Al-4V is an alpha-beta alloy, which means several microstructures of this alloy can be achieved with the help of thermomechanical processing. In this way, the highly customized alloy can be produced for specific applications. For instance, to produce an alloy with homogeneous microstructure, solidification of Ti-6Al-4V should be done at a higher solidification rate. The microstructure of this alloy is highly dependent on the heat treatment and processing history; therefore, these factors also play an essential role in defining the mechanical properties of this alloy. High-temperature X-ray diffraction (HT-XRD) can be used to monitor these phase transformations to analyse the kinetics of this process (Pederson, 2002).

α-β Phases transformations

As discussed, titanium is an allotropic material with a phase transformation from the α phase, which is a hexagonally close-packed (HCP) crystal structure to β phase which, is a body-centred cubic crystal structure (BCC). The titanium transition from α → β occurs at elevated temperatures occurring at 882˚C for commercially pure Ti and 995˚C for Ti-6Al-4V (Ding & Guo 2004). [17] This temperature is known as the β transus. Illustration shown in Figure 5 is a example illustration of titanium alloys transformation from BCC to HCP structure.

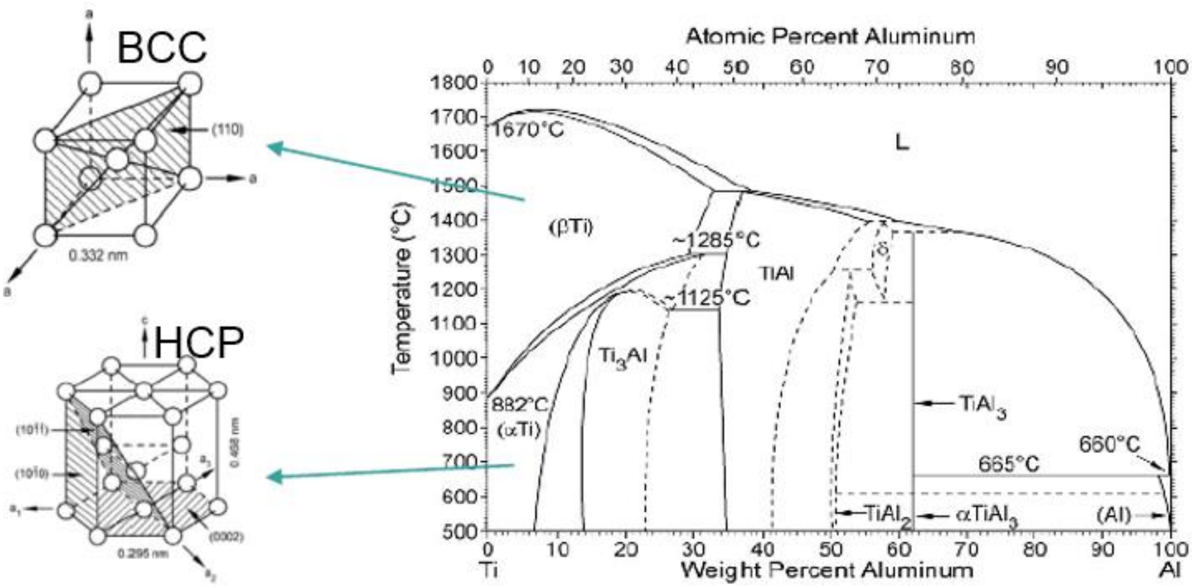


*Figure 5 the effects of alloy elements/stabiliser in phase transformation at different aluminium stabilising content [17].*

Through the addition of different alloying elements, the mechanical performance can be altered to enhance the desired properties for different end use applications. β transus temperature can be altered, with elements preferentially dissolving into either α phase (such as Al, N & O) or β phase (such as V, Mo, Fe, Cr & Ni) [5]. Additions of either α or β stabilisers will increase the temperature range over which the respective phase is stable, with the addition of β stabilisers retaining the β phase at room temperature [3] [14] [18]. Dai et al 2012 [18] study on Ti-6Al-4V found that only Al and Sn elements can increase the ω phase in comparison to other the β, α′, α″, and ω microsture.

The Table 1 below shows alloying elements (stabiliser) with effects on microstructure development.

| Effect | Alloying Elements |
|---|---|
| α-stabiliser | Al, Ga; interstitial: N, O, C |
| β-isomorphous stabiliser | Mo, V, W Ta |
| β-eutectoid stabiliser | Cu, Mn, Cr, Fe, Ni, Co, Si; interstitial: H |
| Strengthening elements | Sn, Zr ( solid solubility in α and β) |

*Table 2 Alloying elements and their effect on titanium alloys [6] [18].*

Nonetheless, it should be noted that numerous heat treatments have been developed to alter the morphology and volume fraction of α+β in Ti-6Al-4V. When heating Ti-6Al-4V above the β transus temperature occurs, entire microstructure enters the BCC β phase, then upon cooling back below the β transus, the grains transform to an acicular structure of transformed α platelets and retained β platelets between them. These platelets are commonly termed laths (see Figure 6).

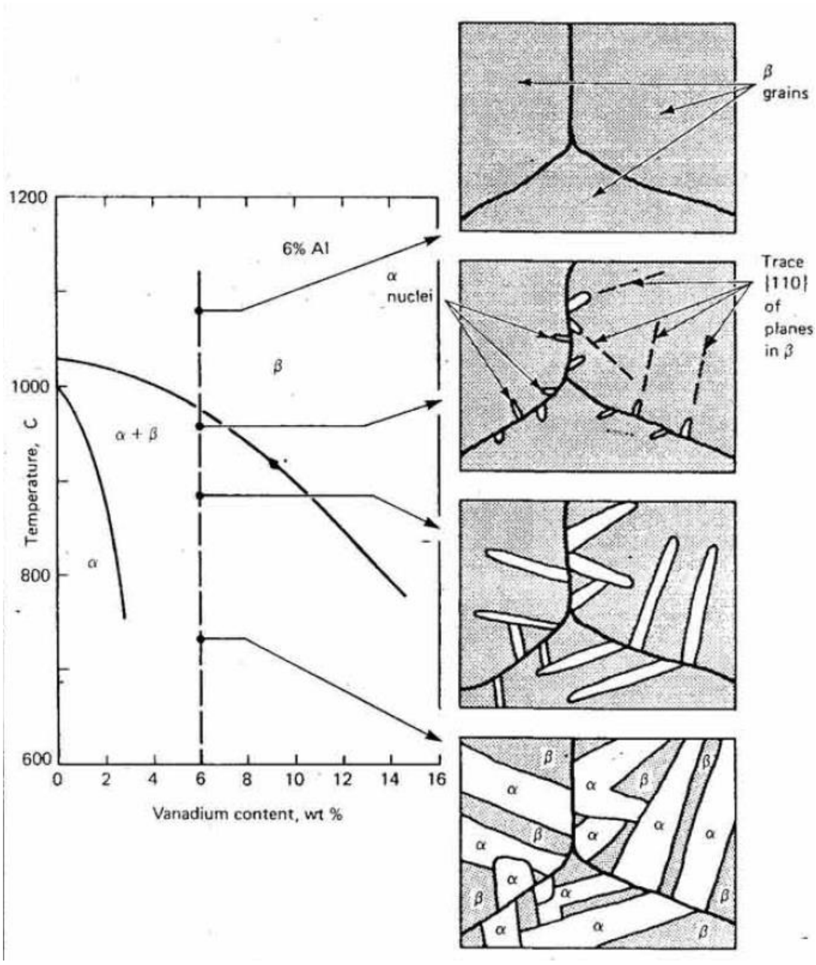


*Figure 6 Diagram illustrating α platelet formation when cooling from above the β transus temperature (Donachie 1988) [2].*

A heat cycle like this is affiliated or akin to EBM process during melting or called ‘builds,’ whereby the material is heated above the β transus temperature and then cooled down during and post-build completion [14]. However, the cooling rate has a significant effect on the microstructure morphology observed at room temperature. At slow cooling rates (typically observed in casting at ~1-5 K/s), α phase will precipitate at the grain boundaries first, with layers of α coating the prior β grain boundary, known as grain boundary α (GBα) and as shown in Figure 7 [5] [19] [20]. Following this, nucleation of common orientation laths at GBα or β grain boundaries will occur in the form of parallel sided laths (known as ‘α colonies’) growth will occur until laths meet an opposing colony nucleated on a different grain boundary. This is termed ‘α colony’ microstructure and shown in Figure 7. The colony length is typically given as a measurement of microstructure size. This is also because the colony size can act as the effective structural unit , meaning the material can act like the colony size is a single grain.

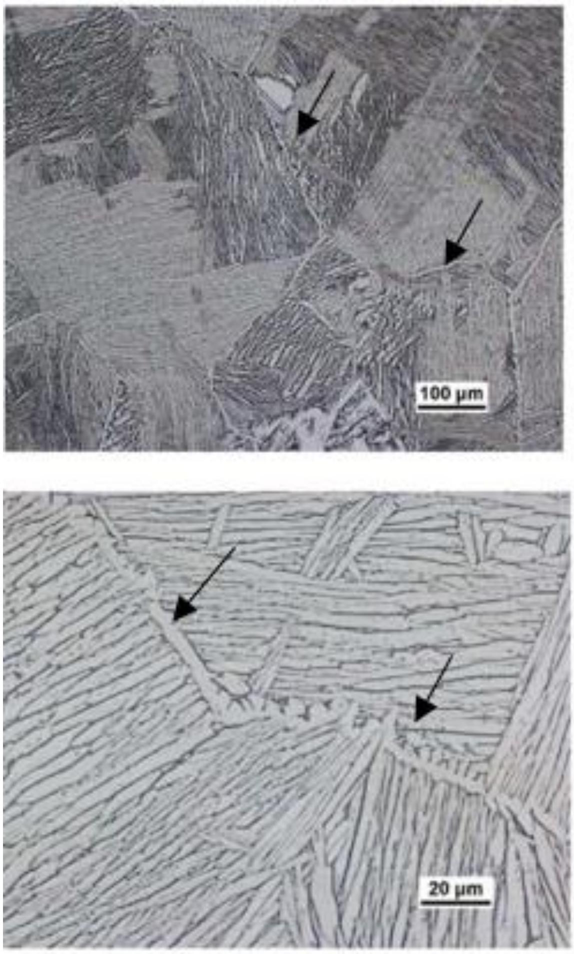


*Figure 7 Typical Ti-6Al-4V α colony microstructure at two magnifications, arrows highlight instance of grain boundary α [13].*

### 2.1.2 Microstructure development

Microstructure phase transformation is pre-determined by the solidifaction rate from the β phase. Sieniawski et al. 2013 [15] reported that kinetics during the phase transformation is correlated to the value of β-phase stability coefficient $K_\beta$ as a result of the chemical composition during the thermomechanical process. Figure 8 shows a Continuous Cooling Transformation (CCT) diagram of Ti6Al-4V at a rate above 18°C $s^{-1}$ thus leading to martensitic microstructure containing the α'(α'') [5] [15].

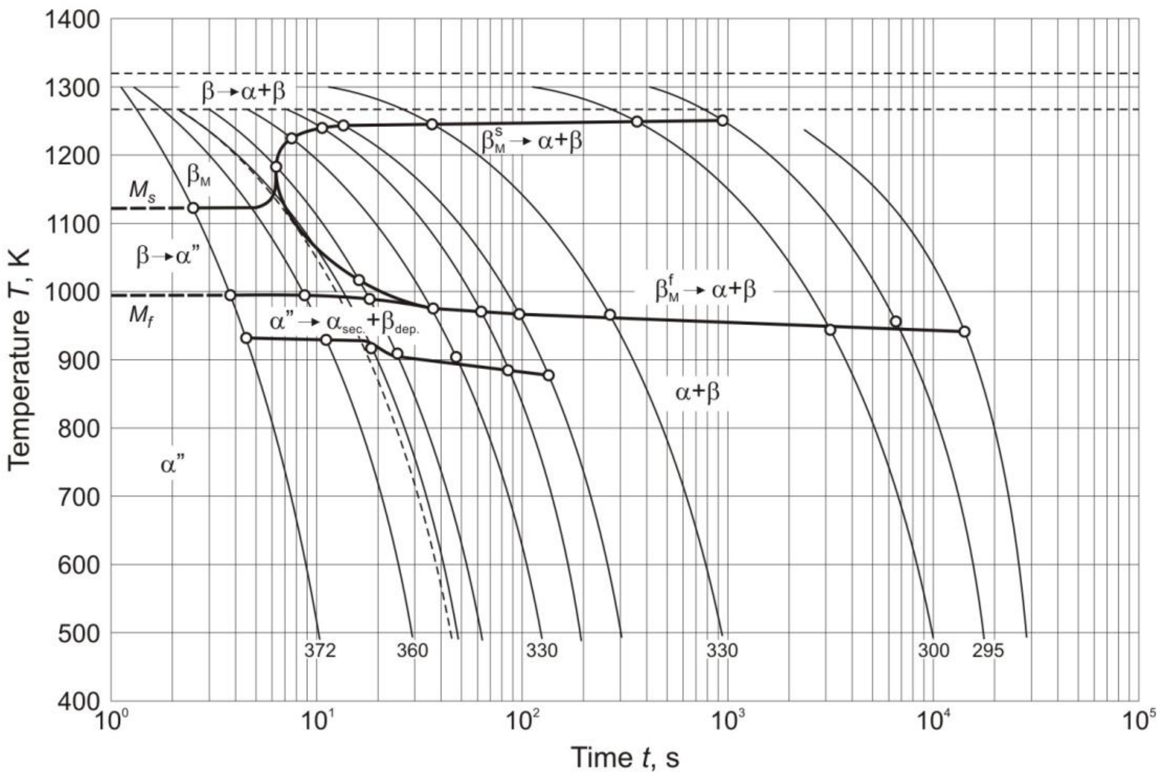


*Figure 8 Continuous Cooling Transformation (CCT) diagram of Ti-6Al-4V alloy [15].*

Increasing the cooling rate will introduce a higher driving force for solidification; hence, a higher number of nucleation sites. This produces precipitation of α laths throughout the β grains in a random arrangement with random orientations, fine regions of β phase will be retained between α laths. This is termed a 'basketweave' or 'Widmanstätten' microstructure, and an example is given in Figure 9. The width of α laths will also decrease significantly with a large increase in cooling rate and is another commonly cited microstructure measurement metric. Further increasing the cooling rate to above 410 K/s can cause titanium to undergo a martensite transformation, α → α' rather than the typical diffusional β→ α+β transformation. This martensite transformation occurs so rapidly that diffusion of alloying elements cannot take place, and so the HCP lattice shears to create the distorted hexagonal lattice structure termed α'. This leaves α' martensite heavily dislocated due to the imperfect shear transformation and with a composition equal to the alloy composition (6 wt. % Al and 4 wt. % V). Due to segregation of alloying elements, the α phase is high in α stabilisers like Al, and β phase is high in β stabilisers like V. The tensile strength of α' martensite is high but the ductility is low, so it is not a favoured microstructure and is avoided through controlling the cooling rate through process parameters. The α' will decompose under typical stress relief heat treatment cycle of 1-2 hrs at 600˚C (Donachie, 1988), if it can't be avoided through process parameter control.

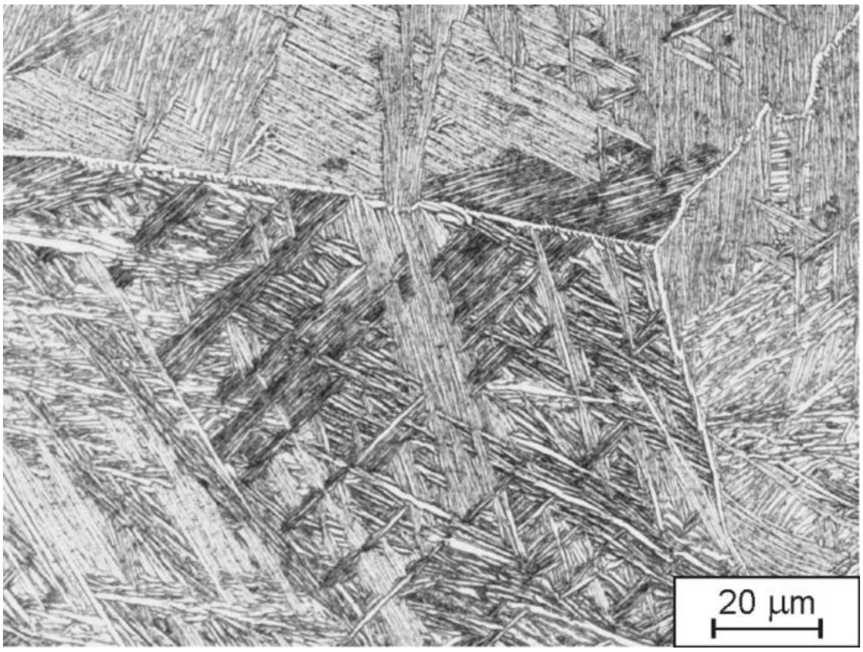


*Figure 9 Ti-6Al-4v ''Basket-weave" or Widmanstätten microstructure post cooling at 9°C s$^{-1}$ temperature [15].*

### 2.1.3 AM Powder Manufacturing

This sction will discuss four chief Additive Manufacture (AM) powder production manufacturing methods GA, PA, Hydride De-Hydride (HDH), Plasma Rotating Electrode Process (PREP), and finally, metallic components with specific emphasis on EBM (EBM) Ti-6Al-4V commercialised by Arcam AB, Sweden. Table 3 shows some of the current powder atomisation processes used to manufacture powder for AM process.

*Table 3 Summary of Powder Characteristics by Manufacturing Process [1].*

| Manufacturing Process | Particle size, μm | Advantages | Disadvantages | Common uses |
|---|---|---|---|---|
| Water atomisation | 0–500 | High throughput<br>Range of particle sizes<br>Only requires feedstock in ingot form | Post processing required to remove water<br>Irregular particle morphology<br>Satellites present<br>Wide PSD<br>Low yield of powder between 20–150 μm | Non-reactive |
| Gas atomisation (inc. EIGA) | 0–500 | Wide range of alloys available<br>Suitable for reactive alloys<br>Only requires feedstock in ingot form<br>High throughput<br>Range of particle sizes<br>Use of EIGA allows for reactive powders to be processed<br>Spherical particles | Satellites present<br>Wide PSD<br>Low yield of powder between 20–150 μm | Ni, Co, Fe, Ti (EIGA), Al |
| Plasma atomisation | 0–200 | Extremely spherical particles | Requires feedstock to either be in wire form or powder form<br>High cost | Ti (Ti64 most common) |
| Plasma rotating electrode process | 0–100 | High purity powders<br>Highly spherical powder | Low productivity<br>High cost | Ti<br>Exotics |
| Centrifugal atomisation | 0–600 | Wide range of particle sizes with very narrow PSD | Difficult to make extremely fine powder unless very high speed can be achieved | Solder pastes, Zinc of alkaline batteries, Ti and steel shot |
| Hydride–dehydride process | 45–500 | Low cost option | Irregular particle morphology<br>High interstitial content (H, O) | Ti6/4<br>Limited to metals which form a brittle hydride |

### 2.1.4 Titanium Powder Atomisation

Most powders are manufactured with chemical electrolytic or atomisation methodologies. Almost all the current atomisation processes use energy source such as plasma torches , induction coils with nozzle to melt a metal in wire feedstock or which then forms spherical droplets and solidify into powder particles [21] [1].

Figure 10 demonstrates AM powder qualities as a result of different powder atomisation process. It can be seen the pores in cross section

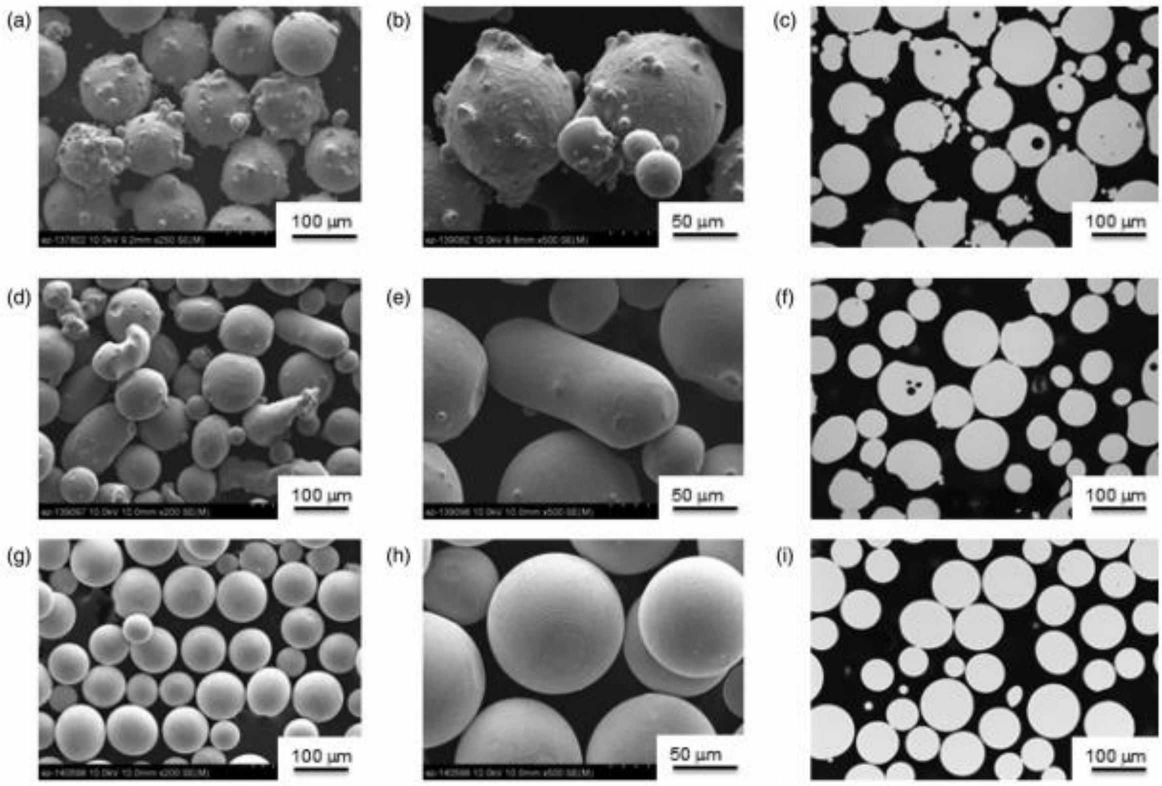


*Figure 10 SEM of AM powder manufactured by (a) GA,(b) Satelite particles on GA powder, (c) gas pores from GA powder (d) PA (e) aggromented particle (f) smaller gas pores than GA powder (g) Prep (h) Prep spherical particle (i)no gas pores [22].*

### 2.1.4.1 Plasma Atomisation

Plasma atomisation (PA), shown in Figure 11, is the process of melting a wire spool feedstock of metal with a plasma torch, and cooling it in an inert tower [23]. Unlike EIGA powder, PA process has much better spherical particles in-comparison to EIGA, however, the cost of powder can be higher compared to EIGA powder. Prep atomisation is known to produce much better improved spherical powder but comes at a higher cost [23] [1], [24].

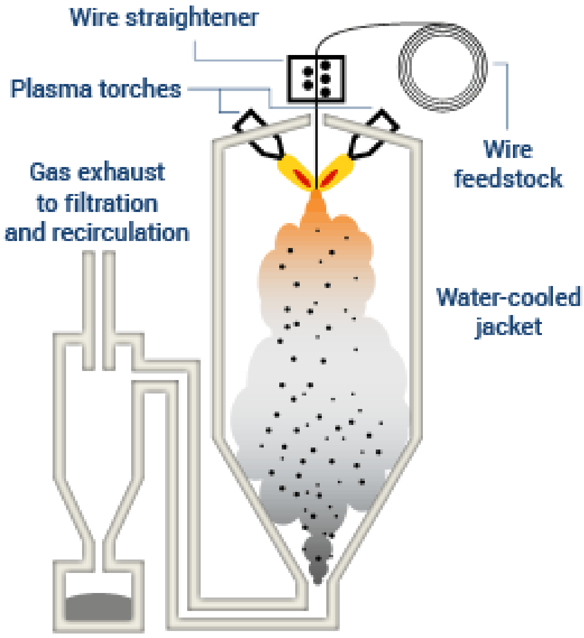


*Figure 11 AP&C Advanced Plasma Atomization process [25].*

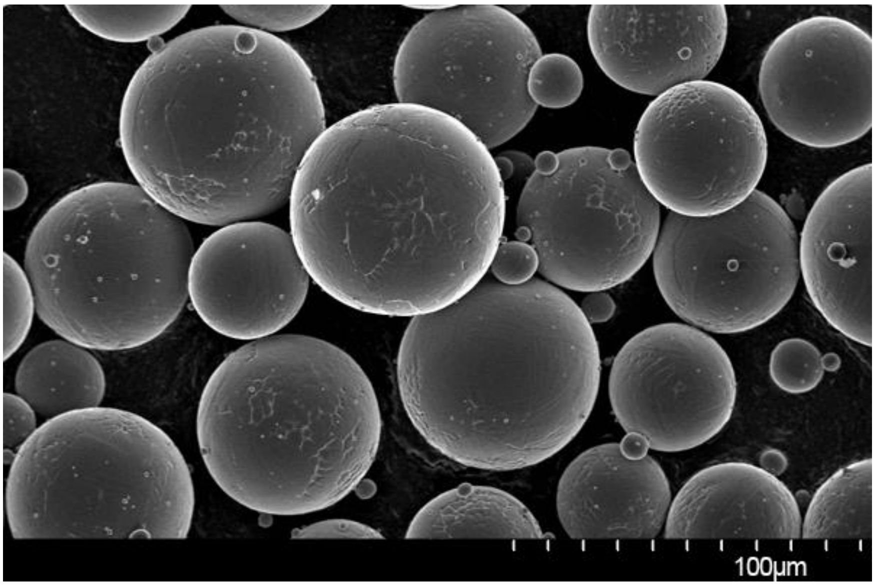


*Figure 12 SEM image of PA Ti-6Al-4V (45-106 µm) [26].*

Spherical particles with a small amount of relatively small satellites are shown in Figure 12 above. The atomisation process environment operates in a vacuum to minimise metal oxidation levels and reduce gas entrapped. Although the process is limited to alloys that can be formed in a wire spool batch, this allows the traceability of the powder batches. According to powder manufacture AP&C [26] PA powder exhibits the following characteristics: It has a spherical particle shape, with minimal satellites or internal pores. The level of metal oxidation is reasonably high, and a particle sizes up to 200 μm. It also possesses good flow and packing properties required for EBM process.

*Figure 13 shows three reactors in 2015 used to manufacture PA powder at AP &C [27].*

*2.1.4.2 Gas Atomisation*

Gas atomisation (GA) process shown in Figure 14, is another atomisation process in which the metal feedstock is melted under an air or inert gas blanket or vacuum, and the melting stream is broken up by gas or air jets, usually air, nitrogen, argon, or helium [28]. Historically, Yang et al. reported the GA process as the traditional method of obtaining or manufacture spherical powder since 1872 and first patent was by Marriot of Huddersfield [28]. Other methods such as ‘free fall,’ ‘confined’ or closed nozzles have further been further developed to improve the quality of powder manufacture. [29]

Apart from titanium, many other materials have been spheroidised by this process, and these include aluminium, cobalt chrome, copper alloys, nickel-based and precious metals to name the few, [29]. Inert gas such as nitrogen or argon is used as the atomising media to reduce metal oxidation . The low heat capacity of gas as the atomising media means that the metal droplets have a relatively high solidification time resulting in spherical powder [28]. The particles size distribution can range usually 15 - 65µm for laser powder bed while EBM will usually have larger particles of 45 -106 µm . The varying range is influenced by ratio of gas to melt flow rate during atomisation, and then powder is sieved prior to shipment to customers [23].

In comparison to PA process, GA has a more extensive range of materials such as but not limited to copper alloys, Inconel, Aluminium alloys; Titanium alloys can be atomised and Spheroidised by this process [28].

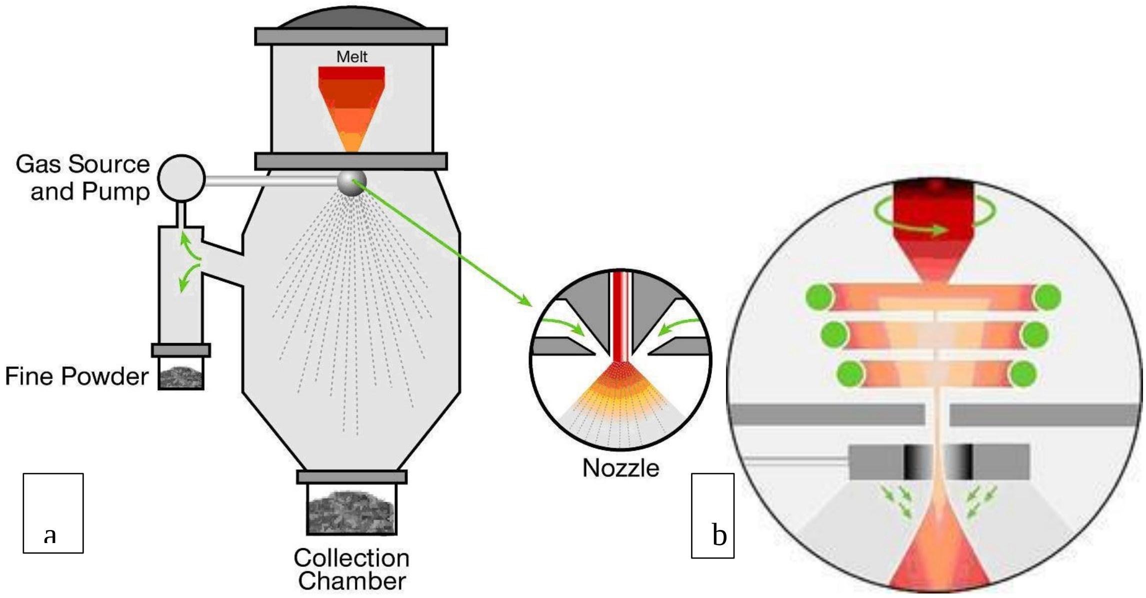


*Figure 14 (a) Gas atomisation processed [23]  (b) Schematic of EIGA atomiser using induction coils to melt feedstock [9].*

Another variation of GA is **Electrode Induction GA (EIGA**), whereby a metal bar feedstock is rotated and melted by an induction coil. This method is mostly used when processing reactive alloys such as Ti6/4. However in comparison to PA the cost of powder is lower due to the use of cheaper gas and less spherical and more satellites than PA. [1]

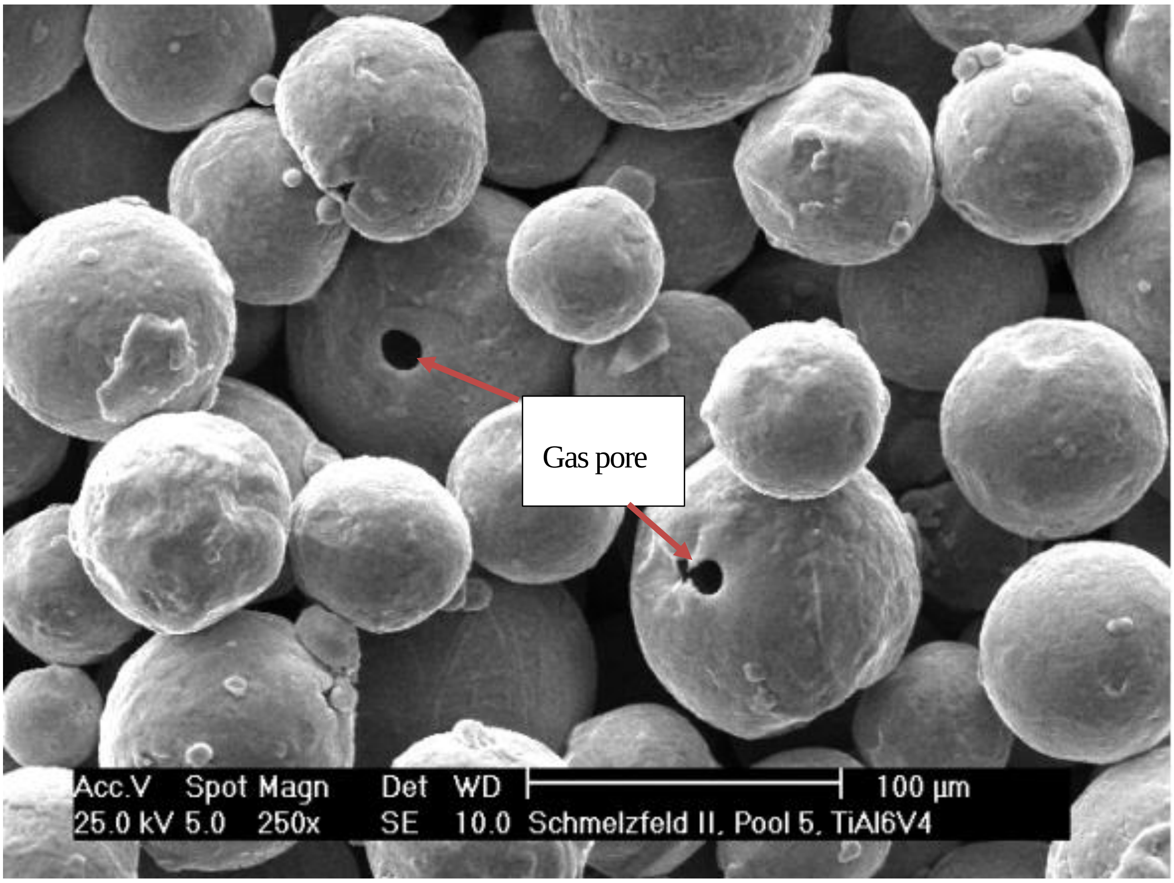


*Figure 15 SEM of Ti6Al4V gas atomised powder particles with pores [19].*

*2.1.4.3 Hydride De-hydride*

The Hydride De-Hydride (HDH) is considered to be a cheap and lower grade of metal powder manufacturing with an irregular particle shape compared to other atomisation process aforementioned methods, which is a mechanical process, whereby titanium sponge is hydrogenated at high temperature to make the material brittle and more susceptible to breakdown in the milling process (IMPD, 2015). Once milled, the titanium lumps are dehydrogenated and followed by post-processing, including screening and classification. [24]

Yang et al. 2015 [28] reported HdH powder as having a high level of metal oxidation and other contamination including chlorine. Particle size can range up to 500 µm due to the irregular morphology of the powder, flowability and packing density are compromised. Therefore, HDH powder is typically not used for HIP and is more suited to press and sintering. Medina Francisco 2013 [24] was able to demonstrate the use on non-spherical powder HDH mixed with spherical powder ration in EBM S12 system to demonstrate the capability and cost reduction and productivity use in AM [24]. HDH process is shown below Figure 16

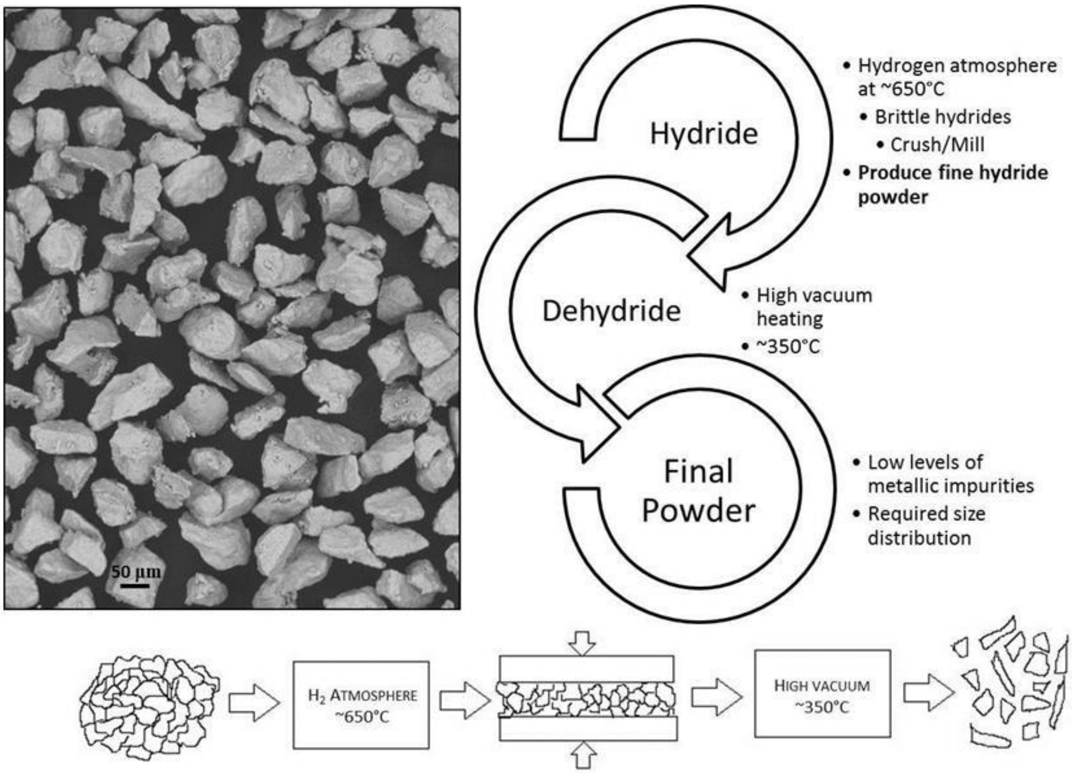


*Figure 17 On the left is SEM image of Ti6/4 powder produced using HDH process. On the right is an illustration of the HDH process [8].*

Plasma Spheroidised (PS) is a method to make irregular powder spherical. This is achieved by heating the irregular powder, such as HDH powder, in a plasma gas stream to melt the particles to increase the sphericity, tap density, flow and purity of the particles [24]

After EBM parameter development or use in any application, the powder is characterised to define its quality in accordance to ASTM standards. (Although at the time of writing this thesis , some of the ASTM standards are still in development). To determine safe use of powder in process or to handle in the EBM system, a minimum ignition energy (MIE) test can be carried out in accordance to standard BS EN 13821:2002 to ensure and minimise any fire ignition of powder due to metal reaction with other metal during handling. [28]). Figure 18 shows the powder characterisation workflow for AM mostly followed to understand the key powder variables.

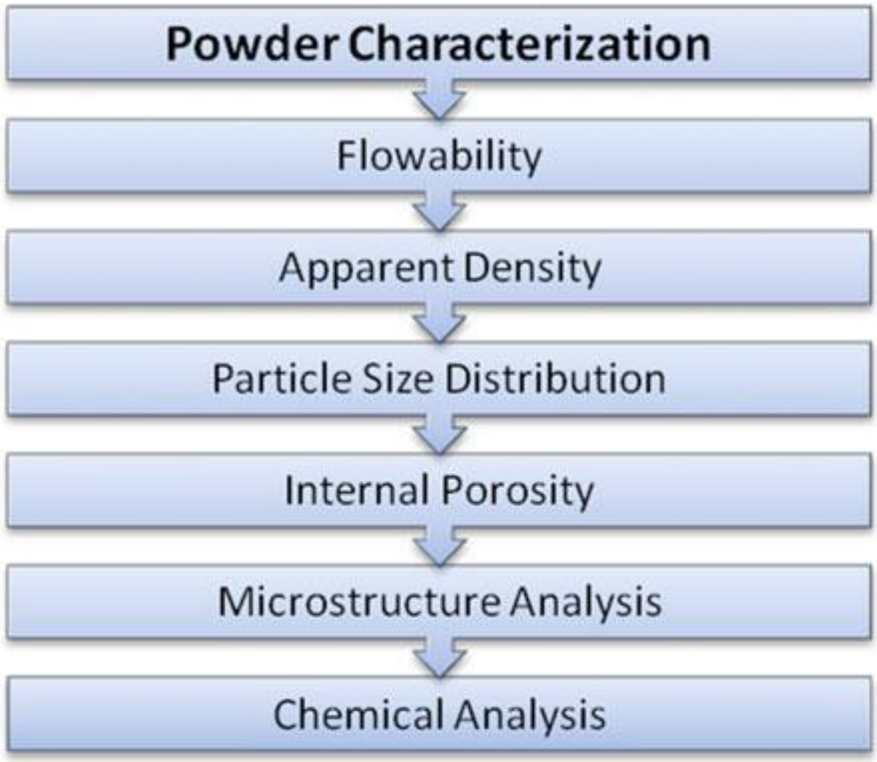


*Figure 18 Powder characterisation workflow ref [28].*

Powder characterisation techniques are used for assessing powder properties. Table 4 below shows some of the most frequently used techniques. This will be discussed further in the experimental methodology section of this report.

*Table 4 Powder Key Process Variables (KPV's) and techniques being used for measurements [1].*

| Particulate properties | | Bulk properties | |
|---|---|---|---|
| **Powder property** | **Assessment technique** | **Powder property** | **Assessment technique** |
| Particle shape (morphology) | SEM<br>Optical microscopy | Apparent density | Hall flow<br>Freeman FT4 |
| | | Tap density | Tapped density tester |
| Particle size and particle size distribution | Sieve<br>Laser diffraction<br>Optical microscopy | Flowability | Hall flow<br>Dynamic flow testing (e.g. revolution, Freeman FT4)<br>Shear cell<br>Angle of repose |
| | | Cohesiveness | Freeman FT4 |
| Particle Porosity | Particle polishing and optical microscope | Surface Area | BET surface area analysis |
| | | Chemical composition | ICP-OES<br>XRD<br>Inert gas fusion<br>Combustion infrared detection |

## 2.1.5 Powder Costs

As the demand for titanium alloy powder increases in AM, the demand and competition to reduce the cost of material are also increased. According to the Wohler's Associates [30], the revenue for AM grew by approximately 81% in 2015, and this is estimated to have been $88.1million compared to £48.7 million in the previous years. The cost of materials for AM can surpass those of traditional manufacturing. Research carried out by Atzeni and Salmi (2012) [31]on aluminium alloy metal part, found that the part costs €2.59 per part when using conventional methods, while AM SLS cost €25.81. This only goes to show that although AM is advantageous in manufacturing complex geometries, light weighted or better mechanical performance, the end product can be costly for production.

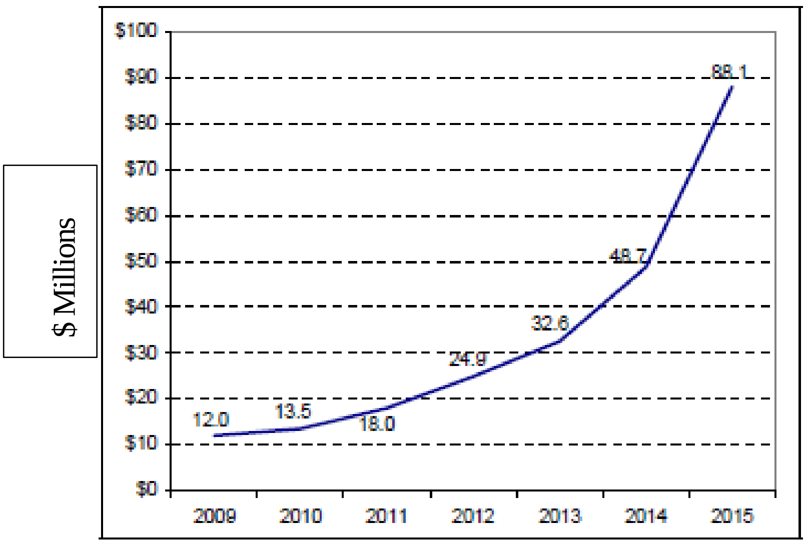


*Figure 19 Shows the AM revenue growth from material and AM equipment [29]*

### 2.1.6 Challenges in AM

The National Strategy for AM summarises the principal barriers to the commercialisation of AM [32]; the initial analysis was based on evidence collected from multiple stakeholders (848 individuals input through a workshop) across the UK, in 2015. The top issues chosen by the participants of the workshop are shown in Table 5.

*Table 5 Key concerns ranked in the national strategy for AM [32].*

| Ranking of top issues | Comments |
|---|---|
| 1. Materials | Materials availability / protection, consistency, standardisation / certification, characterisation. |
| 2. Standards | Mainly for materials, but also more generally (e.g. products made using AM-3DP processes). |
| 3. Cost | Realistic estimate of costs compared to scale of opportunity to allow for viable business case, cost of testing / development. |
| 4. Education / Skills | A broad range of issues including general level of awareness of AM-3DP, what skills will be required / availability of skilled people. |
| 5. Design / Software | Issues of design and software were bundled together by groups – design guidelines, modelling, design opportunities. |
| 6. IP | Balancing need to collaborate with IP concerns, IP and material availability. |
| 7. Measurement | Particularly technology for in-process inspection. |
| 8. Scale-up | Not clear whether this relates to increase in physical volume and/or numbers produced. |

To identify the main challenges, a literature review, an internal workshop, and steering group one-to-ones were conducted with the participants of this project. Figure 20 depicts the main challenges that were identified. The challenges were split into the following six main areas of the AM process chain: design, inspection, data & knowledge management, process, production cost, and development of standards.

*Figure 20 Common challenges in AM [32].*

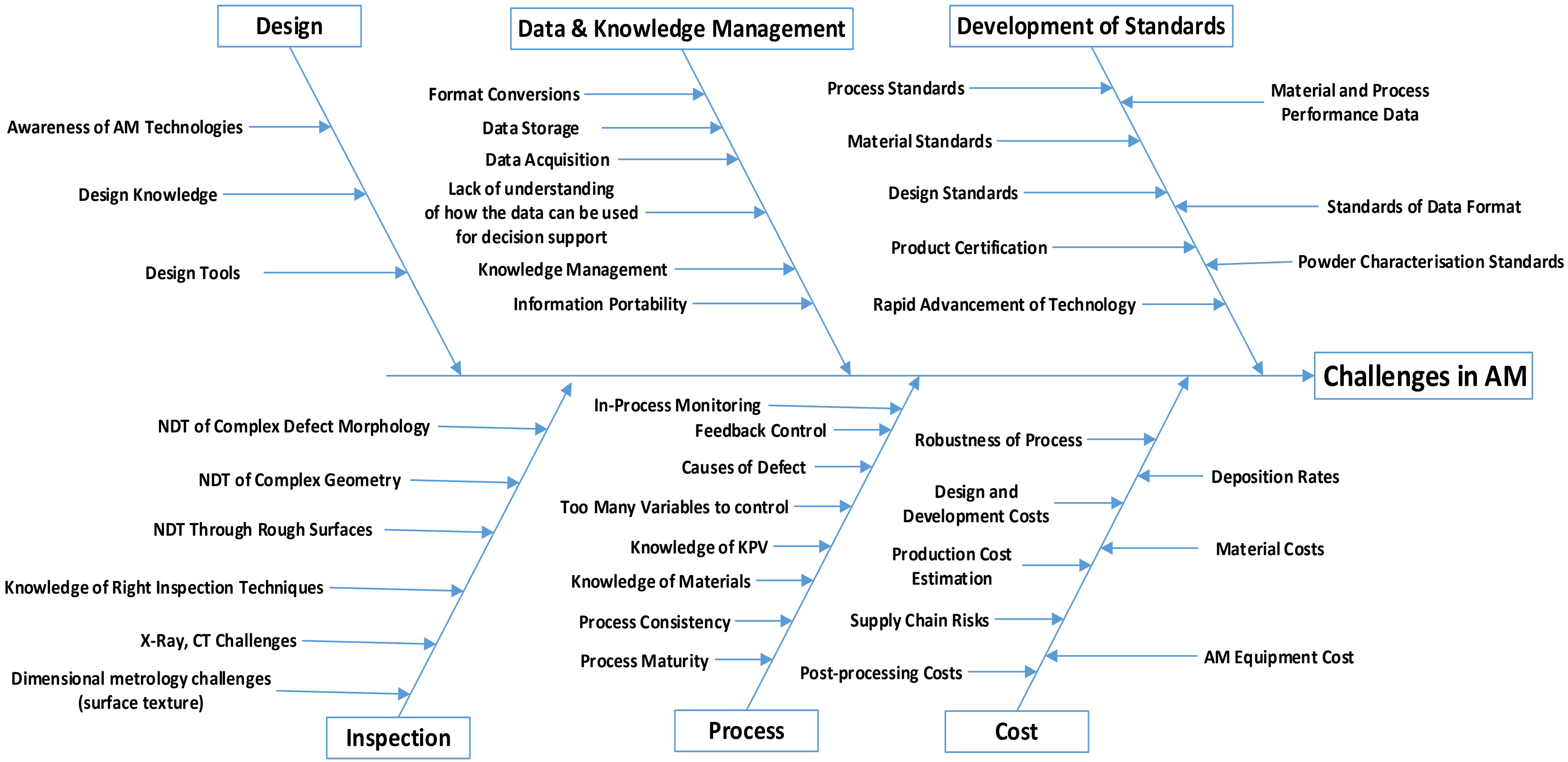

## 2.2 Technology Review of AM

In accordance to the ASTM F-42 [33] committee, AM is defined as:

*"The process of joining materials to make objects from 3D model data, usually layer upon layer, as opposed to subtractive manufacturing technologies*" [30].

AM technologies involve spreading a layer of powder on a base plate and selectively melting areas on the powder bed (pre-defined by 3D CAD data) and melting of the material. The build plate is lowered, and the process repeated so that fusion can occur between the layers. This process is repeated until the required height is completed. Generic process for AM is shown in Figure 22

*Figure 21 AM workflow [33]*

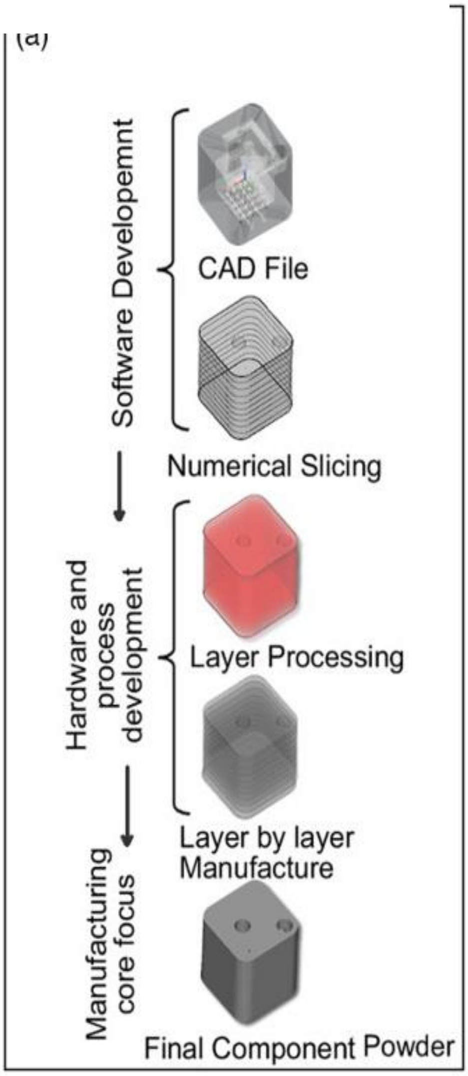


1. **CAD** (Computer Aided Design) – This can involve almost any CAD modelling software and data format is any 3D solid such as e.g. .step, IGES, parasolid format
2. **Conversion to STL format** – This triangulation CAD format is the external closed surfaces and enables basis for calculation of the 'slices.' /layers
3. **File Transfer** – The STL file is then used to orient and generate supports for overhang feature.
4. **Machine Setup** –setup include build settings/parameters, powder recycling, machine cleaning , hardware setup and so on.
5. **Build** – The melt algorithm or parameters are then processed (automated) layer by layer
6. **Remove** – Once the AM process has finished, the part needs to be removed.
7. **Post-Process** – Base plate or parts supports are removed or separated from to be used.
8. **Application** – Parts may require additional post-treatment depending on the application, for example, surface finishing, machining, painting, before they are acceptable for use.

Figure 23 comprises of metal AM processes currently on the market. Different commercial trademarks are given by manufacturers to distinguish their process. This thesis will mainly focus on the EBM (EBM) process highlighted in 'green.'

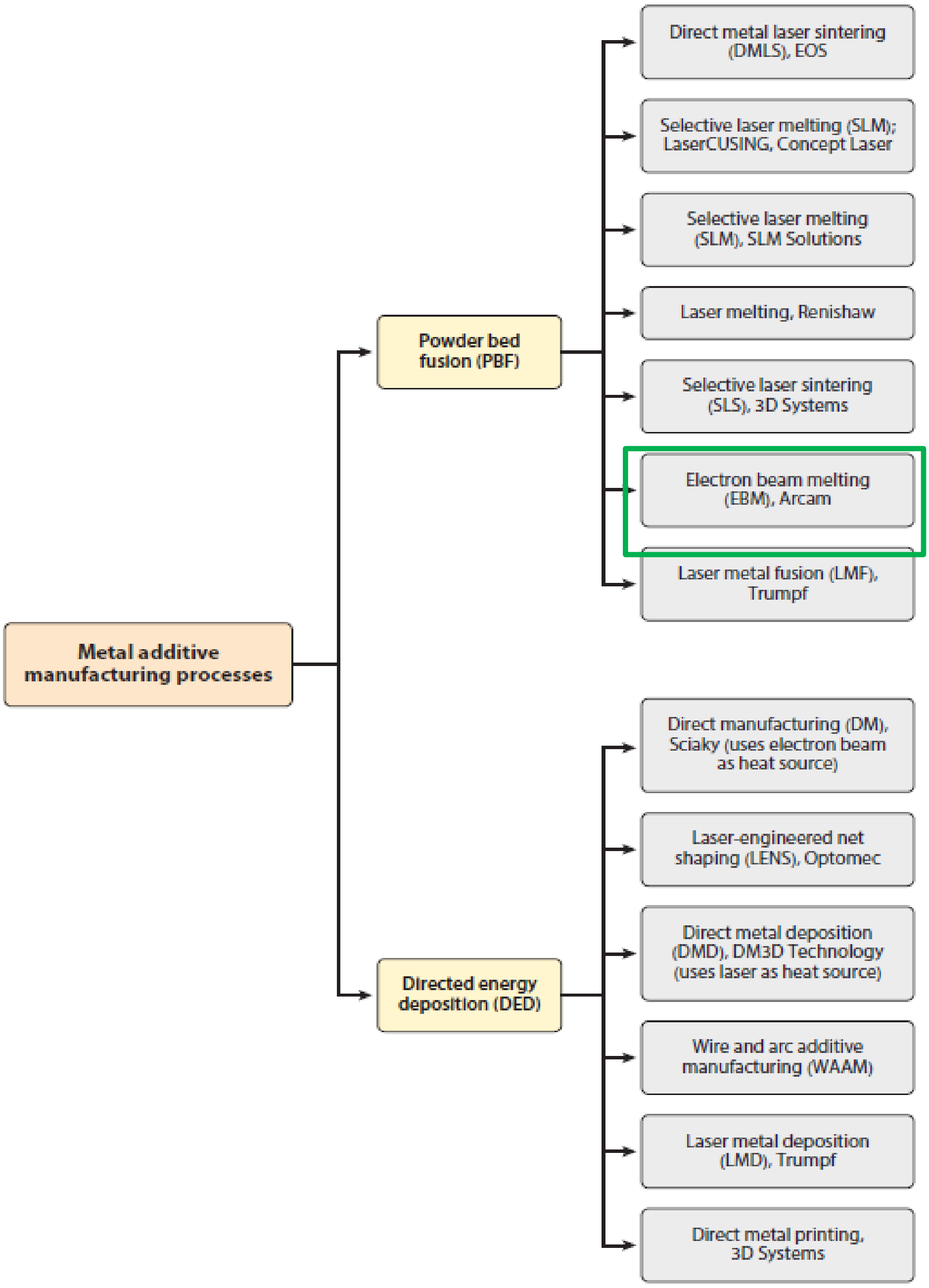


*Figure 23 AM processes, along with their machine providers trademark names, with EBM technology highlighted in 'green,' is the primary focus of this thesis [20].*

### 2.2.1 Laser Powder Bed Fusion (L-PBF)

Laser powder bed (L-PBF) is a technology that utilises a laser as an energy source for powder fusion, Figure 24. The build start baseplate is semi stress relived by heat to approximately 80°C (depending on the build material). Fine powder size approximaterly 15 – 63 µm is covered to layer thickness ranging between 20- 100µm layer thickness evenly onto the build platform using the re-coater (wiper), and a laser beam (between 200 W and 1 kW in power) is selectively applied to the powder bed, melting the areas specified by the 3D model data. Upon completion, the build plate from moves down by a controlled amount specified in the build model, and process is repeated till build completion. The process environment is usually in an inert atmosphere (argon or nitrogen) so as to minimise the introduction of impurities into the build. The completed parts are covered in loose powder at this stage, and they can be removed by brushing or vacuuming and then sieving to be re-used.

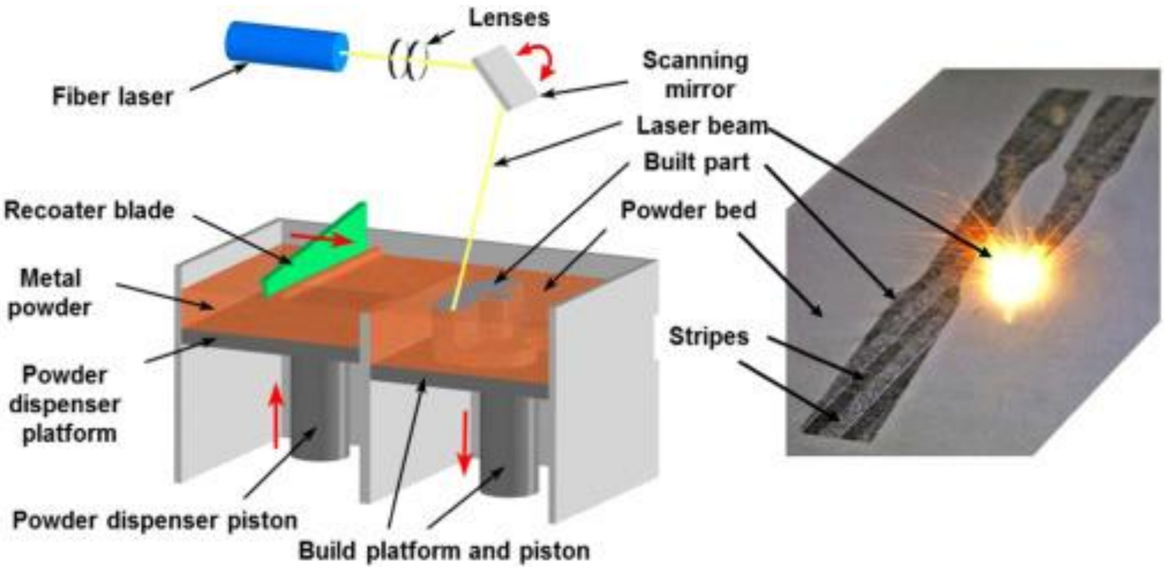


*Figure 24 Laser powder bed fusion illustration of how the process works [21].*

L-PBF process illustrating step by step in shown Figure 24 in the next page, from material feed to part removal.

*Figure 25 The L-PBF build process steps, from material feed to part removal. [21].*

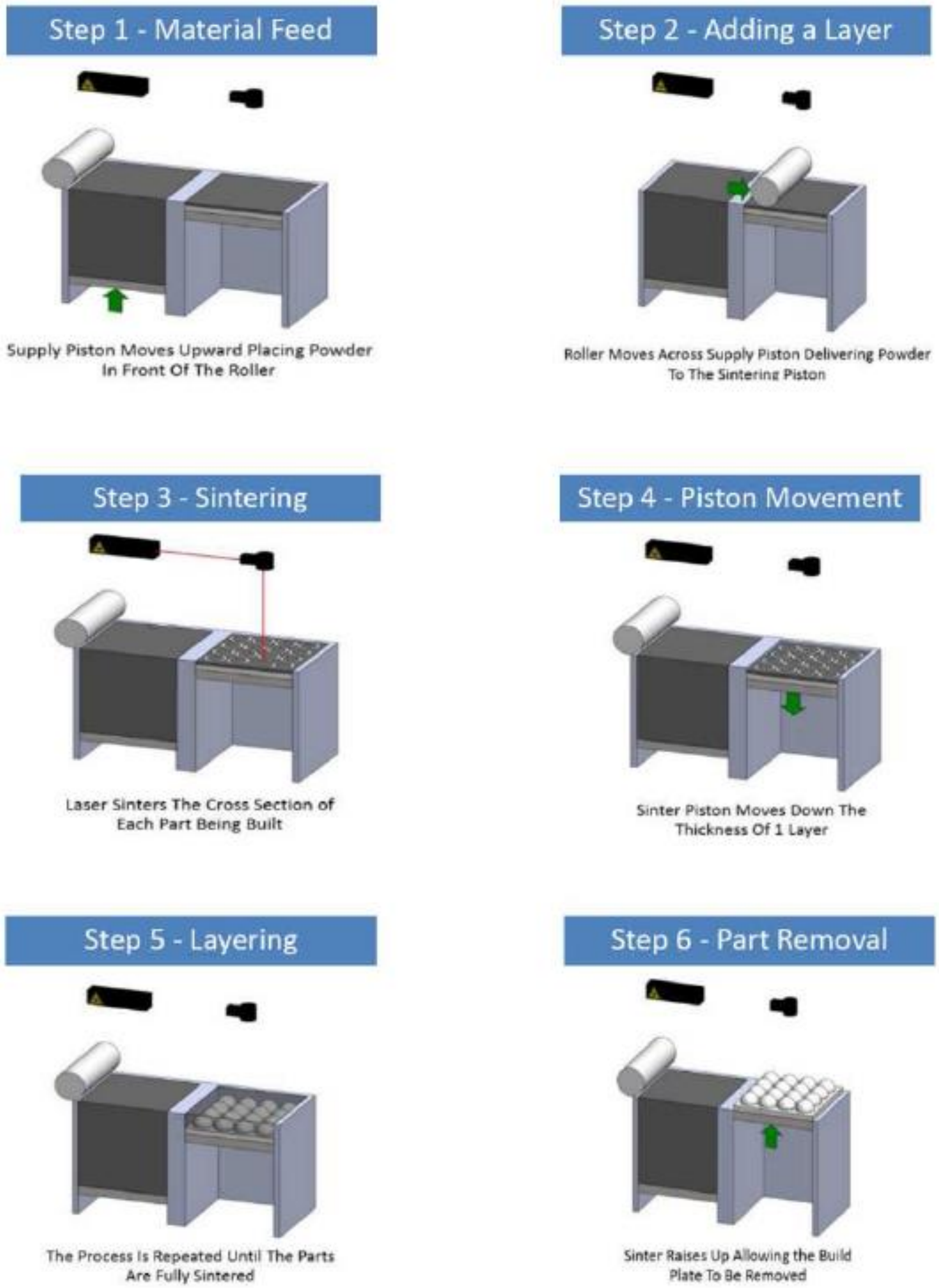

### 2.2.2 EBM Process Overview

Chalmers University of Technology initially developed the EBM process in the late 19th Century, and the Swedish company Arcam AB has further marketed it [34]. Currently, EBM process is primarily used in biomedical (orthopaedic implants) and aerospace industry. In 2016, GE Additive acquired Arcam AB to control majority of share of the company [35] Also, unlike other L-PBF processes, EBM process with up to 3.3 kW gun is used to melt powdered metal. The process is held under a high base vacuum pressure of 5 x$10^{-5}$ mbar for the entire build. Helium is partially purged to 4 x$10^{-3}$ mbar to ensure a clean melt process environment [36] [37]. The controlled vacuum is required to maintain proper chemical composition specification for the build. Figure 26 is EBM process illustration and EBM Q20+ used in this project.

*Figure 26 on the left is Electron Beam Melting process schematic and on the right is the Q20+ model used in this project. [36].*

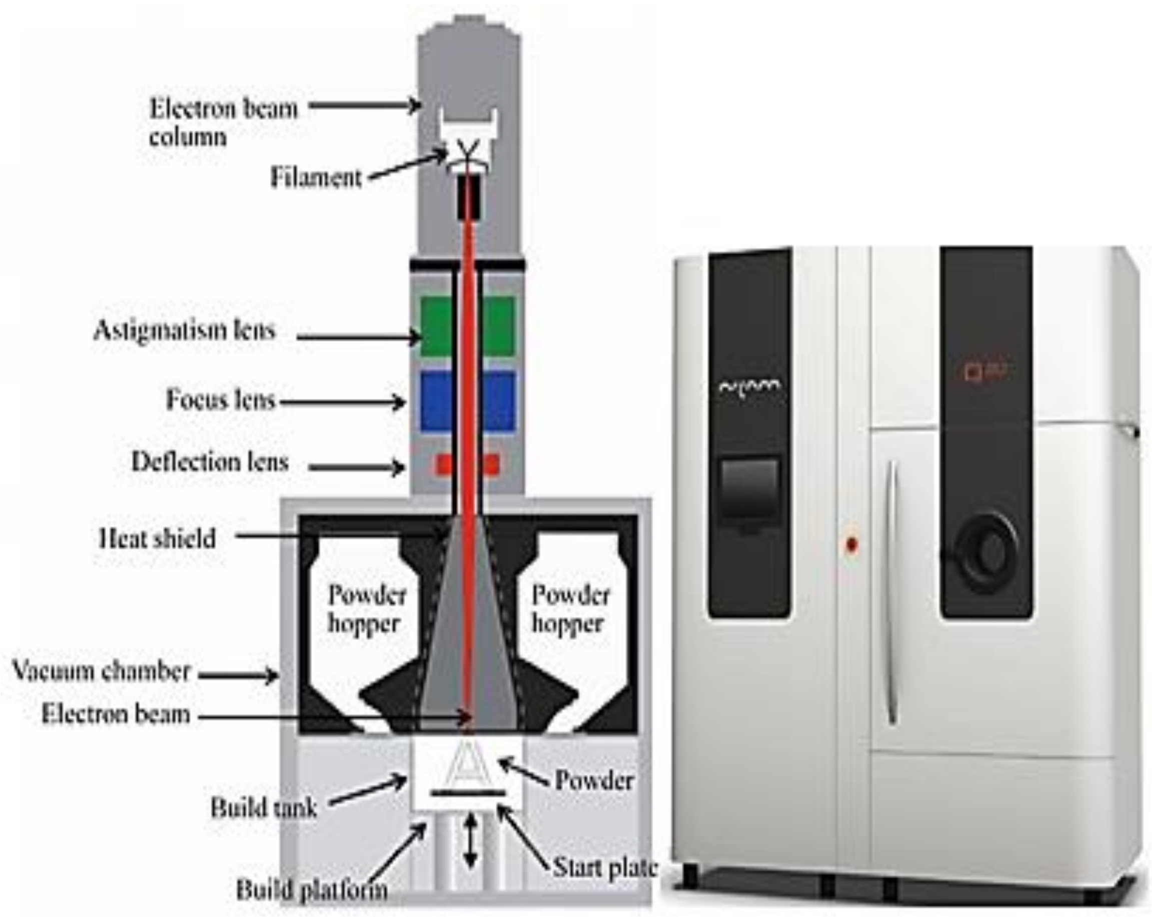


A single layer of powder of controlled thickness typically 50 µm to 90 µm is spread across a flat surface.

1. The support powder around the part is pre-sintered using the electron beam to lightly fuse the particles together to avoid a charge build-up producing a "smoke" (powder become airborne within the build chamber), this is referred to as 'Preheating.'
2. The required part area is then fully melted using the electron beam. Firstly, by melting an outline (contouring) and then 'in-filling' (hatching) the required area.
3. The table is lowered by a controlled amount, and this process is repeated until the build is complete.
4. Upon completion, before opening the door, the build is left to cool down to up to 80-100 $^{o}$C.

This project will mainly focus specifically on the Arcam Q20 machine, shown in Figure 26. The latest Arcam EBM generation has the additional features, such as in-process monitoring and active cooling technologies discussed further on in this literature. Table 6 compares EBM systems currently available on the market.

| **System** | **Electron Source** | **Build Chamber size (mm)** | **Beam Focus Diameter** | **Materials Commercially available** | **In-situ monitoring capability** |
|---|---|---|---|---|---|
| Arcam Q10 | Single crystalline | 200x200x180 | 100 µm minimum – varied during the build | Titanium alloys<br>Cobalt Chrome | Yes (LayerQam and XQam) |
| Arcam Q20 | Single crystalline | Ø350x380 | 180 µm minimum – varied during the build | Titanium alloys<br>Cobalt Chrome | Yes (LayerQam and XQam) |
| Arcam A2X | Tungsten Filament | 200x200x380 | 0.2-1.0 mm– varied during build | Titanium alloys<br>Inconel | No |

*Table 6: Arcam Q10, Q20 and A2X specifications [36].*

Figure 27 is the EBM Q20+ model technical specification from Arcam manufacturer.

*Figure 27 EBM Q20 technical specifications [36].*

| | |
|---|---|
| Max. build size | 350 x 380 mm (Ø/H) |
| Max. beam power | 3000 W |
| Cathode type | Single crystalline |
| Min. beam diameter | 140 µm |
| Max. EB translation speed | 8000 m/s |
| Active cooling | Water-cooled heat sink |
| Vacuum base pressure | 5 x 10-4 mbar (chamber pressure before start of process) |
| Build atmosphere | 4 x 10-3 mbar (partial pressure of He) |
| He consumption, build process | 4 l/h |
| He consumption, build cool down | 100-150 l/build |
| Power supply | 3 x 400 V, 32 A, 7 kW |
| Size Approx. | 2400 x 1300 x 2945mm (W x D x H) |
| Weight | 2900 kg |
| CAD interface | Standard: STL |

**EBM process in detail**

Unlike L-PBF processes which uses photons to selectively melt powder [38]. EBM process uses electrons emitted from tungsten or cathode are to manufacture parts. Electrons have a negative charge of 1.61.6x $10^{-19}$ Coulombs [39].The intention of preheating each layer using the melting process is to sinter the area to be melted partially. The sintering of the layer is referred as 'Preheat' and is sub-categorised into two process steps:

- Preheat 1 (PH1) area is intended to semi-sinter the whole melt area prior to halth or melting of the 2D XY layer as shown Figure 28.

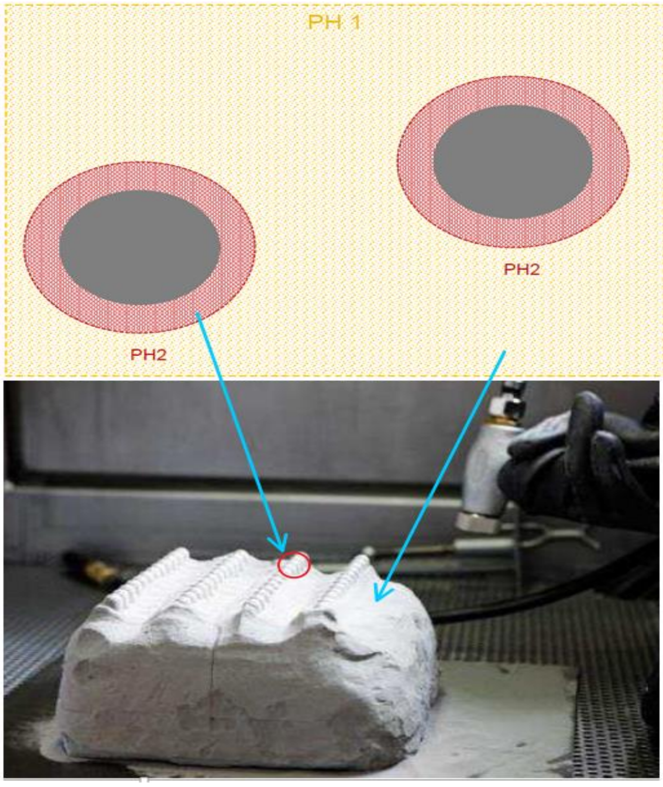


*Figure 28 EBM Sintering or preheating schematic. PH1 - sinters the entire layer while PH2 is additional sintering before melting the part area [37].*

Following the preheating, the part is selectively melted into by applying the:

**Contour**: mainly used to melt the CAD periphery or boundary, which also influences the surface finish of the part.

**Hatch/Melt**: this parameter melts the core area of the part cross-section using beam power, hatch offset distance and speed among other parameters. Numerous researchers have studied the influence of the parameters. This paper will discuss them later on. [40] [41]

The contour strategy uses two passes referred as 'inner' and 'outer' contouring as shown below in Figure 29

The contour strategy uses two passes referred as 'inner' and 'outer' contouring as shown in Figure 29

*Figure 29 EBM scanning strategy illustration for contour and hatch melt pool [37], (a) is the contour scan (b) in-fill hatching [5].*

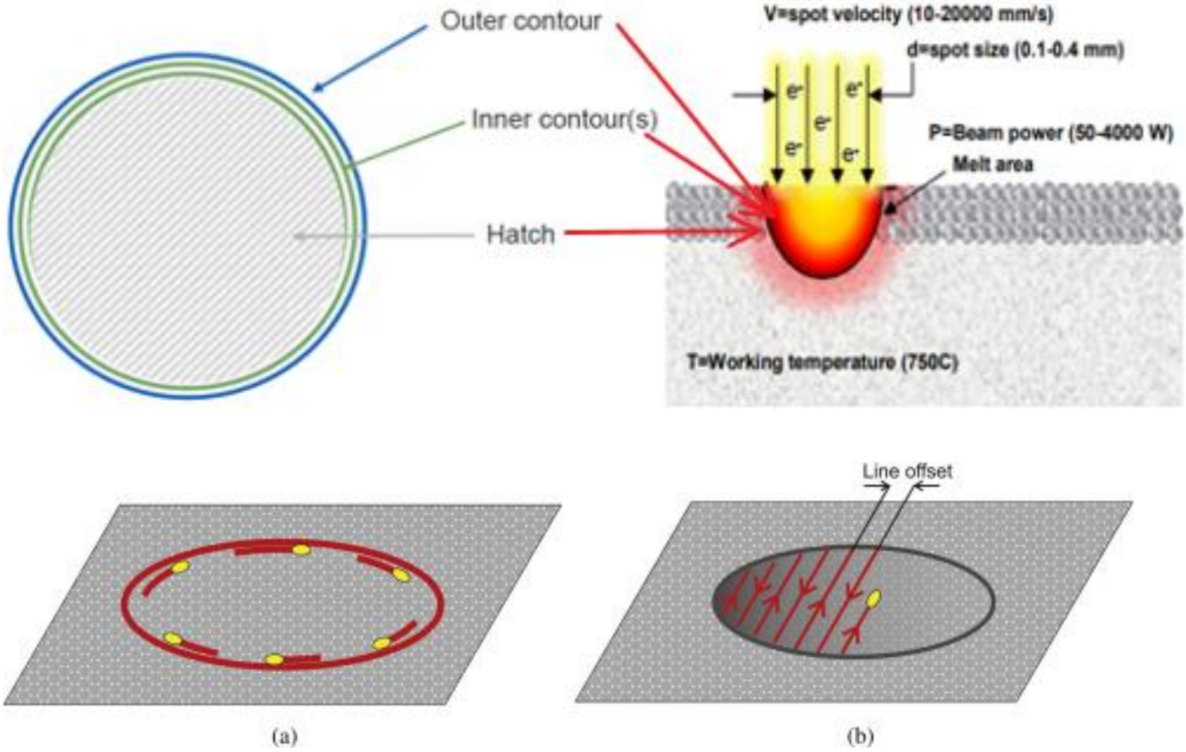


2.2.3.1 EBM process calibration

For EBM AM methods, electron beams are focussed using electromagnetic lenses rather than the physical lenses used in laser optics. The beam focus offset may also be altered in EBM to maintain a consistent melt pool. During contouring, the beam may have no focus offset before being defocussed to produce the core of the part [11]. The parameters used to determine electron beam melt pool characteristics are similar to those used for laser beam melting, i.e., (a) build speed; (b) heat source power and focus (spot size and shape); and (c) layer thickness. Nevertheless there is a fundamental difference in how the melt pool is controlled. In laser beam melting, a heat source with a constant voltage and current is used whereas in electron beam melting complex algorithms are used to alter these values to maintain a consistent melt pool [37].

- Current compensation algorithm – beam current or energy (Joules) is altered depending on the length of the scan hatch line. The higher currents on longer hatch lines to allow for the effects of heat dissipation. [37]

- Speed function – beam velocity is also varied based on the beam current to maintain a consistent melt pool size. [37]

### 2.2.3 EBM Powder Recovery/Recycling

EBM builds are removed from the machine with a semi-sintered block of caked powder around the parts, as seen in Figure 30. Arcam provides a Powder Recovery System (PRS) equipment, which is recommended for use with their EBM machines. It is a sealed air pressure blasting chamber which enables recovery of un-melted caked powder in a build.

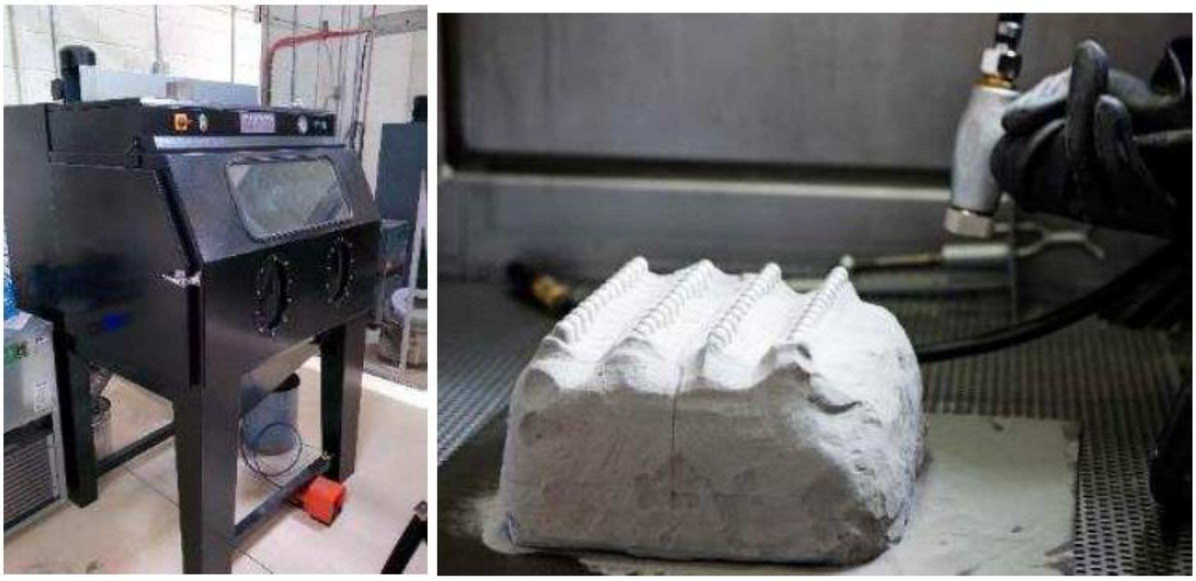

*Figure 30 EBM PRS system (left) and a build inside ready to be blasted (right,).*

The PRS uses the same material as media, and sintered cake/powder can be mixed in the PRS process, sieved, and recycled for the next build. The machine is also used to filter fines from the build material. A fine, in this context, refers to any particle with a diameter of less than approximately 40um. It achieves this using the cyclone unit on the back of the machine. A vacuum is pulled through the cyclone which serves to raise the powder from the bottom of the blast cabinet. As the material enters the cyclone, the larger, more massive particles fall to the bottom of the cyclone, and the fines continue through to the vacuum filter.

Multiple PRS systems are advised if a variety of powders are to be used, as cleaning may be difficult and therefore cross contamination of metal powders is potentially an issue.

### 2.2.4 EBM supports

The purpose for supports in EBM differs slightly from L-PBF due to the consolidated 'sintered cake' material that is built around the part. This provides some level of anchorage and thermal conductivity that loose powder in the laser process does not. This also results in reduced/ no thermal stresses within the part. However, the bottom of the part needs some supports to anchor it to the platform, and on some down skins, there is a need for additional support material to prevent distortion and curling and maintain dimensional accuracy. [42]

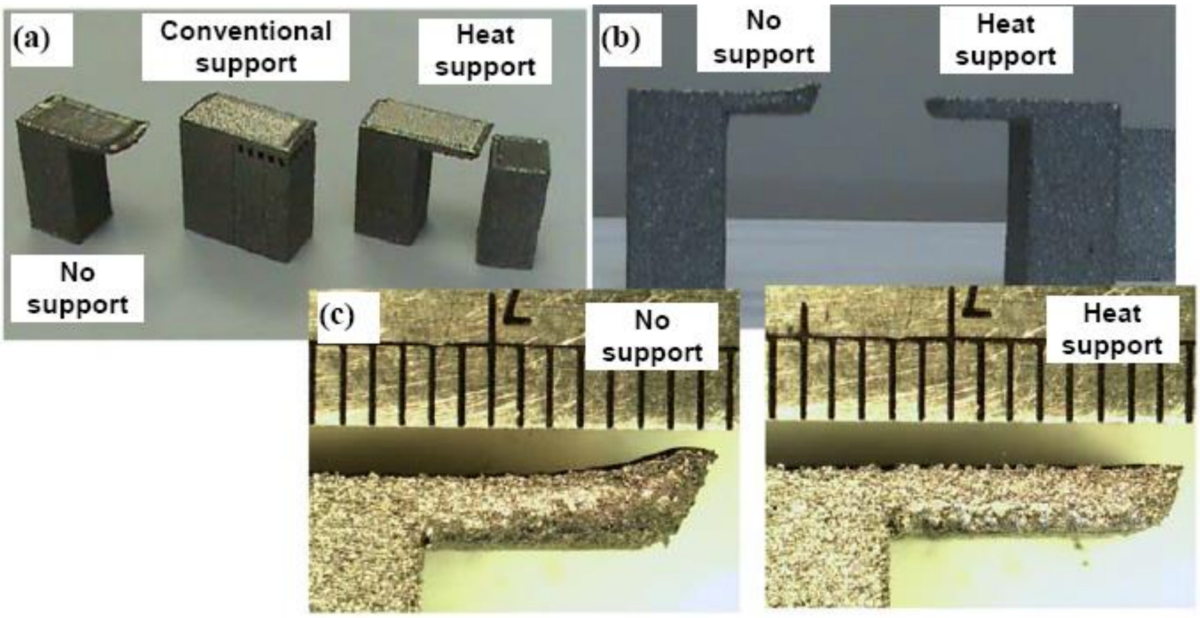


*Figure 31 EBM specimens built with (a) no support with curling indications as a result of thermal heat conduction (b) with and without support comparison [43].*

**Non-contact less support for EBM**

A patent methodology on the use of non-contactless supports by Chou et al. 2014 [43] has demonstrated the use of manufacturing parts and minimising supports requirement on parts [43]. However, the methodology still requires further developments and thermomechanical modelling to apply to end users in the AM community as shown in Figure 31. Cooper et al. [43] study showed the heat support concept through the use of simulations modelling and experimental data comparison and as effective on laboratory specimens. There is no literature currently extending the knowledge of complex AM components.

### 2.2.5 Effects of powder recycling

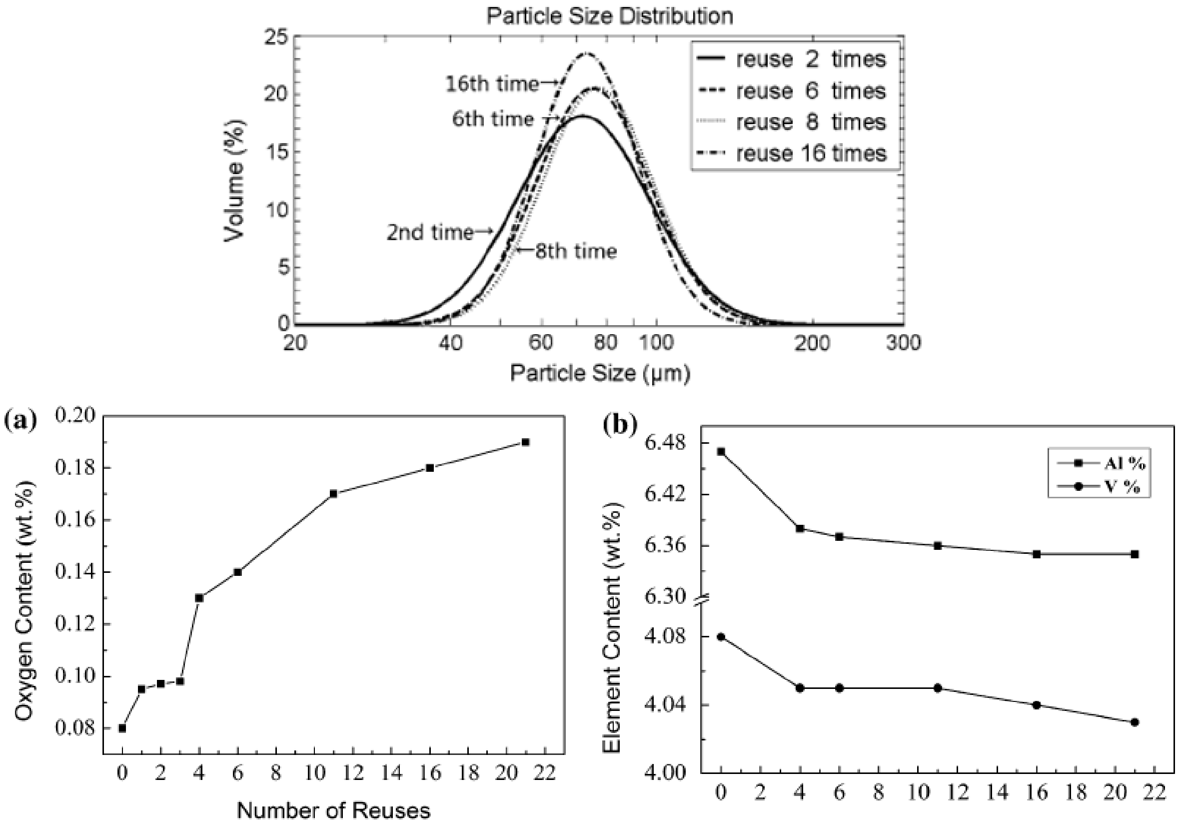


*Figure 32 effects of recycling powder on PSD (top image). (a) Oxygen content increase with number of builds (b) changes of Aluminium and Vanadium on powder recycling of builds [44].*

The effects of recycling powder are detrimental to the quality of powder processing variables during melting. [44] Powder morphology can become less spherical in comparison to virgin powder. Tang et al. found a reduction of satellites after six times reuse of powder, thus improved flowability was also noticed due to minimal presence of satellites. In contradiction to other studies on the effects of satellites on smoke occurrence, no evidence of 'smoke' was observed in the study of Tang et al. [44].

## 2.2.6 Oxygen pickup effects of powder recycling on AM powder

The oxygen pick-up in the titanium powder occurs during the melting and recycling of powder. Water vapour (H2O) can react with hot titanium processing. Moisture picked up in powder can also detrimental to the number of recycles of powder. [45] Thus, AM facilities with temperature and humidity control and better powder handling equipment are currently being developed and improved. A study by Tang et al. found an increase of oxygen from 0.08 wt.% to 0.19 wt.% after 21 recycles as shown in Figure 32 to ensure the study carried out by Tang et al. it was observed that the rate of oxygen pickup is dependent on [44].

An increase of oxygen picked up also resulted in higher YS and UTS. However, no effect on elongation can be observed on the mechanical properties of Ti6Al4V [44], [45]. It has been observed that the rate of oxygen pickup also is dependent on some other factor than the partial hydrogen pressure since in some studies, the pickup rate has been significantly higher than the pressure had indicated. A reason for this might be the effect of CV-EBM, or the morphology of the powder, where, for example, the gas atomized powder has had a higher increase than the plasma atomized [45].

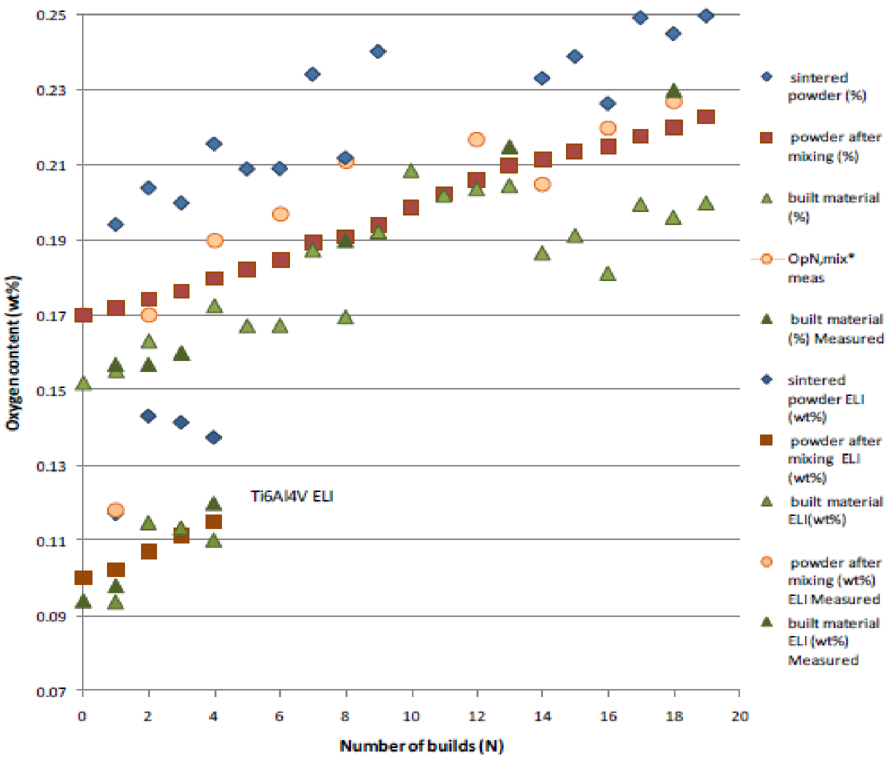


*Figure 33 effects of powder recycling on Oxygen content [45].*

## 2.3 EBM Ti6Al4V metallurgy

This section will give an overview of the metallurgy of Ti-6Al-4V $\alpha + \beta$ microstructure with primary emphasis on materials, microstructure, and phase transformation of alloy manufactured by EBM process. Figure 34 demonstrates that materials development and validation in metals requires a complicated relationship between the microstructure of the metal and the processing parameters to produce the required properties and performance. AM processes are typically complex with many interconnected process variables associated with the technique.

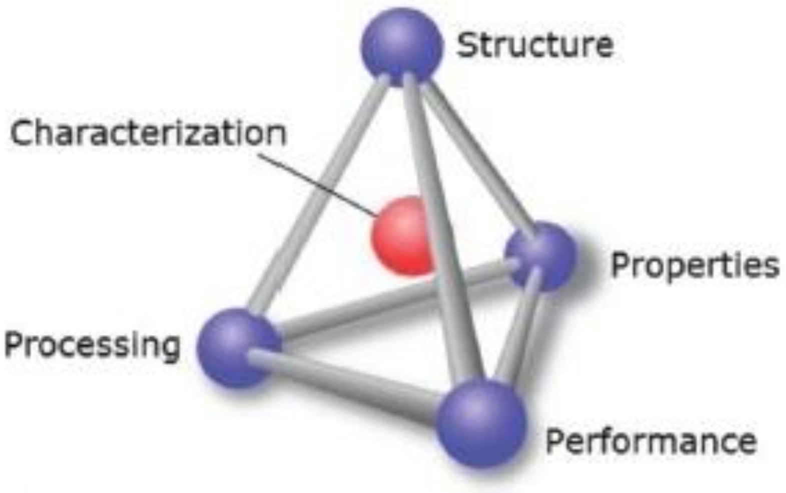


*Figure 35 materials science paradigm used as part of this literature review and study characterisation [46].*

Unlike other conventional manufacturing methods such as casting and use of wrought material, the EBM process is a rapidly cooled manufacturing method with highly directional heat flow away from the electron beam heat source, and towards the substrate plate. As a result, Ti-6Al-4V microstructures are dominated by large columnar prior β grains, formed by the highly directional heat flow and epitaxial growth [13], [47]- [49]. The columnar prior β grains follow or grow across hot melt layers due to epitaxial growth; this occurs through re-melting a previously deposited grain and solidifying the new material, adopting the previous solid crystal orientation.  Within the large columnar grains, a fine α+β Widmanstätten microstructure is observed with the width of the α lath between 0.5 - 2.0 μm. This occurs due to the rapid cooling rates experienced in EBM.

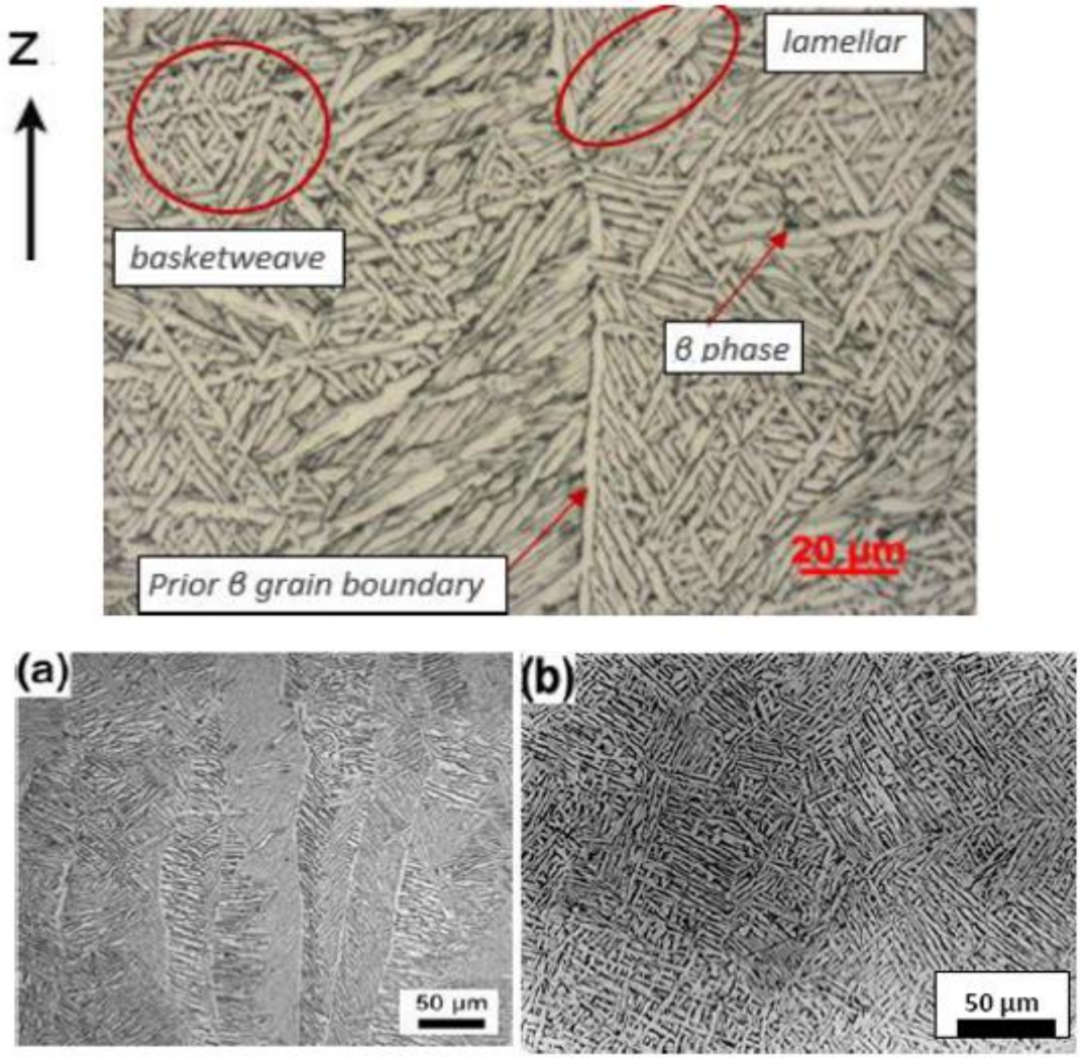


Figure 27 Typical EBM Ti Al4V microstructure; (a) with indications of prior columnar β-grains; and (b) with Widmanstätten and colony α-morphology [13], [19].

### 2.3.1 Thermal history of EBM process on Ti-6Al-4V

Processing temperatures and set times influence the microstructure of Ti6Al4V. [5] In the EBM process, the material goes through several stages within different temperature ranges for different amounts of time. When in a molten state, the material will first be rapidly cooled, where the rate of cooling is mainly due to heat conduction to the surrounding material and will, therefore, be a function of the size of the melt pool [5] [13] [17] [19]. During this process, a typical cooling rate is between 10e5 to 10e6 °C/s, [5], [13] down to a first-holding temperature of about 1000-1200 °C, where the material stays for some seconds, and then drops down to a more stable annealing temperature of 650-750 °C, where it stays for the rest of the build (5 - 50 h) [5] [50]. Subsequent layers will, to some extent, repeat this temperature cycle a number of times, but with the temperature peak levelled out. This processing history will in many ways describe the resulting microstructure.

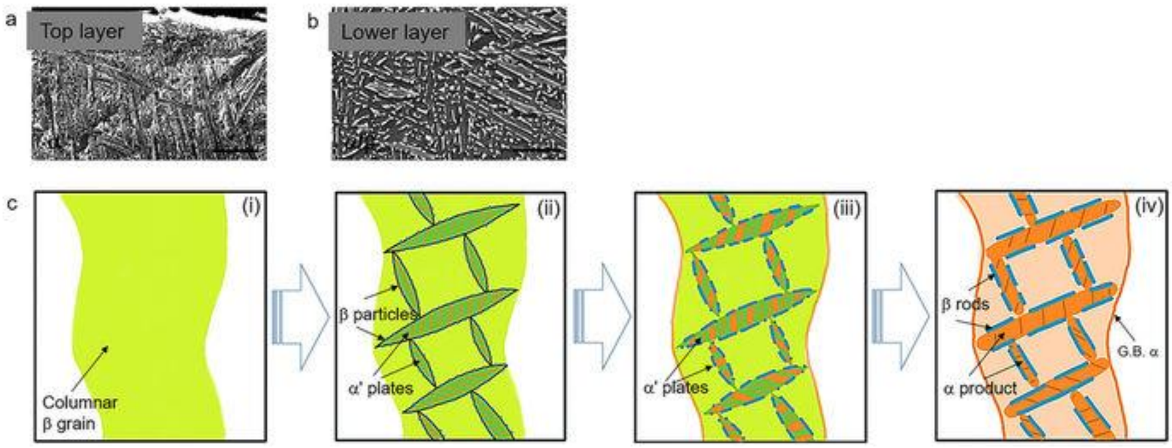


*Figure 36 Microstructure evolution of Electron Beam Melting demonstrated for 10 mm samples [51].*

The general microstructure consists of fine epitaxial grown β-grains, with a α-phase grown from former β-boundaries. The ∝ grains is acicular or 'plate-like' with a Widmanstätten structure [13] [50] [48].

In EBM-manufactured material, some variation in colony size [51]. In general, it is extremely fine with an almost-singular and evenly distributed Widmanstätten structure, whereas some areas are more aligned with much larger clusters of ∝-plates, originating from former β-boundaries. [5] [50] [19].

Nonetheless, slow-cooled cast Ti-6Al-4V will produce a lamellar structure where α lath width can reach 10 μm [14] [19]. In some processing parameter combinations, the cooling rate can exceed that necessary for the β → α' transformation to occur, especially if the build is connected to the start plate which acts as an effective heat sink. Hernández-Nava [52] showed that for a fully α' martensite structure to be formed, the cooling rate must exceed 410 K/s, and therefore under certain EBM processing conditions, the cooling rate must exceed this value. The cooling rate in direct energy deposition (DED) and L-PBF have been shown by numerous sources to far exceed this value with cooling rates calculated reported at $10^4$- $10^5$ K/s [13] [52]. Al-Bermani et al. 2010 [5] reported that EBM processing window temperature ranges between 898K to 973K (625 °C to 700 °C), the actual temperature is still debatable. [13].

Thermal history cycle has been reported to result in complex microstructure transformation due to rapid solidification and cooling of parts. Figure 37 illustrates the thermal cycles during EBM process [19].

*Figure 37 EBM cooling rate of Ti6Al4V microstructure formation [30].*

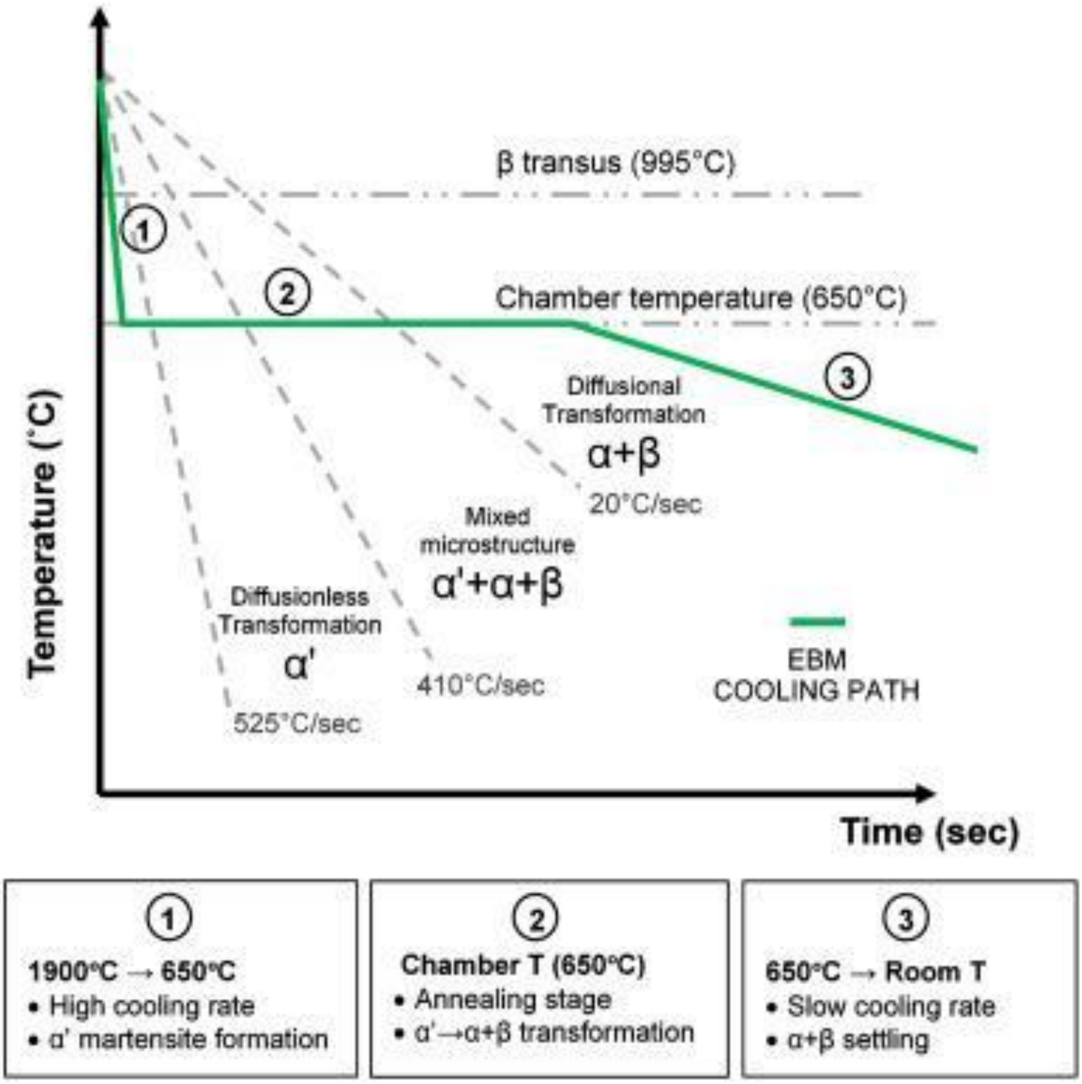


The cooling rate in EBM, even with powder pre-heating, is still shown to exceed $10^3 – 10^4$ K/s, sufficient to cause martensite [5]. However, the build temperature is kept at 650 ˚- 700 °C on the top layer during the build process, and the constant temperature excursion above 700˚C due to the powder-bed pre-heating is sufficient to cause martensite decomposition [13].A typical stress relief heat treatment that is sufficient to fully decompose α' martensite is 600˚C for 1-2 hrs. With build times of 5-15 hrs, decomposition would be expected of any α' formed upon initial cooling.

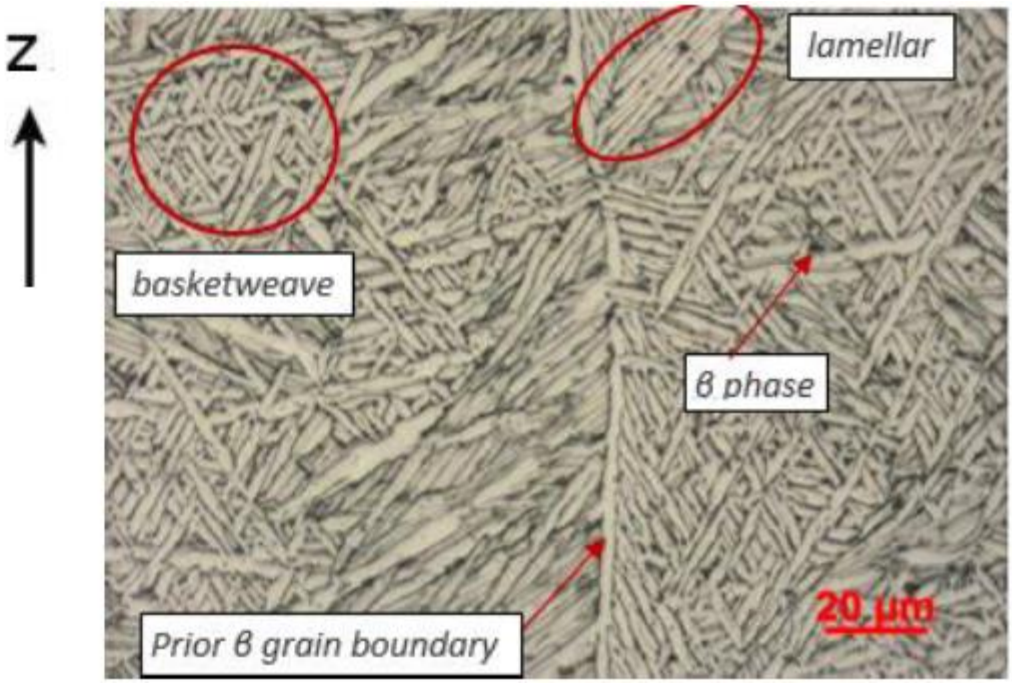


Figure 29 EBM Microstructure HiPed condition [13].

### 2.3.2 Isotropy Morphology Ti6Al4V grains

A close-up reveals a fine plate-acicular ∝ with small-sized colonies. In XY direction, the former βis more isotropic and with a more plate-like ∝, and almost singular orientation. This might be one reason for the high fracture toughness values in RAW condition. In HIP condition, observed in Figure 29, the structure has more of a blocky and plate-like ∝ phase still with elongated former β-grains, with unchanged colony size. No visual difference structure-wise between the non-ELI and ELI version was observed by Swvenson (2009) [45].

### 2.3.3 Reduction of Al and V on AM

Further consideration of EBM processing Ti-6Al-4V is the reduction in Al content through vaporisation. The boiling point of aluminium is relatively low, measured at 2470˚C. In contrast, however, the melting point of titanium is 1668˚C and boiling is not reached until 3300˚C. Melt pool temperatures in EBM of Ti-6Al-4V have been shown to reach 2700˚C. (Galarraga et al, 2017) [19] and V.Juechte et al 2014 ) [40] reported that a reduction in aluminium content of up to 15% was possible in EBM-processed parts. High-temperature processing during EBM process as a result of an increase in energy input affects the microstructure phase transformation, and mechanical properties of an alloy Aluminium has a significant strengthening effect (stabiliser) on titanium by increasing the planarity of slip, therefore a reduction in aluminium has the potential to reduce the mechanical properties and slightly increase the alloy density. Juechter et al. (2014) [40] showed that increased line energy increased vaporisation of aluminium which can lead to non-homogeneous aluminium content. It was also shown that increases in the scanning speed increase the size of the melt pool, and therefore temperature, as reduced time for thermal conduction occurred. This led to increased aluminium evaporation and hence a reduction in the total aluminium content [40].

Use of Stainless Steel baseplate

Stainless steel (SS) baseplate in EBM process is commonly used to build the first few layers of AM parts initially. This results in a region interface with SS in Ti6Al4V. The interface is beneficial to the AM process as it allows easy manual hand removal of parts without the need to wire EDM parts off the baseplates. The SS base plate becomes brittle and nucleates thermal incompatibility or no bonding from bulk. Al-bermani et al 2010 [5] found the region of the interface to contain Cr, Fe, and Ni elements acting as a stabiliser as shown in Figure 38 [32].

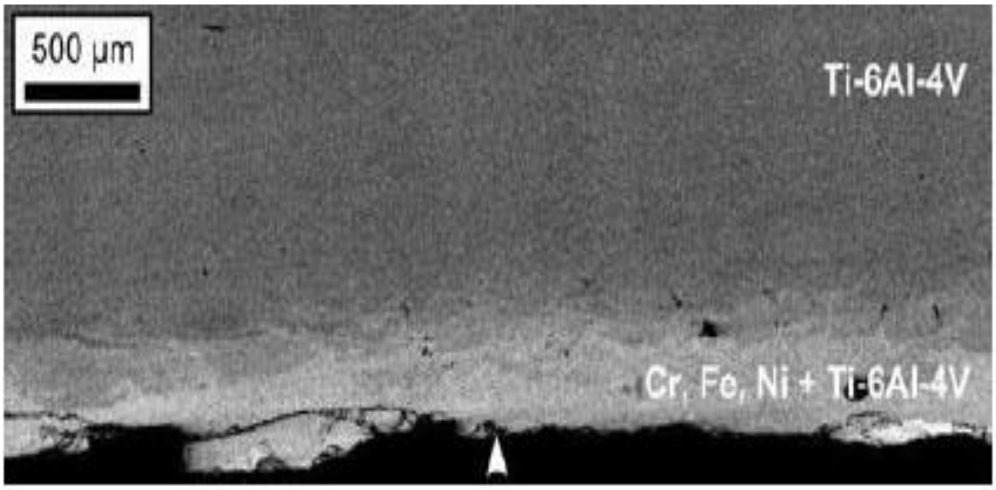


*Figure 39 SS base plate with the Ti6Al4V bulk part. Arrow indicates Z-axis orientation. Evidence of brittle cracks can be observed [5].*

### 2.3.4 EBM Mechanical properties

The mechanical performance or properties of EBM Ti-6Al-4V are strongly influenced by numerous factors; the microstructure, test orientation and build part quality. The mechanical properties are typically compared to conventional processing methods such as cast or wrought, with a specific focus on the ductility which is known to vary intensely with defect population changes. In the review carried out by John J. Lewandowski and Mohsen Seifi, 2016 [53], on Figure 32, it has been shown that mechanical properties above wrought and cast ASTM standards can be achieved through EBM manufacturing of Ti-6Al-4V as shown in

Table 7.

*Figure 40 Comparison of Ti-6Al-4V mechanical properties of as-built and HiPed Additive Manufactured process vs. traditional conventional methods [22].*

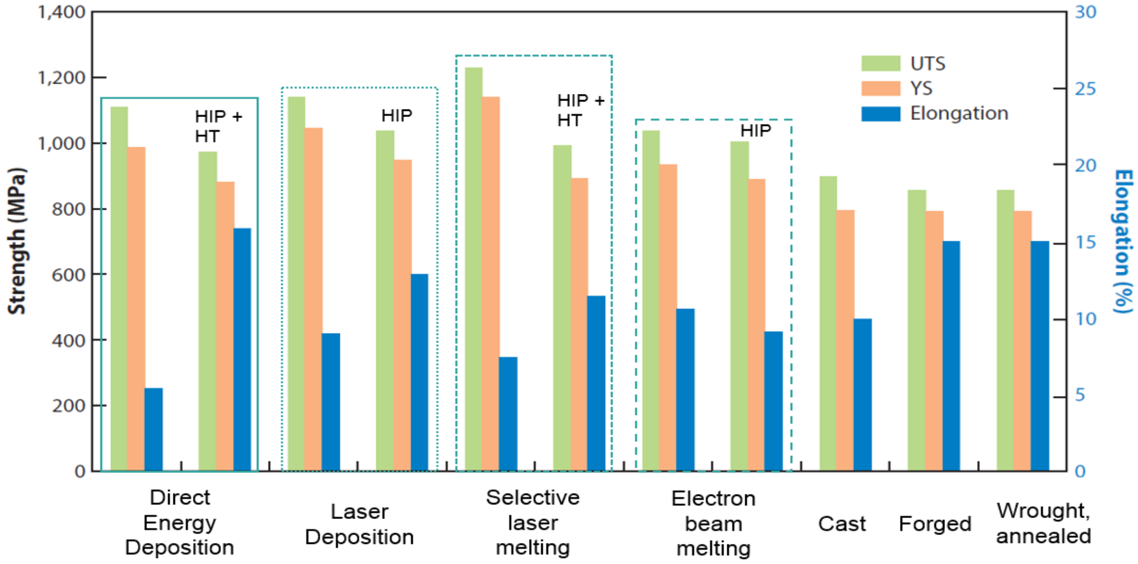


Process induced defects such as porosity and lack of fusion have been shown to influence the tensile strength and ductility among other mechanical properties [54] [50] [55] [56]. Therefore, a significant amount of mechanical property data scatter is expected due to differing porosity/defect morphology and population.

Figure 41 is an illustration of commonly used build direction in X, Y and Z referred in EBM Mechanical properties from different authors and equipment using Ti6Al4V [53]

*Figure 41AM build direction illustration*

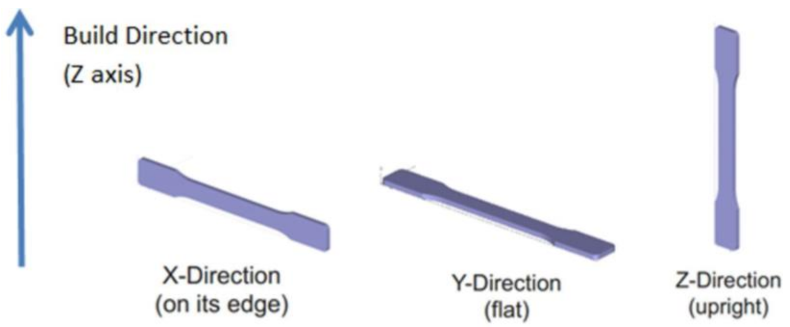


Table 7 EBM Mechanical properties from different authors and equipment using Ti6Al4V [53].

| Machine type | Condition | Specimen orientation | *E* (GPa) | strength (MPa) | strength (MPa) | Elongation (%) | Hardness (Hv) |
|---|---|---|---|---|---|---|---|
| Arcam | Heat treated | *ZX* | NA | 869 ± 7 | 965 ± 5 | 6 ± 0 | NA |
| Arcam A1 | As built | *XY* | NA | 783 ± 15 | 833 ± 22 | 2.7 ± 0.4 | NA |
| | | *ZX* | | 812 ± 12 | 851 ± 19 | 3.6 ± 0.9 | |
| Arcam | As built | *XY* | NA | 870 ± 8.1 | 971 ± 3.1 | 12.1 ± 0.9 | NA |
| | | *Z* | | 879 ± 12.5 | 953 ± 8.8 | 13.8 ± 0.9 | |
| | HIP | *XY* | | 866 ± 6.4 | 959 ± 8.2 | 13.6 ± 0.6 | |
| | | *Z* | | 868 ± 2.9 | 942 ± 2.6 | 12.9 ± 0.8 | |
| Arcam ELI[a] | As built | *XY* | NA | 817 ± 4.3 | 918 ± 1.0 | 12.6 ± 0.8 | NA |
| | | *Z* | | 802 ± 7.9 | 904 ± 6.0 | 13.8 ± 0.9 | |
| | HIP | *XY* | | 814 ± 2.4 | 916 ± 2.5 | 13.6 ± 1.2 | |
| | | *Z* | | 807 ± 8.4 | 902 ± 8.7 | 14.8 ± 0.5 | |
| Arcam A2X ELI[a] | As built | *XY* | NA | 851.8 ± 5.8 | 964 ± 0.3 | 16.3 ± 0.8 | NA |
| Arcam A2 ELI[a] | As built | *Z* | NA | 928 ± 13.3 | 1,011 ± 14.8 | 13.6 ± 1.4 | NA |
| | HIP | *Z* | NA | 813 ± 14.3 | 908 ± 3.2 | 17.7 ± 0.9 | NA |
| Arcam S12 | As built | *XY* | NA | 975 | 1,033 | 16.78 | NA |
| Arcam | As built | *XY* | NA | 881 ± 12.5 | 978 ± 11.5 | 10.7 ± 1.5 | NA |
| | HIP | *XY* | NA | 876 ± 12.5 | 978 ± 9.5 | 13.5 ± 1.5 | NA |
| Arcam S12 | As built | *XY* | NA | 982 ± 5.7 | 1,029 ± 7 | 12.2 ± 0.8 | 372 ± 7.2 |
| | | *Z* | NA | 984 ± 8.5 | 1,032 ± 12.9 | 9 ± 2.9 | 367 ± 8.3 |
| Arcam S400 | As built | *XY* | NA | 899 ± 4.7 | 978 ± 3.2 | 9.5 ± 1.2 | NA |
| | | *ZX* | | 869 ± 7.2 | 928 ± 9.8 | 9.9 ± 1.7 | |
| Arcam S400 | As built | *XY* | 104 ± 2.3 | 844 ± 21.6 | 917 ± 30.53 | 8.8 ± 1.42 | NA |
| | | *Z* | 101 ± 2.5 | 782 ± 5.1 | 842 ± 13.84 | 9.9 ± 1.02 | NA |
| Arcam S400 ELI[a] | As built | *Z* | NA | 1,150 | 1,200 | 16 | 380 |
| Arcam | As built | NA | 118 ± 5 | 830 ± 5 | 915 ± 10 | 13.1 ± 0.4 | NA |
| | HIP | NA | 117 ± 4 | 795 ± 10 | 870 ± 10 | 13.7 ± 1 | NA |

### 2.3.5 Effects of interstitial composition on mechanical properties.

Interstitials such as Oxygen (O), Nitrogen (N), and Hydrogen ($H_2O$) can influence and impact the mechanical properties of titanium. Of these, oxygen is the most significant one and act as an α-stabiliser to strengthen the material. A study by Jaffee et al. [57] and Oh et al. [58] revealed that increase in oxygen encourages an increase in the strength and hardness. However, a reduction in the ductility was also found see Figure 42. [58]. The dislocation of atoms within hcp crystal will cause a shear increase, hence increment in the hardness and strength of Ti alloys

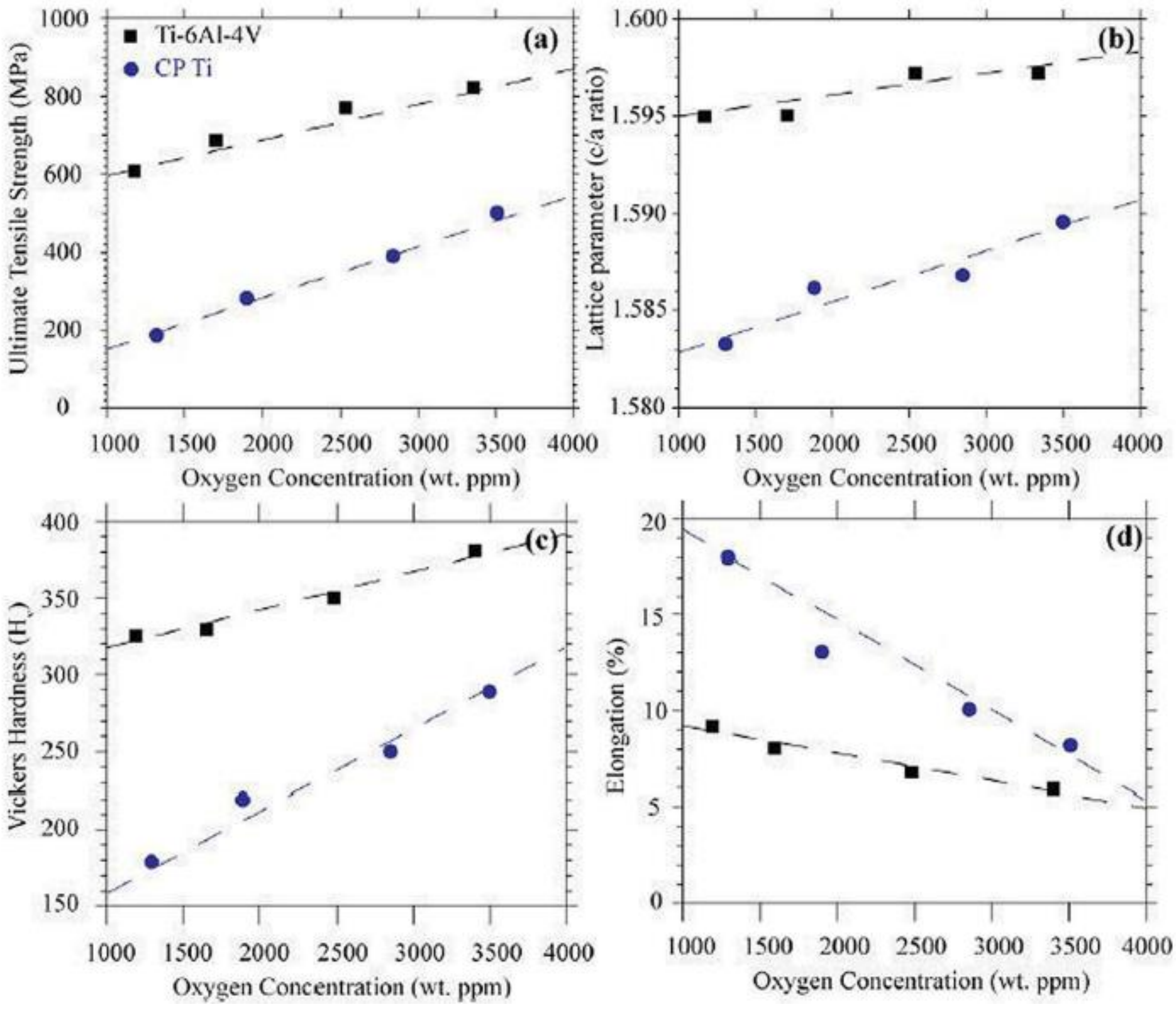


*Figure 42 influence of oxygen wt. % interstitials on mechanical properties of Ti6-4 and CP TI retrieved from [58].*

### 2.3.6 Influence of α lath thickness on mechanical properties

The influence of solidification cooling rate also has an impact on prior- beta grain directions formation which has been reported as following thermal gradients of the build vertical orientation. As shown in Figure 43, the differing microstructure changes seen can be described by the dislocation slip plane theory. Work carried by Mireles and Jorge 2015 [59] , correlated grain structure on mechanical strength It was found that courser grains have much greater stress concentration due to dislocation pile-ups.

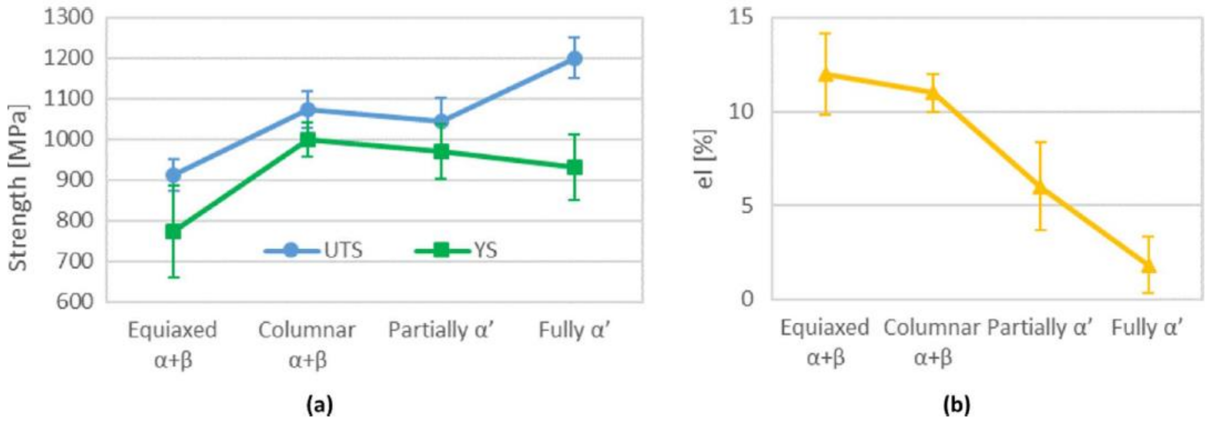


*Figure 43 the effects of α-lath thickness on Ti6-Al-4V ELI. (a) Ultimate tensile strength and Yield strength (b) Elongation for different ti6/4 microstructure [60].*

Nonetheless, Kirchner et al 2016 [61] , found an increase in α-lath as having unfavourable or severe consequence effect mainly at an aging solution [60]. Water cooled solution and heat treatment resulted in the formation of α' microstructure with >30% UTS and 86% lower ductility in comparison to the furnace-cooled solution. Thus elevated build temperature of 650–700 °C during EBM process are more beneficial and results in reasonably lower residual stress [34], [53], [60].

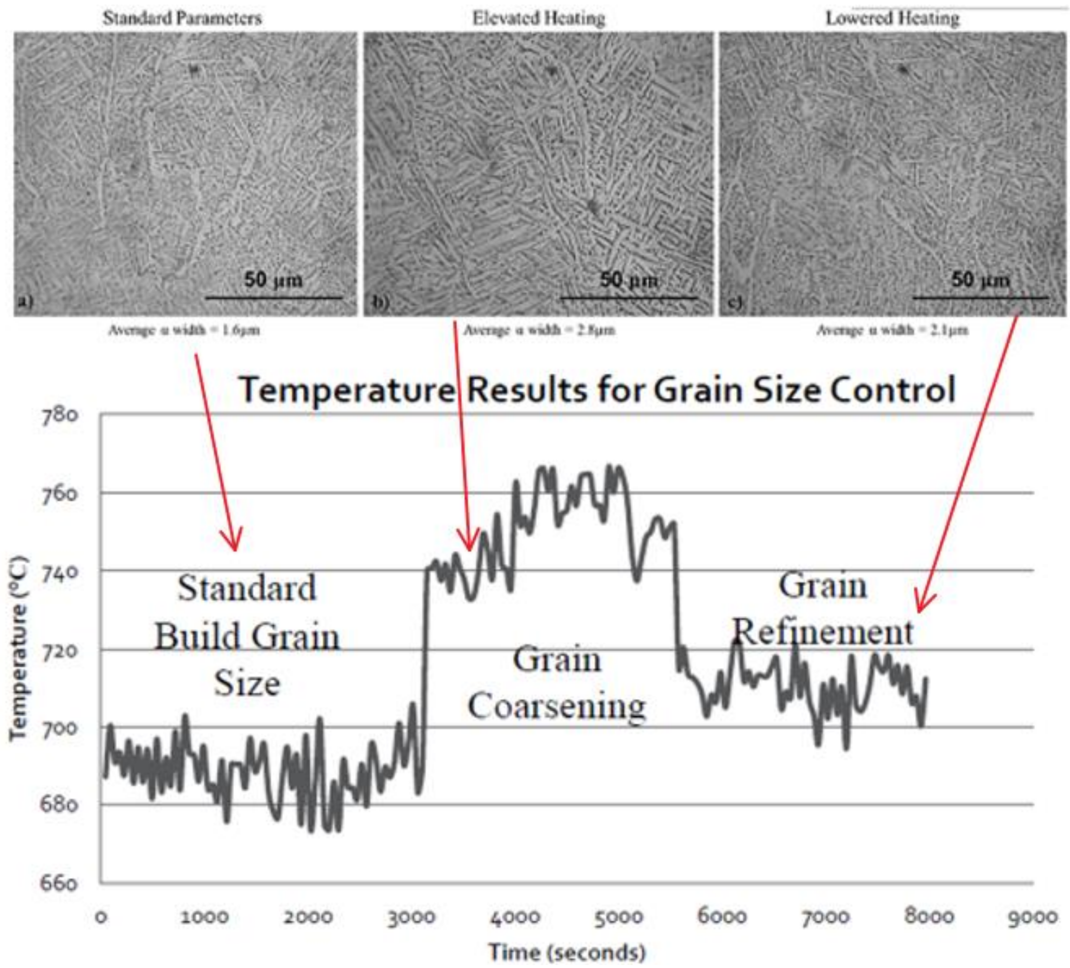


*Figure 44 effects of cooling rate on microstructure formation in EBM Ti6Al4V [59].*

A comparison between RAW and HIP material revealed the presence of micropores in the RAW specimens. According to Donachie, 2000 [2] the fatigue performance life is influenced by grain stuucture i.e. on the lamellae size in the Widmanstätten structure. The finer the needles are in the transformed β-phase, the stronger the material is. It has been observed the epitaxial grown prior β-grains enables isotropy in especially the colony size, with a wide distribution [60]. During HiPing the lamellae grow to approximately twice the size, from 3 µm to 6 µm, and could account for some decrease in fatigue. However, this decrease is insignificant compared to the presence of inclusions or pores in the non-HiPed material. The effect of High Cycle Fatigue life from porosity is known, and there exists a relation between the size of the defects and the shortening of the fatigue life. [45].

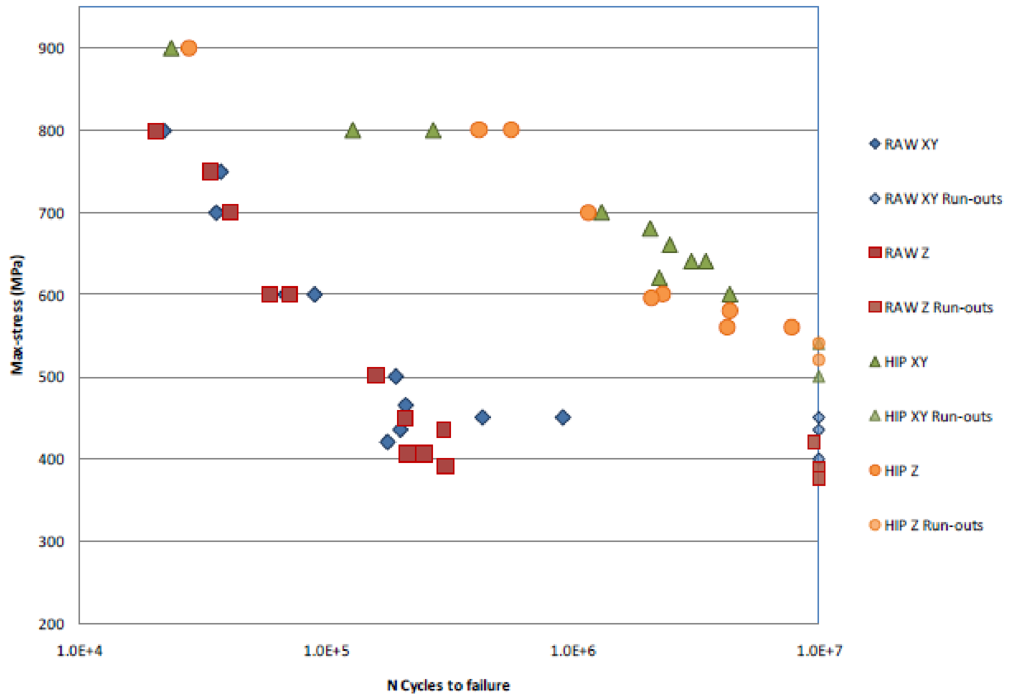


*Figure 45 High cycle fatigue (R=0.1) on Ti6Al4V in raw and HiPed Condition [48].*

### 2.3.7 EBM anisotropy microstructure

Anisotropic mechanical properties have been observed in EBM as-built test bars [53] [49]. This effect has been shown to occur due to the presence of defects and the differing tensile mode acting on these defects when tested. Lack of fusion defects occurs in the XY plane of the build, in between layers where full melting has not occurred as a result of non-optimised parameters. When tensile testing bars built in the vertical direction, any lack of fusion is put into a mode I opening stress Table 8. Spherical porosity does not show the same orientation property bias. Therefore, unless a population of spherical porosity defects occurs in a specific location the mechanical properties are lowest in the building direction (Z).

*Table 8 Differing tensile mode when testing at specific orientations (vertical vs. horizontal) [62].*

| Part | Description | UTS (MPa) | YS (MPa) | % EL | α Lath thickness (μm) | Microhardness (H |
|---|---|---|---|---|---|---|
| 2 | Horizontal | 1029.7±7.0 | 982.9±5.7 | 12.2±0.8 | 0.95±0.31 | 372.0±7.2 |
| 3 | Vertical | 1032.9±12.9 | 984.1±8.5 | 9.0±2.9 | 0.96±0.26 | 367.6±8.3 |
| ANOVA | *p*-value | 0.5 | 0.72 | 0.01 | 0.65 | 0.02 |

Lower % elongation was found for vertically built specimen (30%) in comparison to horizontal build specimens. Although prior-β grain morphology of z-built direction is elongated in the build-up direction, no difference in α lath thickness was found.

### 2.3.7 Part thickness of mechanical properties

A study carried out by Hrabe and Quin (2013) has shown thicker or medium part has higher mechanical properties in comparison to a thin part (small). However, there is no clear evidence yet to suggest if the part located on the powder bed can affect the cooling rate. It was reported that faster cooling rate resulted in fine grains with higher mechanical properties. The formation of Martensite (α') was observed for EBM Ti6Al4V in the specimen with a thin wall [38].

### 2.3.8 Effects of build orientation on tensile properties of EBM specimens

The influence of build direction for EBM manufactured specimens has been researched by many authors; to understand further how complex features, geometries impact the mechanical properties. Differing build orientations in horizontal (XY) and vertically (Z) AM samples have been found to differ in mechanical as-built specimens with many researchers [13], [47], [53]. The differing thermal and cooling rate during EBM process influences the microstructure grain refinement formation such as lamellae structure. As evidenced by Bruno J, Rochman, Cassar, 2017 [47] EBM as-built horizontal (XY) oriented specimens were found to have finer lamellar microstructures as a consequence of higher solidification rate, although the mechanical results had comparable strength and relatively lower ductility in comparison to vertically oriented parts as shown in Table 9

*Table 9 As-built EBM tensile specimen in horizontal (XY) and vertical (Z) orientation [49].*

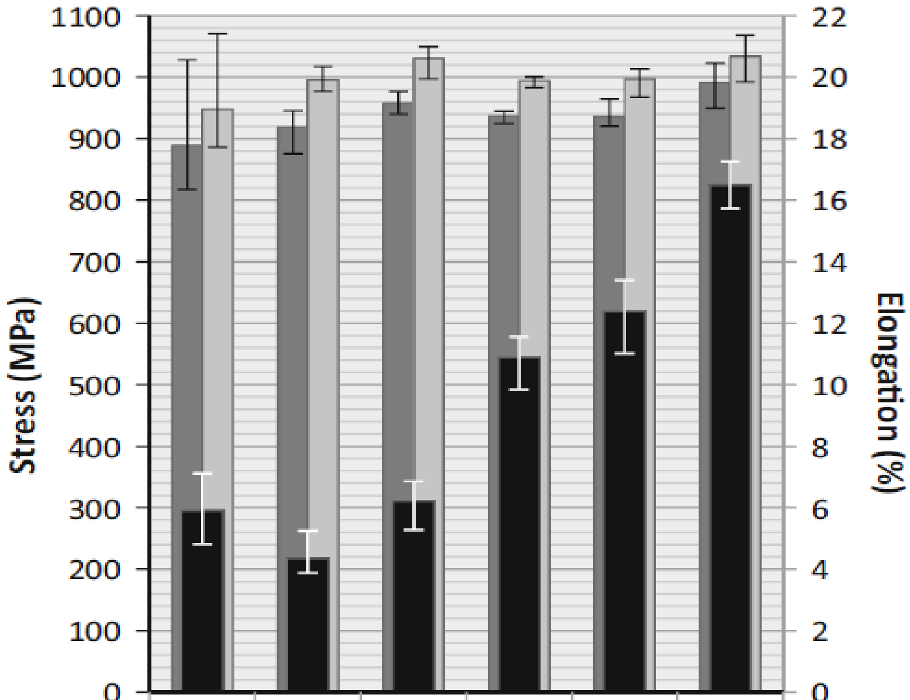


| | XY | ZX | ZX-P | ZY | XY-60 | W-Ti |
|---|---|---|---|---|---|---|
| YS at 0.2% (MPa) | 889.1 | 919.1 | 957.2 | 937.2 | 936.2 | 991.1 |
| UTS (MPa) | 948.1 | 995.7 | 1030.8 | 994.2 | 997.2 | 1033.9 |
| El (%) | 5.92 | 4.35 | 6.22 | 10.9 | 12.4 | 16.5 |

Hrabe et al. [49] also found the elongation for vertically (Z) built specimens having a 30% lower value in comparison to horizontal XY built parts. Lower elongation is mainly due to non-optimised process parameters and process instability during melting inducing process defects. Hou et al. 2017 [62] work using EBM Q20+ machine managed to reduce EBM defects by 76% from default manufacturer parameters. It goes on to show AM process needs to be further understood to understand process repeatability and stability prior to productionasation .

### 2.3.9 Effect of surface finishing of EBM parts

The external surface for as-built surface finishing of AM manufactured is rougher in comparison to a machined part. In comparison to L-PBF whereby fine powder particles of 15-45 µm PSD with small layer thickness of 15 µm -100 µm and laser beam spot of ~100 µm the surface finish is much better or smoother than EBM process; which uses larger powder size usually 45-106 µm and layer thickness of 50-100µm with beam diameter of ~140 µm for Q-series system. Figure 46 shows surface finish difference between L-PBF and EBM.

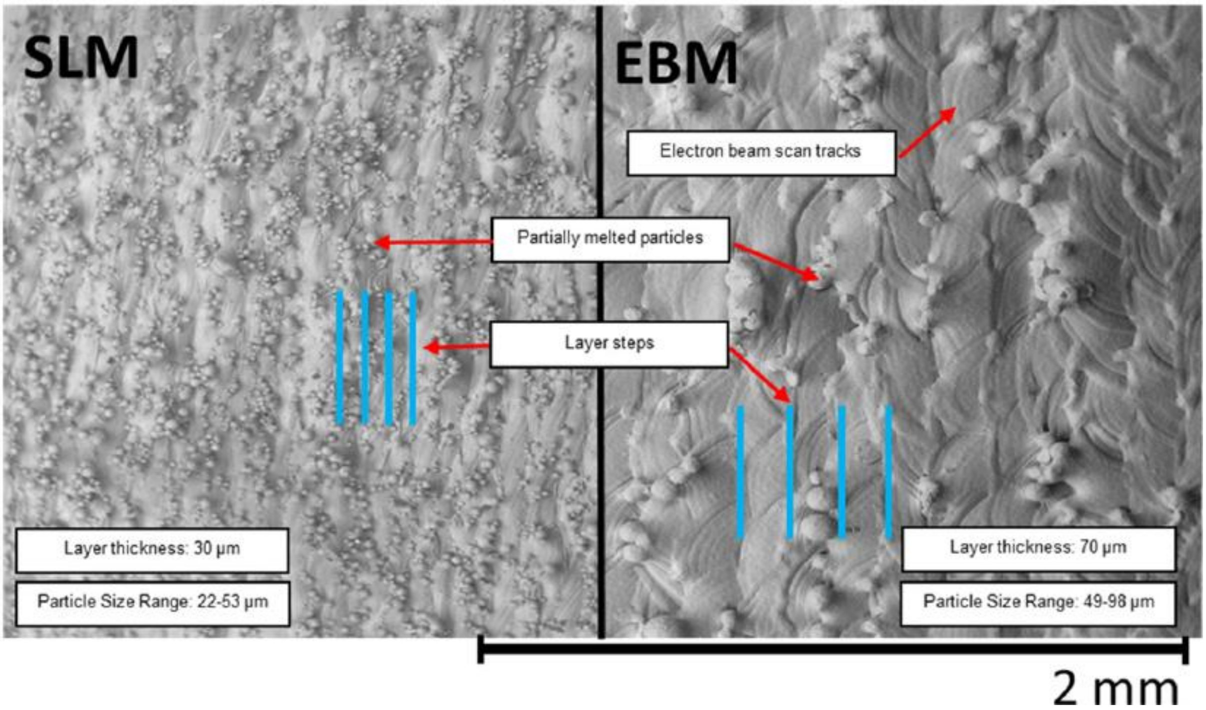


*Figure 46 Surface finish comparison of L-PBF vs. EBM as-built specimen retrieved by Triantaphyllou et al. [63].*

Table 10 shows a summary of the different process variables and primary factors which affect surface finish of an AM part. These are explained further in this section, as are the secondary factors.

Table 10 Key AM process variables affecting surface finish.

| Factors | Features |
|---|---|
| • Layer thickness | • Layer stepping |
| • Geometry slope | • Layer edge deformation |
| • Particle size | • Balling marks |
| • Beam parameters | • Particle adhesion |
| • Downward-facing surfaces | • Lay |

However, this is not always a negative impact on some parts where rougher might be required such as in orthopaedic medical impacts. Triantaphyllou et al. [63] report the EBM surface finish as having a wavy appearance with partially melted powder particles on the surface of as-built parts.

The surface finish of AM is known to have much influence on the fatigue driven application. It has been observed and discussed by many authors [20] [64] that surface finish technique needs to consider for a different application of AM manufactured parts. Murr et al. [20] established yield strength and tensile strength of as built +machined specimens and polished specimens had 1350 MPa and 1451 MPa. Figure 47 shows tensile bars for as-built L-PBF vs. EBM specimen [63].

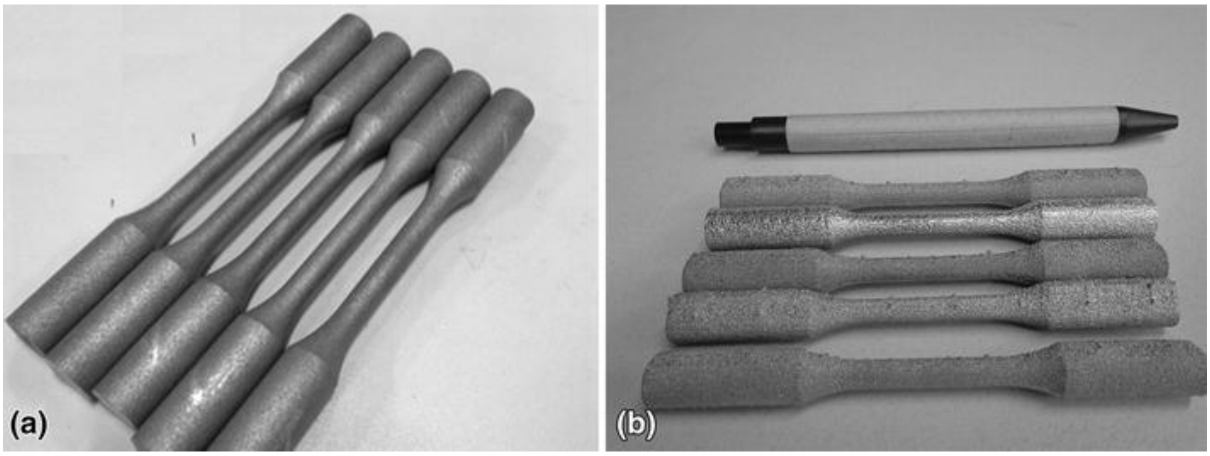


*Figure 47 Surface finishing of (a) L-PBF as-built specimen. (b) Rougher surface for as-built EBM specimens retrieved from [65].*

Effects of surface finish on mechanical properties

The influence of rough surface finish of AM build specimens have been reported by many authors [66] [67] [68]. It is known non-smooth surface can initiate crack propagation hence AM complex geometries or components needs to consider the post surface finish of parts for fatigue driven applications. Greitemeier et al 2017 carried out the study of laser powder bed and EBM build surface as shown in Figure 48, lower Ra specimens had better results than rougher EBM surface. However, defects and microstructure should be also be considered as dominating factors for the AM specimens [68].

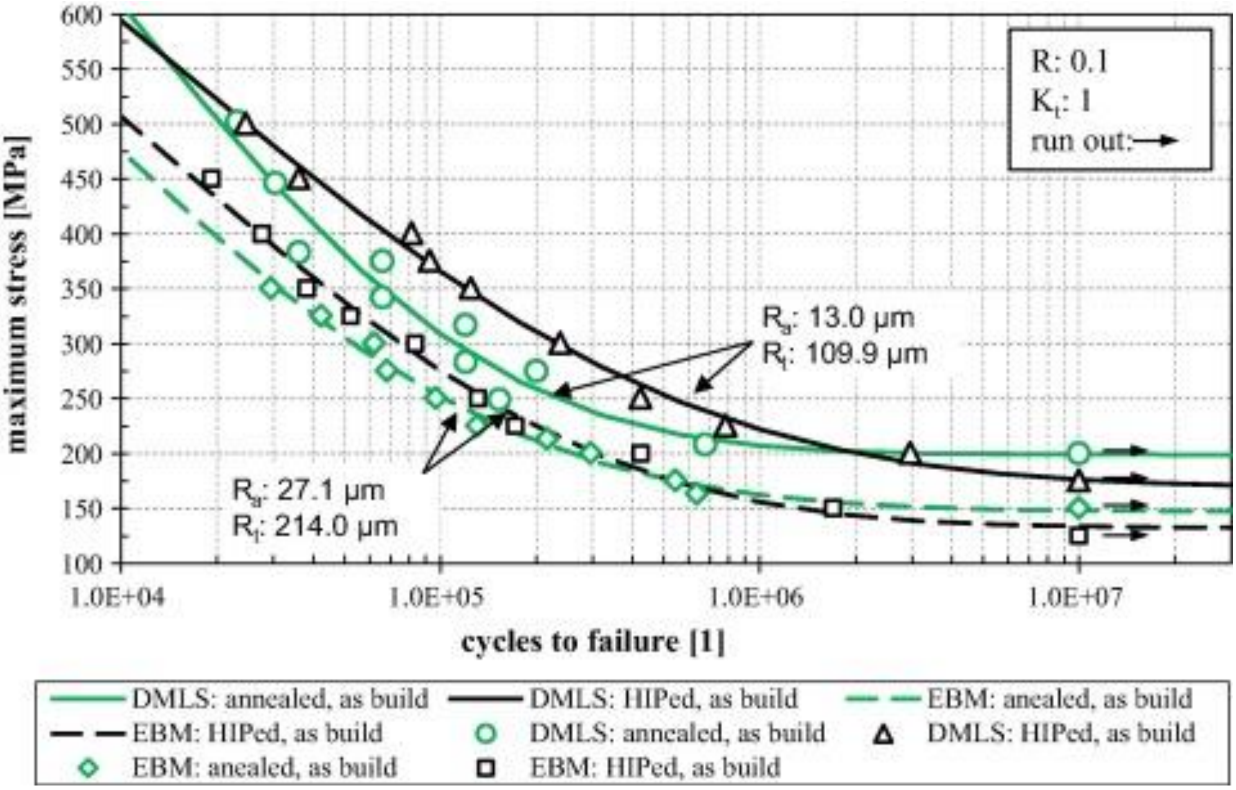


*Figure 48 High cycle fatigue comparison of Laser powder bed vs Electron Beam Melting; with different surface finish treatment influence on specimens [66].*

Layer thickness and geometry

One of the main features which attribute to the AM surface texture is layer stepping (also known as "stair stepping"), which is inherited in layered manufacturing. Larger layer thickness and powder size are some of the key variable that affects the surface finish of AM parts [63] [69].

Also, during the melting of metal powders, the melt pool on the edge of the borders is insufficient to sinter particles fully. This leads to the particles not merging completely with the layer, hence tending to stick to the surface at the step edges as shown in Figure 46.

## 2.4 AM Porosity and Defects

It is known that deviation away from optimised process parameters in AM can result in increased defect populations and therefore reduced mechanical properties (Gong et al., 2013) [70] [54]. The term 'defects' is used to group unintended macroscopic, microscopic and chemical heterogeneities in the build that may cause it to be out of specification requirement for a component or application.

These defects can be spherical pores, lack of fusion /un-melted particles and gas entrapped from element vaporisation [39] [30] [40]. Defects independent of process parameters can also occur due to raw material inherited powder porosity that is assimilated into the manufacturing AM build. Each of these defects will affect the mechanical properties through increased stress concentration and reduction in the load-carrying area [41]. Table 11 shows typical defects found in EBM, these defects have been reported by many authors referenced in the table.

*Table 11 EBM typical common defects found in ports and material.*

| Defect Name | Example defect | Authors references |
|---|---|---|
| Lack of fusion | 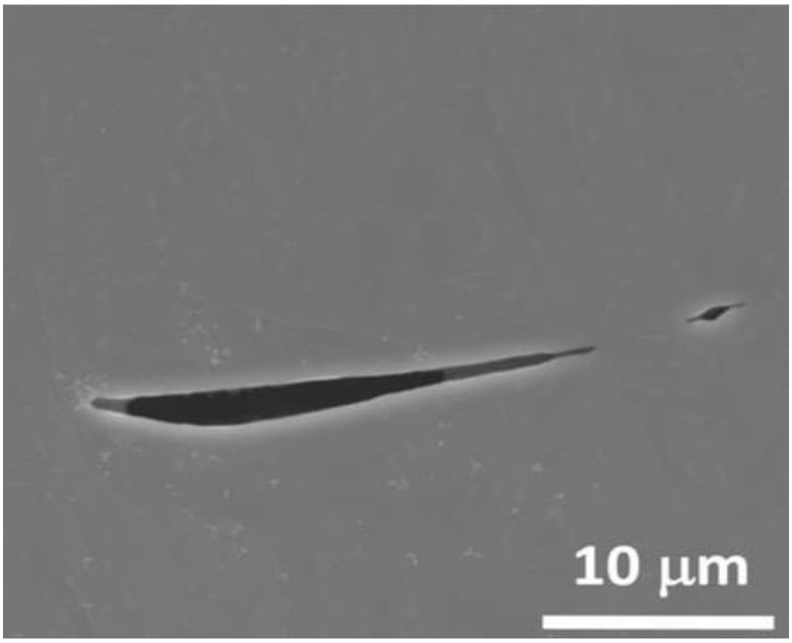 | [42] [55] [52] |
| Porosity | 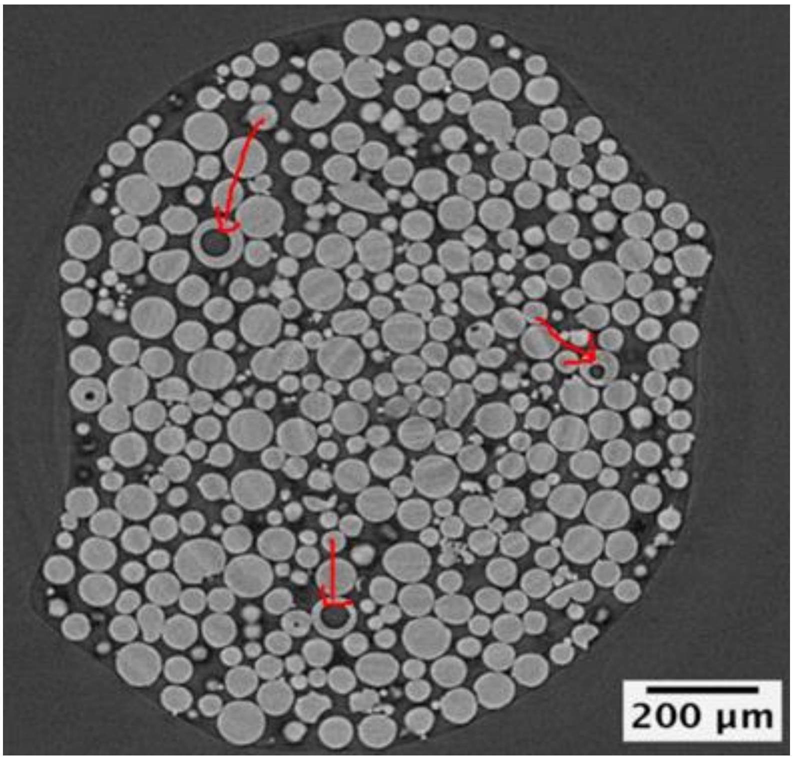 | [39] [56] [71] [61] |

| | | |
|---|---|---|
| Un-melted/ Unconsolidated powder | 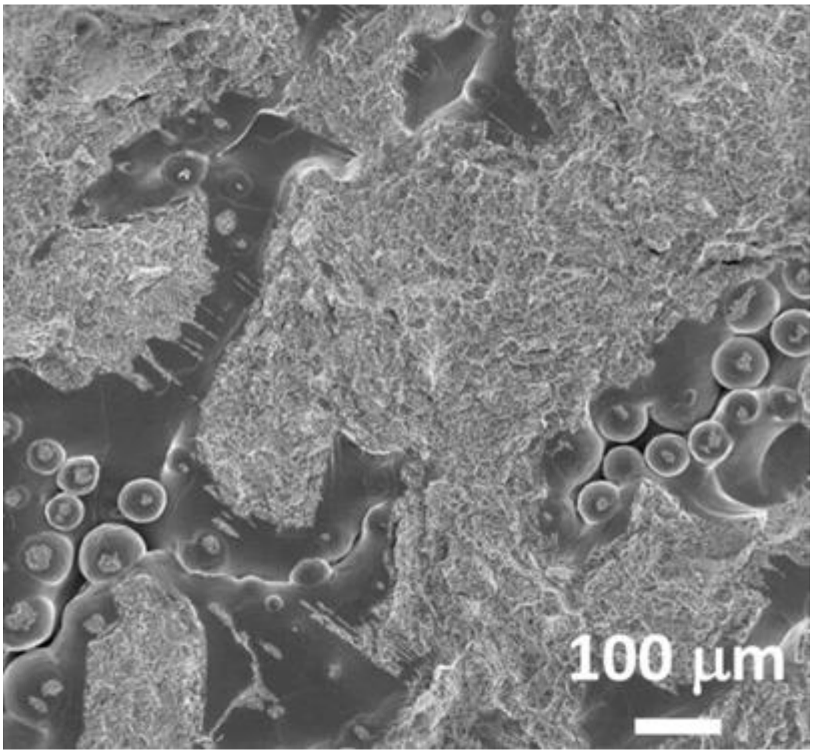  | [30] [70] |

## 2.4.1 Lack of fusion

The effects of defects on mechanical performance of AM parts have extensively and is still currently being studied by many authors [53] [24] [70] [62]. However, limited information and sources explain the underlying phenomenon causes of defects. Lack of fusion defects is predominately reported caused by the use of non-optimised process parameters and process instabilities of AM hardware and parameters [70]. Figure 49 shows typical LOF defect and spherical pores defects found in EBM in process

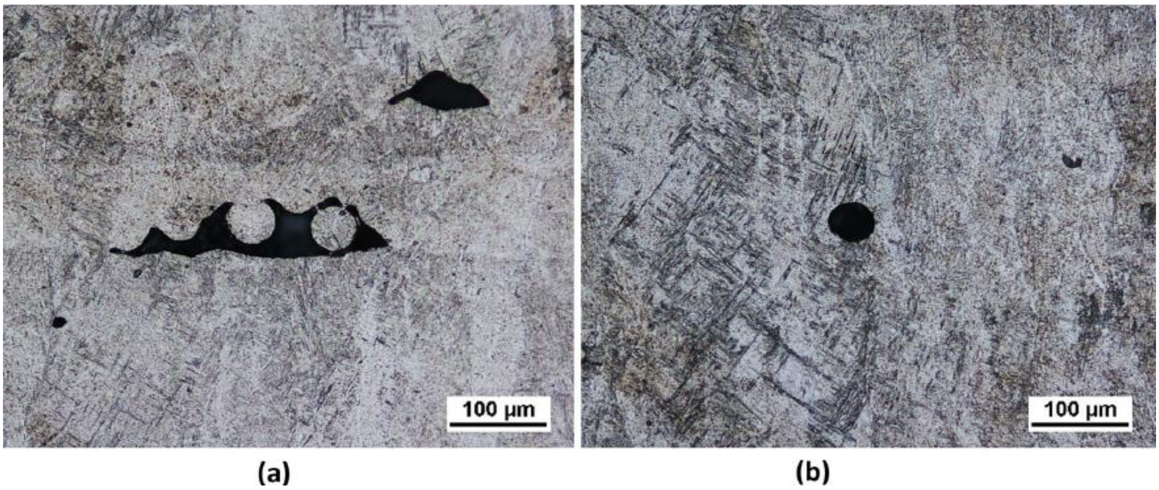


*Figure 49 (left) Irregular lack of fusion porosity), (right) spherical gas porosity [19].*

Pores

Due to tiny size pores in AM, traditional methods such as cross-sectional cutting of samples or Archimedean density does not always give a full representative volumetric information on pore(s) location, morphology size/ spatial distribution. Modern technologies such as X-ray micro-tomography (μXCT) although expensive to operate, has become an alternative tool to characterise complex 3D geometries for defects and pores. [71]

Research carried out by Cunningham, et al. [71] demonstrates the effects of powder porosity manufactured using PA and PREP powder as shown in Figure 50, it was found gas pores size distribution was similar or inherited to as-built parts. However, at much lower volume fraction. Although HiPing closed the majority of pores, Cunningham et al. [71] observed pores approximately 5 µm, thus not eliminating all pores. Majority of AM users seem to think HiPing closes all pores but this goes to show limitations on inspection for tiny pores which require expensive and much more sophisticated technology to see pores of that magnitude.

It should also be noted that when AM parts are in operation at elevated temperatures, there can be tendency of gas pores (argon) regrowth by almost 200% as reported by Cunningham, et al. [71], where they found β-solution of HiPed +heat treated at 1050°C for 10 min resulted in reformation of pores . Nonetheless, lof defects were found not to regrow [71] as shown in Figure 50.

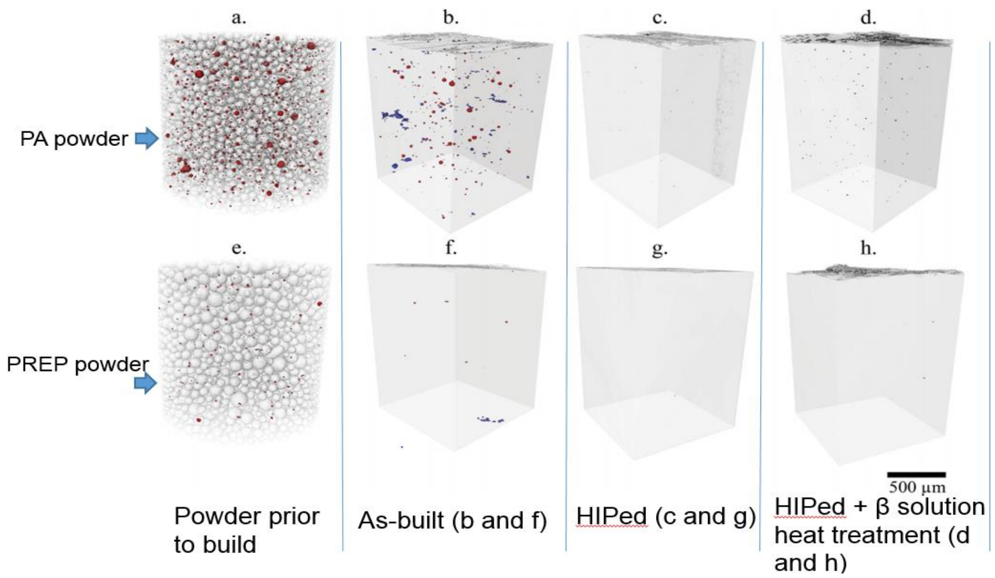


*Figure 50 µSXCT data of as-built porosity for Plasma Atomised powder (a-d) and TIMET powder (e-f) [71].*

### 2.4.2 Effects of process parameters on defects

Beam focus sharpness during melting has been demonstrated to cause lack of energy penetration during melting of AM parts. Gong et al. 2013 reported and found that an enlarged focus on the melt pool reduced the vertical energy input. [70]

Gong et al. 2013 among other authors also demonstrated the effects of line offset in EBM process papers. They found porosity increased when the line offset value increased above 0.17mm as shown in Figure 51

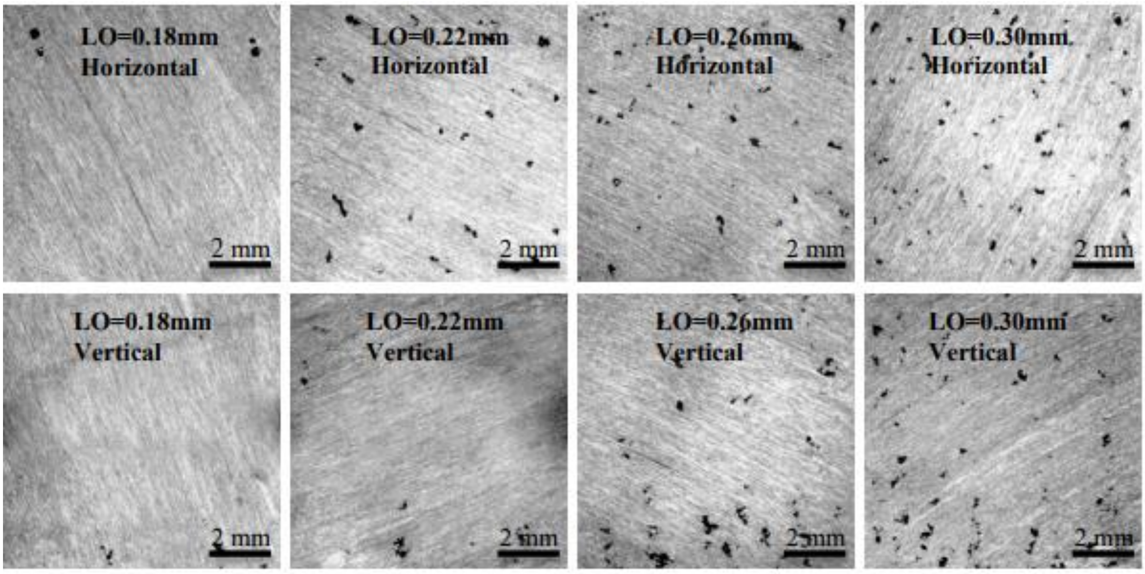


*Figure 51 effects of line effect in EBM process porosity (Gong et 2013 [70].*

Changes in input energy density as a result of non-optimised parameters have also intensively been studied by many researchers. Among other researchers, Gong et al. 2013 [70], found LoF defect morphology is mainly influenced by the sharpness of the beam and line offset. These two main parameters were also found to be influenced by the sharpness of the beam. By Kirchner et al., 2015 [61] who showed that a process window of line energy existed between 100 J/m and 200 J/m where fully dense components were built. Higher energy input above 300J/m resulted in swelling or overheating of the top surface melt pool while energy input below 100J/m also cause porosity as shown in Figure 52 [61]

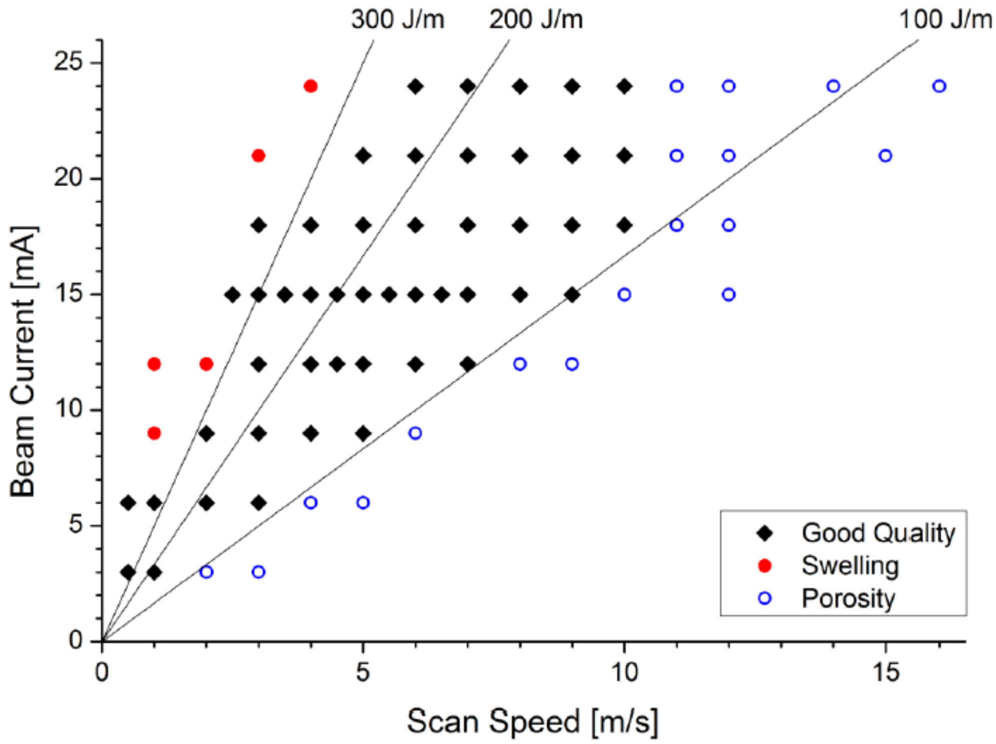


*Figure 52 Effects of EBM energy input on part quality /defects [61].*

Sam Tammas-Williams et al. 2015 [54] demonstrated the use of different scan strategies having an effect on the formation of defects on the parts. It was found that using contour only strategy resulted in fewer defects in comparison to hatch setting as shown in Figure 53. This is likely due to changes in energy input of contour and speed functions. Although the research was carried out on the A2 series machine, this phenomenon might not be directly applicable to new Q series machine currently as it uses rotational hatching than XY rotation in A series machine. The effects of these parameters on surface finish, thin struts/wall, and bulky geometries still need to be understood. [54]

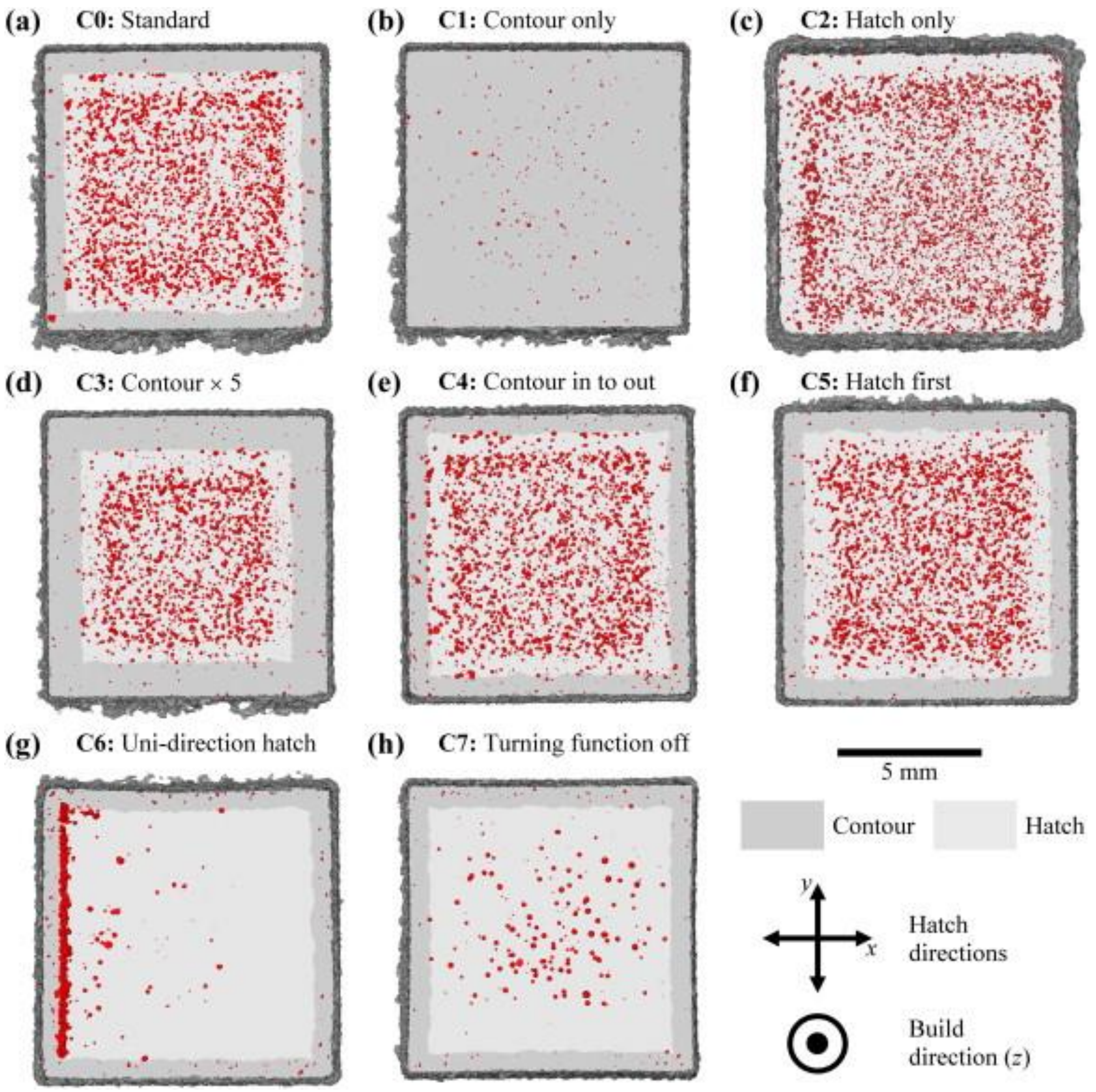


*Figure 53 The effects of process optimisation strategy on defects formation between contour only vs. Hatch [54].*

### 2.4.3 Process optimisation effects on microstructure

EBM melt parameters have a extensively been studied by many authors to understand the effect on the thermal history of the build settings/ parameters , which is closely related to the microstructure observed and resultant mechanical properties [49] [37] [50]. For example, key variables such as; beam power, spot diameter, scan speed and pre-heat temperature all affect the thermal history of the part and therefore the solidification and nucleation mechanics [62] [5]. Table 12 shows some of the key parameters adjusted by the EBM control software during melting.

Parameters that alter the heat input can strongly affect the build structure and microstructure, numerous sources have part quality or defects is mostly influenced in the amount of porosity, swelling (overheating), lack of fusion and surface finish among other variables [50] [48] [40]. Parameter optimisation is therefore essential across materials with the amount of melting energy per unit area, sometimes called the 'line energy' or 'specific energy density,' a key variable in melting.

*Table 12 example of EBM A2X process themes parameters. EBM complex algorithm automatically calculates and adjust values above to maintain energy/heat input [50].*

| | | | | |
|---|---|---|---|---|
| PreHeat | | | Focus offset | 125 ± 75 mA |
| | | | Heating focus offset | 250 ± 150 mA |
| | | | Offset to part | 5 mm |
| | | PreHeat 1 | Max beam current | 30 ± 10 mA |
| | | | Beam speed | 11,000 ± 3000 mm/s |
| | | | Max No. repetition | 39 ± 4 |
| | | | Ave current | 14.8 ± 4 mA |
| | | PreHeat 2 | Max beam current | 38 mA max |
| | | | Beam speed | 11,000 ± 3000 mm/s |
| | | | Max No. repetition | 21 ± 4 |
| | | | Ave current | 16.8 ± 4 mA |
| | | | Max heat time | 28 ± 7 sec |
| Melt | Contours = 3 | Outer contour | # Spots | 50 |
| | | | Spot time | 0.8 ms |
| | | | Multispot overlap | 0.5 mm |
| | | | Current | 5 mA |
| | | | Focus offset | Nominal post calibration ± 10 mA |
| | | | Speed function | 6 |
| | | Inner contour | Current | 12 mA |
| | | | Focus offset | 0 |
| | | | Speed function | 30 |
| | Hatch | | Current | 17 mA |
| | | | Focus offset | Nominal post calibration ± 10 mA |
| | | | Speed function | 36 |
| | | | Line order | 1 |
| | | | Line offset | 0.2 mm |
| | Heating | | Max heat time | 25 s |

### 2.4.4 The effect of cooling rate in EBM materials

A related effect to this is increased build height, which has also been shown to alter the microstructure through thermal means. Tan et al. showed a gradation of the microstructure occurring as the building height increased with α lath width getting larger as the build gets taller. This finding was also confirmed by Al-Bermani et al. 2012, who showed that α lath width increased from 1.73 to 3.04 μm as the building height increased. This effect is due to a decreased cooling rate at the top of the build, likely due to a reduced capacity for the powder bed to conduct heat as any annealing time effect would show the opposite result of coarsening the bottom of the build more through increased time at temperature. Thinner structures have also been shown to alter the microstructure with α' martensite observed due to the faster cooling rates in thinner structures through less heat input due to shorter scanning times and smaller line energy.

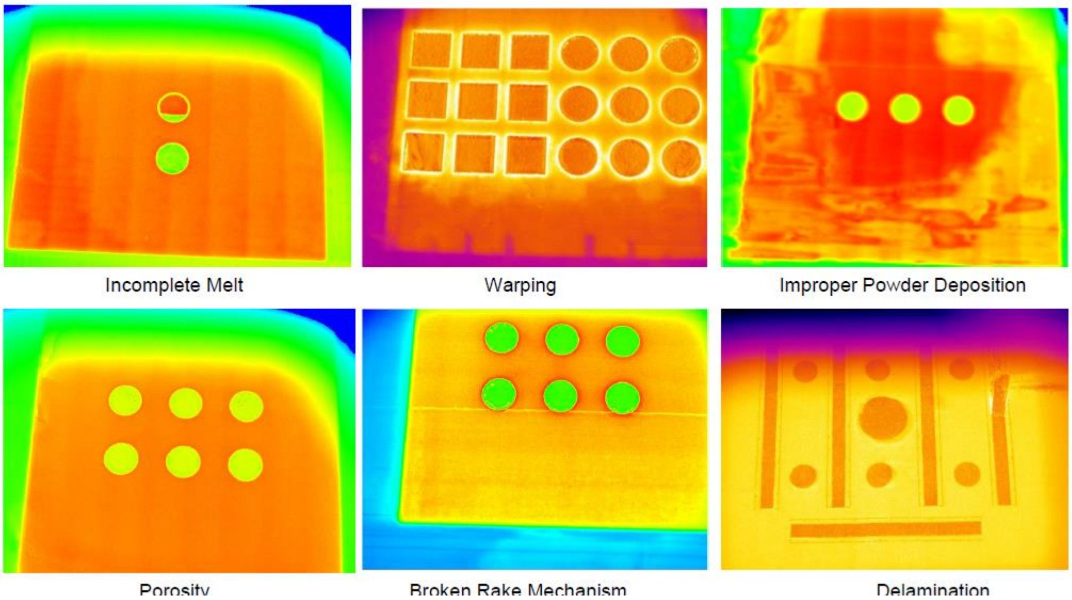


*Figure 54 defects found using Infrared images on EBM machine [59].*

### 2.4.5 Inclusions

Inclusions are the result of contaminants in the material/powder and can be split into two classes: interstitials and foreign bodies. Interstitial contaminants arise from the powder itself. The level of contaminants present in a powder must be within a specified limit. Should the percentage of impurities become greater than this specification, then the powder is out of specification.. The powder can become out of specification as it is re-used between builds. These inclusions can result in reduced mechanical properties in the built component.

The second type of containments is foreign bodies. These can result from debris from the AM process or post-processing equipment, e.g., broken rake teeth used to spread the powder in EBM

## 2.5 Post Processing of AM Parts

AM surfaces are typically post-processed in one of several ways to improve their surface texture. The material properties of as built parts produced using additive manufacturing differ from parts produced using traditional manufacturing methods.

The high level of roughness associated to additive manufactured components leads to increased crack initiation zones [68] . It has been found that reducing the roughness of as printed Ti-6Al-4V from a Ra value of 17.9µM to a Ra value of 0.3µM can increase the fatigue strength of components from 300Mpa after $3x10^7$ cycles (as built) to 775Mpa after $3x10^7$ cycles. [72]

Barrel finishing improves the surface of components by rotating a mixture of parts, abrasive media and carrying agents in a barrel. The relative motion between the parts and the media abrades the surface of the component. The process rounds corners, deburs and smooths surface asperities, this leaves the surface smooth and has the potential to leave a polished surface. Figure 55 is an illustration or sketch of centrigual high energy finishing with surface finishing media and part.

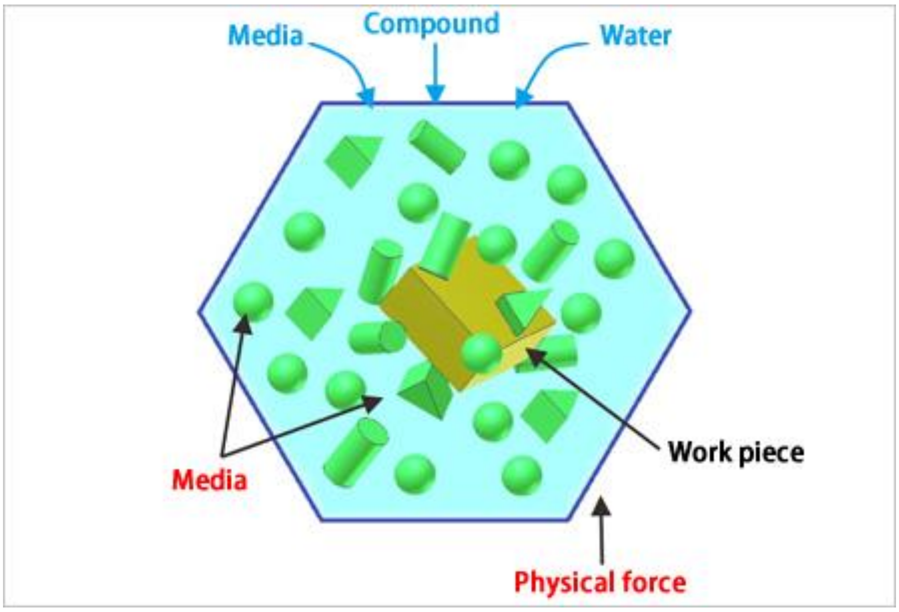


*Figure 55 Barrel finishing illustration of component in abrasive media to improve surface finish.*

Shot peening is typically performed to improve the fatigue life of metallic components, the process involves cold working the surface with the use of spherical particles impinging at a set velocity. The surface upon impingement yields but is restrained by the subsurface substrate, this effect induces residual compressive stresses in the surface of the material which is favourable when the part undergoes tensile loading [73].

Laser polishing

Laser polishing reduces the roughness of an additively manufactured surface by melting a layer of material approximately 50-200 µm in depth, dependant on parameter levels, such that any surface asperities (un-melted powder particles in the context of additively manufactured parts) are melted and re-flow into areas where surface valleys were. As such, the height difference between the peaks and valleys on a surface is reduced. Furthermore, the aspect ratio of any peaks or valleys should also be reduced [74].

### 2.5.1 Surface Measurement of AM

Surface measurement of AM components may be carried out with the following objectives:

- For feature extraction, as an input to empirical models or physics simulations to investigate the correlation between the features and the performance of the product.

- For process control. A standard surface roughness parameter is determined.

Triantaphyllou et 2014 [75] described the challenges for surface texture measurement for AM. [75] A recent review paper by Townsend 2016 [76] grouped measurement technologies into profilometry, aerial topography, volumetric topography and 2D imaging. An overview of the surface measurement technologies is given in Table 13 and the sub-sections below. [77]

*Table 13. Surface measurement technologies suitable for AM parts [77].*

| Surface measurement technologies | Technology class |
|---|---|
| Contact stylus | Profile |
| Sectioning and measurement on section | Profile |
| Confocal microscopy | Aerial |
| Focus variation | Aerial |
| X-Ray CT | Volumetric |
| Scanning Electron Microscopy | 2D imaging |
| Optical Microscopy | 2D imaging |

Profilometry methods

Townsend *et al.* (2016) note that while traditional profile measurement (e.g. of Ra parameters) via stylus-based contact instruments is a very commonly used method, it is inherently limited to simple surfaces or surfaces where there is one predominant lay. As-built EBM components have highly complex surfaces which will likely require aerial topography characterisations. Contact stylus and optical methods are not able to capture re-entrant features, such as those shown in Figure 56.

The surface profile can also be characterised by sectioning a component or coupon, mounting, imaging under a microscope, as shown in Figure 56. The profile is then extracted by image processing [75], and surface parameters can be calculated.

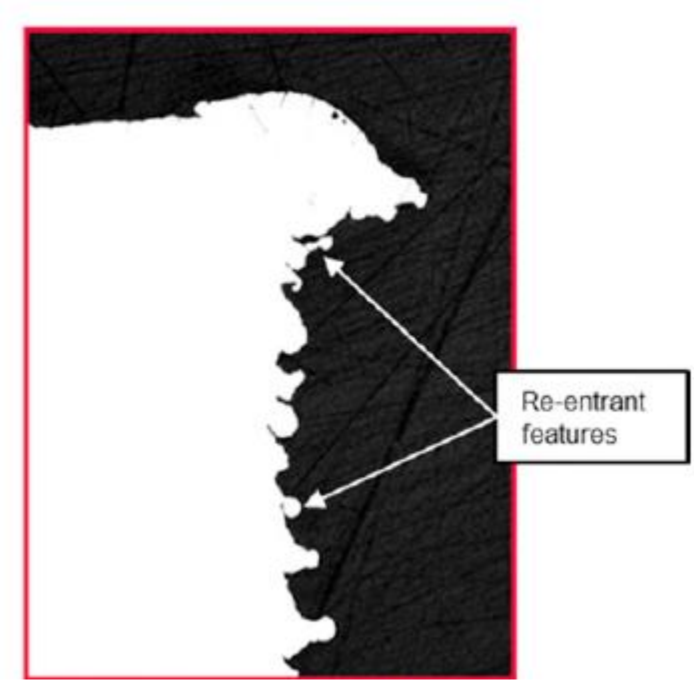


*Figure 56. Image of Electron Beam Melted sample that has been sectioned and mounted to allow the surface profile to be extracted. Re-entrant features are indicated. Source: [75].*

### 2.5.2 Non-destructive Evaluation review of AM

Non-destructive evaluation (NDE) is a group of test methods that image the product without damaging it. The primary focus of NDE tests are material discontinuities that affect the structural integrity. However, some of the methods are also capable of finding, for example, remnant powder, which could affect other aspects of product performance such as, e.g., fluid flow [54].

NDE can be carried out at any point after the metal has solidified either in-situ on the powder bed or ex-situ. However, in-situ NDE is relatively immature and is not considered further in this report.

Todorov et al. 2014 [78] identified common NDE methods and assessed their suitability/potential for various levels of geometric complexity. Todorov et al. 2014 [78] differentiate between X-ray computed tomography (XCT) and microfocus X-ray computed tomography. In microfocus XCT, the focal spot size of the source is in the order of 10-100 µm, compared to conventional systems which can have spot sizes up to ~10 mm. The focal spot is nominally independent of component size and geometric complexity [54] [55]. However, in an X-ray source, the focal spot size is not fixed and tends to increase in size with the power of the electron beam. [46] Higher beam powers are typically called for when scanning larger or denser samples. A non-infinitesimal focal spot will cause blurring due to geometric unsharpness if the geometric magnification of the sample is used. This effect, important at high magnification, is minimised by using a small focal spot.

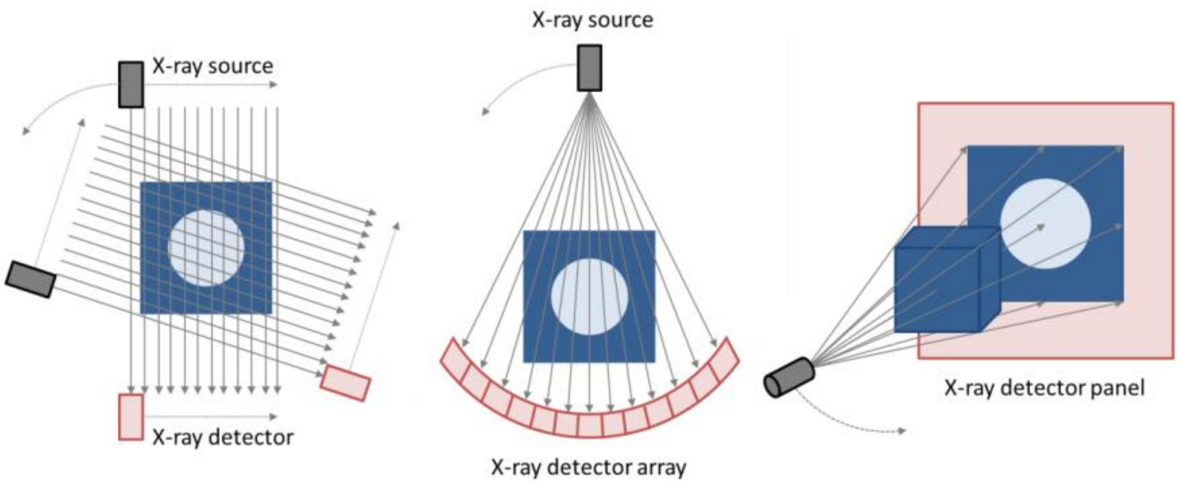


*Figure 57 Schematic of X-ray detector array when scanning component [79]*

Other nonlinear acoustic test methods also have potential, but Todorov did not identify the broader category. Radiography, visual testing, and dye penetrant testing are discounted by Todorov et al,2014

[78] but may have some applicability to detection of material discontinuities in complex AM geometries such as lattice structures and so are discussed here.

X-Ray computed tomography (XCT)

XCT relies on the systematic collection of a large number of X-ray images to build up a 3D volume representation of the component. XCT has potential to detect material discontinuities (pores, cracks, and contaminants) or remnant powder in a lattice structure (see Figure 58).

To obtain the X-ray images, the component is rotated on a stage between the X-ray source and detector. Imaging is most commonly carried out once the component has been removed from the build plate. Figure 58 shows an example of AM complex part with powder remnants and voids in the internal part using radiography inspection.

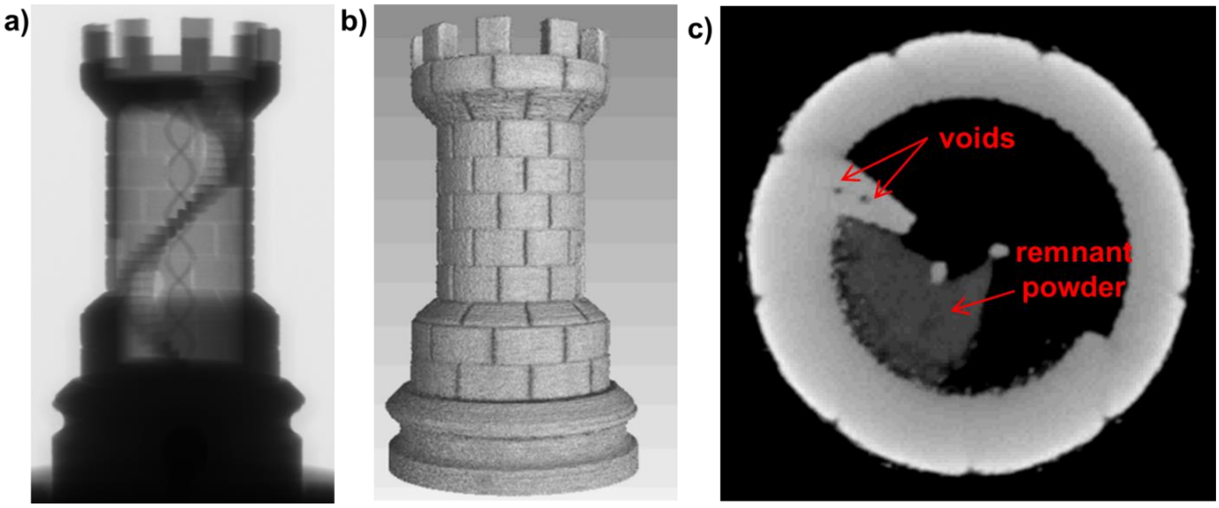


Figure 58. Images of electron beam melted rook with overall dimensions approx. 20 mm dia. × 50 mm a) digital X-ray image b) surface rendering of reconstructed X-ray CT data c) section through X-ray CT voxel data. Voids and remnant powder can both be observed in (c). Remnant powder is partially sintered and has a lower density than the fully melted material and thus is a darker shade of grey. Images courtesy of The MTC

Since the X-rays propagate through the component, generating a back-projected image, there is no specific limitation regarding geometries, making XCT one of the highest potential candidate test methods for lattice structures.

The main limitations of XCT are:

- The contrast between the material discontinuity or remnant powder and the surrounding or adjacent material, which is provided by the relative X-ray absorption of the two media.
- The spatial resolution of the imaging system, which is related to the focal spot size, the detector pixel size, and the magnification. The component size limits the magnification. For detection, the material discontinuity or remnant powder has to be large enough relative to the spatial resolution of the scan.
- The ability of the X-rays to penetrate the component is linked to the greyscale contrast requirement for detectability, which in general will be reduced by longer material path lengths (caused by thicker component sections) encountered over the course of the scan.
- The size of the component that can be fit into the XCT chamber / X-ray beam, especially as in most system designs the sample needs to be rotated in the beam through a full revolution over the course of the scan. [78]

Radiography

2D X-ray imaging (film, computed or digital radiography) has some capability to detect remnant powder and material discontinuities [54] [55] However, the method will be difficult to set-up where there is high geometric complexity. If the likely orientation of a defect is unknown, then multiple shots will be needed to ensure adequate coverage. See, for example, Figure 58 where the voids and remnant powder are readily visible in the XCT data but not in a single digital 2D X-ray image. With high geometric complexity, it is also challenging for the inspector to plan a shot which gives adequate sensitivity and contrast across broader regions. The net result is that multiple shots may be needed. Nonetheless, radiography is likely to be less expensive than XCT, even if multiple images are acquired.

Interpretation of the X-ray images obtained is also likely to be more difficult than for XCT. The challenges with inspection planning and interpretation push people towards XCT for complex AM geometries currently.

Nonlinear Acoustic Testing

The sensitivity of nonlinear acoustic test methods to internal porosity and remnant powder is uncertain as this technology is reasonably immature. It is unlikely that porosity will be detectable if the associated mass reduction is not greater than the acceptable component-to-component variation in mass.

Similarly, remnant powder is expected to damp vibration / acoustic propagation but will only be detectable if the variation in damping is greater than the acceptable component-to-component variation in damping. [78]

Nonlinear acoustics is a large research field and, due to challenges in making the tests industrially robust, application for NDE is still not mature. Resonant testing is one of the families of methods, an example of which is process compensated resonance testing [80]. Numerous transducer configurations can be used, depending upon the sample geometry and what is being interrogated (for example, a volume or an interface). More information on nonlinear acoustic testing for NDE and materials characterisation can be found here [81].

Ultrasound – Acoustic NDT

This NDT inspection method uses an electromagnetic acoustic (EMA) way of ultrasound excitation. The method can be used for measuring flaw detection, location and dimensional measurements [82]. Although the process is contactless, Lopez et al, 2018 [82] reports that the process requires proximity; This process is mainly suitable in environment with high temperatures; geometric suitability constrained can be challenge for complex AM process. No literature has been found yet to understand the influence of low sensibility for small defects pores if they inspected. Standards are also not yet adopted for this method. [82].

Visual Inspection

AM geometries with complex shapes such as lattice structures or thin wall will have high levels of obstruction/occlusion. Thus, visual inspection is likely to have only some limited application for such geometries, either to inspect the outer volume and to check for gross material discontinuities (deformation, large cracks, etc.) and/or to check lattice structures with large, open cells. Borescopes can be used as an aid, to check internal volumes of a component to ensure powder is removed [83].

Dye Penetration

This technique enhances the visual detectability of surface defects, such as surface cracks or open pores, by using a dye. It is therefore limited in applicability to surface breaking defects and component regions that can be viewed optically (potentially using a borescope). Coverage will be limited as for visual inspection.

The high level of surface roughness in as-built AM components, particularly those made by EBM, will compromise the utility of the technique as the adherence of the dye to the surface features will give rise to many false calls, as shown in Figure 59. It may only be suitable for use on AM components after surface finishing [84].

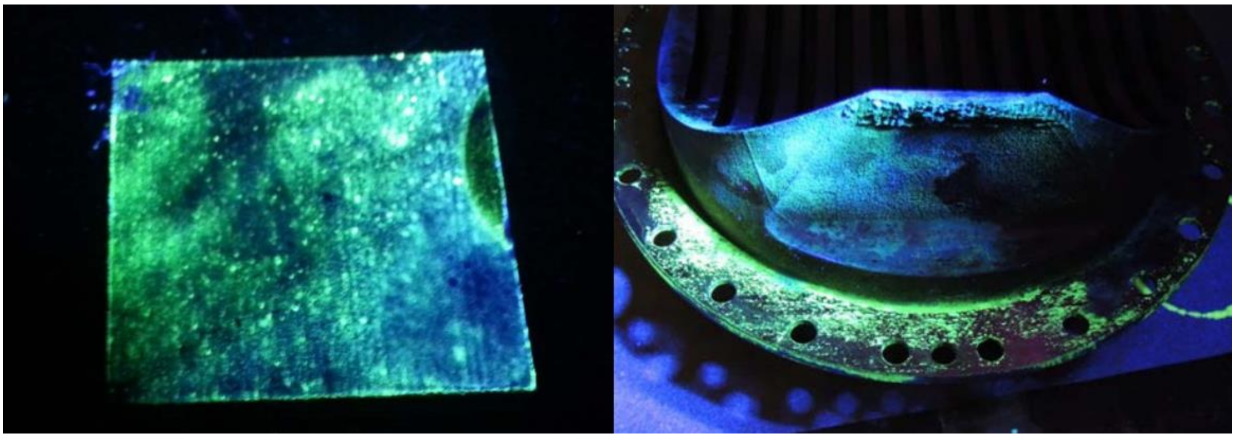

Figure 59. Penetrant testing of AM Ti64 block (left) and (right) showing noise due to surface roughness [84]

### 2.5.3 In-situ monitoring

At the moment most AM systems are focussing on inline monitoring systems that measure the temperature of the layer being built, use of image processing to find defects, etc [85]. This information is used to inform the user and potentially stop a failing build before it wastes material. For qualification and certification, it is envisaged that these inline measurement systems may add to the evidence that the porosity and internal geometry of a built part is within those outlined in the design stage.

Table 14 lists some of the key process variable monitored during the build. These variables are reported post build completion to check any deviation tolerance. If any hardware and variable deviates it can results in process instability and could result in parts induced defects. [37]

*Table 14 some of the Arcam's EBM Key Monitoring variables that can be reported [34]*

| Variable | Measurement Device |
|---|---|
| Max process idle time/layer | Machine computer's internal clock |
| Average process idle time | Machine computer's internal clock |
| Min buffer remaining | Machine computer's internal measurement |
| Max Z deviation | Feedback from Z-direction motor |
| Filament current | Internal loop high voltage unit |
| Arc-trips / 10 minutes | Machine computer's internal measurement |
| High voltage range | Internal loop high voltage unit |
| Column temperature | K-type thermocouple mounted in the upper column |
| Bottom temperature | K-type thermocouple mounted below start plate |
| Max chamber pressure | Chamber vacuum gauge |
| Max column pressure | Upper column vacuum gauge |
| Filament has been peaked | Internal loop high voltage unit |
| Number of abnormal pulses/layer | Powder sensors |
| Min grid voltage / layer | Internal loop high voltage unit |
| Min grid voltage deviation | Internal loop high voltage unit |
| Max cycle time | Machine computer's internal clock |

Although latest EBM Q-series generations machines have the cameras to in-situ monitor builds for defects during process optimisation. Other researchers have been able to measure and map the temperature profile of the melt pool to determine and correlate this simulation studies. Among other authors, Price et 2013 [86] were able to measure 2D temperature profile of EBM process at different melting stages as shown in Figure 60. [86]

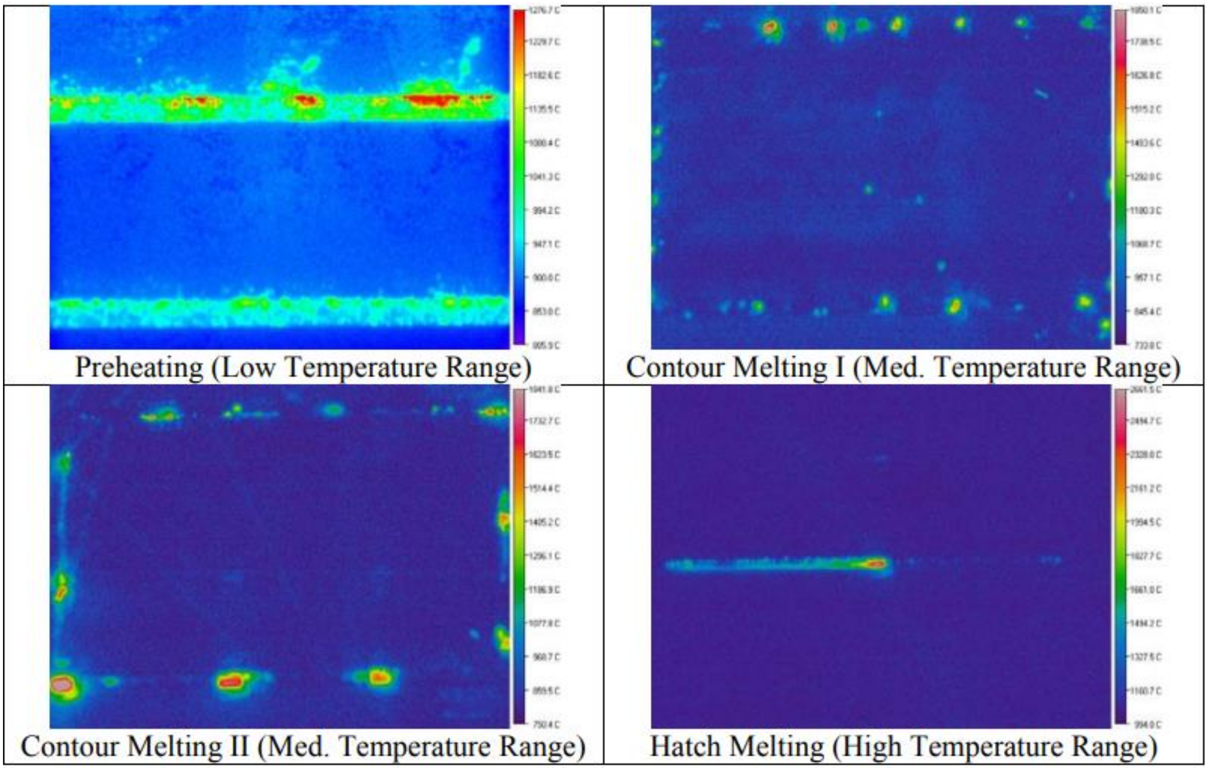


Figure 60 Near-Infrared Camera images taken during different EBM stages [86].

Among other challenges reported by Everton et al. 2015 [85], variables such as spatial resolution, view limitations and substantial data processing are some the challenges in AM process that can result in less accuracy measurement and feedback during AM machine to have a full closed loop system capable of identifying defects and making necessary decision to correct. Below Figure 61 demonstrates the Arcam's layerQam technology currently on Q-series machine. The camera-based technology can view approximately 150µm defects [48].

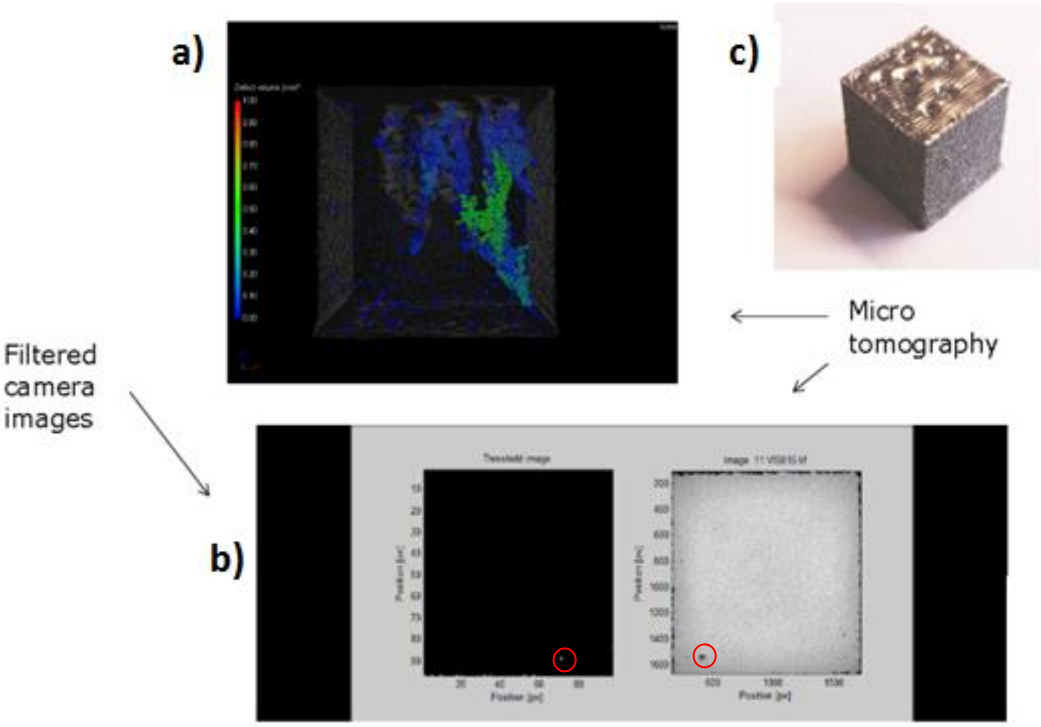


*Figure 61 An example of the LayerQam™ image results. a) A 3D image produced by the combination of separate layer images produced by the LayerQam™. The coloured key on the left-hand side represents the defect volume; b) a 2D image of a single layer. The red circle [48]*

In- Situ SEM –XQam

Arcam has recently launched EBM Q20 plus series machine with an X-ray detection and monitoring system called xQam™. According to Arcam [87], "the system is being developed to offer in-situ automatic Scanning Electron Microscope (SEM by utilising secondary electron and X-rays emitted during the EBM melting process" [87] as presented in Figure 62 below.

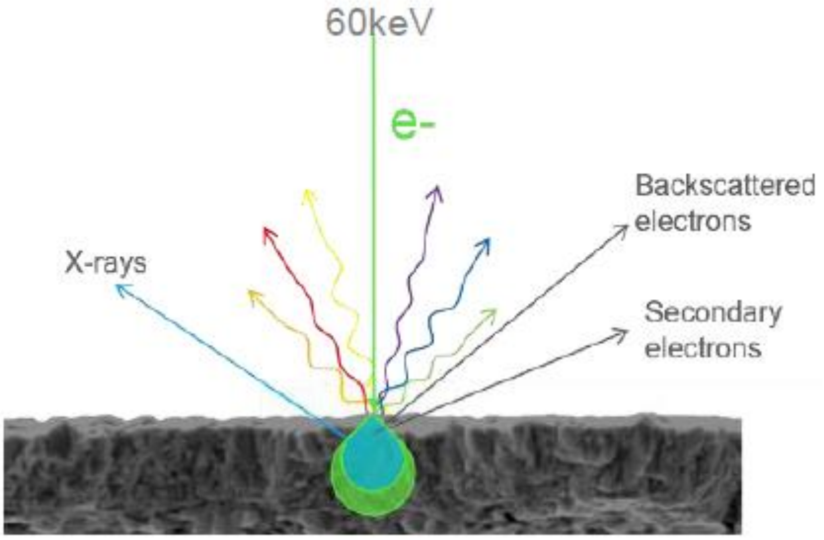


*Figure 62 Arcam xQam system utilising the X-Ray emission from EBM process for process monitoring Figure 62*

Arcam future equipment functions will include in-process monitoring for powder bed EBM topography, chemical composition and defects monitoring [87].

### 2.5.4 AM post-processing

Every post-processing operation has a possible effect on the quality, as it changes the physical properties of the component. In L-PBF, due to the residual stresses generated in the part, there is significant post-processing required (for example heat treatment). Support structures are also essential to support the material and allow for the alleviation of the residual stresses. In case for thin overhanging structures (<1mm), where support structures are essential to prevent warping. The supports almost always require removal once the heat treatment is complete, and this may cause damage to the component as witness marks can be seen where the supports were placed. It is therefore important to determine the optimal orientation of the part during the build model generation process. Other post-processing steps such as finishing processes like laser polishing or tumbling can be used to improve poor surface quality caused by remaining support structures and the rough surface of the as-built component.

Support removal

Unlike L-PBF, fewer supports are required for EBM process due to the semi-sintered cake powder surrounding the part, but the supports that are required for additional heat transfer should be possible to remove in the same way as L-PBF supports. Figure 63 shows an example of EBM part with supports and tools used to.


*Figure 63 EBM part with tools used to remove supports [88]*

#### 2.5.4.1 EDM Wire Cutting

This is a computer controlled cutting process that can be used to cut part from support, using the platform level or part height as a datum, and then again to cut the supports from the build platform. It is possible to program the path of the wire, so a specific profile is cut. If wire cutting is used to cut hollow supports, there may be loose powder trapped inside. This could cause health and safety issues with the EDM operatives: ensure correct operating procedures are followed according to the material. It may be safer to use solid extrusions to attach the part to the platform and wire cut through the solid bulk.

#### 2.5.4.2 Manual Removal

Parts can be chiselled from the platform and support removed by hand, using pliers and other hand tools, or crushed in a vice, which can loosen the teeth attached to the part. Manual removal is sometimes the only way small, intricate parts with support can be removed.

#### 2.5.4.3 Machining

Machining can be used to remove supports from parts only after they have been removed from the platform. Hand removal of supports usually leaves witness marks on the part where the support teeth had been attached. These have to be smoothed manually or by machining, blasting or mechanically finishing these surfaces.

The empty platforms can be resurfaced mechanically, e.g., by machining, EDM wire cutting or spark erosion and reused.

### 2.5.5 Thermal Heat treatments

Hot Isostatic Pressing (HIP)

This section aims to review and discuss the use of thermal heat processing in AM for defects, pores, microstructure and mechanical performance changes. Schematics shown in Figure 64 illustrates the effects of heat treatment of AM parts

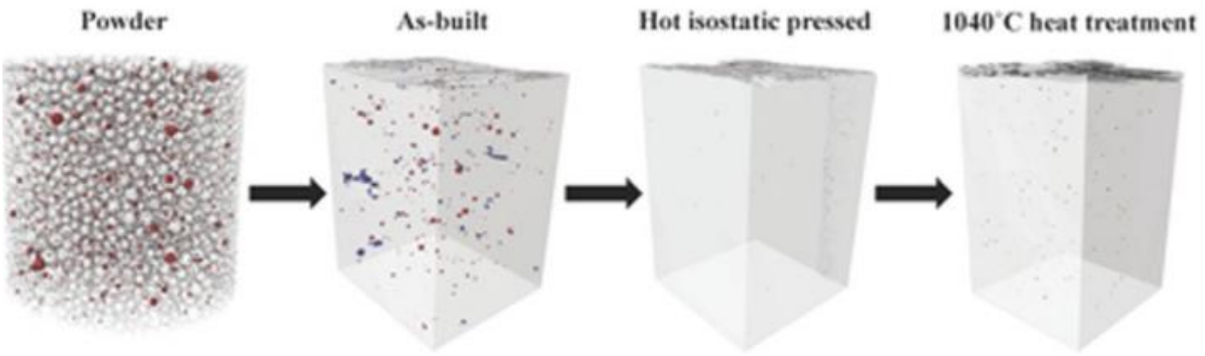


*Figure 64 Schematics showing the effects of Heat treatments in AM PBF [19]*

A vast majoring of researchers have in the decade reported the effects of HiPing AM parts to close pores, defects, change microstructure and mechanical performance. [62] Among other authors [89] found due to build 'Z' directional solidification and rapid cooling of Nickel-based alloys, the AM L-PBF samples experienced anisotropy microstructure with an "epitaxial grown microstructure," this same phenomenon has also been found for components manufactured using Titanium material in EBM process [54].Table 1 are typical thermal heat treatments parameters carried out for Ti-6Al-4Vmaterial.

*Table 15 Typical thermal heat treatments for Ti6Al4V material, [34], [90]*

| | |
|---|---|
| Alloy | Ti–6Al–4V |
| Stress relief | 2 hours, 700–730°C usual for L-PBF [90], EBM not required |
| Hot isostatic pressing (HIP) | 2 hours, 900°C, 900 MPa [73]180 ± 60 min, 895–955°C, >100 MPa [34] |
| Solution treat (ST) | Not typical |
| Aging | Not typical |

Internal porosity and surface roughness can have a detrimental effect on the fatigue resistance of the part. A HIP process can close these internal pores by applying uniform pressure to the surfaces of the part, which forces the pores to close and therefore improves both the mechanical and fatigue resistance and the ductility of the part. X-ray tomography can be used to examine the porosity and defects location before and after HiPing on AM complex parts. Figure 65 shows typical EBM AM defects for as-built condition in a non-stable process or inherited pores from powder supplier.

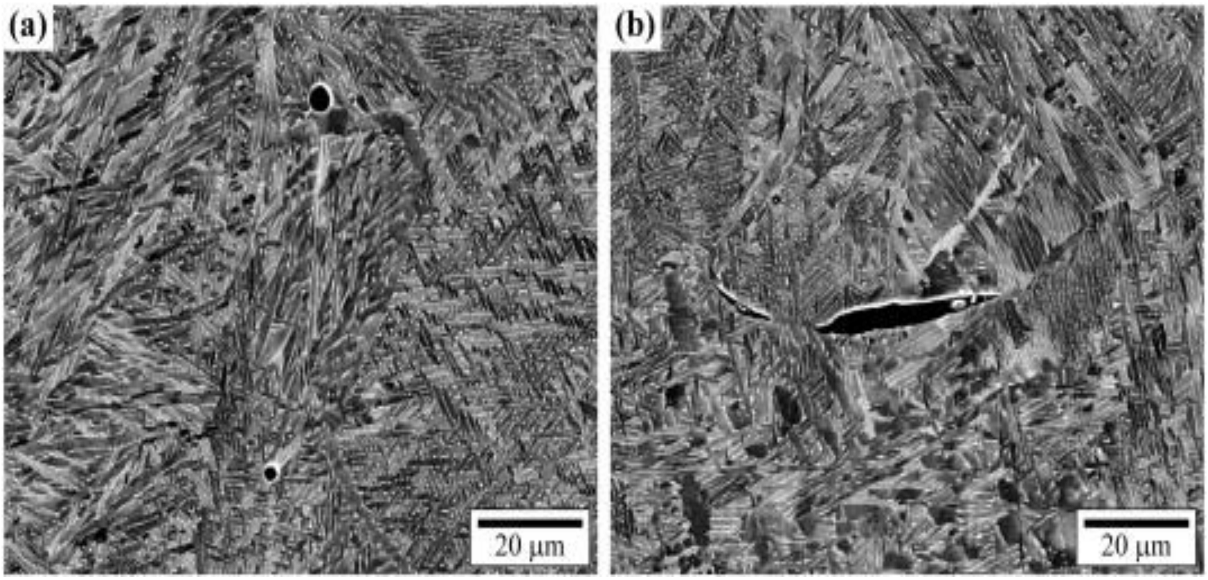


*Figure 65 Example of AM defects found in EBM a) spherical gas pores inherited from raw powder (b) lack-of-fusion defect due to process parameters [54]*

However, HIP will not close surface interconnected pores or defects as shown by work with [54]. Figure 66 is an example of samples deliberately build with defects (internally and externally), this goes to demonstrate the pros and cons of HiPing. Hence it may be beneficial to machine the surface after HIP to ensure there is a dense outer surface.

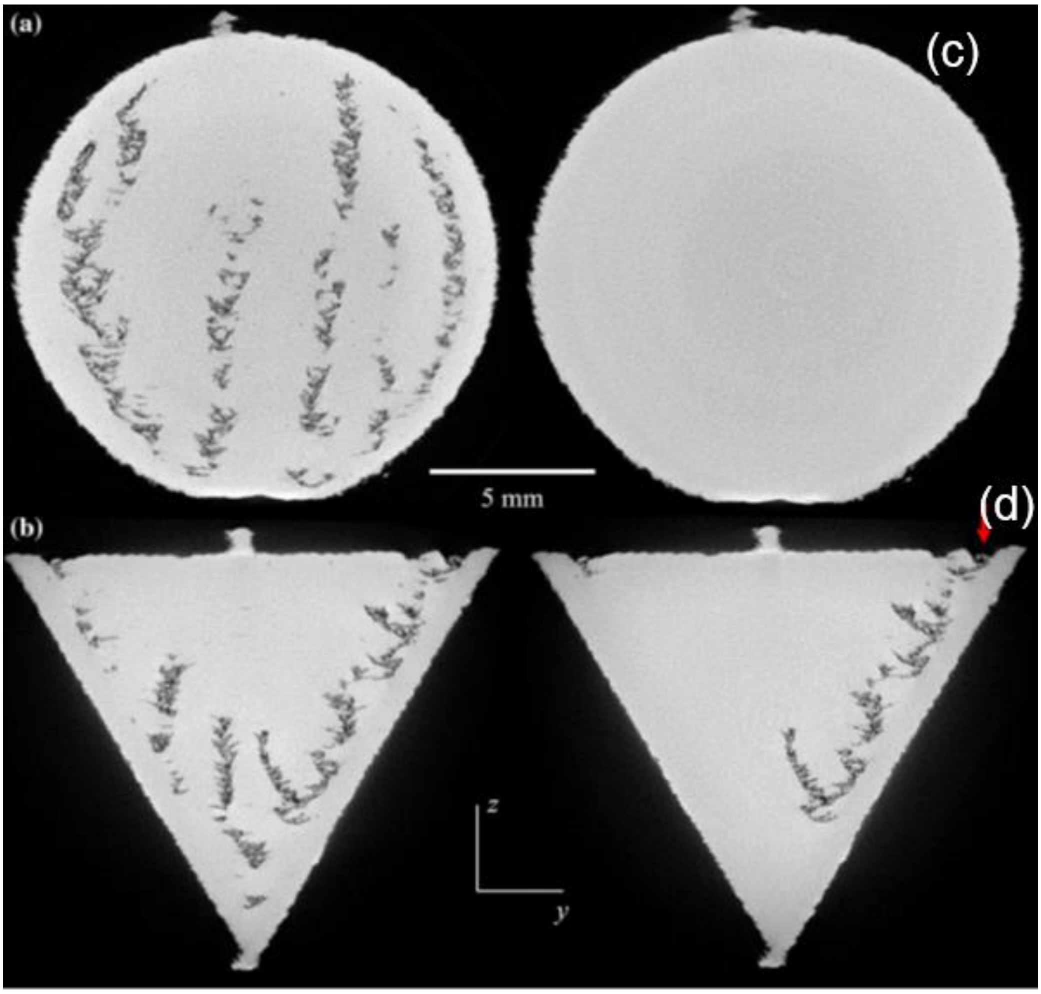


*Figure 66 XCT data indicating pores and defects in parts (a) large sample scanned with 9.9µm voxel size (b) high XCT resolution of 2.1µm scan iindicating lack of fusion defects (c) Sample scanned and NO defect found after HiPing (d) Indications of surface connected defects of a HiPed sample. [54]*

*2.5.5.1 Effect of heat treatments and HiPing on Ti-6Al-4V*

In the study carried out by (Kahlin, Ansell, & Moverare, 2017) [67], on the fatigue behaviour of Ti-6Al-4V with EBM and L-PBF. It was found both LS and EBM HiPed data had similar HV in comparison to wrought reference material. However, there was a decrease in HV for both LS and EBM after heat treatment (HIP) [67].Figure 67 shows the difference in Ti-6Al-4V hardness for laser and EBM process. Influence of HiPing was found, HiPed samples had reduced HV which indicates lower strength in the material as a result.

*Figure 67 Vickers hardness (HV) of Laser and EBM Process of Ti6/4 material. Higher HV can be noticed for LS in comparison to EBM. [67].*

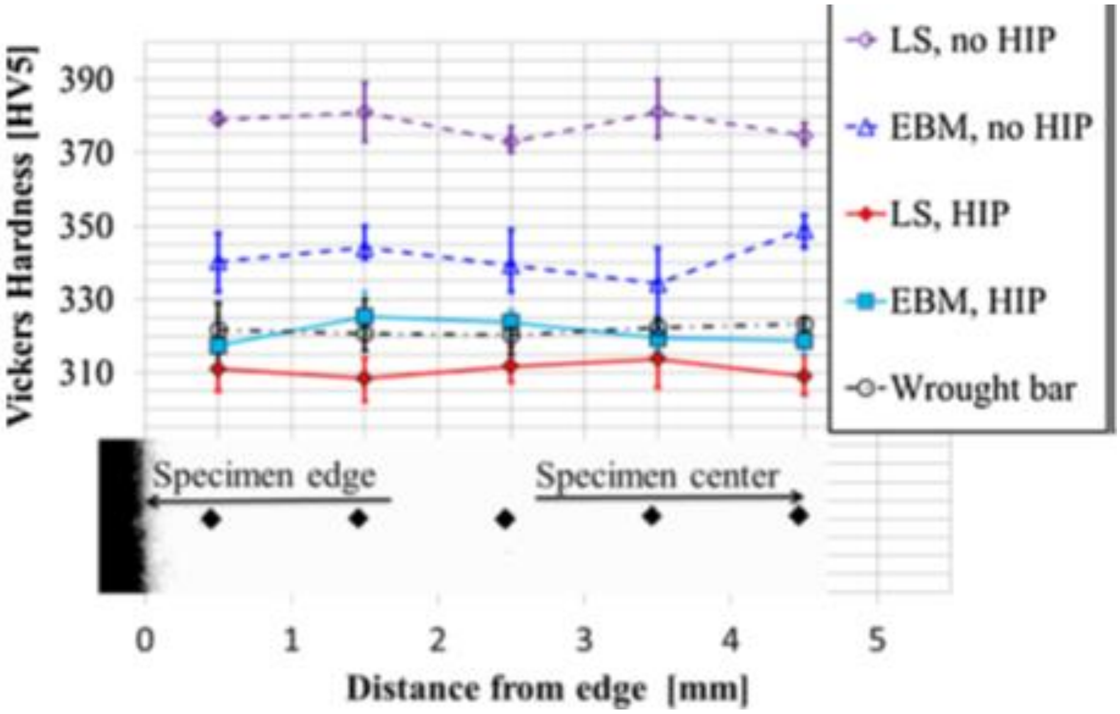


Unlike other AM process, EBM process which preheats (~650-700degrees) each layer to stress relief material during manufacturing and this takes place in the vacuum chamber. So far, the majority of L-PBF material and process is performed in an argon or nitrogen filled chamber. During the build, any internal pores will, therefore, be filled with argon or nitrogen. If a HIP process is then carried out, the gas trapped inside the pores may not successfully dissolve into the alloy, which can then cause thermally induced porosity if the part is heat-treated or reaches a high temperature during its use, causing pores to reappear. Heat treatment (without pressure) promotes stress relief and may obtain desirable microstructure.

*2.5.5.2 Effect of Hot Isostatic Pressing on Ti-6Al-4V on microstructure and mechanical properties*

Heat treatment has been demonstrated to improve both static and dynamic (fatigue) mechanical performance of AM manufacture samples [56] [60] [53]. In some cases, AM manufactured components can match or have better mechanical properties than conventional cast or forge manufacturing [67].

The traditional, different heat treatments can still be applied to AM manufactured specimen to tailor the mechanical performance of a product. These heat treatments in Ti6/4 usually can increase the ductility of the material but have a reduction in tensile strength. This is mainly due to the coarsening of grain during phase transformation of a microstructure [60].

In EBM whereby, a process is performed at high temperature (~650 °C -700 °C), the stress relieved carried out for L-PBF is not required. This results in no or minimal formation of martensite microstructure and mechanical properties are reported closer to the above-wrought material. In accordance to ASTM F2924 [91], it is recommended to carry out Ti6-4 HIP cycle at 920 °C for two hours under a pressure of 100MPa [34]. In the AM community, it is arguable whether the heat treatment currently for conventional methods such as casting should be applied for AM manufactured samples with a different microstructure formation. It has been demonstrated by Hrabe et al. 2013 [49] that heat treatment parameters can be tailored or changed to change mechanical and microstructure performance of AM part. The rapid solidification of fine alpha lath grains in as-built samples can be tailored to possibly on close the defects by pressure but also minimising the grain structure changes [68].

### 2.5.6 Microstructure changes due to Heat treatments

Alpha (α) plate spacing has recently been demonstrated to influence the microstructure by differentiating or tailoring the heat treatment temperature. Work carried by [60] showed an increase in α-place as a result of changing heat temperature as shown in Figure 68. Hrabe et al., 2015 found courser equilibrium acicular or Widmanstätten microstructure formation as result of changing heat treatment parameters. Nonetheless, for stress-relieved samples, they found no changes in microstructure in comparison to as-built samples. These findings contradict with other researchers, [60] but go to demonstrate different heat treatment parameters can result in differing properties as shown in Figure 69.

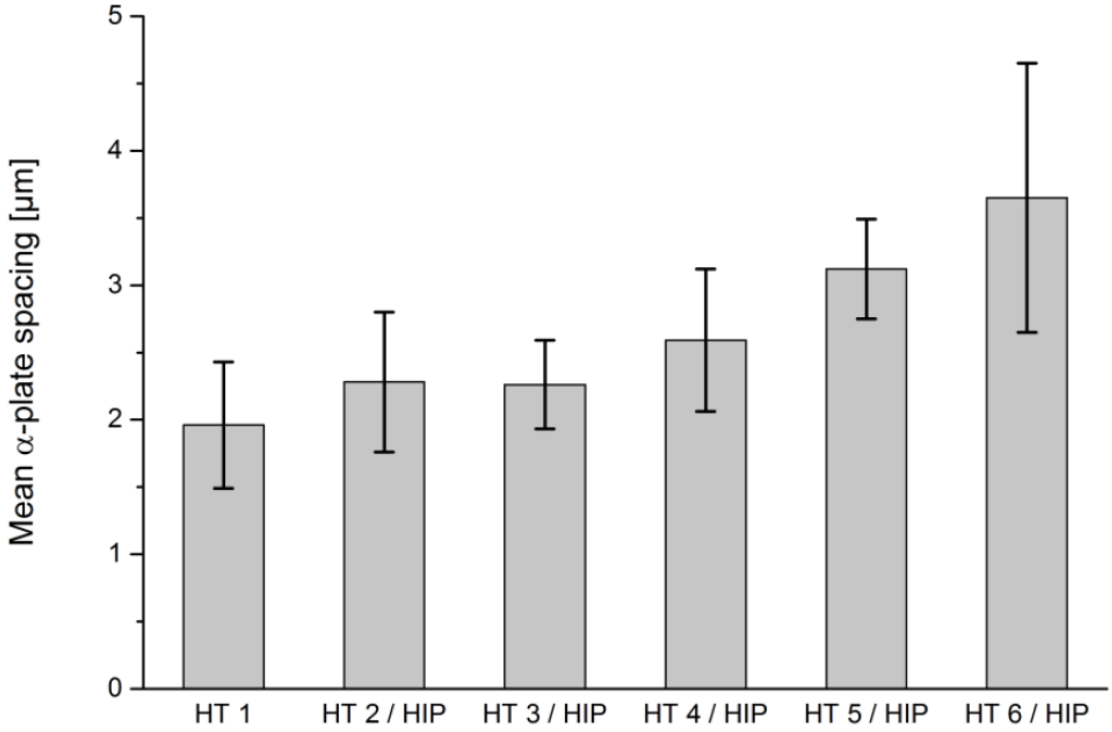


*Figure 68 Effects of different heat treatment on the microstructure alpha lath of Ti6/4 of AM manufactured samples. HT represents heat treatments between 650 °C and 1050 °C, marked with HT 1 to HT 6 in ascending order¸ HT 2 to HT 6 were hot isostatic pressing (HIP) treatments with pressures up to 200 MPa and durations ranging from 0.2 h to 2 h. [60]*

Nonetheless, Kahlin et al. [67] reported post-HiPing as having no impact on fatigue life for as-built EBM surface. Although the study findings stated HiPing as capable of closing internal pores, defects and coarsening of microstructure, it was found not to cause no improvements in fatigue performance.

It can be seen in Figure 69 that microstructure grain texture can differ in AM part because of thermal heat treatment post processing. This will result in different mechanical properties in different conditions.

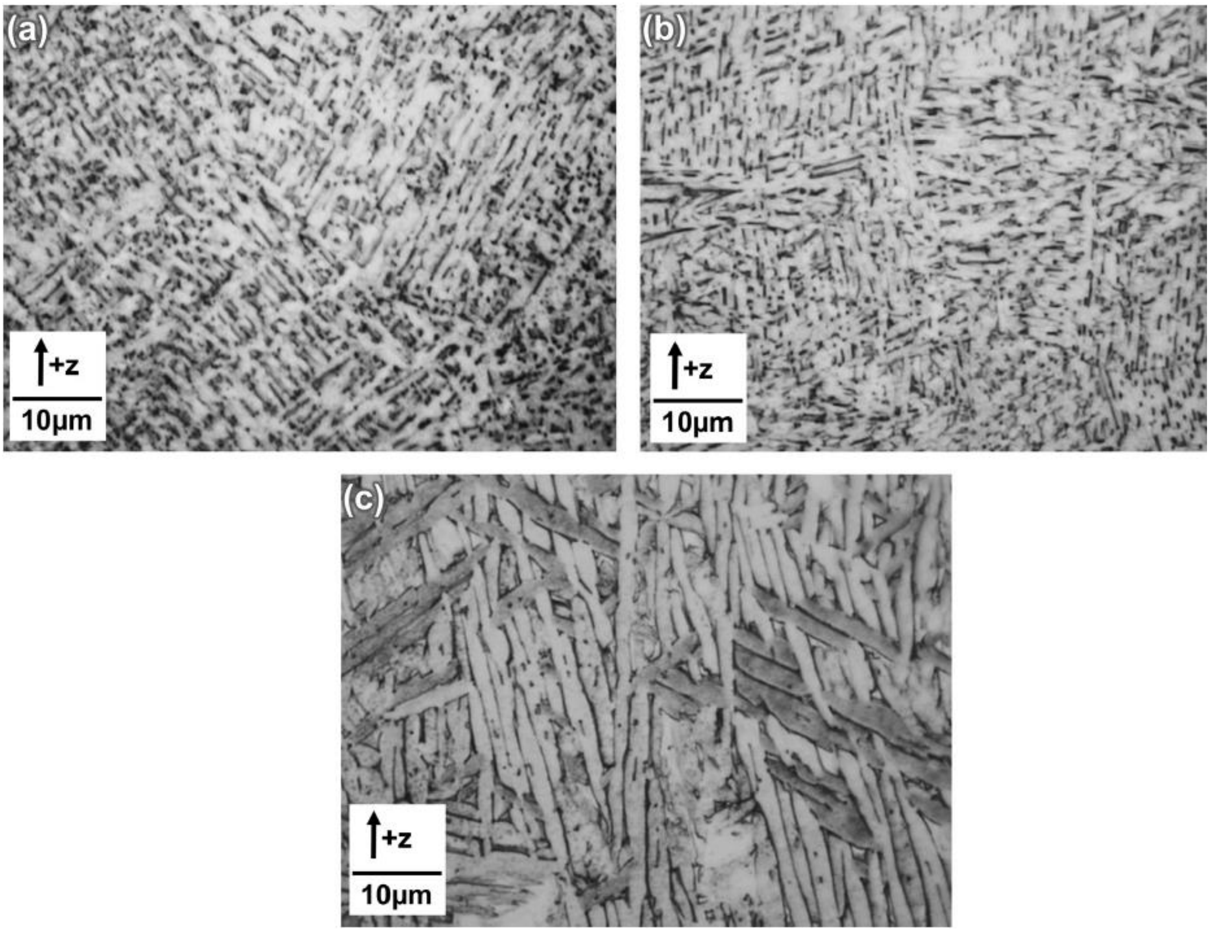


*Figure 69 optical microscope indicating differential microstructure texture for (a) as-build (b) heat stress relieved and (c) HiPed condition [68]*

## 3.0 EXPERIMENTAL METHODOLOGY

This section describes the experimental methods carried out to characterise Ti6Al4V powder manufactured using Plasma Atomised (PA) powder and Electrode induction melting GA (EIGA). Figure 70 is the experimental methodology of this project.

*Figure 70 Experimental methodology for this project*

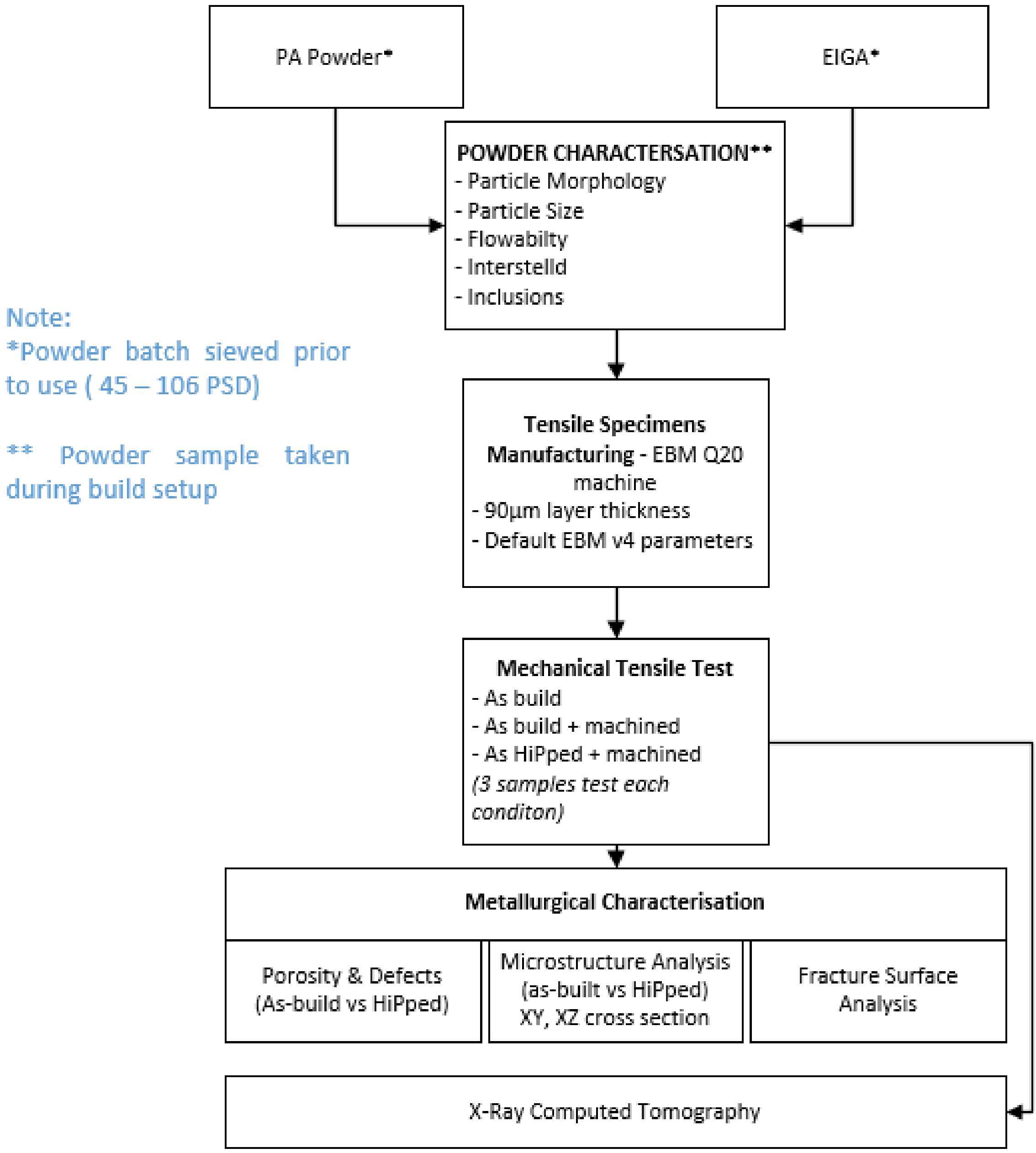

### 3.1.1 Powder Characterisation Methodology

Table 16 is powder characterisation analysis including powder testing and relevant standard.

*Table 16 Powder characterisation methods, testing and relevant standard for PA and EIGA powder analysis*

| Powder analysis | Powder testing method | Relevant standard |
|---|---|---|
| Particle morphology | Scanning electron microscopy (SEM) | - |
| | Static image analysis (G3) | ISO 13322 |
| Particle size | Laser diffraction | ASTM B822 |
| Traditional flow and packing properties | Tapped and apparent densities, Hall Flow, Hauser Ratio and Carr's Index | ASTM B527<br>ASTM B213 |
| Advanced flow techniques | Stability and variable flow tests | - |
| Oxygen, hydrogen and nitrogen analysis | Inert gas fusion | ASTM E1409 |
| Carbon and sulphur analysis | Combustion infrared detection | - |
| Bulk chemical analysis | Inductively Coupled Plasma spectroscopy | ASTM E2371 |
| Particle Inclusion | X-ray Computerised Topography | - |

### 3.1.2 Powder sampling

Ti-6Al-4V powders were received in 2.5 kg containers. To obtain representative powder samples for testing the powder was blended and sampled in accordance with ASTM B215-10. The powder was decanted into a secondary container before blending for 1 minute at 15 rpm. After completion of the blending cycle, the powder was repeatedly passed through a sample splitter to sample down to volumes of powder suitable for testing. In accordance with ASTM standards, three representative sub-batches of 300g (e.g., GA-1, GA-2, and GA-3) of each powder were created to allow the use of fresh powder for each test. Once ready for testing, the powder samples were conditioned for > 48 hours in a desiccator with an environmental temperature of 22 °C (±3 C) and humidity of 34% (±4%).

### 3.1.3 Particle size distribution (PSD)

To measure PSD, laser diffraction spectroscopy was used. This directly relates the intensity of light scattered by a particle to its size, based upon the Fraunhofer diffraction regime [92]. Laser diffraction analysis performs best for spherical particles [93], and powders specified for use in AM typically exhibit high sphericity.

A Malvern Mastersizer M3000 shown in Figure 71 was used, with operating parameters as described in Table 17 Test parameters used for laser diffraction measurements. Tests were performed according to ASTM B822 [94].The equipment uses scattered laser light to infer the volumetric particle size distribution of a powder sample dispersion. The angle at which laser light is diffracted, reflected and refracted by a particle is proportional to its particle size. A series of detectors placed in an array around the sample measured the light intensity at different scattering angles.

*Figure 71 Malvern Mastersizer 3000 particle size analyser*

Table 18 list the test parameters carried out using the laser diffraction measurement. These values were automatically calculated from the measured distribution, using the integrated Mastersizer software. This software fits model data, based on the test parameters, to the recorded data. The residual between the model and measured data indicates fit, with a good fit indicated by a residual of below 1% [95]. For this study, all residuals were below 0.60%.

*Table 17 Test parameters used for laser diffraction measurements*

| | Dispersant | Particle Absorption Index | Particle Refractive Index | Dispersant Refractive Index | Scattering Model |
|---|---|---|---|---|---|
| Ti64 | Water | 0.100 | 2.150 | 1.330 | Mie |

*Table 18 – Parameters used to describe particle size distribution [96]*

| **Parameter** | **Definition** |
|---|---|
| **D10** | Size below which 10% of distribution lies |
| **D50** | Size below which 50% of distribution lies |
| **D90** | Size below which 90% of distribution lies |

### 3.1.4 Particle imaging

Optical tests were carried out using a Keyence digital optical microscope and a scanning electron microscope (SEM) Hitachi TM3000. Cross sections of powder samples were prepared by mounting loose powder in Bakelite before polishing through to ½ the average particle diameter to assess particle porosity. Additionally, the loose powder was mounted on conductive sticky tape to allow assessment of the morphology, surface finish, particle agglomeration particle deformation and the presence of satellites.

### 3.1.5 Flow behaviour

Flow behaviour was investigated using a Freeman FT4 Powder Rheometer. A Stability & Variable Flow test was performed on each sample. In this test, the flow tester blade is moved vertically through a sample of powder, performing a clockwise motion on the downward stroke, and an anticlockwise motion on the upwards conditioning stroke. The total energy required for the blade to perform the downward flow pattern can be used to quantify a powder's tendency to flow – greater energy implies a higher resistance to flow.

A sequence of 11 flow tests is performed. The first seven form the stability test and are all performed at a tip-speed of 100 mm/s. If the powder shows no significant change in flowability energy, it is classified as stable – i.e., that the flow induced in each test does not fundamentally alter the powder flow properties. The final four tests form the Variable Flow test, with tip speed decreasing with each subsequent test number.

Flow tests were used to derive the parameters listed in Table 19, which were used for statistical comparison. The mathematical definition of these parameters is shown in Figure 72, against a typical plot of results generated using the integrated Freeman FT4 software

In all tests, the vessel diameter used was 25mm.

*Table 19 – Parameters used to describe flow behaviour, derived from Freeman FT4 rheometer measurements [97]*

| **Parameter** | **Definition** |
|---|---|
| Basic Flowability Energy (BFE) / mJ | Energy required for a downward powder flow; taken at the end of stability test. |
| Stability Index (SI) | The ratio of BFE at start and end of stability test sequence; SI ≈ 1 indicates powder is not altered by being made to flow. |
| Flow Rate Index (FRI) | The ratio of BFE at start and end of variable flow test sequence; FRI ≈ 1 indicates powder insensitive to flow rate. |
| Stability Energy (SE) / $mJ.g^{-1}$ | Flow measurement– performed in an upwards flow pattern. Work done normalised against mass. |
| Conditioned Bulk Density (CBD) / $g.cm^{-3}$ | Split mass divided by split volume after an initial conditioning cycle of powder. |

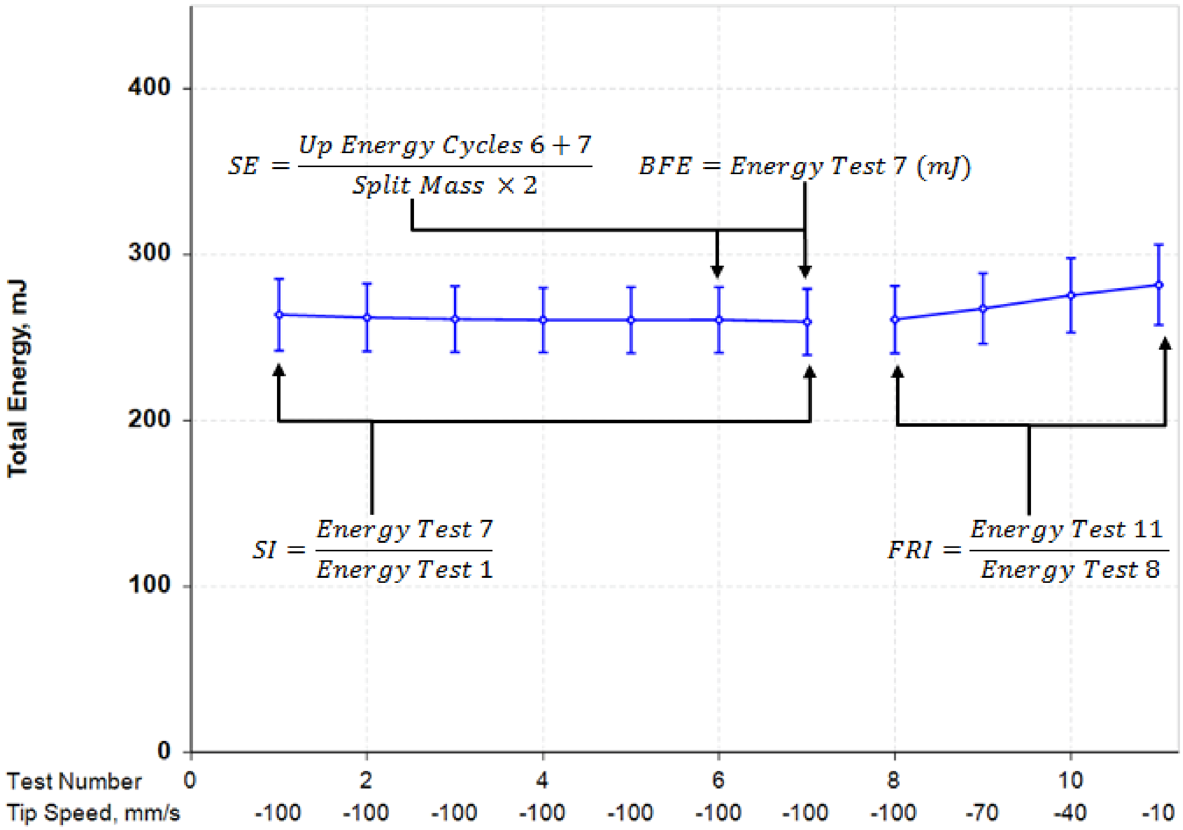


*Figure 72 - Plot of a typical Stability and Variable Flow test. Derivations of key parameters are labelled.*

### 3.1.6 Flowability and packing

The flow rate of the powder was determined using the Hall Flow technique ASTM B213-11. The time required for a 50 g sample of powder flow through the calibrated orifice of a Hall Flowmeter funnel was measured. The flow rate was reported in seconds, and each sub-batch was tested three times.

1. Apparent density (ASTM B212-12) [98] – measured using the Hall Flowmeter funnel. In this process, the powder is flows into a container of 25 through the Hall Flowmeter, and the mass of is reported as the apparent density ($AD_H$).

2. Tapped density (ASTM B527-06) – utilises tapping apparatus (Autotap density analyser) that taps a graduated glass cylinder (with a calibrated volume of 25 $cm^3$ or 100 $cm^3$ at 20 °C) against a firm base. The tapping stroke is 3 mm, and the number of taps is 3000 at a frequency 260 taps/min. The mass is reported as the tapped density ($TD_H$).

The ratio of tapped density to apparent density can be used to calculate the Hauser Ratio (HR) and Carr's Index (CI%) as shown in Equation 1 and Equation 2, respectively. These indices have been used as a measure of powder flowability. According to the Hauser Ratio and Carr's Index values: typically, HR > 1.25 and CI > 25 suggests a powder with poor flowability whereas HR < 1.25 and CI < 15 indicates good flowability (see Table 5).

*Equation 1 Hauser Ratio (HR) calculation*

$$HR = \frac{\rho_t}{\rho_a}$$

*Equation 2 Carr's Index (CI%) calculation*

$$CI = \left(1 - \frac{\rho_a}{\rho_t}\right) \times 100\%$$

| Flow Characteristic | Hausner Ratio | Carr's Index |
|---|---|---|
| Excellent / very free flow | 1.00 - 1.11 | ≤10 |
| Good / free flow | 1.12 - 1.18 | 11 – 15 |
| Fair | 1.19 - 1.25 | 16 – 20 |
| Passable | 1.26 - 1.34 | 21 – 25 |
| Poor / cohesive | 1.35 - 1.45 | 26 – 31 |
| Very Poor / very cohesive | 1.46 - 1.59 | 32 – 37 |
| Very, very poor / approx. non-flow | >1.60 | >38 |

*Table 20 Flowability indicators and categories of powder flow from USP 29-NF24 (2006).*

### 3.1.7 Powder rheology

The Freeman FT4 rheometer is not currently accredited with a professional standard but is in the process of gaining accreditation from ISO at the time of writing this thesis. The Freeman FT4 measures both dynamic flow properties of a powder sample by forcing a helical flow pattern through a powder bed with a precision blade and shear properties by using a shear cell arrangement to shear a bed of powder under varying operating conditions, used to simulate powder flow in the process. For each test, each sub-batch was tested once.


*Figure 73 The FT4 Powder Rheometer® equipment [97]*

### 3.1.8 Chemical composition

Inert gas fusion using a LECO ONH-836 for measurement of oxygen, nitrogen, and hydrogen content. Samples of approximately 1g were weighed , and added to a capsule. This was dropped into a graphite crucible containing graphite powder. Tests followed the appropriate ASTM E1937 standards [99] [100].

For measurement of bulk elements, Inductively Coupled Plasma Optical Emission Spectroscopy (ICP-OES CS744) was used, following relevant standards [101]. Samples of 0.2g were weighed out. Ti64 samples were dissolved using 5ml hydrochloric acid, while IN718 samples were dissolved using 10ml hydrochloric acid, 5ml nitric acid, and 2ml of hydrofluoric acid. Digestion was performed in a microwave digester at 210ºC. Once digested, samples were transferred to 100ml volumetric flasks and made up to volume using deionised water. A sample was taken and added to an ICP tube and tested using a Thermo-Fisher iCAP 7400 at an RF power of 1200W.

ICP, ONH, and CS results were measured with reference to the specification of alloys. The elements measured, and their specified range, are shown in Table 21.

*Table 21 – Chemical specification of Grade 5 Ti-6Al-4V (Ti64)*

| **Ti64** | **Composition /wt. %** | | | | |
|---|---|---|---|---|---|
| **Al** | 5.50 – 6.75 | Fe | < 0.30 | Ti | Balance |
| **V** | 3.50 – 4.50 | O | < 0.20 | | |

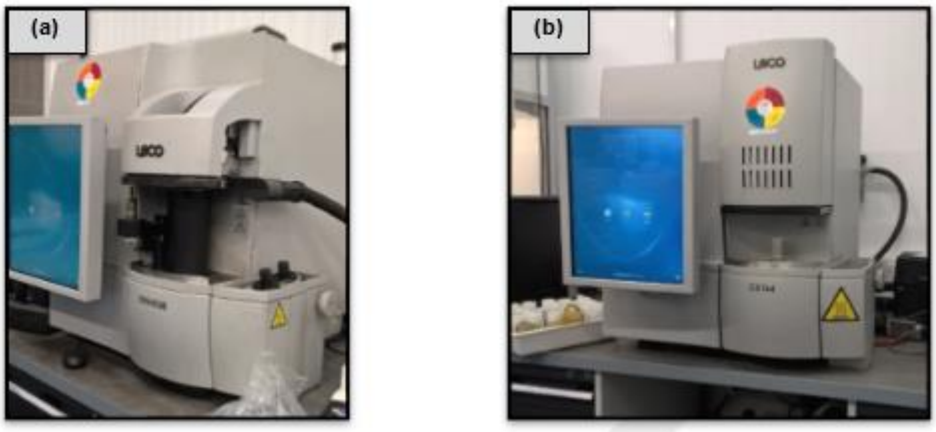


*Figure 74 shows a) LECO OHN 836 (b) LECO CS 744.*

### 3.1.9 Build preparation

Sixteen cylinders (10mm diameter x 60mm height), were oriented vertically in the z-direction using Magic’s version 20 Materliase software for AM build file preparation. Stl files were then sliced (90 µm) using Arcam Build Assembler software as shown in Figure 75.

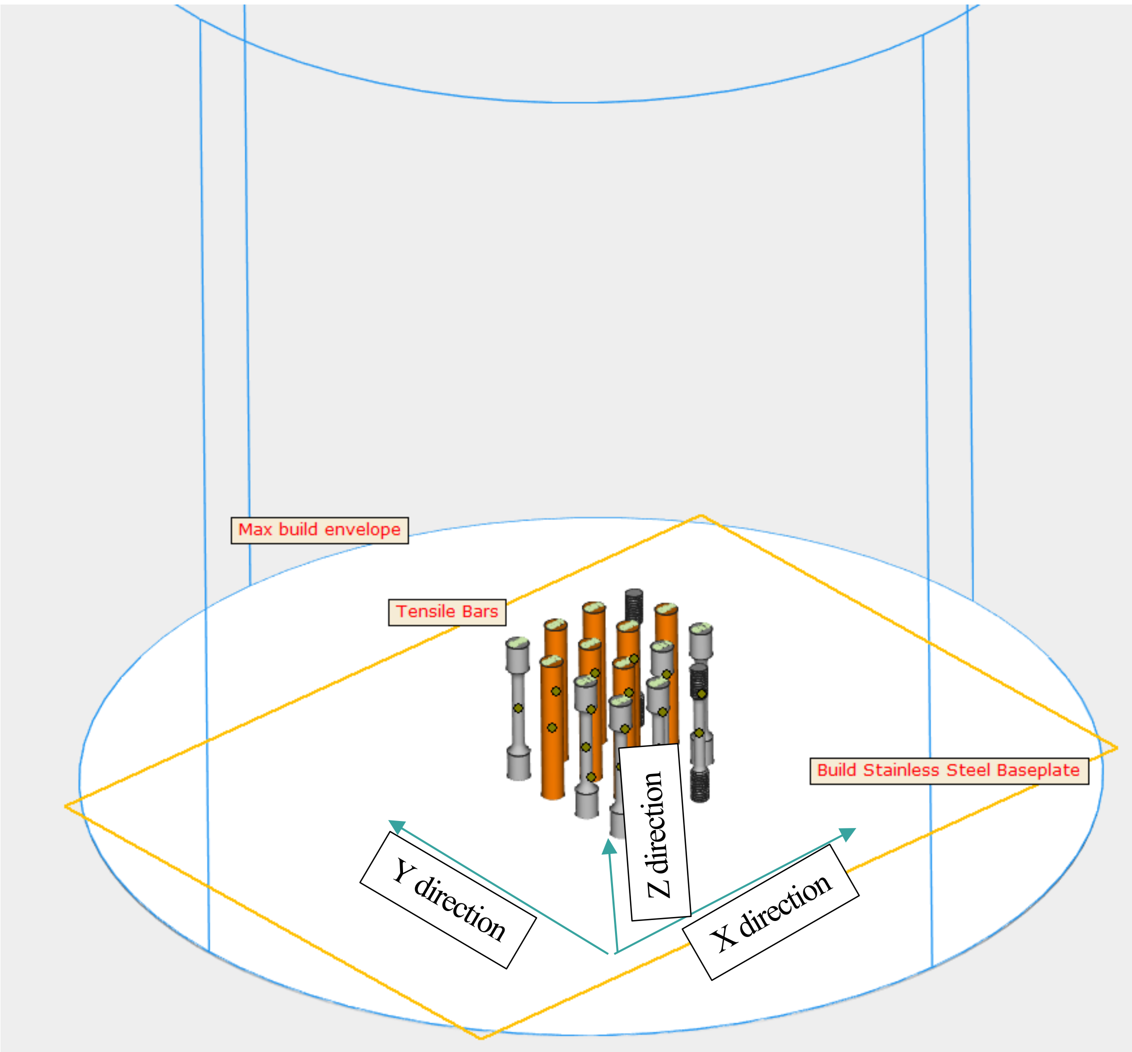


*Figure 75 Vertical build tensile bars in EBM build envelope, build direction shown in X,Y and Z.*

EBM manufacturing of test samples

The EBM specimens were built using Arcam Q20 see Figure 76 at The Manufacturing Technology Centre Ltd, Coventry, United Kingdom.


*Figure 76 EBM Q20 machine used to manufacture test specimens at the MTC*

The parts were built using the standard Q20 parameters set for Ti6Al4V supplied by Arcam, using a 90 µm layer thickness. Below parameters can be seen in Table 22 Indicates Q20 build parameter used

*Table 22 Indicates Q20 build parameter used*

| | |
|---|---|
| **Layer thickness** | 90 µm |
| **EBM Software Version** | V4.2 |
| **Theme**<br>**(Arcam default theme at the MTC)** | Q20 Preheat theme v4.2<br>Q20 Melt theme v4.2 |
| **In-Monitoring System** | LayerQam |
| **Cathode** | Single crystalline, (~45hrs burn time) |
| **Powder production method used** | Plasma Atomised Process (AP&C) & EIGA (TLS) |

Cathode used:

Below is the cathode (lanthanum hexaboride (LaB 6) used to emit electrons and selectively melt parts. Cathode had done 45 hrs burn time when builds in this study were carried as shown in Figure 77.

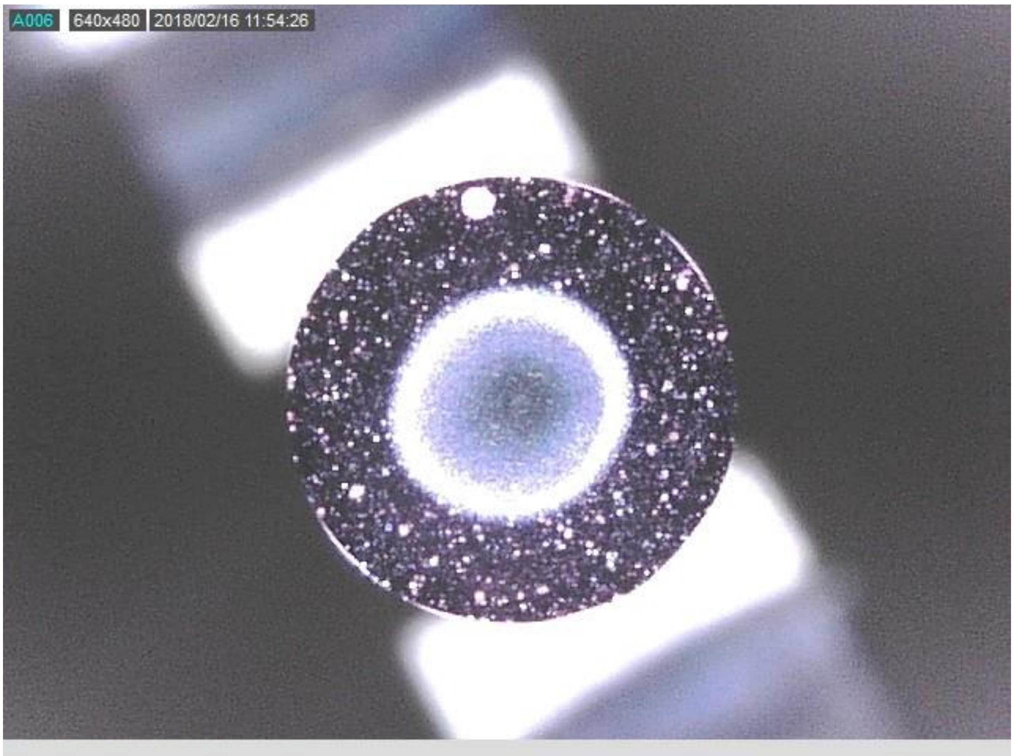


*Figure 77 Cathode (lanthanum hexaboride (LaB 6)) used in EBM builds*

### 3.1.10 Metallographic Specimen Preparation

Mechanical tensile testing was carried in accordance to ASTM E8/E8M [91], for titanium-based alloys the speed of testing should be 0.003 to 0.007 mm/min through yield. As built specimens and non-machined gauge diameter were threaded at the ends to allow clamping as shown in Figure 78. [102]

*Figure 78 Tensile testing Illustration example of (a) sample being tensile tested. (b) Stress-Strain diagram used to calculate mechanical strenth,strain, elongation of material. [102]*

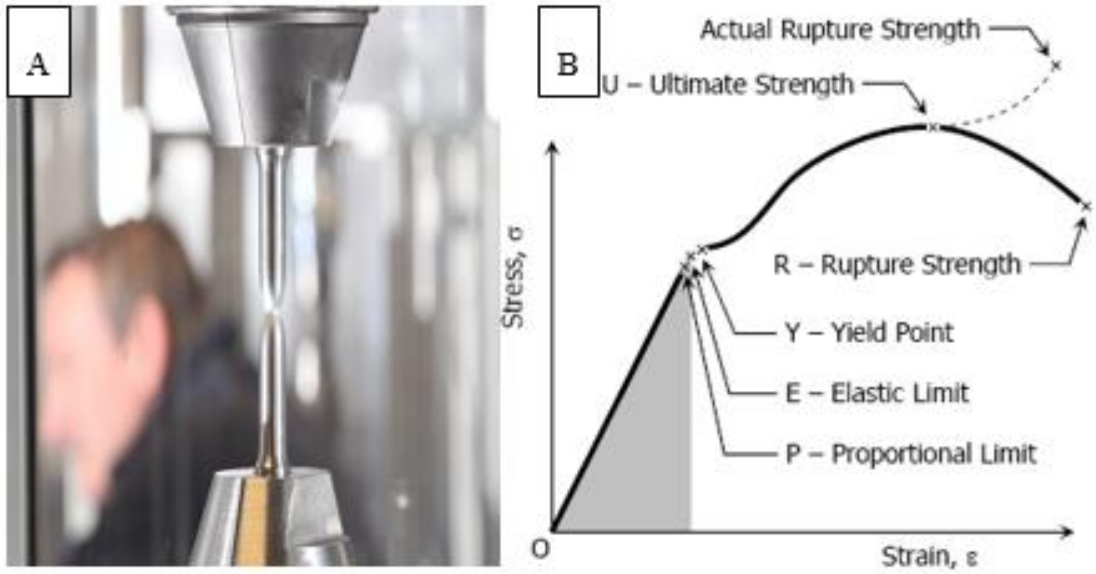


Test specimens were slowly extended by pulling until material fractures. normal stress σ and the strain ε can was obtained. Maximum ordinate in the stress-strain diagram is the ultimate strength or tensile strength. For the standard blank dog bone, specimens were thread machined at the end for the grips. 18 specimens in total were tested per each condition as shown below on Table 23.

*Table 23Tensile test conditions and number of samples carried out for this study.*

| **Tensile test condition** | **PA Powder material** | **EIGA Powder Material** |
|---|---|---|
| As-build specimens: | 3 off | 3 off |
| As-build+ machined | 3 off | 3 off |
| HiPed + machined | 3 off | 3 off |

Metallographic Specimen Preparation

Cut-up's or cross-sectioned specimens for microscopy were prepared in accordance to ASTM E407-07 [103] by cutting using a Secotom precision cutter. Samples were mounted in resin, and polished through a sequence of 400, 1200, 2400, and 4000 grit papers, before polishing for 5 minutes on a MasterMet polishing cloth with a silica polishing suspension. Where metallographic contrast was required, etching was performed with Kroll's reagent.

Scanning Electron Microscopy (SEM)

SEM Deben TM3000 equipment was used to characterise powder particles and cut-up specimens. Images were then taken as different magnifications to check for defects, pores and microstructure analysis. EDX was also used to check chemical elements.

Micro-Hardness measurement

Hardness measurement was all carried out using a Buehler MicroMet 6030 equipment in accordance to ASTM E10-17 [104]. A 500gf load for 15 seconds was used during the automatic measurement process.

### 3.1.11 Non- Destructive Testing

The X-ray Computed Tomography Nikon XT Higher resolution 225 system was used to inspect the tensile parts pre-HiPing. Currently at the time of writing this report, there were no standard for analysing and inspecting AM specimens. At the core of this equipment is a 180 kV / 1200 W micro-focus X-ray source, offering sufficient power to penetrate dense specimens, such as turbine blades and cast engine parts. key parameters used for the XCT 225 tensile part see Table 24 X-CT Parameters used to characterise tensile bar with explanation of parameters used

*Table 24 X-CT Parameters used to characterise tensile bar.*

| XCT Parameters | | Explanation |
|---|---|---|
| 180 kV | Voltage | Voltage determines significantly the energy of the x-rays produced |
| 210 µm | Resolution | Spatial resolution relates to the ability to distinguish between items that are close together |
| 210 µA* | Current | Current will determine the flux of x-ray photons produced |
| 1.5 mm | Copper pre-filtration | Pre-filtration used to suppress lower energy parts of the x-ray spectrum |
| 5.77 | Magnification | Magnification of 5.77 giving a voxel size ("resolution") of 35 µm |
| 1 ms | Exposure | Exposure time influences directly the number of photons captured to make images |
| 5770 | Projections | 2 frames per projection |

### 3.1.12 Post Processing

Heat treatment

Thermal heat treatment, Hot Isostatic Pressing was carried out with Hauck in accordance to ASTM F2924-14 with the following parameters recommended:

– 920° C, – 100 MPa, – 120 minutes [33]

Surface finish

Surface finishing measurements were performed at MTC using optical measurements at gauge diameters tensile test specimen of the build using Alicona IFM. The parameters were chosen to allow for optimal measurement of the surface texture of the coupons as shown in Table 25. Recommended ASME B46.1-2009 [105] standard was followed on as built and machined specimens

Table 25 Optical Measurement – Alicona IFM specification

| | |
|---|---|
| Magnification Objective Lens | IFM G4 20x |
| Working Field of View | 2.85 mm × 2.16 mm |
| Sampling Distance | 978.5417nm x 978.5417nm |
| Vertical Resolution | 269.6471nm |
| Lateral Resolution | 2.9356um |

From each of the measured topographies, a least squares plane was used to remove the form, and the resulting topography was S-L Gaussian filtered [106].

## 4.0 EXPERIMENTAL RESULTS

Following the above characterisation methodology, two powders (PA and EIGA) were fully characterised, and results are discussed in this section:

### 4.1 Powder Characterisation results (EIGA vs. PA)

#### 4.1.1 Virgin PA Ti6Al4V ELI (45um – 106)

This section covers the powder characterisation results obtained for the virgin, extra low interstitial (ELI) Ti 6/4 powder supplied by Arcam, produced by the plasma atomisation (PA) method.

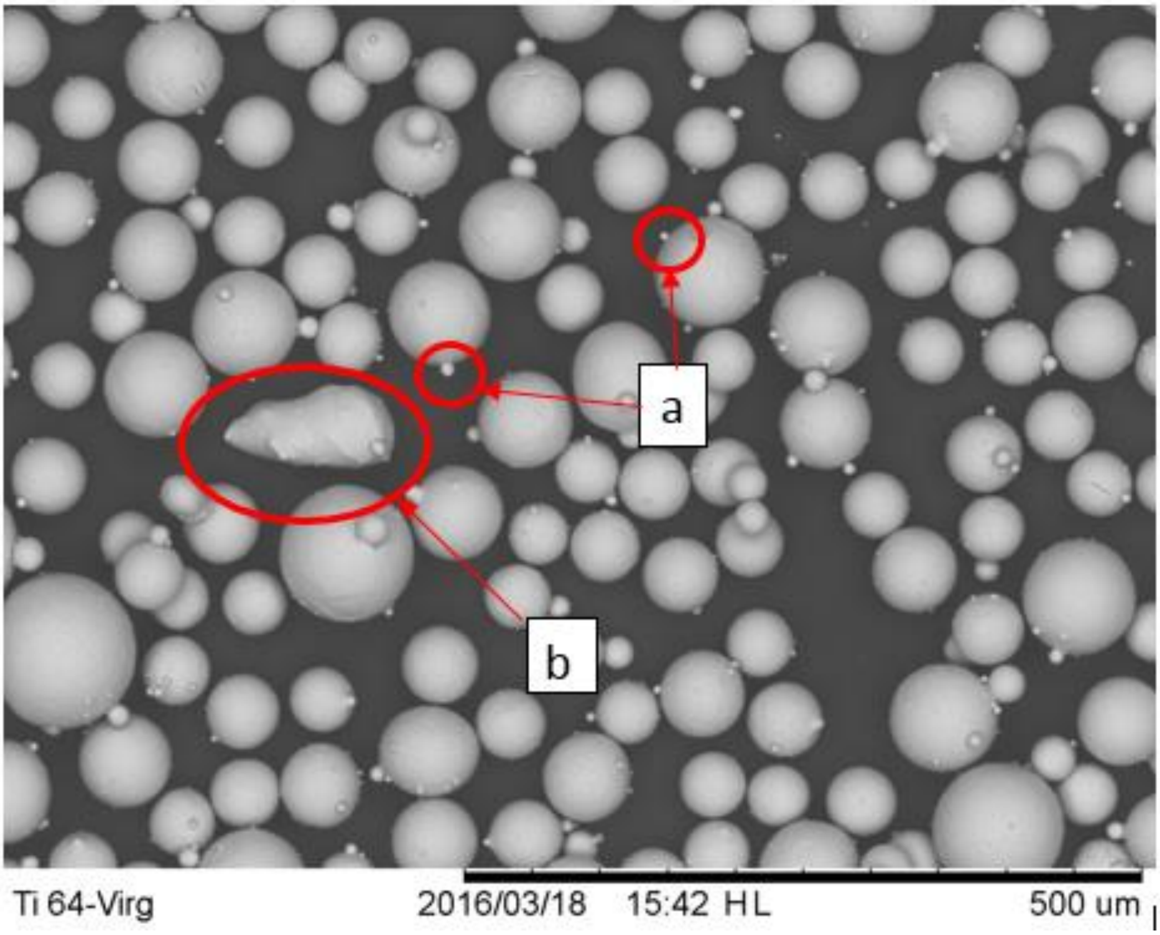


Figure 79 Virgin Ti 6/4 powder at 200x magnification (a) satellite particles, (b) elongated particles, (c) deformed or agglomerated particles.

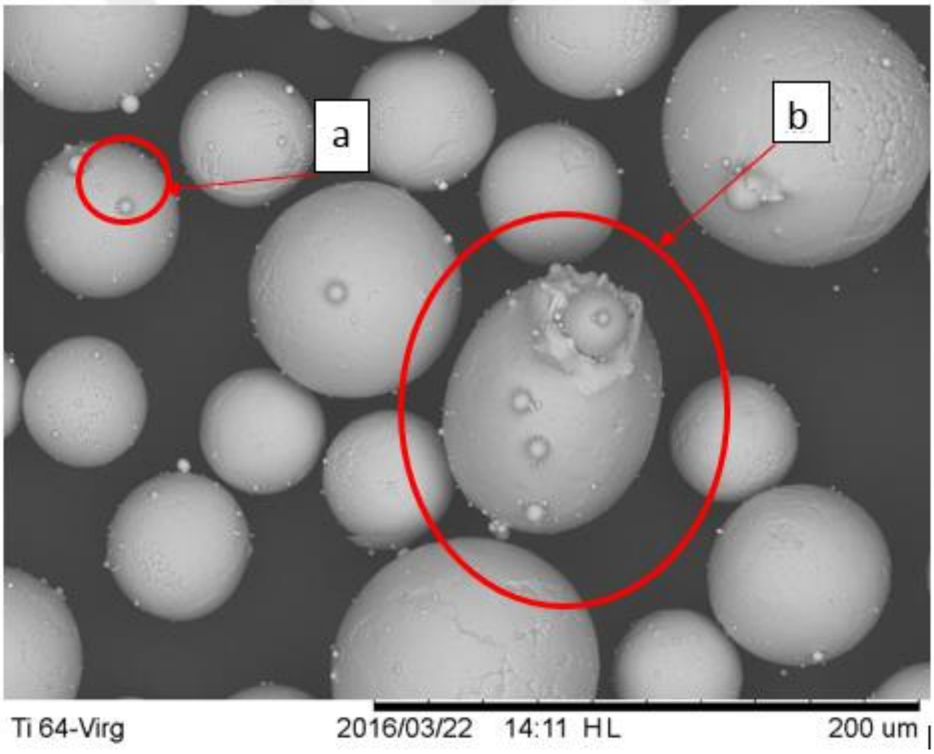


Figure 80 Virgin Ti 6/4 powder at 500x magnification (a) satellite particles, (b) elongated particles, (c) deformed or agglomerated particles.

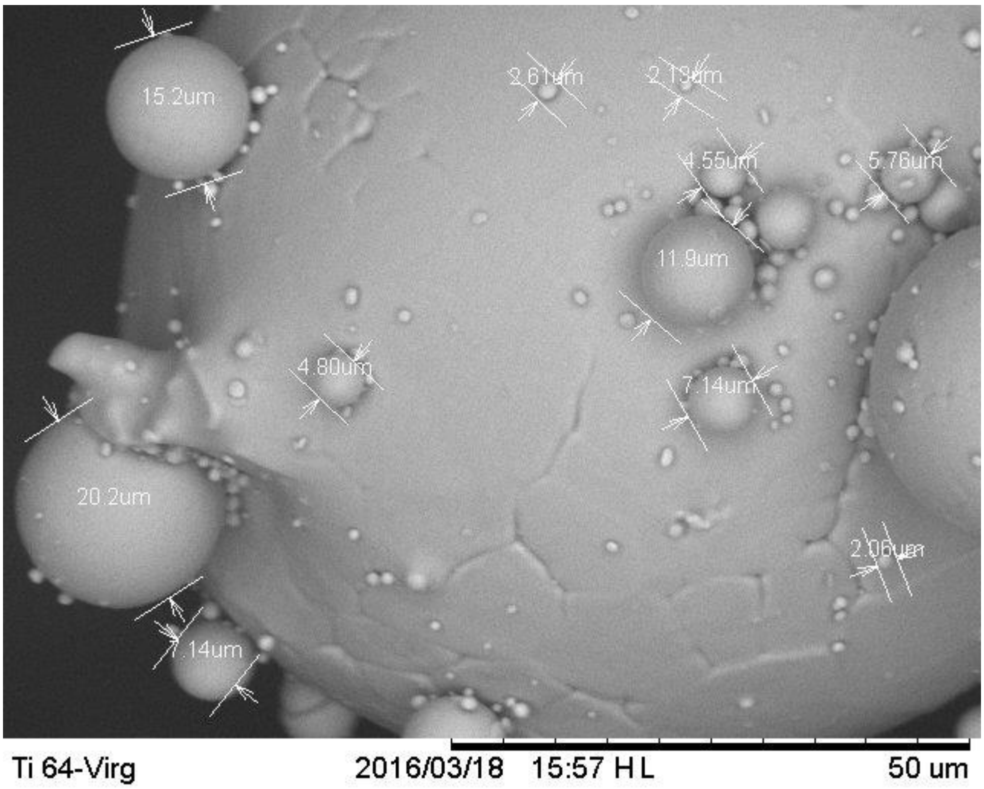

Figure 81 In-depth analysis of the PA powder size of the microsatellites can be appreciated at magnification x1800. Fine particles appear to be in sizes ranging between 1-20 µm.

The graph indicates that less than 5% of the powder in <45µm as indicated in the material specification, and almost 100% of the powder is <150µm.The PSDs can be described by d10, d50 and d90, which correspond to the particle size below which 10%, 50% and 90% of the volume of particles reside

| Sample ID | | Particle size (µm) | | |
|---|---|---|---|---|
| | | D10 | D50 | D90 |
| Ti6/4-ELI | Mean | 52.4 | 75.0 | 108.3 |
| | RSD (±%) | (±1.72) | (±1.68) | (±1.07) |

Traditional Hall flow technique

*Table 26 Powder flow and packing properties of Ti-6Al-4V*

| Sample ID | | Hall Flow (secs/50g) | Apparent Density (g/cm3) | Tapped density (g/cm3) | Hauser Ratio | Carr's Index |
|---|---|---|---|---|---|---|
| Ti6/4 | Mean | 20.35 | 2.55 | 2.86 | 1.09 | 7.89 |
| | RSD (± %) | (±0.33) | (±0.25) | (±0.00) | (±0.00) | (±0.00) |

Table 26 shows the the Hall flow analysis complies with the supplier specification max. 24 secs/50g, the apparent and tap density values showed the compressibility of the powder. According to the HR and CI results, on Figure 82, the material can be categorised as an Excellent/ very free-flowing powder.

| Flow Characteristic | Hausner Ratio | Carr's Index |
|---|---|---|
| Excellent / very free flow | 1.00 - 1.11 | ≤10 |
| Good / free flow | 1.12 - 1.18 | 11 – 15 |
| Fair | 1.19 - 1.25 | 16 – 20 |
| Passable | 1.26 - 1.34 | 21 – 25 |

*Figure 82 Flowability indicators and categories of powder flow from USP 29-NF24 [141]*

Inclusions of high density material indicated in EBM powder and material can be seen in Figure 83 as result of atomisation process.

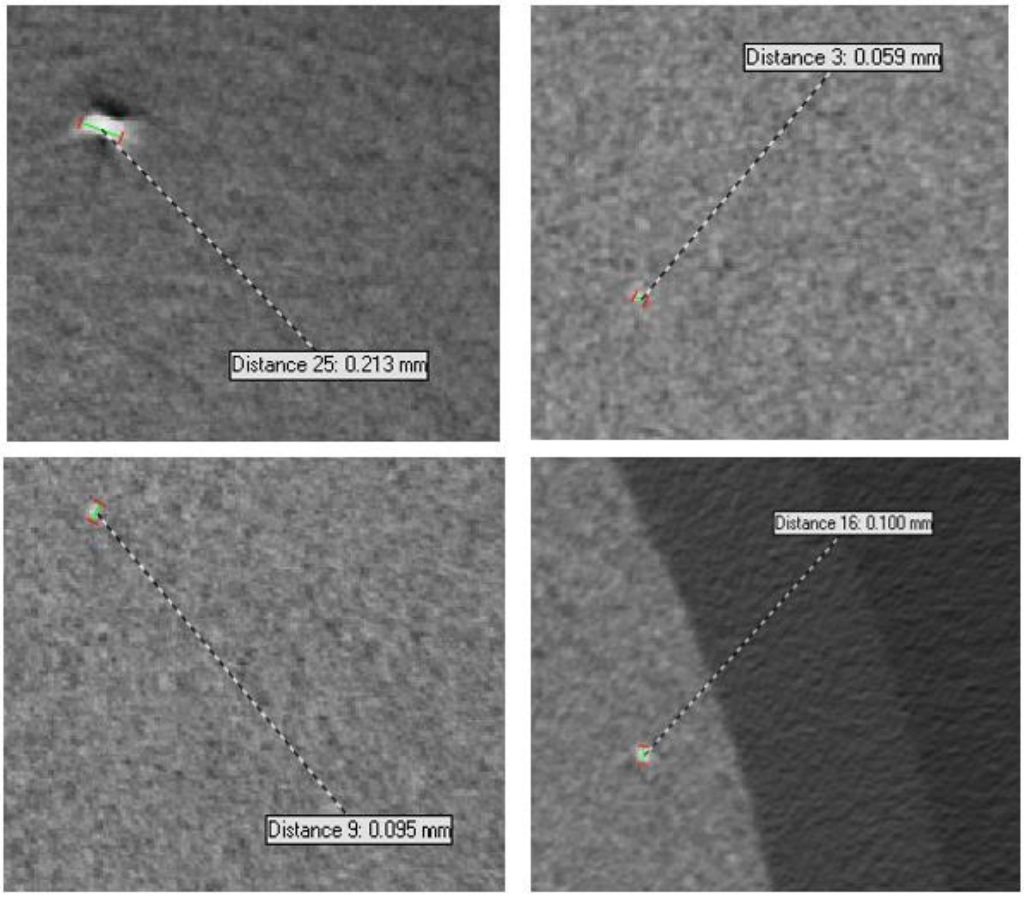


*Figure 83 powder inclusion found in PA powder using X-CT*

### 4.1.2 Comparison of EIGA vs. PA as build powder

*Virgin EIGA Ti64AlV*

Powder Morphology

Study of morphology using SEM and Static Image Analysis microscopy showed higher sphericity in PA powder. Broken particles, open porosity, agglomerations, and a high frequency of satellites were also observed in the EIGA powder. Representative SEM micrographs are shown in Figure 84.

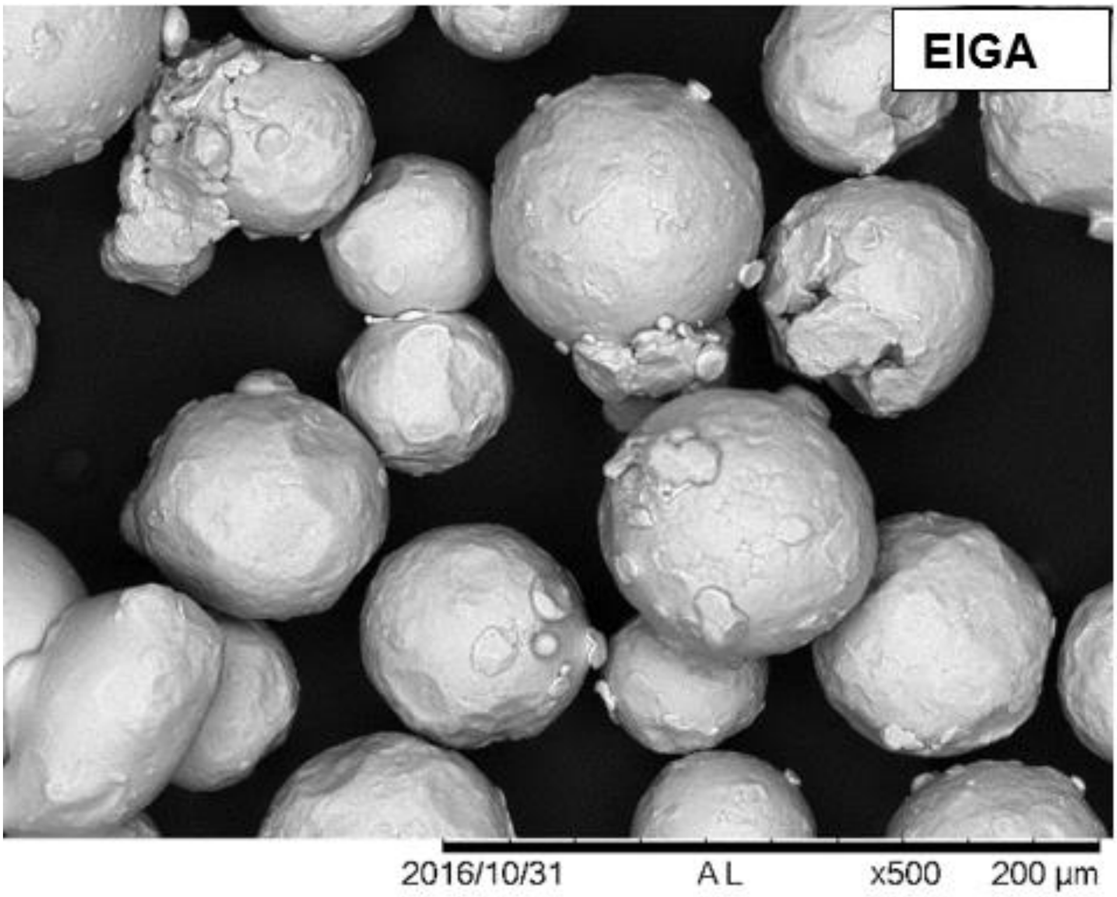


*Figure 84 Powder morphology SEM image analysis for EIGA powder*

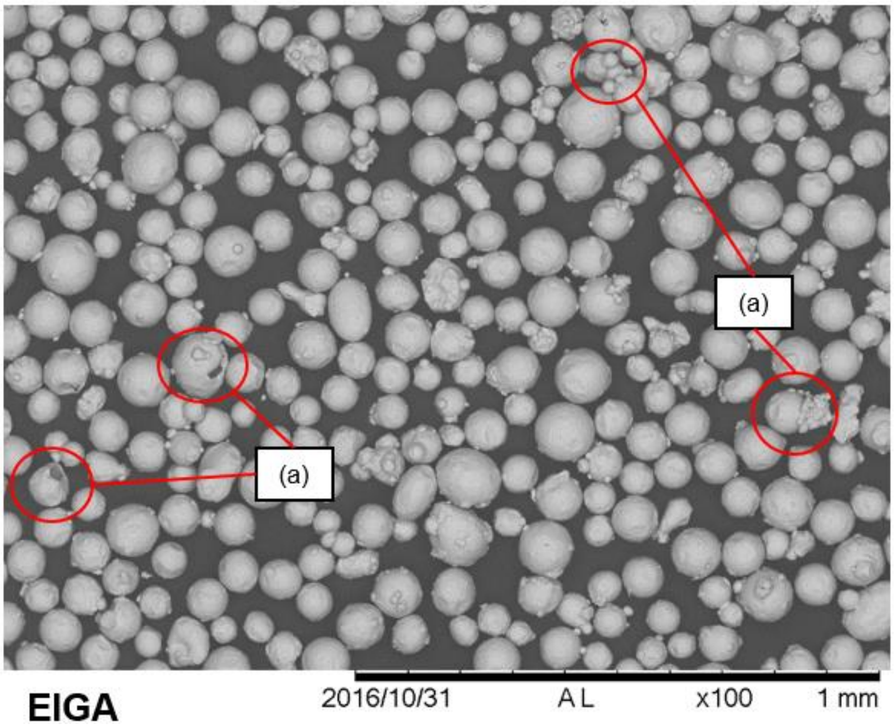


*Figure 85 SEM high magnification X100 of EIGA with indicationa of (a) Open porosity and agglomeration*

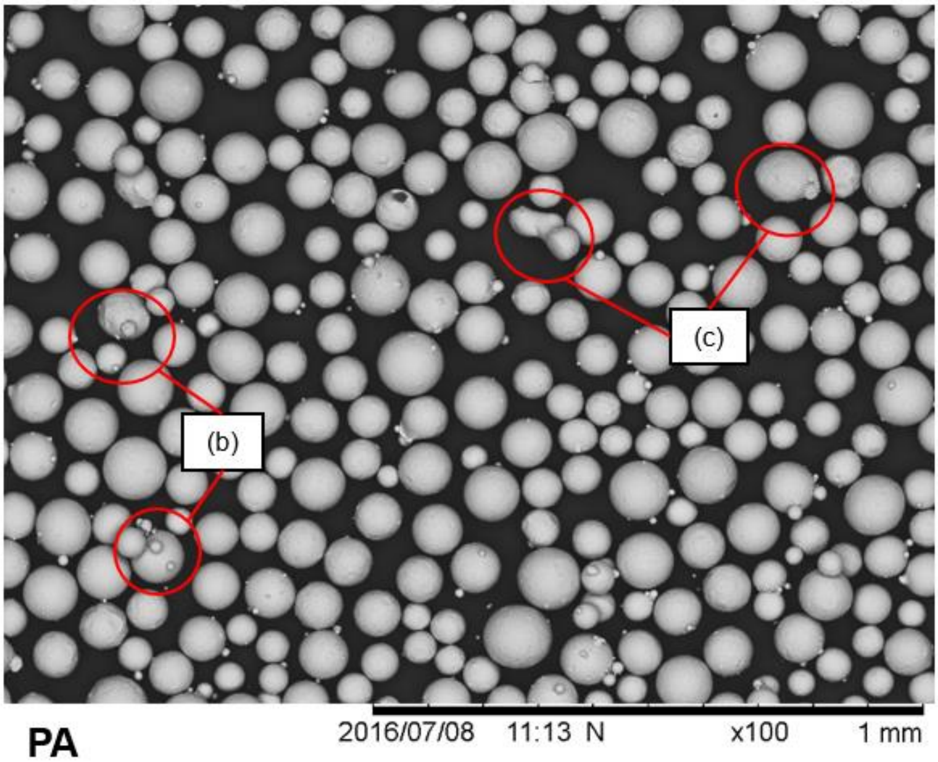


*Figure 86 PA SEM powder morphology with (b) small satellites and (c) elongated particles*

### 4.1.3 PA build powder Ti6Al4V

*SEM Morphology analysis*

The PA powder is also observed to consist of highly spherical smooth particles. Nevertheless, in comparison to the virgin powder, some defects can be observed which appear different to those observed previously. Figure 87 shows there is evidence of semi-sintered powder (a), and there are cases where the surface of the spherical particles appears to contain 'dents' (b) suggesting that something has occurred at the surface of the sphere which may result in changes in surface chemistry (interstitial contamination). There is limited evidence of satellites on the particle surfaces (c). Also, there is also evidence of particles with open porosity hollow particles d shown in Figure 88

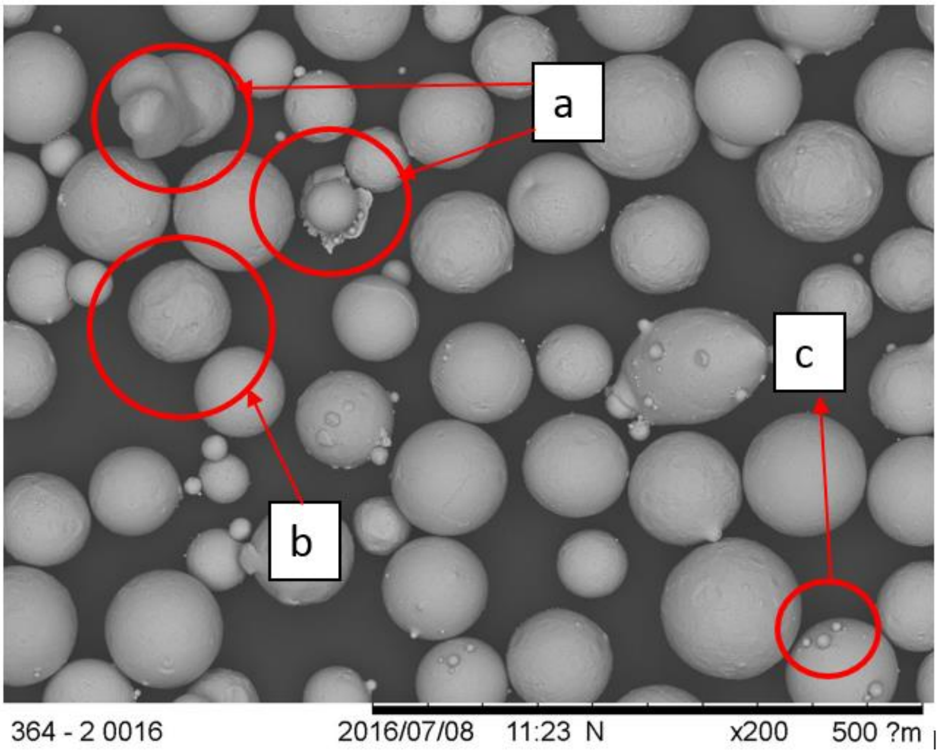


*Figure 87 PA build powder sample at 200x magnification (a) semi-sintered powder, (b) dented particles, (c) fine satellite particles.*

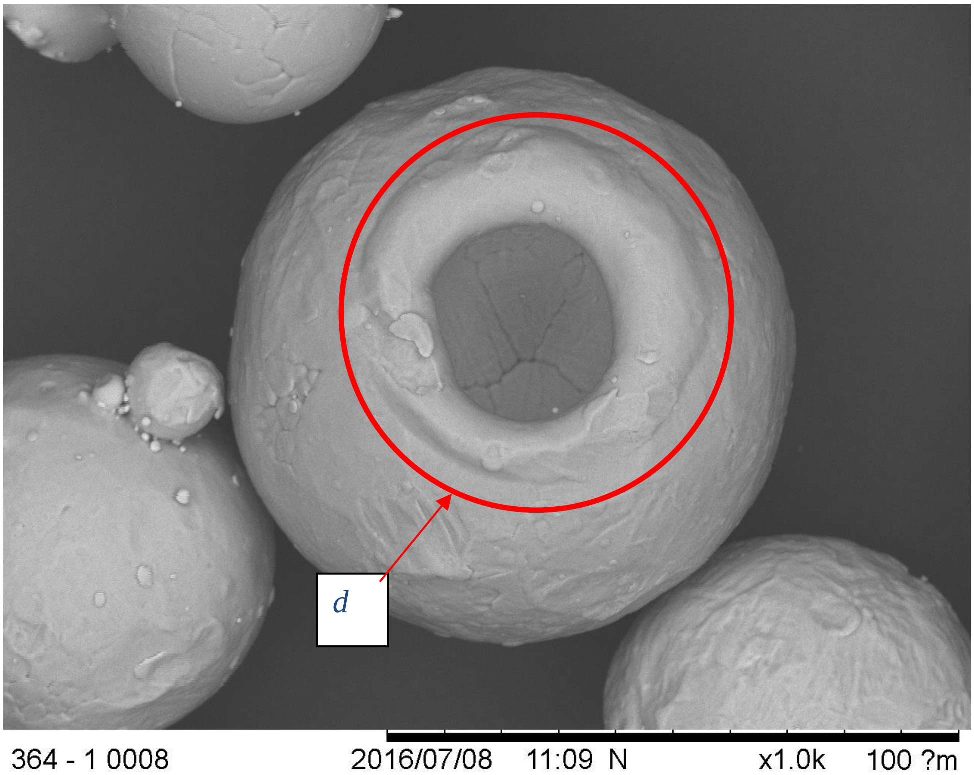


*Figure 88 PA Ti 6/4 powder sample magnification showing signs of open porosity hollow particles (d)*

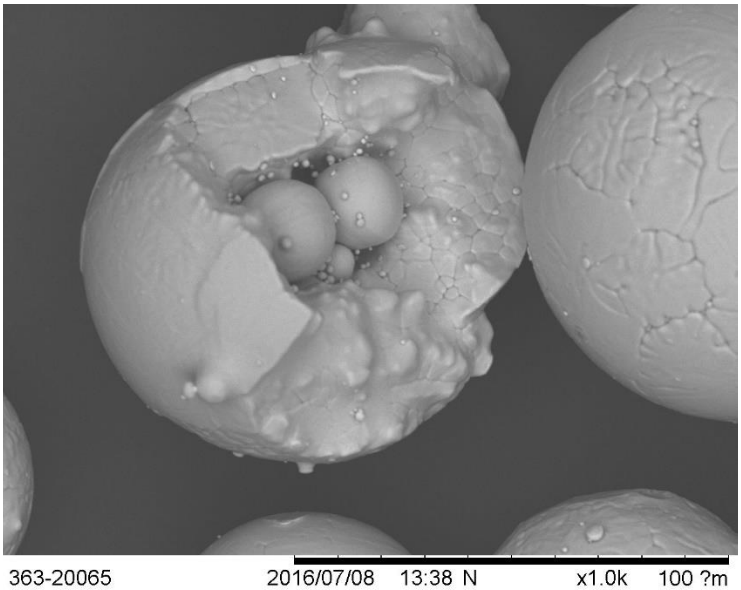


*Figure 89 PA powder sample at 200x magnification example of the deformed particle due to the powder manufacturing process*

### 4.1.4 Particle size Distribution (virgin vs. recycled)

The measured particle size distribution (PSD) for virgin vs recycled is presented in Figure 90. It can be observed that the distributions were symmetrically log-normal and the Gaussian distribution fall in the expected powder size distribution of 45-106 µm for EBM process. The virgin powder has a broader distribution with a slightly more substantial amount of coarse particles (>70 µm).

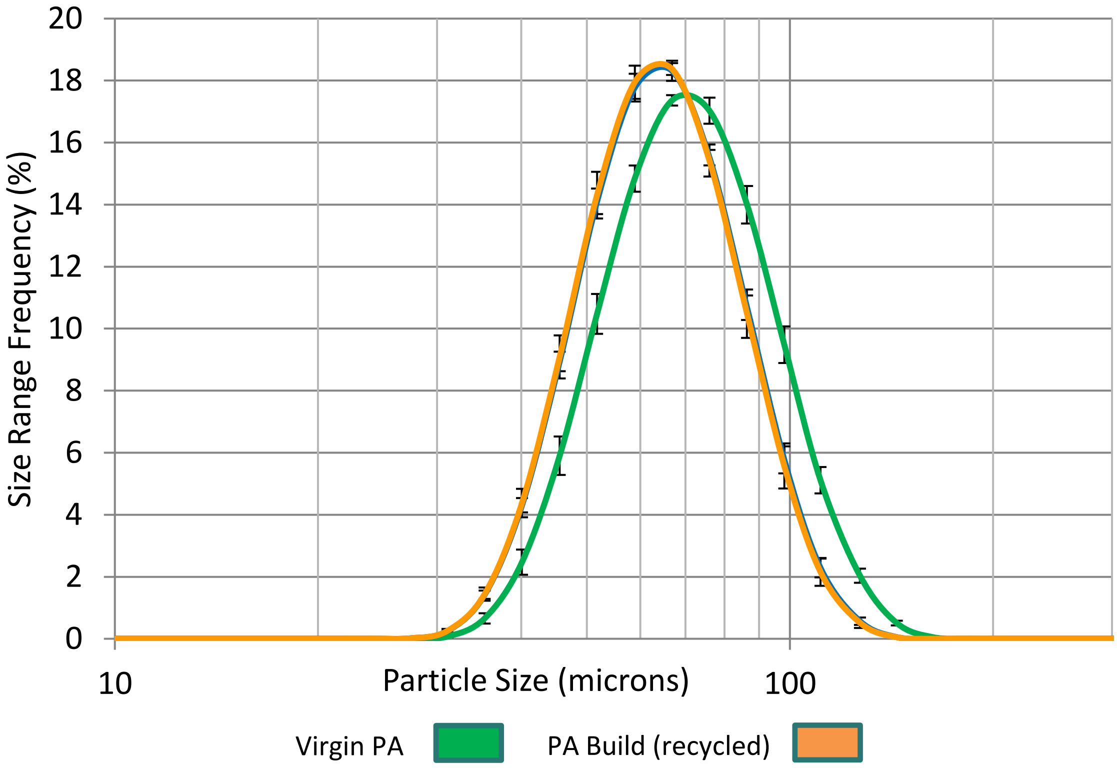


*Figure 90 Particle size distribution PA Ti6/4 powder grade 45 to 150µm virgin powder (green), used PA build powder (Orange)*

## 4.1.5 Powder porosity

Cross-sectional studies showed significantly higher closed porosity in EIGA powder than PA powder as shown in Figure 91. These closed pores suggest entrapment of argon as particles solidify during atomisation process. Similar results were found by Cunningham et al. 2016 [55], and reported argon has as having low solubility in metal and hence difficulties in pore removal [41].

EIGA and PA powder porosity was 0.157 (± 0.072) % and 0.023 (± 0.021) irrespectively. Sames et al., 2016 [24] report that spherical, gas pores similar to ones found in this study are formed during atomisation process and thus can translate into as-built parts. However, it should also be noted that pores can be formed by processing parameters not fully optimised for the material.

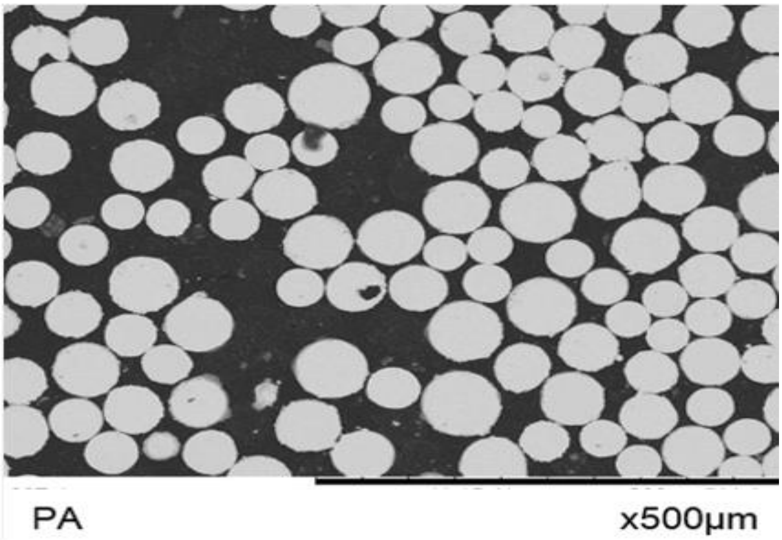


**PA Volume % Porosity**

0.023 ± 0.021

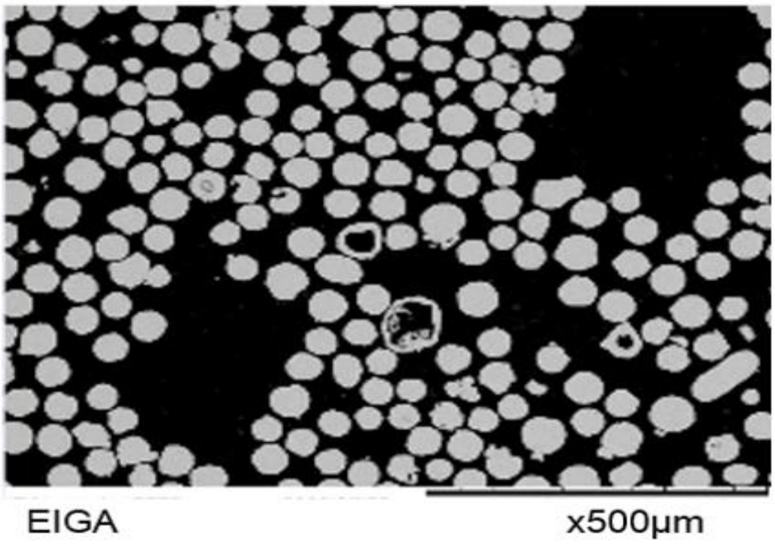


**EIGA Volume % Porosity**

0.157 ± 0.072

*Figure 91 Porosity cross section of EIGA and PA powder indicating high porosity in EIGA powder*

### 4.1.6 Powder particle microstructure

Powder microstructure was also characterised to correlate the phase present using SEM equipment in powder before melting in EBM process. The powder cross-section as shown in Figure 92 a finer microstructure of which has influence in the initial grain formation and inevitably affecting the EBM material texture (microstructure).

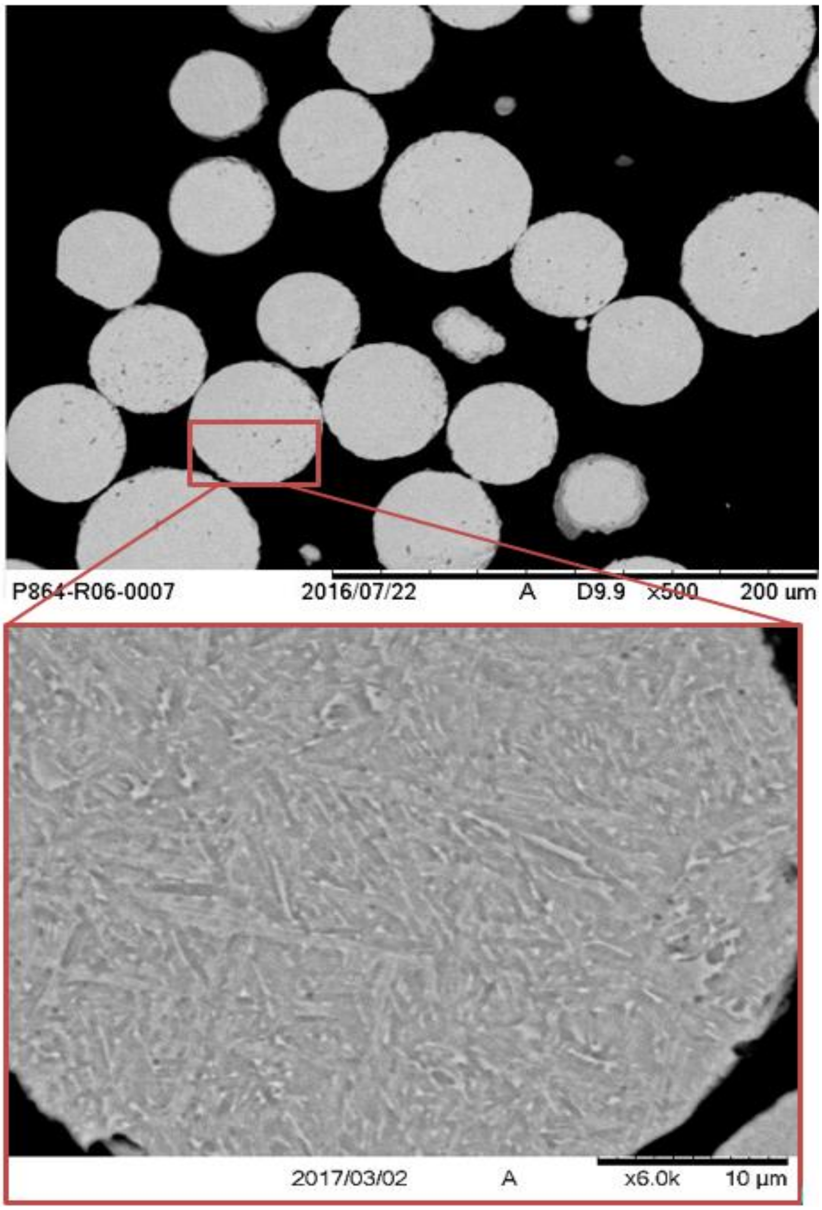


*Figure 92 PA cross-section SEM images with closer magnification on particle microstructure.*

### 4.1.7 Particle size distribution (PSD) of EIGA and PA

The particle size distributions (PSD) of the two powders is shown in Figure 93, with typical size distribution descriptors (D10, D50, and D90) shown below. Both powders exhibit more than 90% of material within the nominal 45-106 µm particle size, with a slightly broader distribution observed in the PA in comparison to EIGA powder. Similar PSD have been found and reported by many authors [71] [24] [44]. Volume porosity of EIGA and PA powder was measured to 0.157 % (± 0.072) and 0.023 % (± 0.021) irrespectively. The data correlates with the other researcher's findings such as Cunningham et al. [71] where they found gas pores formation in gas atomised powder and less or no pores in PREP powder.

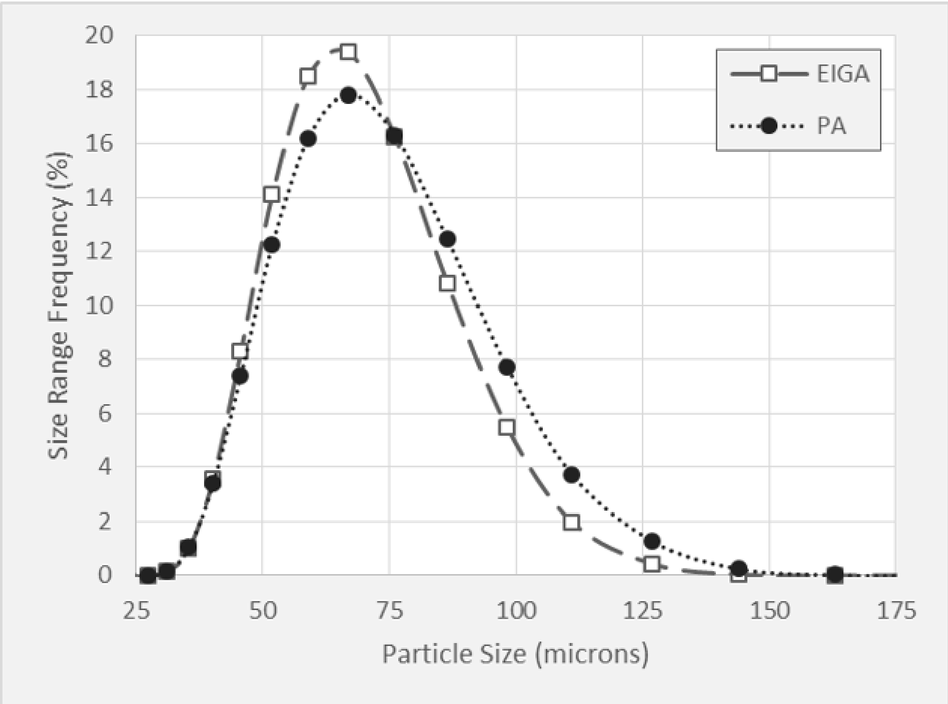


| | Size /micron | | | | |
|---|---|---|---|---|---|
| | D10 | D50 | D90 | D[3,2] | D[4,3] |
| EIGA | 49.5 ± 0.8 | 68.8 ± 0.7 | 95.7 ± 0.7 | 66.8 ± 0.7 | 71.0 ± 0.7 |
| PA | 50.1 ± 0.9 | 71.6 ± 1.2 | 103.3 ± 2.1 | 69.1 ± 1.2 | 74.4 ± 1.2 |

*Figure 93 Powder Particle Size Distribution of as-built EIGA and PA used to manufacture test specimens.*

### 4.1.8 Particle classification

Percentage volume fraction of different particle classes for EIGA and PA are shown in Figure 94. PA Powder shows higher sphericity in comparison to EIGA as seen in SEM, with a lower fraction of irregular particles. A slightly higher coarse fraction in PA can be seen and can be correlated with the particle size analysis. Both powders show low fines fraction of 0.56% and 0.44% for PA and EIGA irrespectively

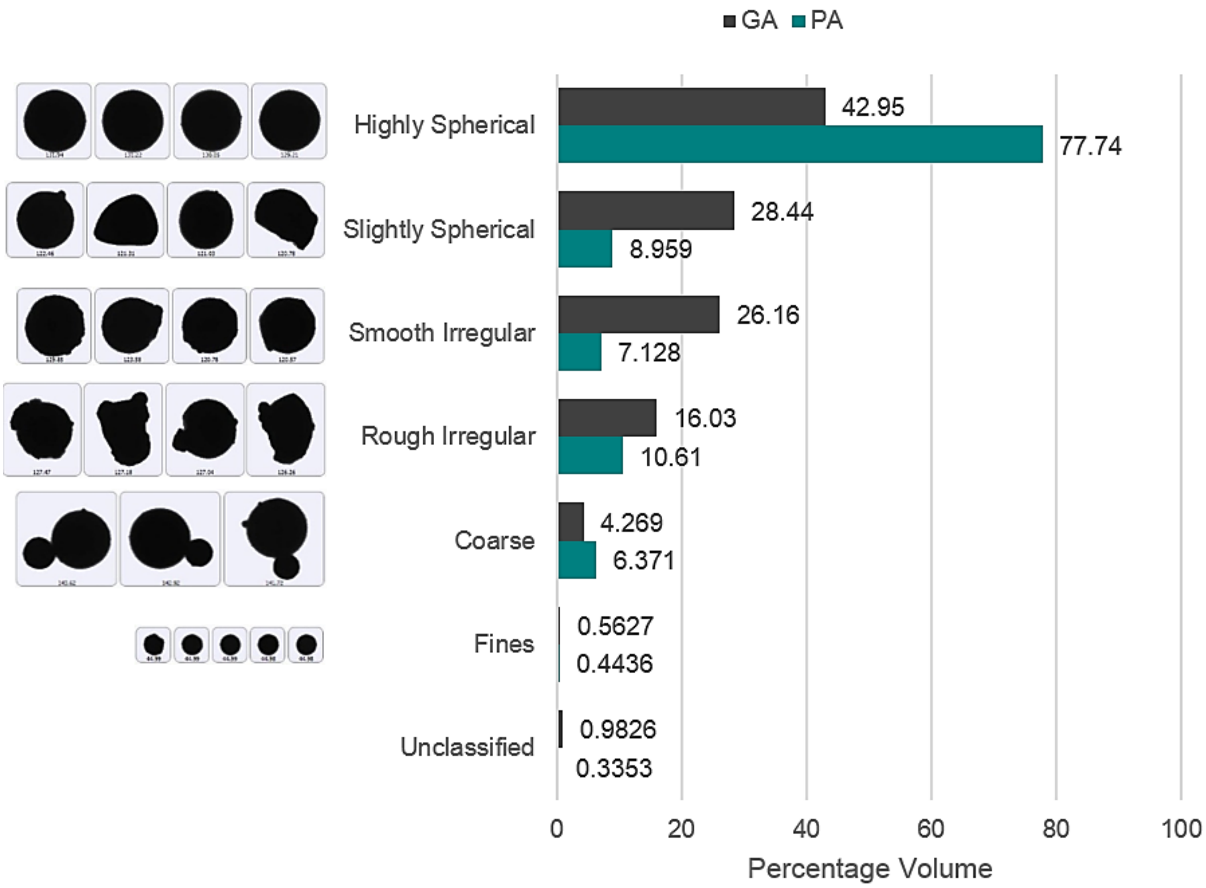


*Figure 94 EIGA vs. PA Powder classification in the sphericity, regularity, course and fine particles.*

### 4.1.9 Chemical composition

Both powders (EIGA and PA) were found to lie within specification for chemistry composition in accordance with ASTM F2924 requirements as shown in Table 27. However, it can be observed that PA powder had higher oxygen of 0.18 wt. % in comparison to EIGA powder with ~0.11 wt. %. This can be due to differences in some recycles for both powders resulting in higher oxygen pick-up for PA powder. According to MTC's powder traceability record, the powder had been recycled well over 38 times in comparison to virgin EIGA, which had only been used once.

*Table 27 Chemical Composition of EIGA and PA powder used*

| | Composition /wt.% | | | | | | | |
|---|---|---|---|---|---|---|---|---|
| | Ti | Al | V | Fe | Y | O | N | H |
| ASTM F2924 | Bal | 5.50 – 6.75 | 3.50 – 4.50 | < 0.300 | < 50 ppm | < 0.200 | < 0.050 | < 150 ppm |
| EIGA | Bal | 6.47 ± 0.01 | 4.08 ± 0.06 | 0.196 ± 0.002 | 5.3 ± 5.6 ppm | 0.112 ± 0.002 | 0.011 ± 0.0003 | 14.1 ± 2.9 ppm |
| PA | Bal | 6.57 ± 0.02 | 4.17 ± 0.04 | 0.206 ± 0.004 | 2.2 ± 0.1 ppm | 0.180 ± 0.001 | 0.016 ± 0.0010 | 21.0 ± 2.9 ppm |

Table 28 is powder density and flow rates for EIGA and PA build. No significant changes seen in apparent and tapped density. However, flow rate indicates slow flowability of powder in EIGA powder compared to PA powder, this can be interlinked to small particles 'satelites' in EIGA virgin powder.

*Table 28 powder apparent and tapped density of Ti6/4 EIGA and PA*

| | Density /g.cm$^{-3}$ | | Flow Rate /secs/50g |
|---|---|---|---|
| | Apparent | Tapped | |
| **Spec** | **-** | **-** | **< 25** |
| EIGA | 2.43 ± 0.01 | 2.86 ± 0.00 | 24.21 ± 0.31 |
| PA | 2.57 ± 0.01 | 2.84 ± 0.02 | 19.62 ± 0.69 |

## 4.2 Metallurgy and Mechanical results

The tensile samples were successfully manufactured using EIGA and PA powder on EBM Q20 machine as shown in Figure 95 below. This section of the report will report the findings on the microstructure and mechanical properties. Porosity and defects from both powders have also been discussed and correlated with the literature review. NDT using X-ray – Computed Tomography and Fracture analysis has also been carried and discussed in this section

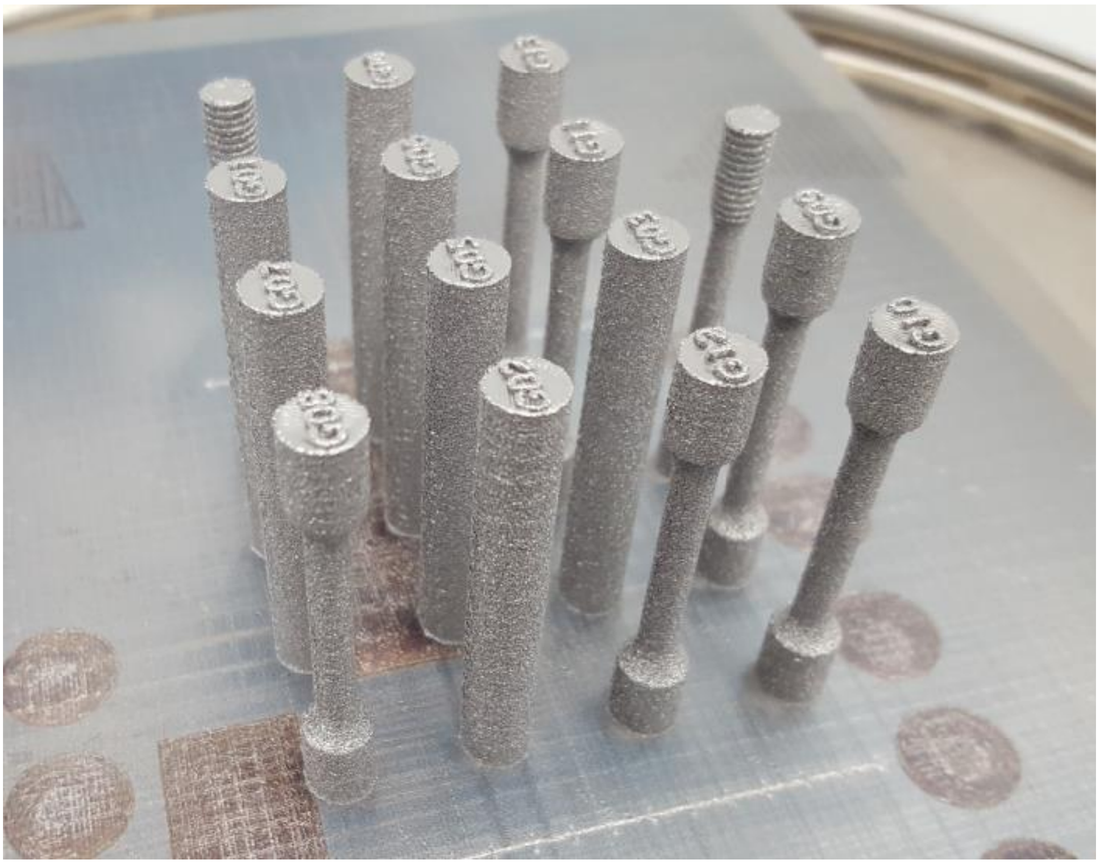

*Figure 95 As-built tensile specimens from EIGA powder. Specimens are shown on stainless steel base plate.*

### 4.2.1 Manufactured specimens

EIGA and PA powder specimens were manufactured successfully. As shown below Figure 96 it can be seen the first few layers usually 1-2 mm can be contaminated with steel base plate if parts are built on the base plate instead of supports if required. The stainless steel can be re-used as long it's clean. Energy-dispersive X-ray spectroscopy clears indicated 'Fe' elements in the TI6Al4V as build specimens.

*Figure 96 Build showing stainless steel base plate required to manufacture EBM parts. First layers indicating steel contamination with EBM TI6/4 manufactured specimens*

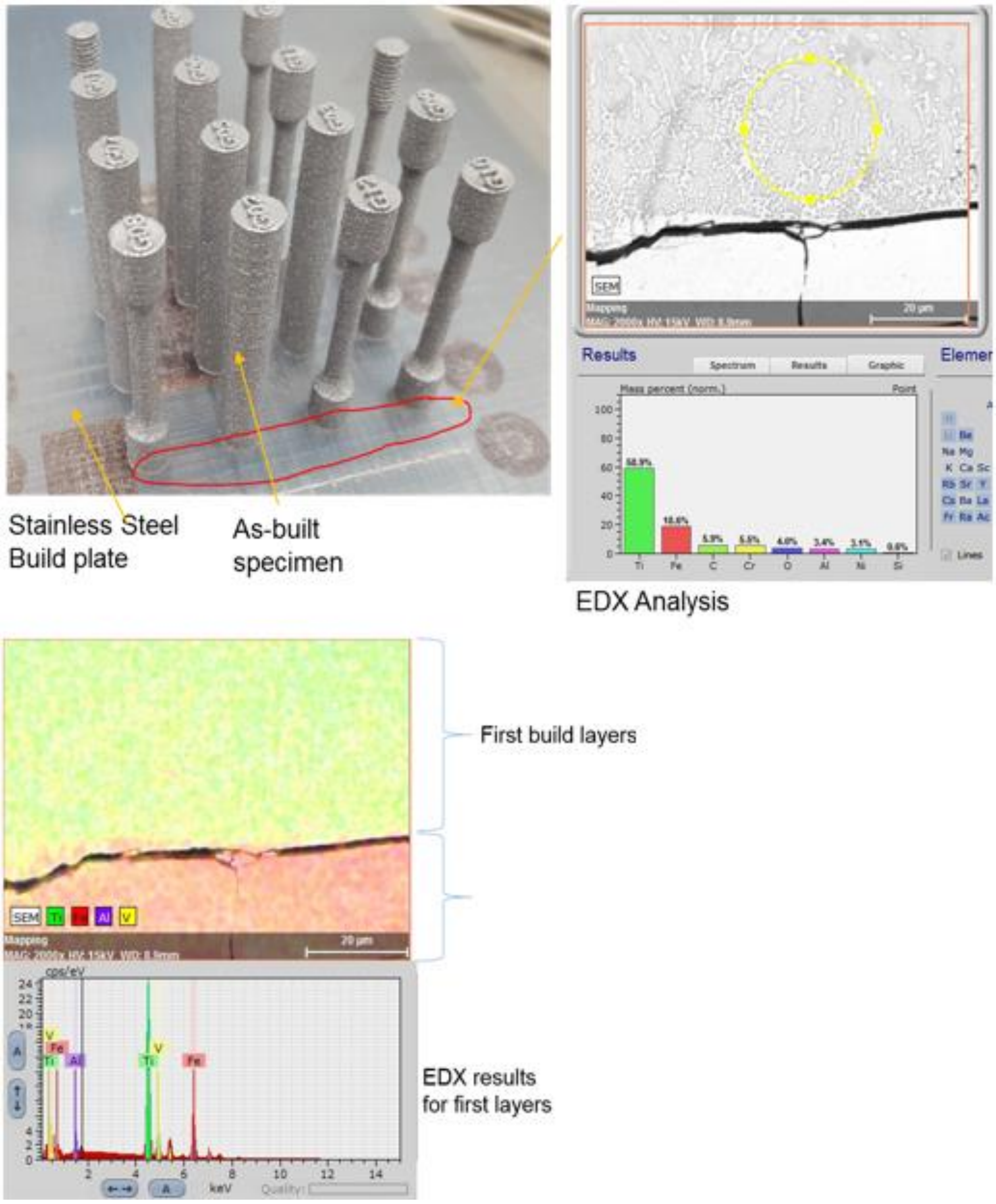

### 4.2.2 As-build defects of EIGA built samples

As-built samples were found to be dominated by a spherical pore or round shaped voids (approx. ~30µm – 100µm). It is most likely to have originated from the entrapped gas (argon) within the gas atomised powder particles. Cross-section samples of powder also showed the same results as reported in the powder characterisation section. The main defects are shown in Figure 97 Specimen A, B and C predominantly gas pores, no lack of fusion on un-melted particles found.

*Figure 97 EBM as-built EIGA samples indicating spherical gas pores (argon). From bottom of build is (a) bottom sample in XZ (b) middle sample XZ (c) top sample, XZ (d) Z- Build direction is also shown (e) XY cros s section with closer zoom-in gas pore.*

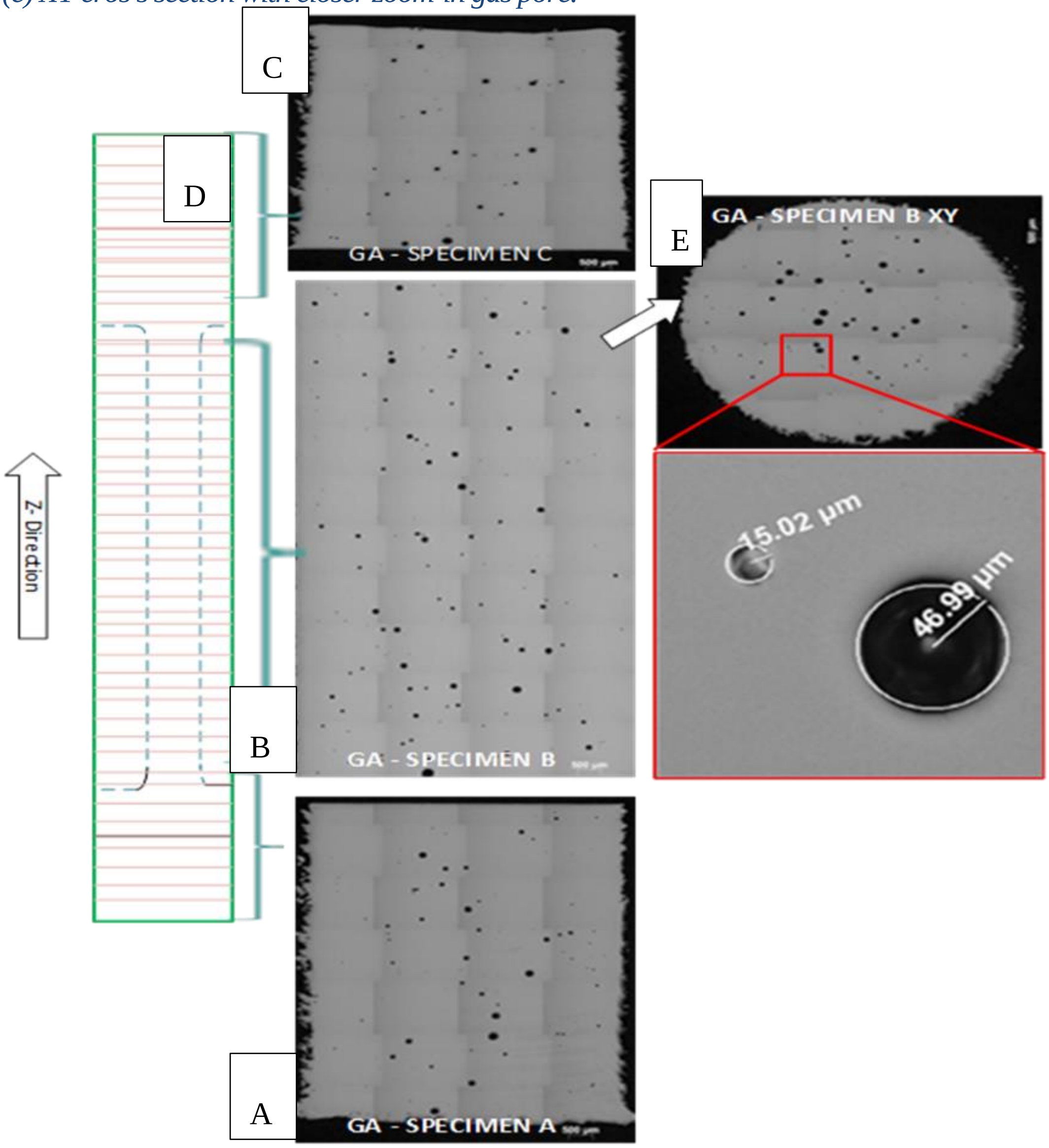

defects in the middle section (i.e., specimen B). The defects seem to be trapped more in the middle of the sample due to process parameters from contour→Hatch strategy. S. Tammas-Williams, 2015 reported this same phenomenon and reported the finding due to the high energy input in hatch parameters different from contours [54].

As for EIGA built samples, it is clear from this study that the argon gas entrapped is inherited in the melted parts. Murr et al. 2009 also found similar findings for build related issues when specimens were manufactured using EIGA [107].

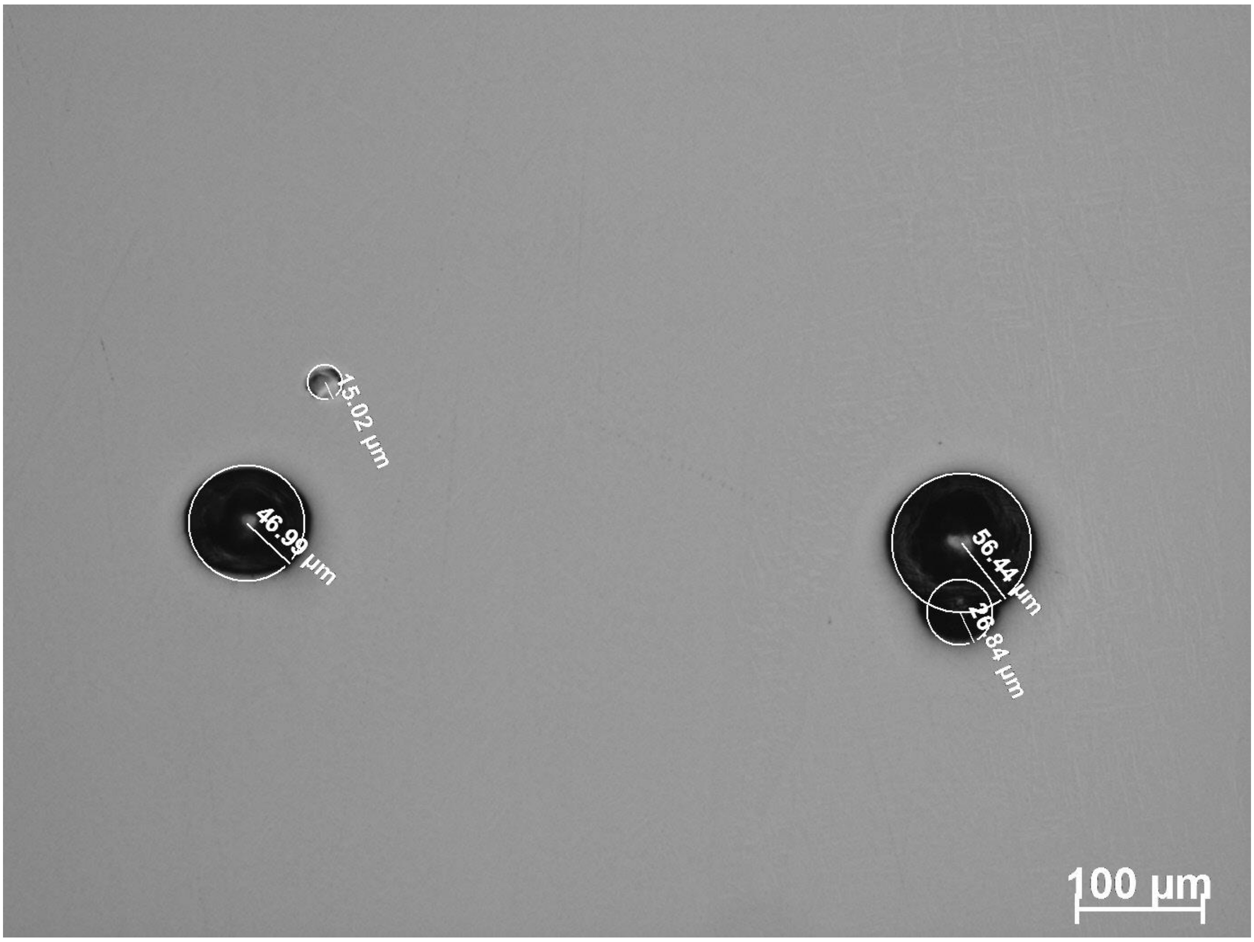


*Figure 98 Gas pores found in as-built EIGA tensile specimens.*

Similar results from EBM, Arcam manufacture factory acceptance build. It has been reported that it is typically to find porosity the range of <0, 3 % in powder and <0, 2 % in the melted material using helium pynconmetri.

### 4.2.3 As- build defects of PA built samples

The main defects found in as-built PA specimens shown in Figure 99 predominately lack-of-fusion defects approx. 84 µm to 119 µm. Some moderate level of spherical gas pores approximately ~40 µm were found. These defects have been reported by many authors resulting from process instability and use of non-optimised parameters. It should be noted no optimisation of parameters were carried out in this study. A study carried out Hou et al. [62] on the same EBM Q20 equipment demonstrated and optimised parameters which were capable of reducing defects by ~72% from the default parameters.

*Figure 99EBM as-built PA samples indicating some small lack of fusion defects. From bottom of build is (a) bottom sample in XZ (b) middle sample XZ (c) top sample, XZ (d) Z- Build direction is also shown (e) XY cross section with magnified defects ~50 µm.*

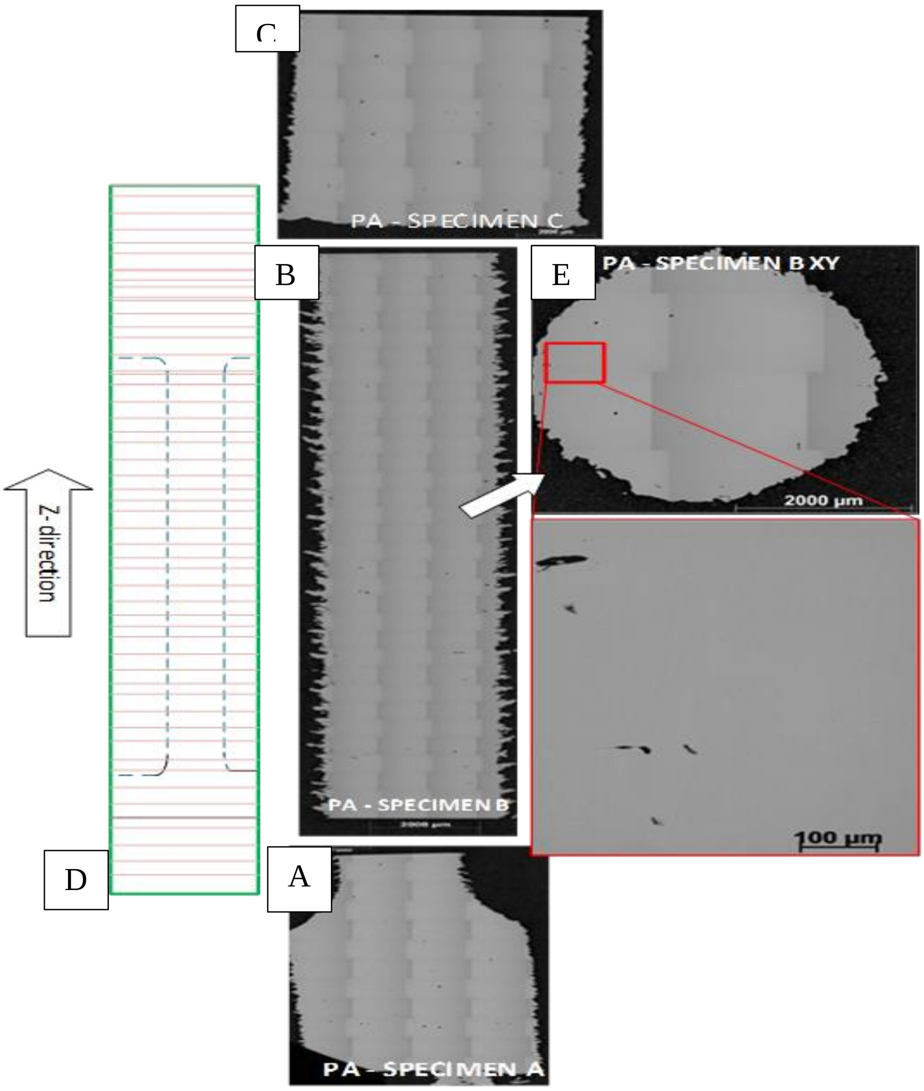

Instabilities during beam melting or process instability as a result of AM hardware could have led to beam tripping which can leave regions of un-melted powder [70].

High magnification in Figure 101 shown below with an indication of lack of fusion for as-built parts.

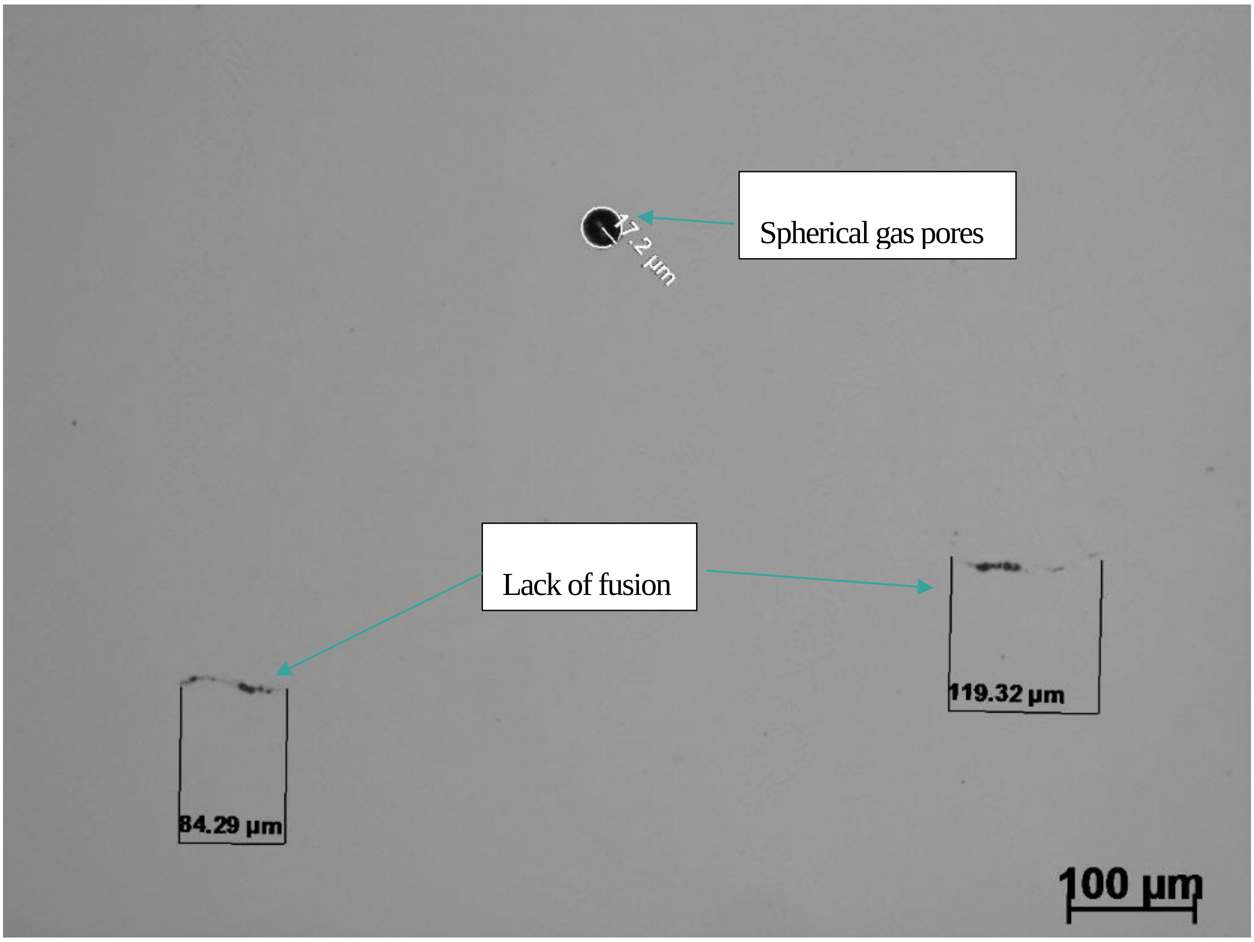


*Figure 100 lack of fusion defects from as-built PA specimens with some gas pores*

Critical defects such as un-melted or lack of fusion were observed thus indicating process instability or insufficient energy input thereby poor melting as a result of not optimised parameters or process instabilities has been reported by many authors [62] [53] [53]

### 4.2.4 Effects of HiPing EBM manufactured samples

HiPing as-built test specimens has eliminated process-induced defects such as spherical gas porosity and internal defects. These spherical or round shaped voids originate from the entrapped gas (argon) within the gas atomised powder particles as shown in Figure 102. The findings are similar to those found in this literature review [54] [55]

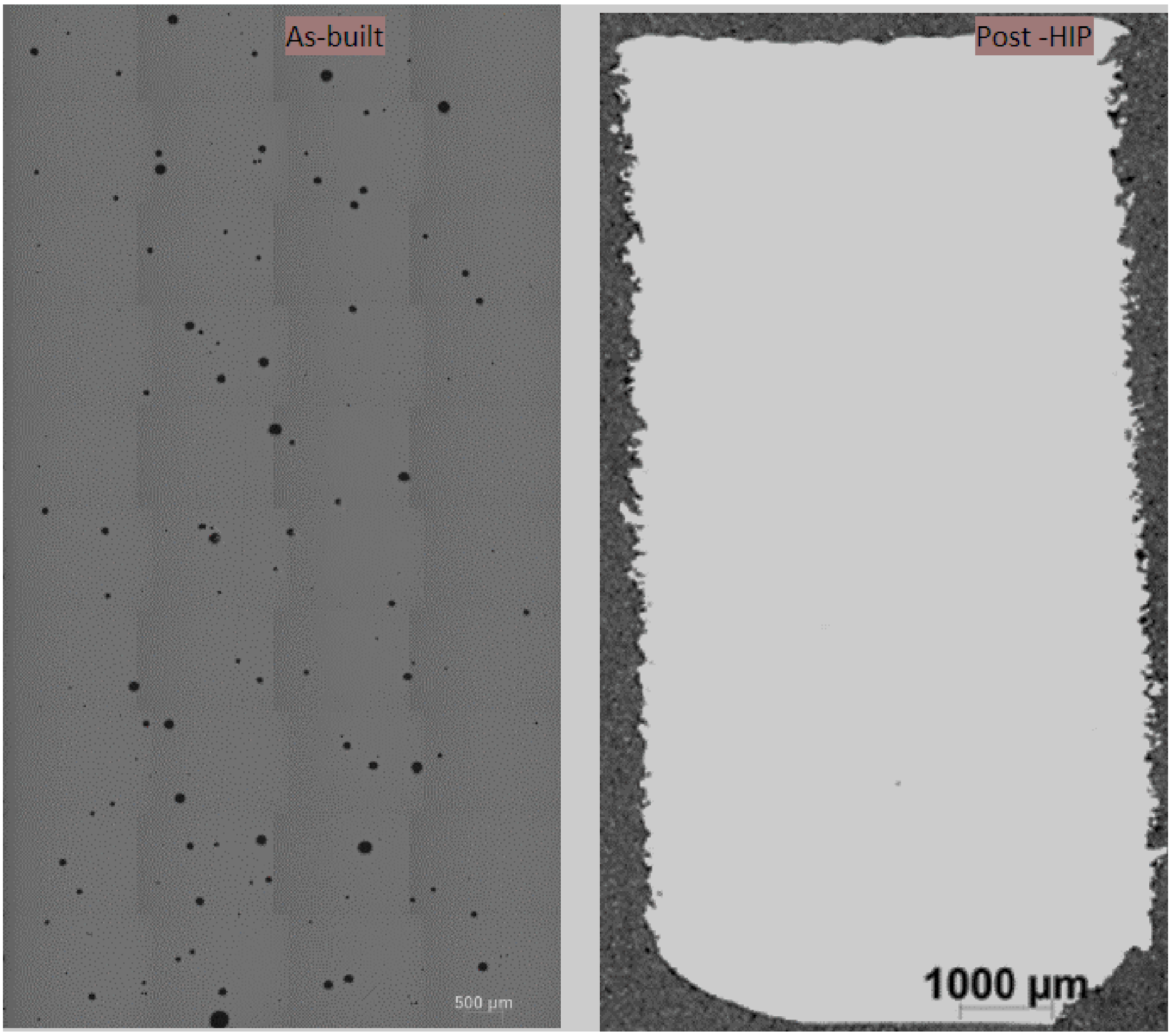


*Figure 102 showing effects of HiPing as-built and post HiPed samples for EIGA powder*

Using ImageJ software on the EIGA as-built cross area specimen to analyse the volume fractirion. The below volume fraction was quantitatively analysed with:

- EIGA Sample (as-built) **0.75%** pore Volume Fraction
- EIGA sample (after HiPing) No pores found

Figure 103 is EIGA pre and post HiPing cross section indicating closing of gas pores.

A

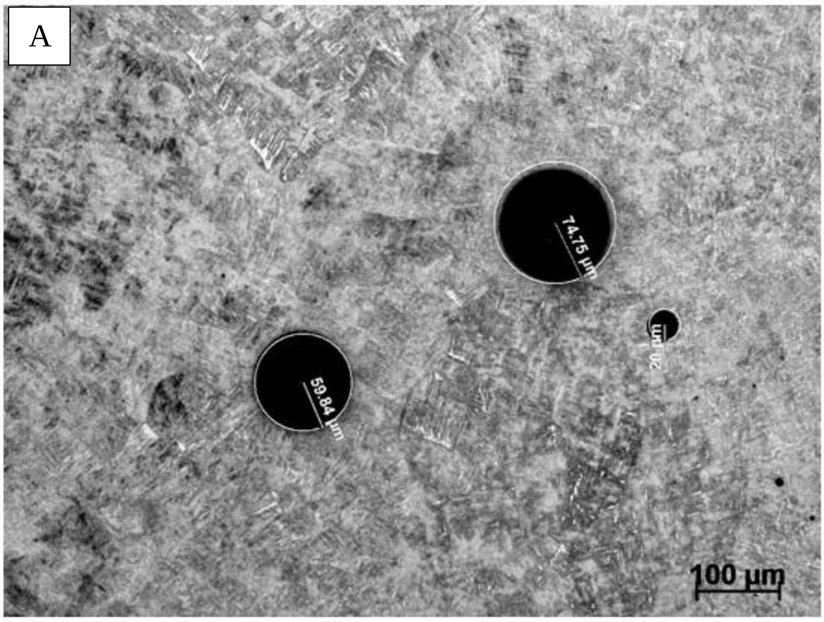


B


*Figure 103 EIGA powder with (a) Gas pores (argon) pores in as built and (b) No pores seen after HIPing on EIGA specimen*

## 4.3 The microstructure of EBM Ti-6Al-4V (for as-built vs. HiPed)

### 4.3.1 As-built microstructure evaluation

General microstructure of EBM for both PA and EIGA Ti-6AL-4V powder specimens shown on Figure 104 and 107consist mostly of very fine α –phase plates and basket-weave microstructure also referred as Widmanstätten structure. The morphology of the ∝ grains was found to be acicular or plate-like grains for both. Similar findings have been reported by authors among some of them are [68] [19] [53]. The rapid solidification/ cooling rates of 150 -250 °C/s has been reported by many other authors [5]. However, in comparison to conventional methods such as those in the wrought process cooling rates of approx. 10°C/s results in coarse grain structure [108].

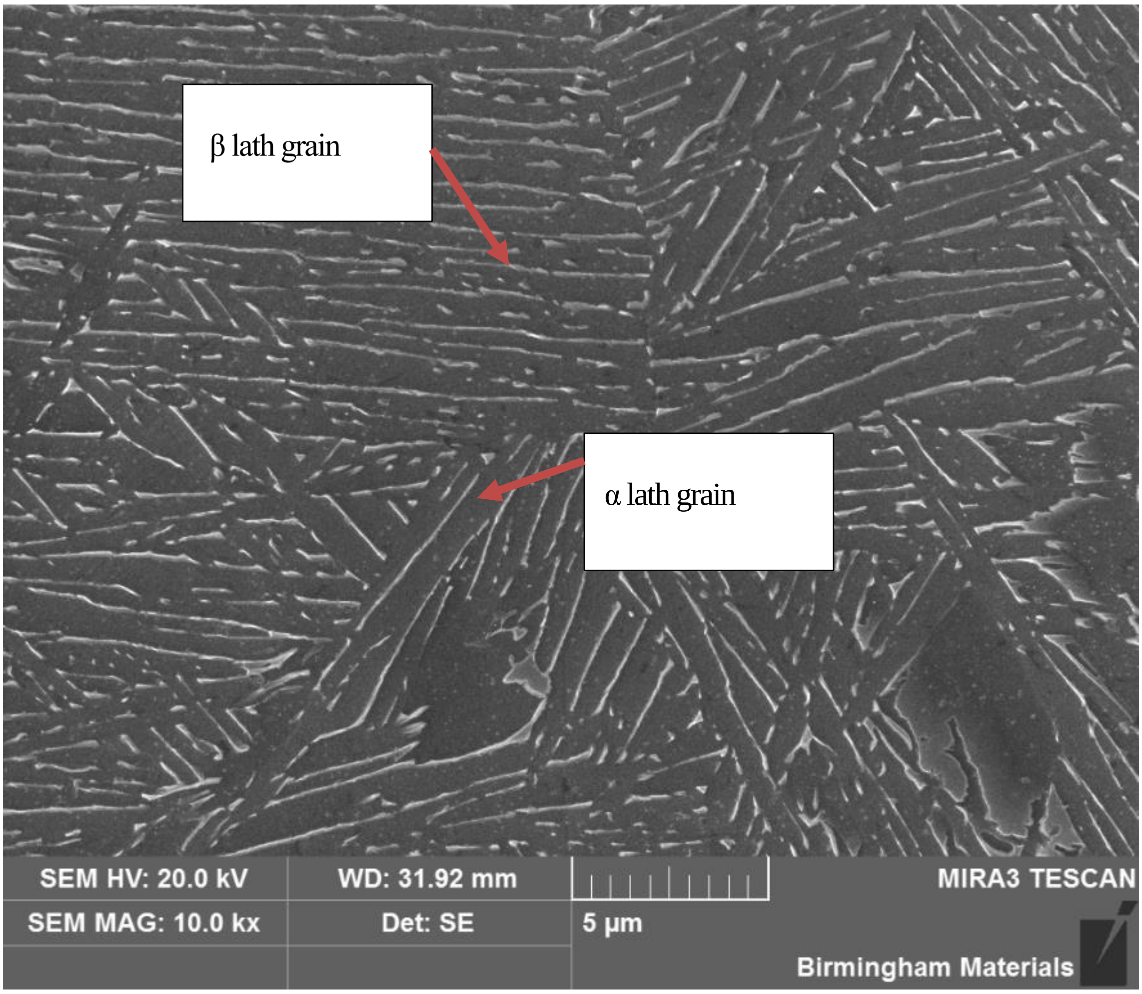


*Figure 104 the as-built EBM microstructure for PA powder*

There is no indication of $\alpha_{GB}$ having or possessing any particular orientation in correlation with prior β phase. In Figure 105, pores in EIGA as-built specimen can be seen and do not show any effects of the grain phase formation as a result of their presence.

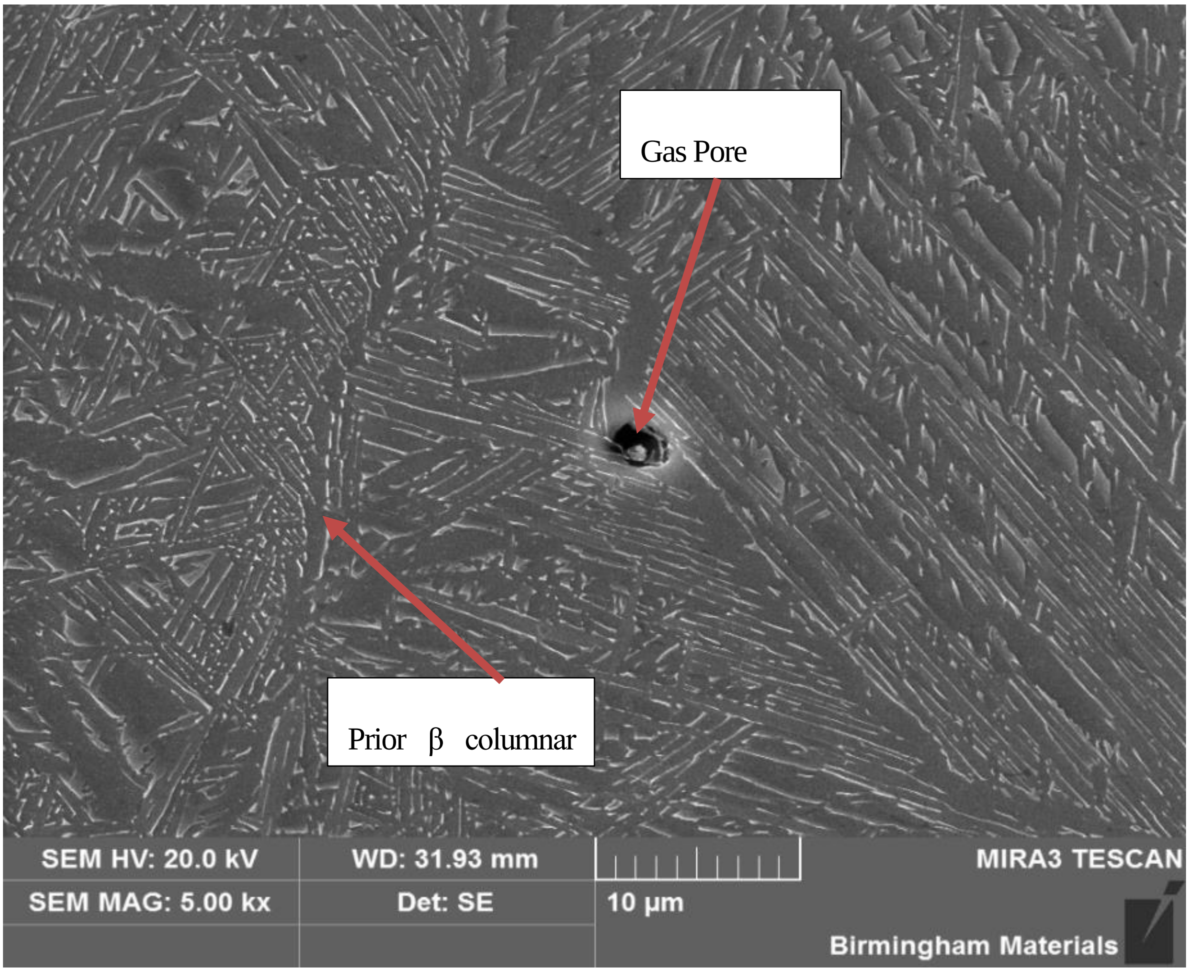


*Figure 105 indication of gas pore on the microstructure of as-built EIGA specimens.*

Below Figure 106 shows expected microstructure from studies carried out by Svensson,2012 [25]. It's been reported by other authors [25][9] [8] that smaller beta grain size is superior in ductility as long as the material is not transformed into alpha prime martensite. The finer alpha lamellae seen in this study are probably the reason for the significantly higher yield and tensile strength properties found in this study for EIGA and PA powder.

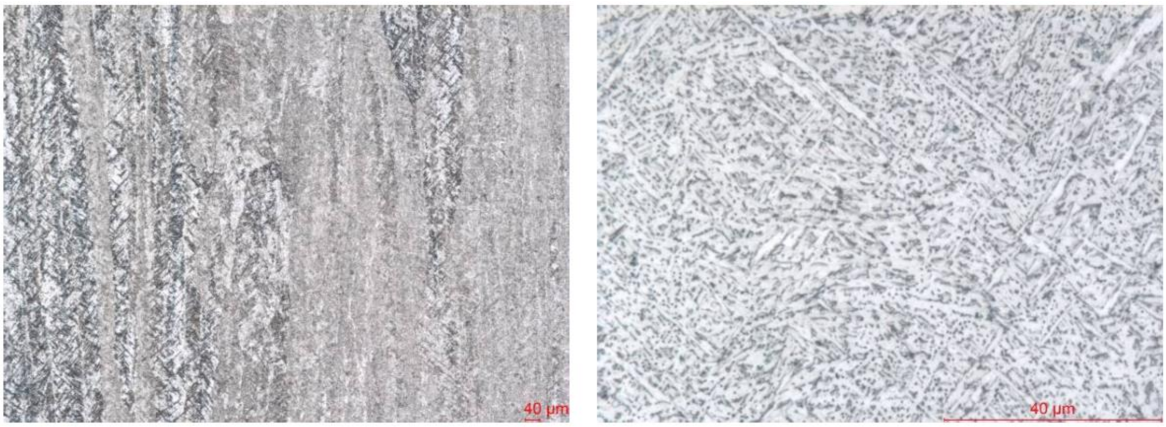


*Figure 106 Arcam EBM manufacturer expected microstructure for as-built parts [25].*

### 4.3.2 Effects of HiPing on microstructure

It was observed that EBM build samples composed of fine α lath lamellas and a small amount of β phase on as build parts. However, post HIPing the grain structure is coarsened and larger α lath appear more larger. The coarsening after HiPing is due to high temperature and pressure close to β transus temperature (1253 ± 10 K) as built as shown in Figure 107. From microstructural analysis using optical microscopy and image analysis measurement, the EIGA as-built specimens had approximately 0.49 µm - 0.68 µm in comparison to HiPed specimens at ~1.81 µm α lath. This equates to approximately 200% increase. As a result, β phase volume % reduction from 11.8% to 8.8%.

Study carried by Hrabe et al. 2012 [56] found microstructure α lath approx. 0.96±0.26 µm for vertical as- built samples. Columnar grains are still the typical feature but with the alpha lamellar structure more developed than the as-built specimens.

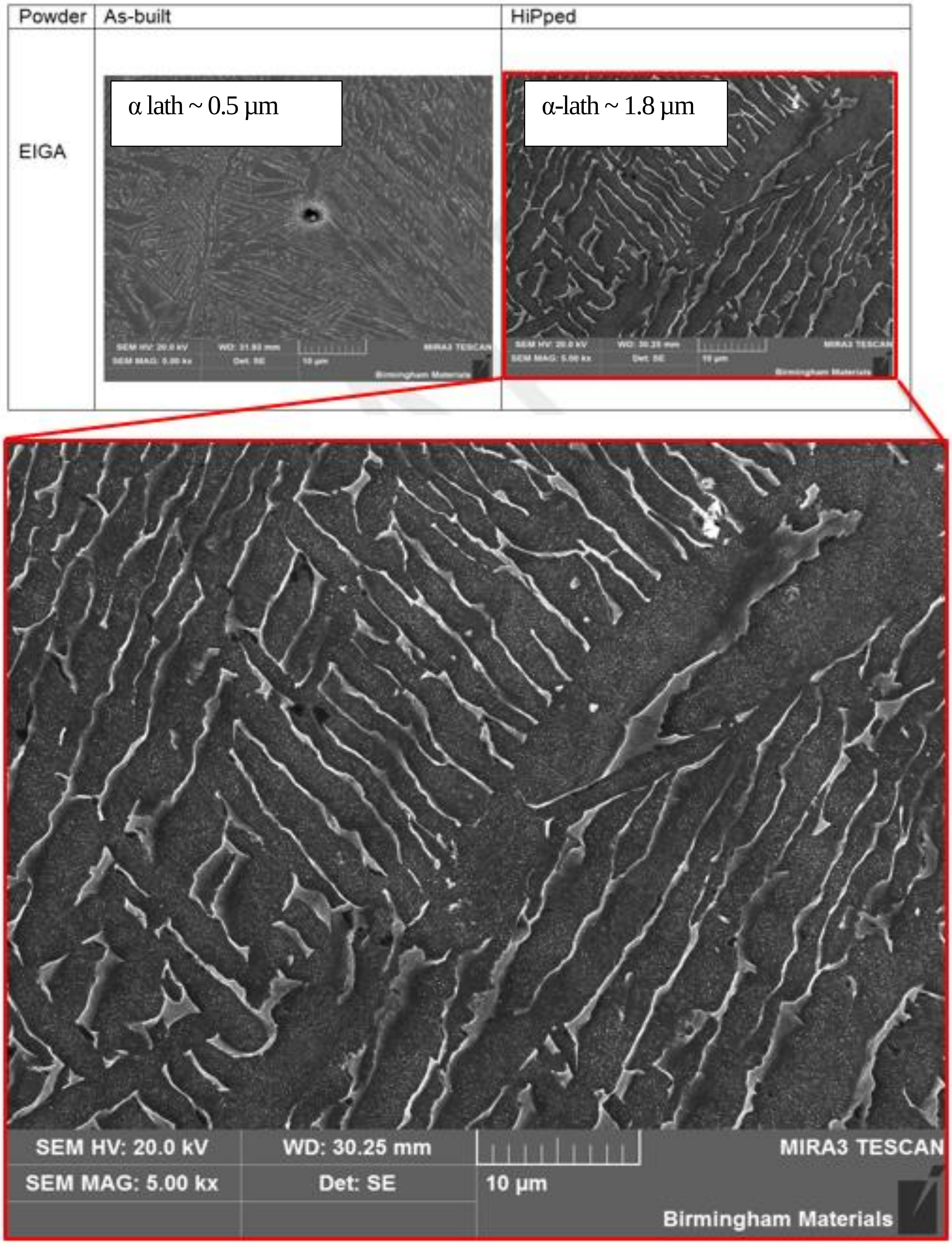


*Figure 107 Microstructure for Ti-6Al-4V post HiP indicating courser grains.*

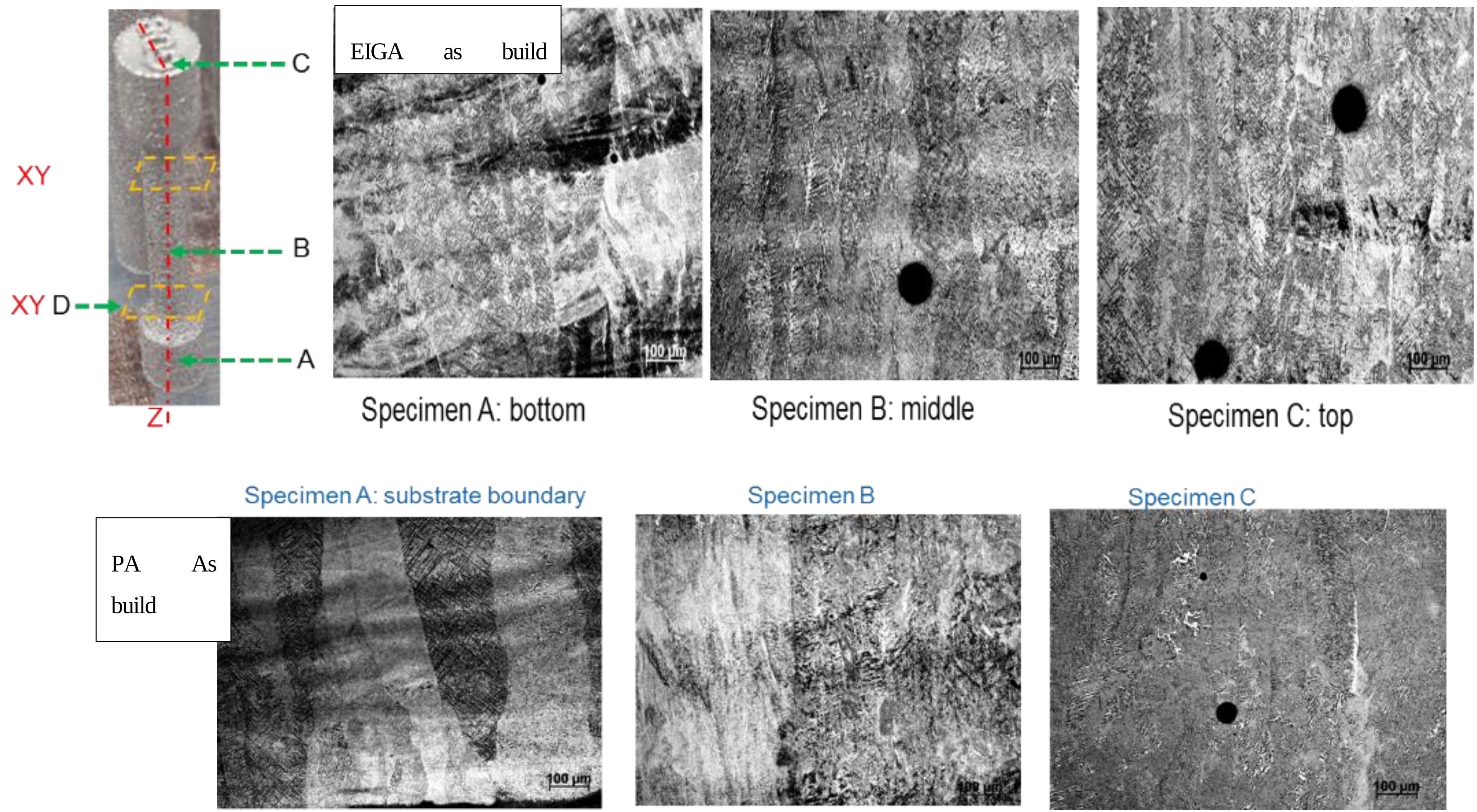


*Figure 108 EBM EIGA and PA specimens as built from bottom, middle and top.*

## 4.4 Mechanical properties

### 4.4.1 EBM as built vs. HiPed specimens

Three specimens per each test condition were mechanically tested following ASTM E8 standard. Figure 109 shows the mechanical tensile results for the EIGA and PA powder build samples. As indicated the samples were tested under three different conditions for as-built, machined and HiPed to understand the effects of post processing AM parts. It can be observed that majority of all samples had yield strength (YS) and Ultimate Tensile Strength (UTS) above 810 MPa and ~900 MPa irrespectively and all above the ASTM F1108 Ti-6Al-4V for cast materials.

*Figure 109 YS, UTS and % El for EIGA and PA as -built, as-built + machined and HiPed + Machined.*

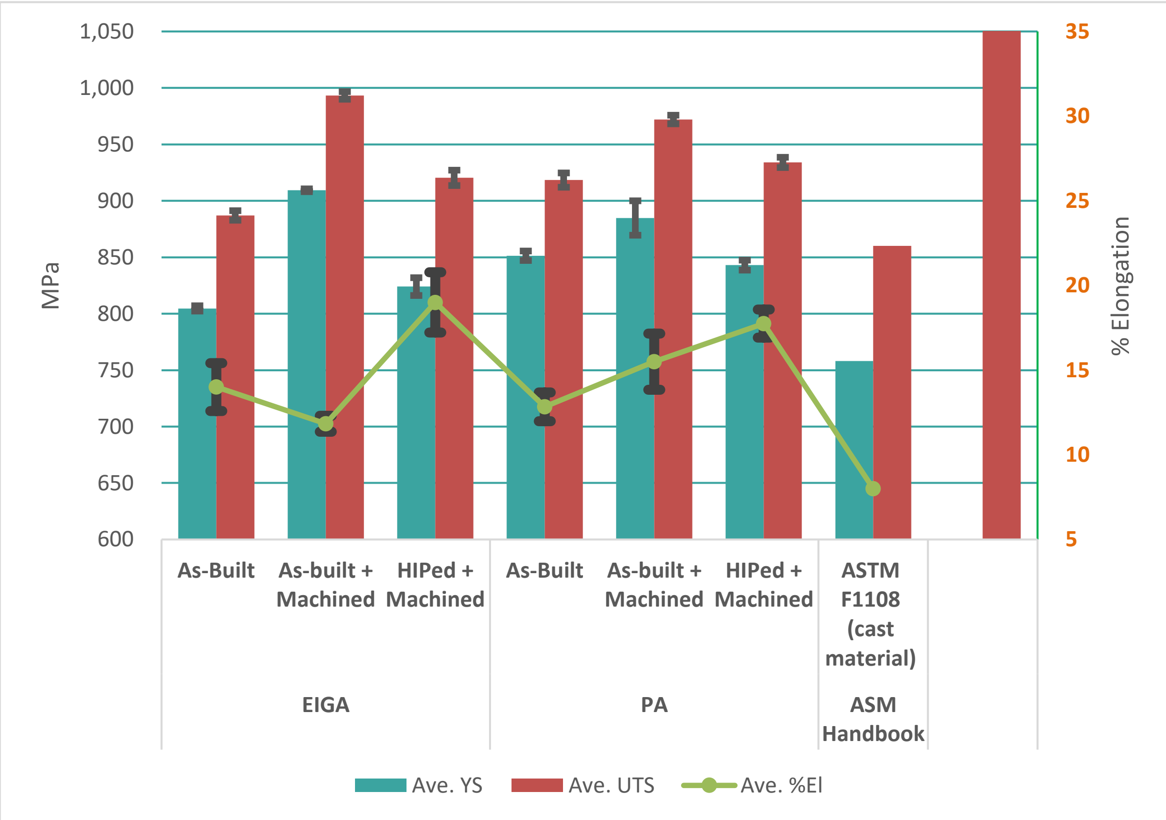

### 4.4.2 Effect on mechanical properties: HIPed+ machined vs as-built + machined

The tensile test results indicated that HiPing decreases YS and UTS of Ti6Al-4V by approximately 8% (or ~ 60-70 MPa). This is due to microstructure alpha laths coarser than as build as discussed in section 4.3.1. Similar trend and finding are reported by other researchers, Al-Bermani [5] and; John J. Lewandowski and Mohsen Seifi [53] found the coarsening of alpha lath more 'effective in the slip length and thus causes the decrease of Ys and UTS'.

The influence of HiPing is also indicated with specimens which were HiPed and machined having higher % elongation, thus indicating closing or elimination of internal defects as observed from the cut-up section SEM results in Figure 103. Lack of fusion and spherical gas pores for as-built specimens can be seen on the lower elongation % in comparison to HiPed specimens. A reduction of approximately 5- 6 % post HiPing can be observed.

The table below is mechanical results from EBM, Arcam manufacturer factory verification report for the Q20 machine.

| *ASTM Standard Specifictaion* | *Min. Yield Strength Rm [N/mm²]* | | *Min. Tensile Strength Rp 0,2 [N/mm²]* | | *Min. Elongation A [%]* | *Min. Reduction of Area Z [%]* |
|---|---|---|---|---|---|---|
| | *Dim. 0.187 (4.75mm) to under 1.75 (44.45mm)* | *Bars and Forgings: Up to 2.0 (50mm)* | *Dim. 0.187 (4.75) to under 1.75 (44.45)* | *Bars and Forgings: Up to 2.0 (50)* | | |
| *ASTM F136* | *>795* | | *>860* | | *>10* | *>25* |
| *ASTM F1472* | | *>860* | | *>930* | *>10* | *>25* |
| ***Tensile Rod #*** | | | | | | |
| *1* | *888* | | *991* | | *17,5* | *40* |
| *12* | *884* | | *990* | | *18.5* | *47* |
| *21* | *886* | | *990* | | *17.5* | *44* |
| *34* | *880* | | *943* | | *12.5* | *40* |
| | | | | | | |
| *5XY* | *845* | | *968* | | *13.0* | *29* |
| *6XY* | *851* | | *968* | | *13.5* | *33* |
| *7XY* | *841* | | *961* | | *13.5* | *28* |
| *8XY* | *846* | | *961* | | *13.5* | *33* |

*Figure 110 Arcam EBM expected as-built + machined tensile properties [34].*

Thermal heat treatment by HiPing post-processing EBM as build samples has shown microstructures of parts made by EBM can be homogenised for the as-built anisotropic grain microstructure and reduction of process-induced defects. The lower elongation of as-built specimens is due to rough surface finish resulting in localised stress concentration in comparison to smooth machines samples with higher elongation.

### 4.4.2 Effects of surface finish on mechanical properties

This section compares the effects of as-built surface finish again machined samples. As can be seen in Figure 111 the surface finish for EBM samples can be improved by machining or polishing among other post-processing condition. This section compares the effects of surface finish on the mechanical properties of PA and EIGA EBM build specimens.

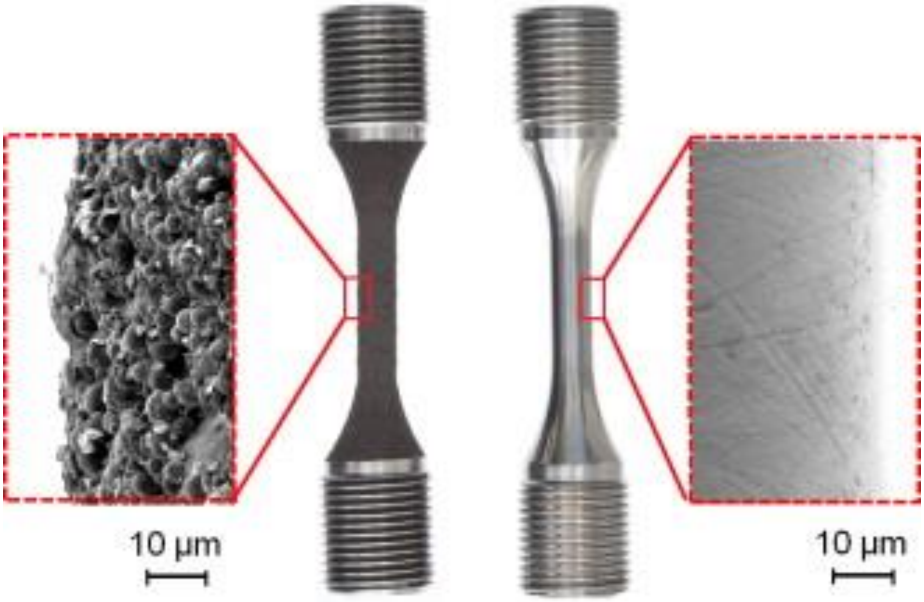


*Figure 111 EBM surface finish for as-built (on the left) and (right) machined specimens.*

It was observed that machining specimens resulted in changes in mainly the % el to failure; PA as built YS and UTS had almost comparable/ similar data at 851 MPa and 884 MPa irrespectively. However, a smoother machined surface resulted in an increased % el of 21% in comparison to as build condition.

97% improvement of surface (by machining) resulted in 8% increase in strength, and 20% increase in ductility.

Murr et al. 2009 [20] found similar findings for YS and UTS as 1350 MPa and 1130 MPa for machined and as-built specimens built using EBM. It can be concluded that rough and rippled EBM surface have larger stress concentration in the mechanical performance of a product. This is more detrimental for fatigue driven application parts

In order to enable better understand of EBM as buid samples surface finish. 3D Optical measurement system was carried out on PA specimen. The characterised area was 5 mm x 5 mm square. Below Figure 112 shows the sample and 3D scan results.

*Figure 112 Surface finish measurement of as-built samples using optical 3D measurements*

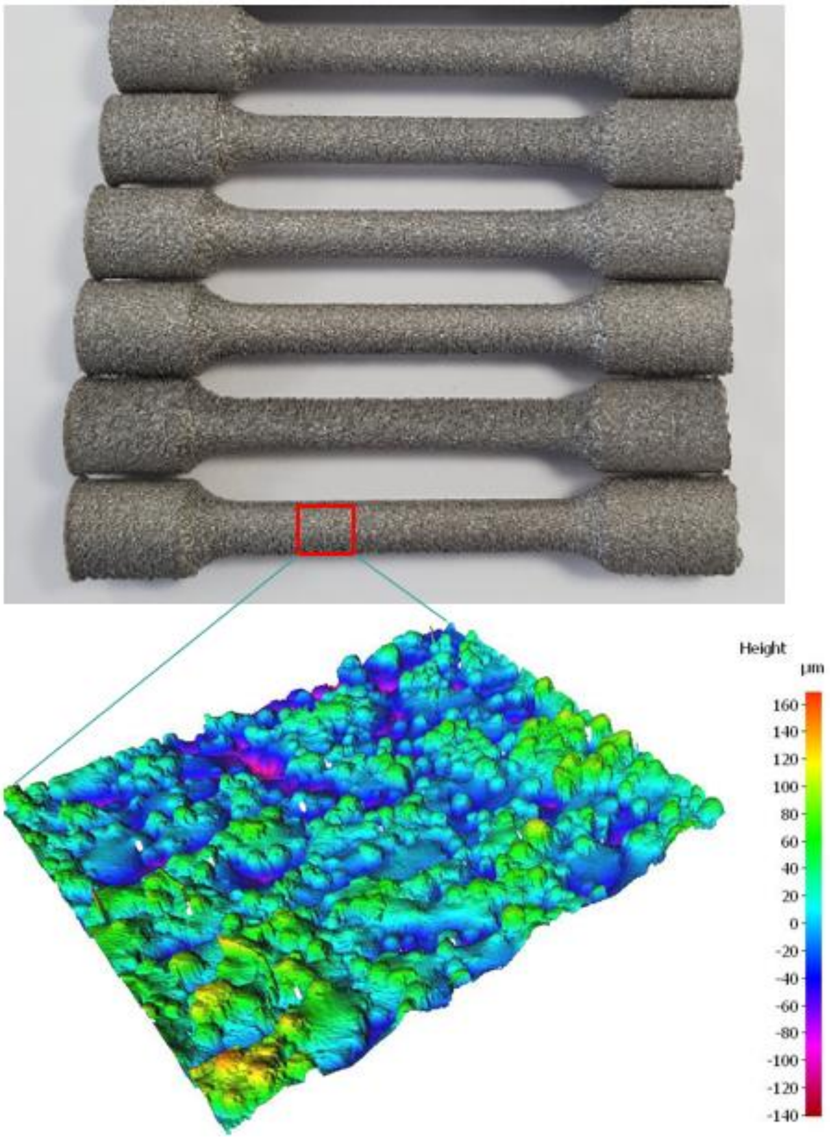

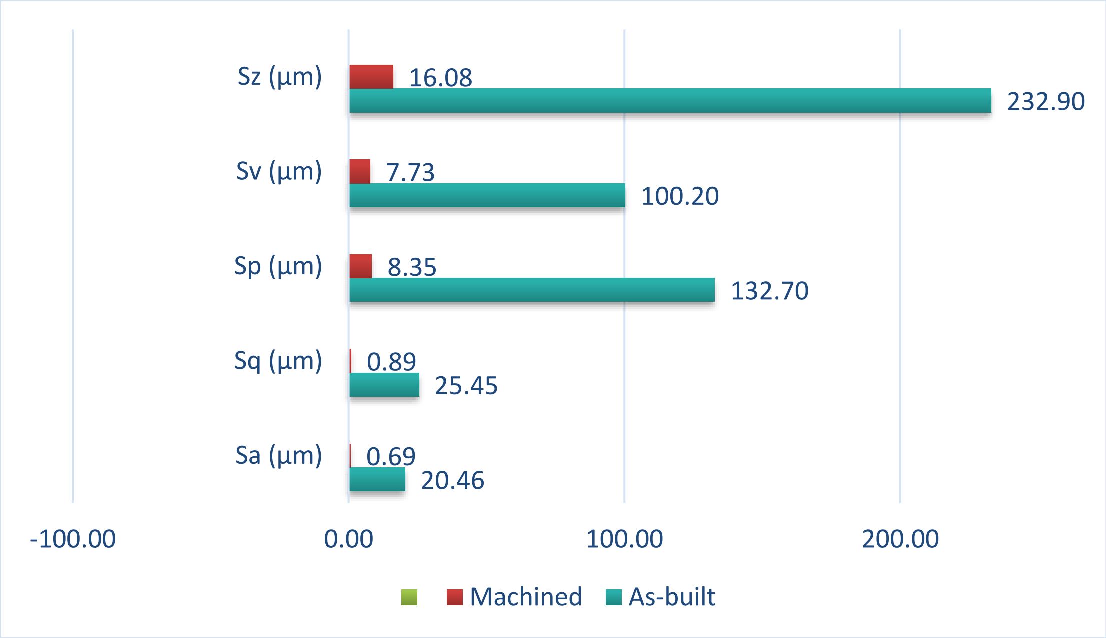


*Figure 113 EBM specimen surface finish of as-built vs. machined topography.*

The results found goes to show the importance of surface finishing on AM manufactured part. The rippled wavy as build surface has a fundamental role in the development of surface stress concentration as it intends to fail earlier during applied stress in comparison to the smoother machined surface. Similar findings were reported by Lalit R 2013 [64] who found the tensile strength of machined and as build specimens were 1028 MPa and 928 MPa irrespectively. The % elongation for both conditions was 14% and 3% irrespectively [64]. However, machine surface was much smoother.

*Machined surface finish*

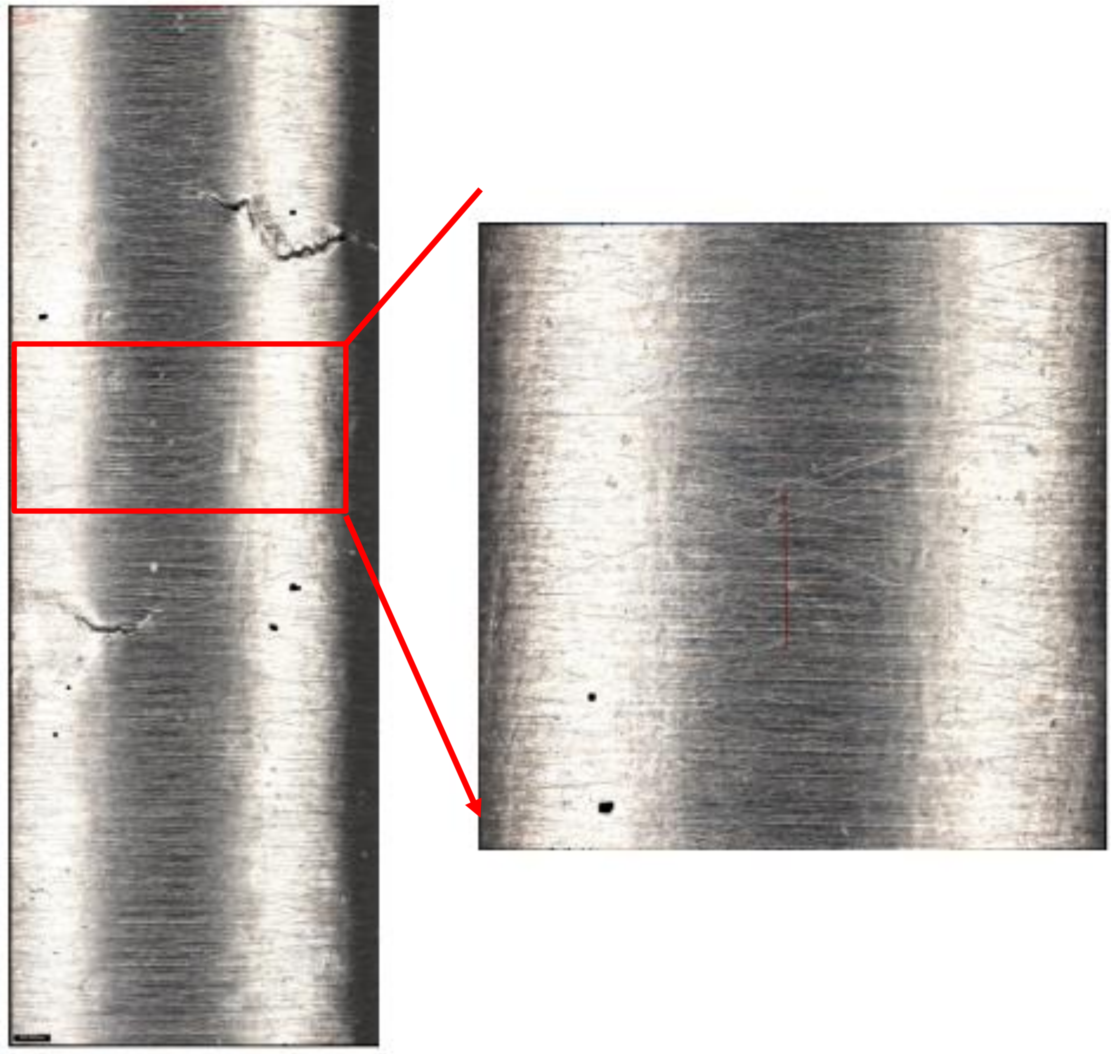

*Figure 114 showing the machined surface for as built specimen. Defects on the surface can be seen resulting to low elongation in mechanical properties.*

## 2.4.6 4..4.3 Effects of Oxygen interstitial on mechanical properties

As previously observed and discussed that PA had higher oxygen of 0.18 wt. % in comparison to 0.11 wt. % for EIGA. It has been observed that an increase in higher oxygen resulted in higher YS and UTS for both materials in same HiPed+ machined condition. The difference in oxygen levels are due to number of recycles of used the PA material while EIGA powder virgin while PA powder batch had been recycled for a longer period. Although difference is slightly small by less than 2% for the YS, UTs and % El, it is difficult to see the influence of oxygen interstitial on both materials. Some researchers have observed influence of oxygen in mechanical properties but this can be cannot be concluded in the small difference on the powders [45] [44].

*Table 29 Effects of oxygen on tensile strength of EBM specimens built using EIGA- 0.1 wt% Oxygen and PA-0.18wt%.*

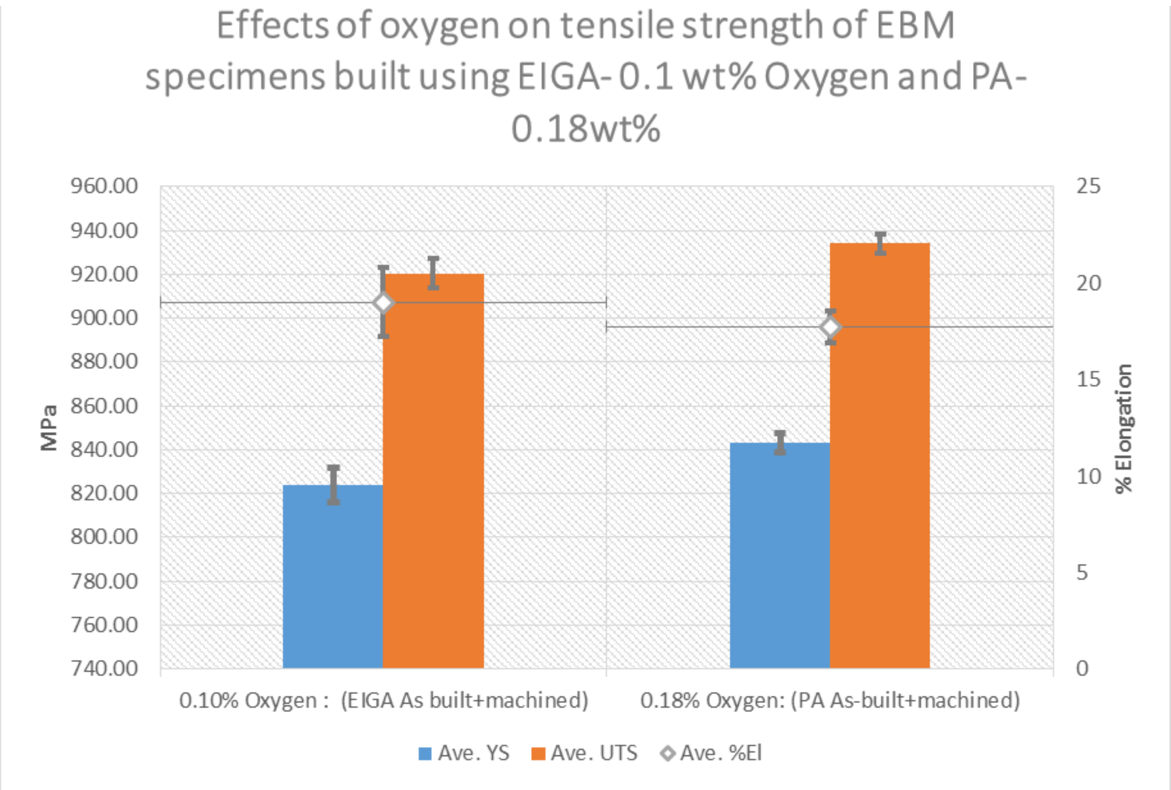

## 4.5 X-ray Tomography

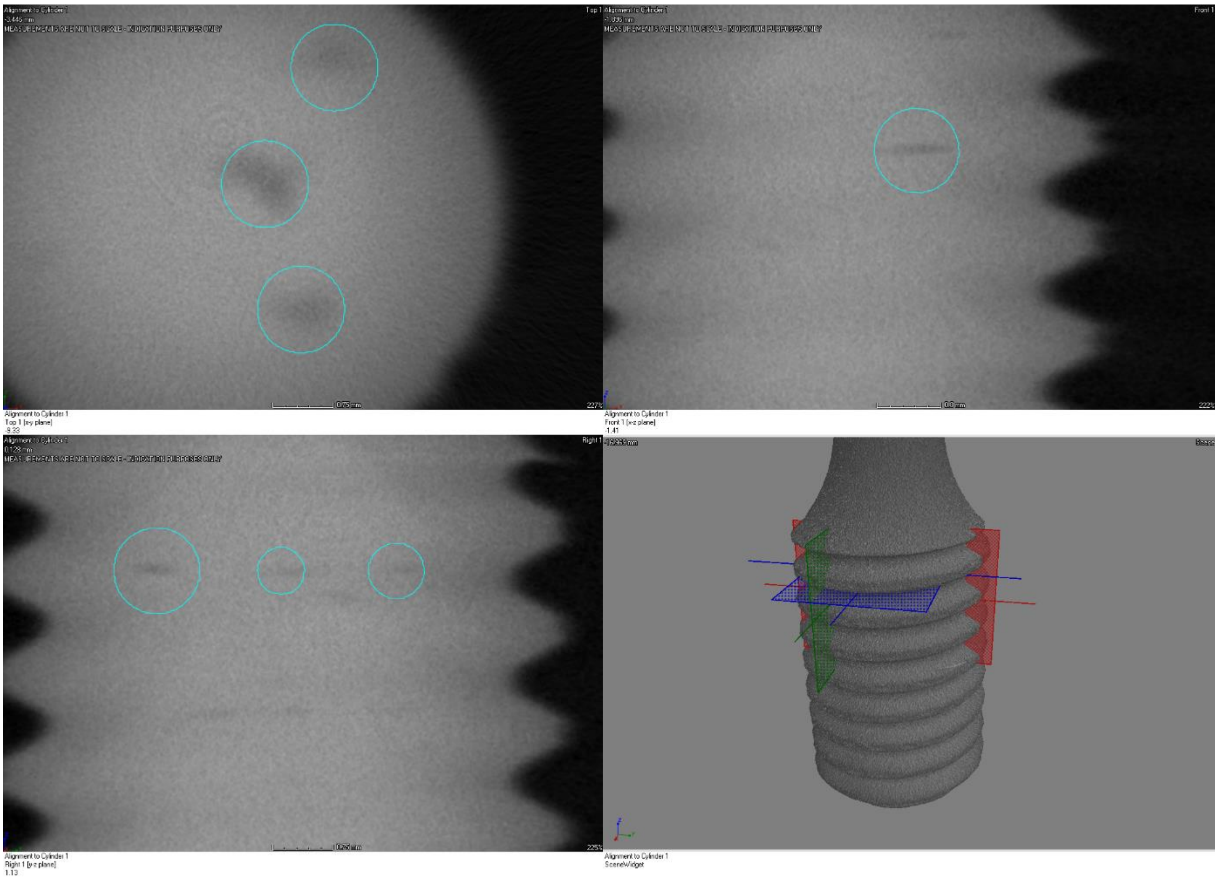

*Figure 115 X-ray tomography of as-built PA samples manufactured using EBM indicating internal defects.*

X-ray tomography for as-built PA samples indicated lack of fusion defects on both internal and near external surface of the parts as shown in Figure 115 and Figure 116. The measured defects were in the range of approximately of 0.5 – 1 mm defects. Voxel size during the scan  x-ray resolution is limited and affected by many other factors such as blurring, x-ray photons scatter, beam hardening and mechanical movement among some of the variables.[26].

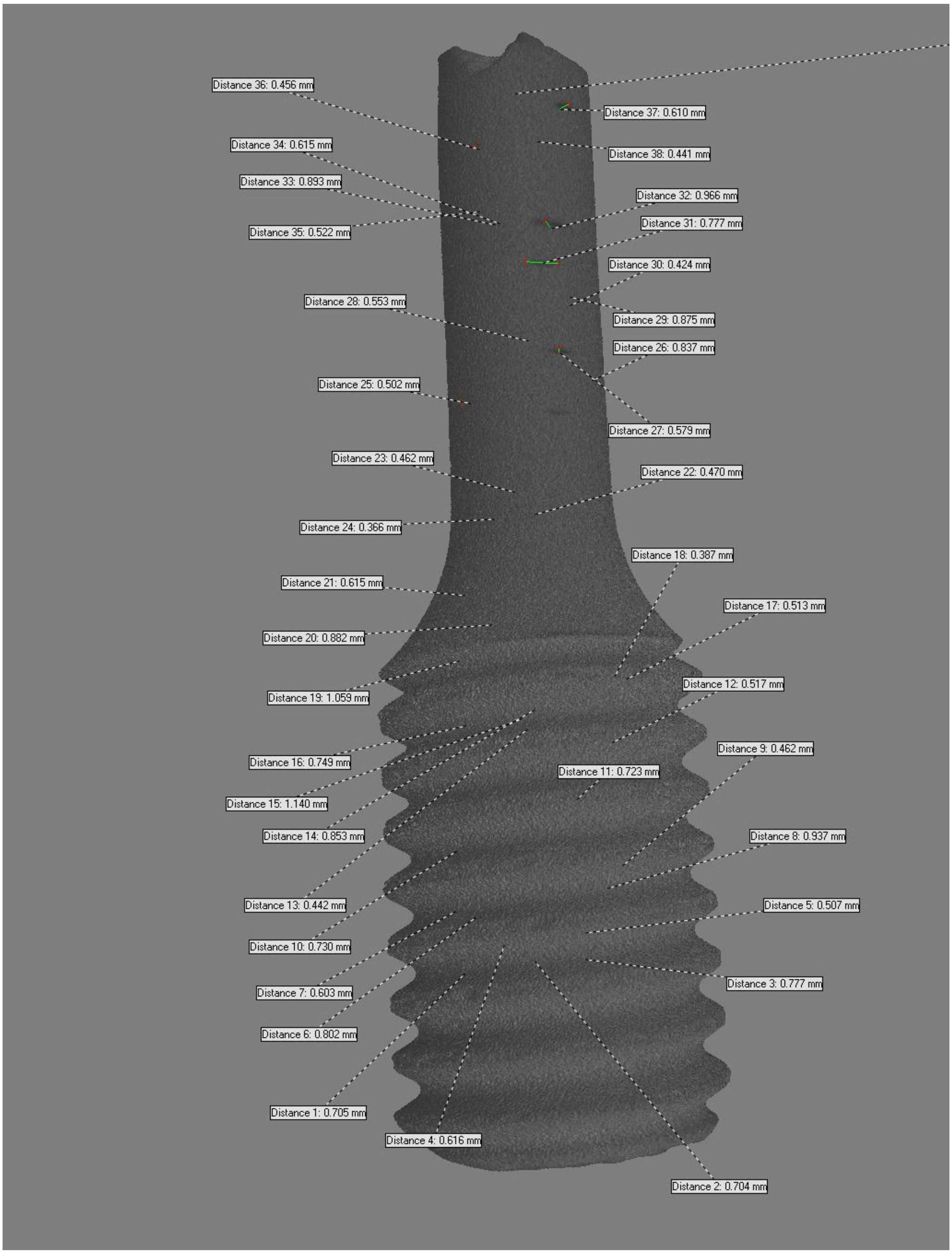


*Figure 116 x-ray tomography indicating internal defects for as-built PA powder in EDM. Defects are a result of non-optimised parameters*

## 4.6 Statistical ANOVA Analysis

The statistical Analysis of Variance (ANOVA) technique was carried out to determine and collate the process induced defects with the measured response to null the hypothesis. The 2nd polynomial regression model was applied and shown in Table 30, whereby the 95% confidence was applied. If a p-value (or probability value) is achieved to be ≤0.05, then it indicates strong evidence again the null hypothesis, thus rejecting the results. Elongation for as-built and machined was found to be above >0.05 p-value, resulting in either the defects are likely to have been machined and invisible to the surface.

Table 30: Analysis of Variance (ANOVA) statistical model used to analyse tensile test data

| GROUP ANOVA RESULTS | | | | | | | | | | | |
|---|---|---|---|---|---|---|---|---|---|---|---|
| | | | | GA | | | | PA | | | |
| Condition | Result | F | p | Mean | StDev | CI1 | CI2 | Mean | StDev | CI1 | CI2 |
| As Built | YS | 188.460 | 0.001 | 804.670 | 2.890 | 797.500 | 811.840 | 851.330 | 5.130 | 838.590 | 864.080 |
| As Built | UTS | 33.730 | 0.007 | 887.000 | 5.200 | 874.090 | 899.910 | 918.330 | 7.770 | 899.040 | 937.630 |
| As Built | Elon | 1.000 | 0.385 | 14.000 | 1.730 | 9.700 | 18.300 | 12.833 | 1.041 | 10.248 | 15.419 |
| Machined | YS | 75.290 | 0.002 | 909.333 | 1.528 | 905.539 | 913.128 | 884.750 | 17.610 | 856.720 | 912.780 |
| Machined | UTS | 260.240 | 0.000 | 993.330 | 4.160 | 982.990 | 1003.680 | 972.000 | 4.400 | 965.000 | 979.000 |
| Machined | Elon | 5.720 | 0.077 | 11.833 | 0.577 | 10.399 | 13.268 | 15.500 | 1.915 | 12.453 | 18.547 |
| HIPed | YS | 37.130 | 0.003 | 824.000 | 9.640 | 800.040 | 847.960 | 843.000 | 5.100 | 834.890 | 851.110 |
| HIPed | UTS | 84.870 | 0.001 | 920.330 | 8.330 | 899.650 | 941.020 | 934.000 | 5.230 | 925.680 | 942.320 |
| HIPed | Elon | 16.510 | 0.019 | 19.000 | 2.180 | 13.590 | 24.410 | 17.750 | 0.957 | 16.227 | 19.273 |

Machined stretch marks could be seen on the fractured surface, which could have resulted in the crack propagation nucleation. Further fracture analysis was carried out and discussed in next section.

## 4.7 Fractography

In this section, the fracture analysis was carried out for tensile tested specimens to understand the cause of failure. As seen in Figure 117, the fractography analysis shows PA powder containing un-melted particles for as-built samples, while EIGA as-built samples contained predominately-spherical gas pores. EIGA gas pores of approx. 40- 50 µm were observed on the fracture surface compared to PA pores 15 – 25 µm.

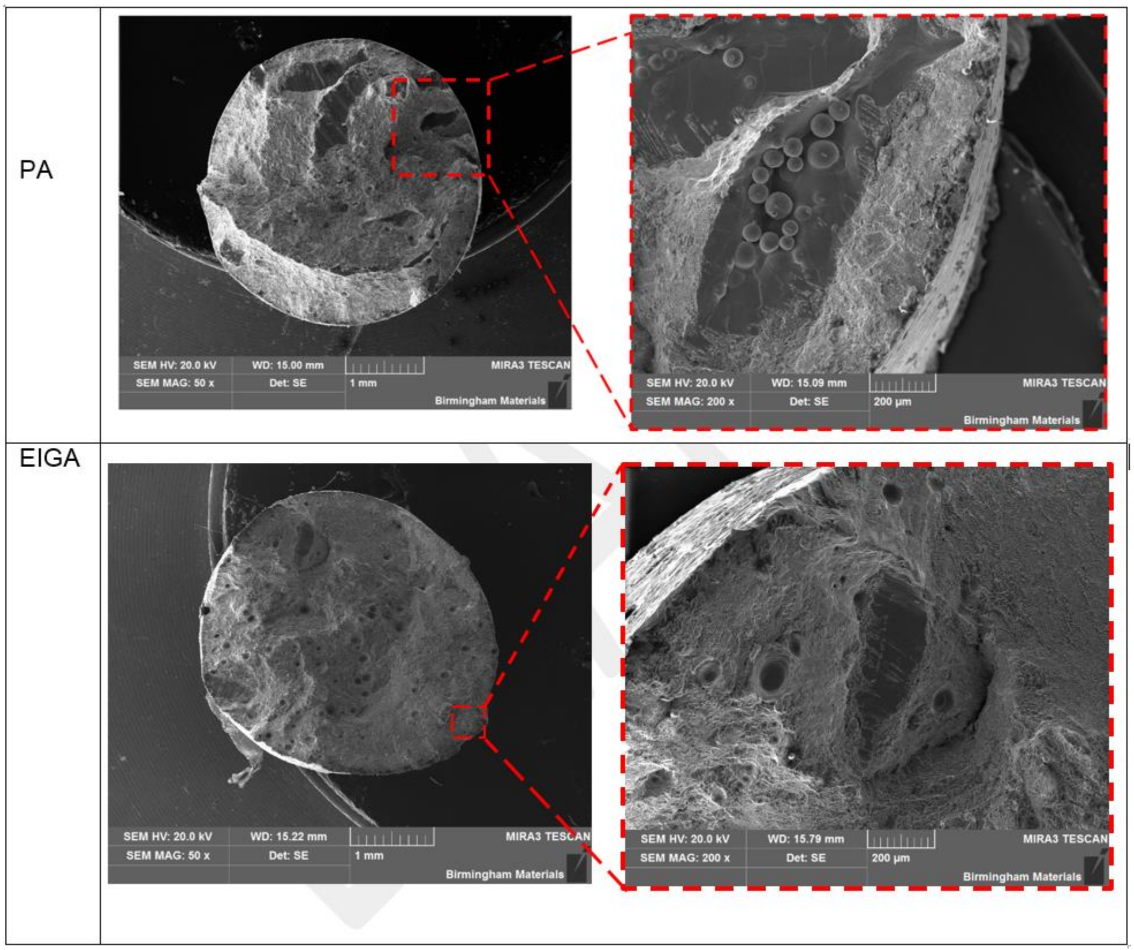


*Figure 117 Fracture analysis of as-built test specimens PA samples with lack of fusion defects and while spherical pores for EIGA pores*

*4.7.1 EIGA fracture analysis of as-built (gas pores) EBM tensile specimens*

Figure 118 shows fractured surface for as-built EIGA specimens indicating spherical gas pores. There is clear indication of some gas pores on the machined surface, thus crack propagation initiating was observed to be ductile with dimples.

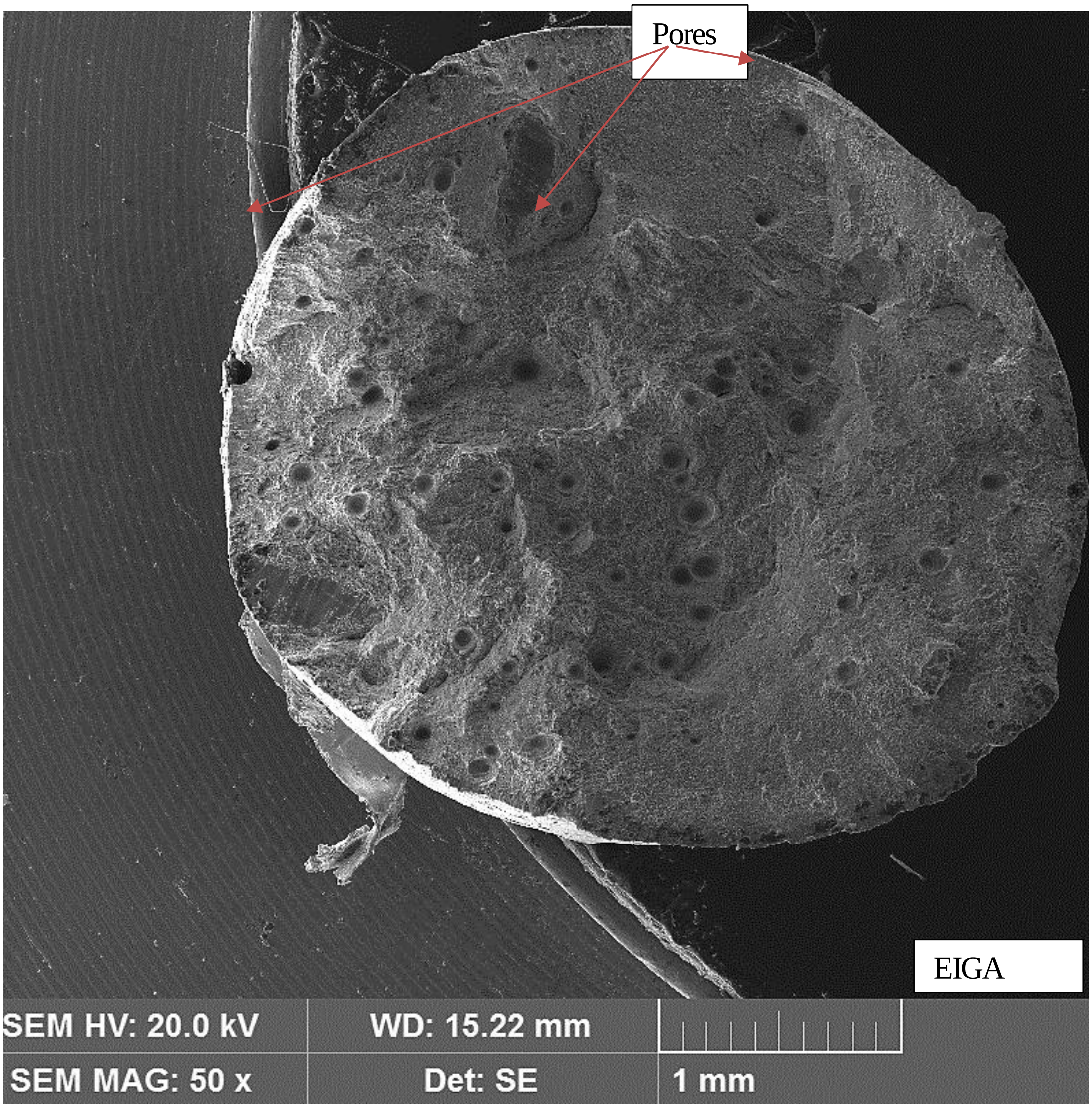


*Figure 118 Fractograpgy of EIGA as-built specimens with indications of gas pores*

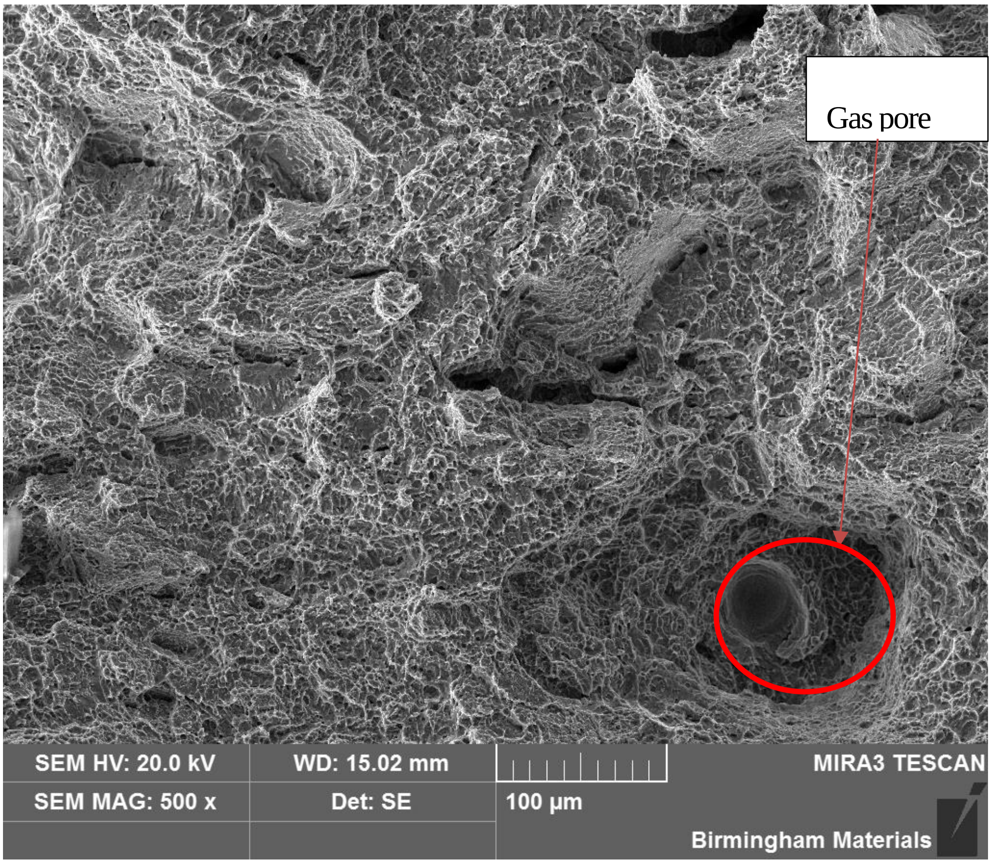


*Figure 119 EIGA as-built fracture specimens indicating gas pores.*

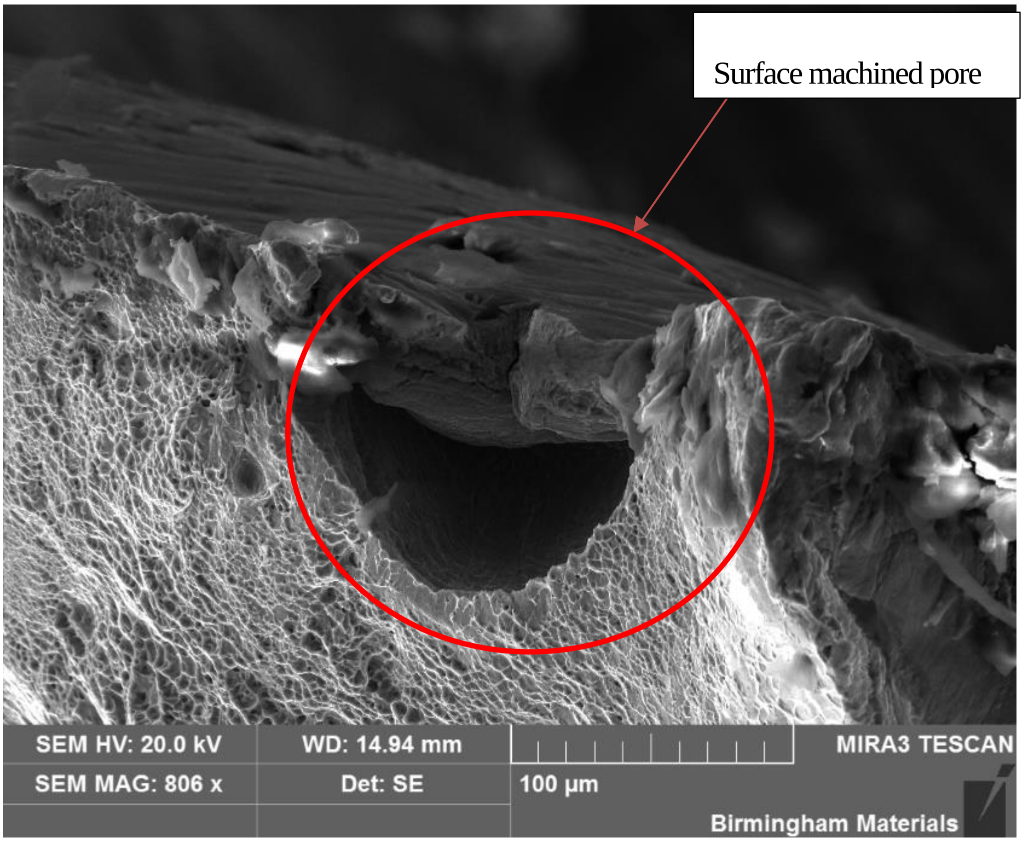


*Figure 120 Gas pore exposed to the surface due to machining*

*4.7.2 PA fracture analysis of as-built EBM specimen*

Figure 121 below shows as-built fracture analysis of PA powder. The Ti6Al4V material can be seen as having a ductile dimples surface.

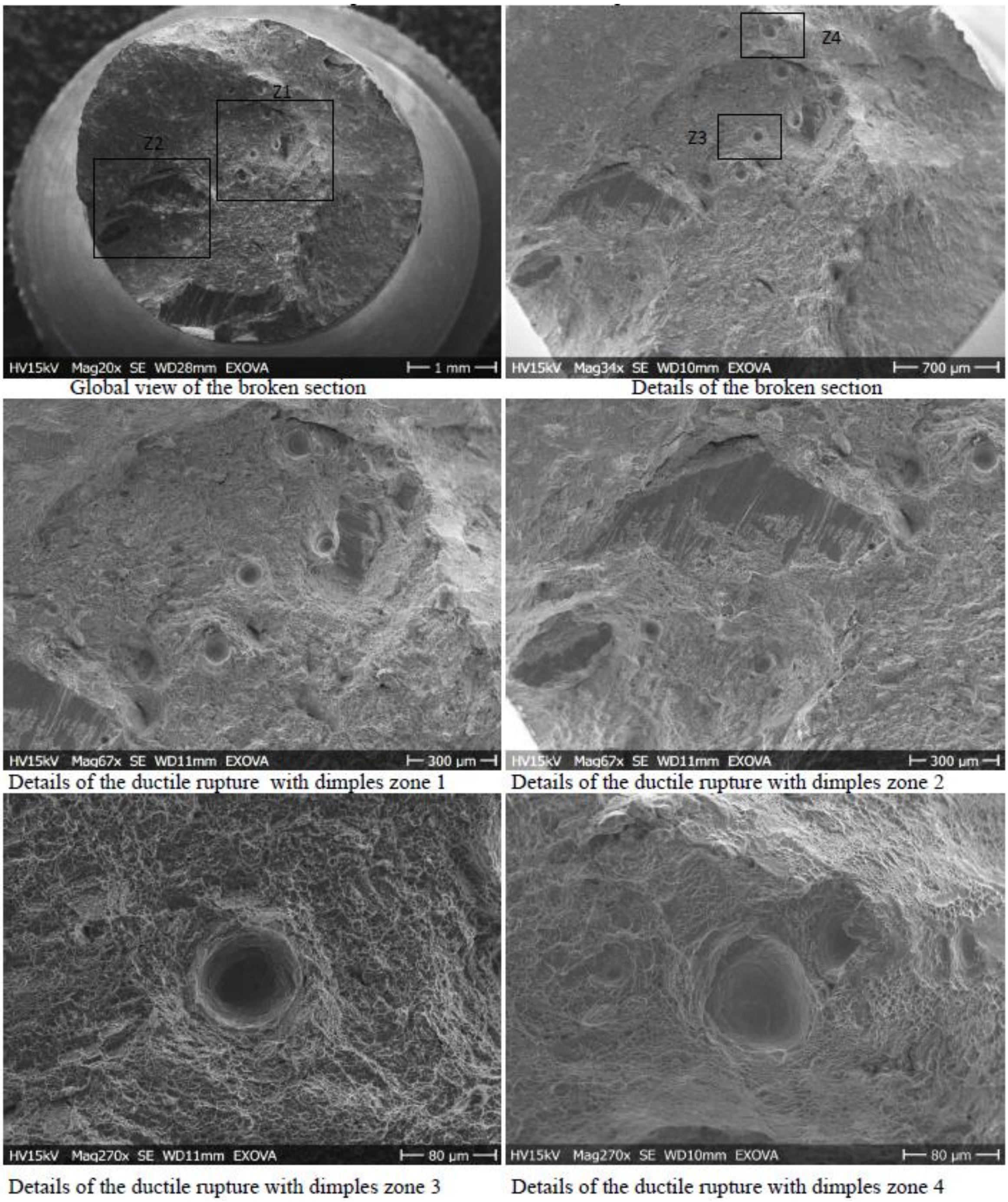


*Figure 121 PA as-built fractography analysis.*

Unlike the EIGA specimens which were predominated with gas pores, the PA as-built samples in Figure 122 had defects mainly of un-melted particles and lack of fusion on the fractured surface. The leading cause of defects can be linked to in-process stability and use of non-optimised parameters. Considering that the samples were built using generic and non-optimised EBM Arcam melt themes; it can be stated this as a possibility.

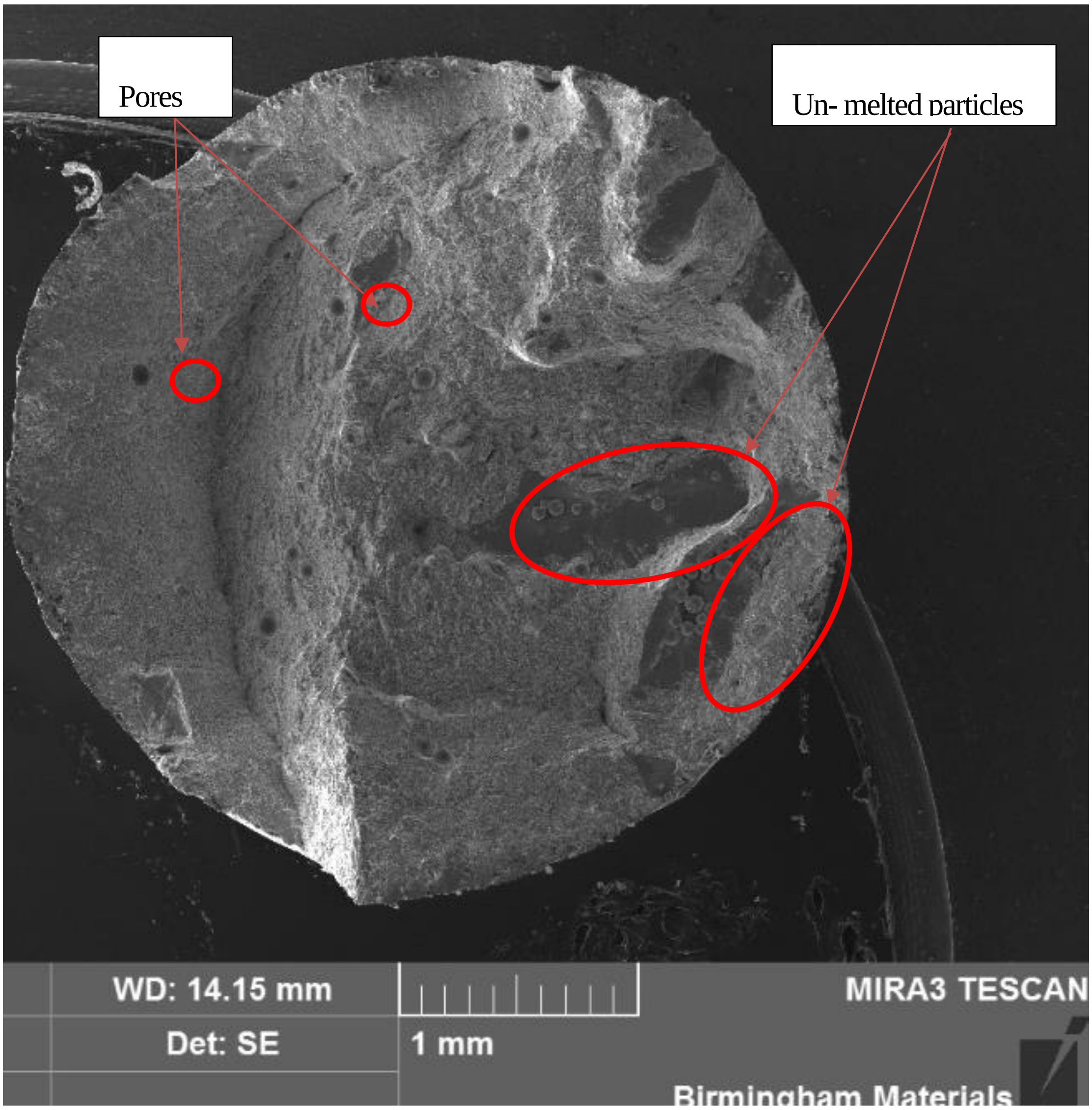


*Figure 122 fractography of PA as-built specimen manufactured using EBM*

Similar observations of EBM defects have been reported by many authors [70]. There is a correlation in process induced defects as a result on non-optimised parameters for the material and powder. In this study PA and EIGA powder specimens were build using the same parameters. However it can be seen from the study, that PA specimen have more defects in comparison to EIGA sample. It goes to show that some process instability could have occurred during the PA build.

# 5.0 CONCLUSION

This section details key conclusion from this study.

## 5.1 EIGA vs. PA powder

A comprehensive powder characterisation of EIGA and PA powders has been carried out in this study to understand the quality and behaviour of two powders manufactured using different processes, and the as-built specimens. From the data generated in this investigation, some key conclusions can be found.

- PA and EIGA Ti6Al4V powders can be manufactured and used for EBM process. However, manufacture generic parameters require optimisation to improve parts quality such as defects during the process.
- Porosity volume fraction is less for EIGA powder compared to PA powder
- During atomisation process of both powders, gas (argon) pores are inherited in the powders. Gas pores can be found in parts. EIGA process had more and bigger gas pores in comparison to very small pores in PA material.
- In terms of morphology, the PA powder has a spherical morphology with smooth particle surface finish compared to EIGA powder with presence of samll particles refered as 'satellites'.
- Comparison of PA virgin sample with recyled PA powder batch for the build it was noted fine satellites are reduced/removed from the particle surface during powder reycling in the powder recovery blasting and sieve equipment. This resulted in better in better flow properties compared to virgin material.
- The recycled PA powders showed evidence of dents in some of the particle surfaces; this characteristic seems to be the result of the recovery powder steps.
- Chemical composition of both powders was found in acceptable specification. Recycled PA powder still had main elements such as interstitials (oxygen), and aluminium in spec. Although EIGA showed lower oxygen and small higher increase in aluminium possibly to new virgin powder.
- Gas pores have been found to be inherited in EBM build specimens. However, Hot Isostatic Pressing has been observed to close internal pores in both PA and EIGA build specimens.

## 5.2 Mechanical properties of EIGA vs PA specimens

Mechanical tensile properties for EIGA and PA have been observed to be similar when processed with same parameters. Below are key findings:

- Yield and ultimate tensile strength for both powders batch specimens were found above the ASTM F2924 standard and Ti-6Al-4V cast material.
- As-built specimens from both powders had higher strength compared to Hot Isostatic Pressed samples. The difference was observed due to finer grain microstructure for as-built specimens and courser large grain microstrcutre post HiPing.
- It has been shown in this study that, EBM specimens rough as built surface finish (~25- 30 Sa) can affect the tensile properties ductility. Surface finishing resulted in almost 20% increase in ductitiy and 8% in strength, Thus almost 97% improvement in surface finish.
- PA as-built specimens were found to contain lack of fusion defects this can be linked to process instabilities and un-optimised parameters.
- The microstructure of as-built EBM specimens can be homogenised when HiPing is applied, however, as a consequence, the microstructure grain size is coarsened and results in a reduction of yield and ultimate strength of a part.
- It has been demonstrated that EBM specimen's surface finish can be improved by machining and polishing thus enhancing the mechanical performance of a part
- Defects have been found to affect the ductility of material % elongation. Internal part defects were closed with HIPing. However, any surface interconnected defects unable to be closed, thus resulting in low % elongation due to defect opening and propagating into part.
- Machining specimens have been found to increase the elongation. However, for as-built parts with defects, this can result in defects exposed to the surface and causing crack propagation.
- Process parameters optimisation is required to reduce and eliminate defects to the industrialisation of EBM process, and this was carried out and demonstrated with same parameters and PA powder on journal article 'Optimising the Dynamic Process Parameters in EBM To Achieve Internal Defect Quality Control.'

### 2.4.7 5.3 Microstructure evaluation of EIGA vs PA specimens

- Microstructure for both material was consist, similar and mostly of very fine α –phase plates and basket-weave structured microstructure also referred as Widmanstätten structure.
- For both EIGA and PA powder, the microstructure consisted of finer alpha lamellae in prior beta grains for as-built specimens. The morphology of the ∝ grains was found to be acicular or plate-like grains for both materials.
- Isotropic microstructure with small to larger columnar grains was observed for samples build from the bottom to top vertical build direction.
- Fine α –phase plates microstructure has been found to cousen post HiPing EBM as built parts. This also resulted in homogenised and improved microstructure
- Nonetheless, aforementioned HIPing of parts has been found to reduce the strength of PA and EIGA built specimens.
- Hot Isostatic Pressing thermal heat treatment have been found to close internal pores and defects; as a result as-built specimens or parts microstructure can also be homogenised resulting in grain structure coarsening.

# 6.0 FUTURE WORK

In this paper, a comprehensive study has been carried out on AM powder and microstructure and mechanical tensile properties. Future work will on interest to understand:

1. Optimise EBM parameters to reduce or eliminate pores and defects

   In this study, it has been observed that manufacture default parameters require optimisation. Future work could focus on reducing and eliminating spherical pores by changing energy input and scanning strategies for better mechanical performance.
2. Effects of EBM surface finishing on fatigue properties

   In this study, it has been observed that EBM has fine grain microstructure in comparison to cast and wrought raw material. It will be of interest to understand crack growth rate. It might be possible to have EBM specimens with higher fatigue cycles due to as-built fine microstructure.
3. Differing microstructure using EBM

   Within EBM process parameters, it is possible to change the processing surface temperature by using different energy input during preheating and melting. Future work could develop process parameters with differing microstructure with fine to coarse grain structure thus differing mechanical properties.

Bibliography


[1] R. B. ,. R. T. Jason Dawes, “Introduction to the Additive Manufacturing Powder,” *Exploring the production and supply of metal powders for AM processes*, 2015.

[2] M. J. Donachie, “Titanium: A technical guide,” *The Materials Information Society,* vol. II, 2000.

[3] ASM International, Materials Properties Handbook: Titanium Alloys, ASM International, 1994.

[4] J. O. Milewski, Additive Manufacturing, Santa FE: Springer International Publishing, 2017.

[5] S. S. Al-bermani, M. L. Blackmore, W. Zhang and I. Todd, “The Origin of Microstructural Diversity, Texture, and Mechanical Properties in Electron Beam Melted Ti-6Al-4V,” *Metallurgical and Materials Transaction A, Volume 41A,* vol. 41, no. 13, pp. 3422-3434, 2010.

[6] AZoM.com, “Titanium Alloys in Medical Applications,” 19 july 2003. [Online]. Available: http://www.azom.com/article.aspx?ArticleID=1794.

[7] B. Bikramjit , Biomaterials for Musculoskeletal Regeneration, Singapore: Springer, 2016.

[8] “Titanium metal for Medical Applications,” Titan Engineering, [Online]. Available: https://www.titanium.com.sg/2016/09/26/titanium-for-medical-applications/. [Accessed 19 February 2017].

[9] Oerikon, “Additive Manufacturing Reshapes Industries,” [Online]. Available: https://www.oerlikon.com/stories/2016/06/10/additive-manufacturing-reshapes-industries/. [Accessed 16 February 2018].

[10] Abraham,. and A. Martin , Encyclopedia of sustainable technologies, Cambrisge: Elsevevier, 2017.

[11] F. H. Froes and H. B. Bomberger, “The Beta Titanium Alloys,” *JOM*, vol. 37, no. 28, 1985.

[12] Chattoraj, “Stress corrosion cracking (SCC) and hydrogen-assisted cracking in titanium alloys,” in *Stress Corrosion Cracking*, Elsevier, 2011, pp. 381-408.

[13] A. A. Antonysamy, “Microstructure, Texture and Mechanical Property Evolution during Additive Manufacturing of Ti6Al4V Alloy for Aerospace Applications,” The Univeristy of Manchester, Machester, UK, 2012.

[14] R. Abbaschian and . R. E. Reed-Hill, Physical Metallurgy Principles, Stamford: Cengage Learning, 2008.

[15] J. Sieniawski, W. Ziaja, K. Kubiak and M. Motyka, Microstructure and Mechanical Properties of High Strength Two-Phase Titanium Alloys, n.d: InTech, 2013.

[16] G. H. Campbell, . T. B. Lagrange, W. E. King, J. D. Colvin, A. Ziegler, N. D. Browning, H. Kleinschmidt and H. Bostanjoglo, “The HCP To BCC Phase Transformation in Ti Characterized by Nanosecond Electron Microscopy Solid-Solid Phase Transformations in Inorganic Materials 2005,” *The Minerals, Metals & Materials Society*, 2005.

[17] R. Ding and Z. X. Guo, "Microstructural evolution of a Ti–6Al–4V alloy during β-phase processing: experimental and simulative investigations," *Materials Science and Engineering: A,* vol. 365, no. 1-2, pp. 172-179, 2004.

[18] J. H. Dai, X. Wu, Y. Song and Yang, "Electronic structure mechanism of martensitic phase transformation in binary titanium alloys," *Journal of Applied Physics,* vol. 112, no. 12, p. 123718, 2012.

[19] H. Galarraga, R. J. Warren, D. A. Lados, R. R. Dehoff, M. M. Kirka and P. Nandwana, "Effects of heat treatments on microstructure and properties of Ti-6Al-4V ELI alloy fabricated by electron beam melting (EBM)," *Materials Science and Engineering: A,* pp. 417-428, 2017.

[20] L. Murr, S. Quinones, S. Gaytan, M. Lopez, A. Rodela, E. Y. Martinez, D. H. Hermandez, E. Martinez, F. Medina and R. B. Wicker, "Microstructure and mechanical behavior of Ti-6Al-4V produced by rapid-layer manufacturing, for biomedical applications," University of Texas, El Paso, 2009.

[21] J. J. Dunkley, in *Atomization: Introduction, in ASM Handbook,* Ohio, ASM International, 1998, pp. 35-52.

[22] W. J. Sames, F. A. List, S. Pannala, R. R. Dehoff and S. S. Babu, "The metallurgy and processing science of metal additive manufacturing," *International Materials Reviews,* vol. 61, no. 5, pp. 315-360, 2016.

[23] LPW Technology LTd, "lpwtechnology," [Online]. Available: http://www.lpwtechnology.com/technical-library/technical-information/methods-of-powder-production/.

[24] F. Medina, “Reducing metal alloy powder costs for use in powder bed fusion additive manufacturing: Improving the economics for production,” ETD Collection for University of Texas, El Paso, 2013.

[25] “Our Technology - AP&C Advanced Plasma Atomization Technology,” 20 july 2016. [Online]. Available: http://advancedpowders.com/plasma-atomization-technology/our-technology/.

[26] Advancedpowders.com, 20 July 2016. [Online]. Available: http://advancedpowders.com/wp-content/uploads/APC-Corporate-brochure-fall-2015.pdf.

[27] “AMG Advanced Metallurgical Group,” 2010. [Online]. Available: http://www.amg-nv.com/Innovation/Titanium-Aluminide/default.aspx.

[28] L. Yang, K. Hsu, B. Baughman, D. Godfrey, F. Medina, M. Menon and Soeren Wiener, Additive Amnufacturing of Metals: The technology, Materials, Design and Production, Cham: Springer, 2017.

[29] F. Medina, “REDUCING METAL ALLOY POWDER COSTS FOR USE IN POWDER BED,” THE UNIVERISTY OF TEXAS AT EL PASO, Texas, 2013.

[30] WohlersAssociates, “What is Additive Manufacturing? | Wohlers Associates,” 18 July 2016. [Online]. Available: https://wohlersassociates.com/additive-manufacturing.html.

[31] E. Atzen and A. Salmi, “Economics of additive manufacturing for end-usable metal parts,” *The International Journal of Advanced Manufacturing Technology,* vol. 62, no. 9-12, pp. 1147-1155, 2012.

[32] P. Dickens and T. Minshall, "UK AM National Strategy," 2015. [Online]. Available: http://www.amnationalstrategy.uk/wp-content/uploads/2015/05/UK-AM-National-Strategy-Update-Report-2.2.pdf. [Accessed April 2016].

[33] ASTM International, "Committee F42 on Additive Manufacturing Technologies," ASTM International, [Online]. Available: https://www.astm.org/COMMITTEE/F42.htm. [Accessed 15 March 2017].

[34] Arcam.com, "ArcamAB," 16 October 2017. [Online]. Available: http://www.arcam.com/wp-content/uploads/Arcam-Ti6Al4V-Titanium-Alloy.pdf.

[35] "GE Agrees to Purchase Controlling Shares of Arcam AB," GE, 15 November 2016. [Online]. Available: https://www.ge.com/additive/press-releases/ge-agrees-purchase-controlling-shares-arcam-ab. [Accessed 21 April 2018].

[36] "Arcam Q20 Specification Sheet," 2014. [Online]. Available: http://www.arcam.com/wp-content/uploads/Arcam-Q20.pdf. [Accessed April 2016].

[37] Arcam AB, "Electron Beam Melting Level 2 training," Arcam, Gothernberg, 2017.

[38] "Photon," electron6, n.d n.d n.d. [Online]. Available: http://electron6.phys.utk.edu/phys250/modules/module%201/photons.htm. [Accessed 28 Novemeber 2017].

[39] K.-H. Grote and E. k. Antonsson, Springer Handbook of Mechanical Engineering,, East Califonrnia Bouveard: Springer, 2009, p. 655.

[40] V. Juechter, T. Scharowsky, R. F. Singer and C. Körner, “Processing window and evaporation phenomena for Ti–6Al–4V produced by selective electron beam melting,” *Acta Materialia,* vol. 76, pp. 252-258, 2014.

[41] S. Shao, . M. J. Mahtabi, N. Shamsaei and S. M. Thompson, “Solubility of argon in laser additive manufactured a-titanium under hot isostatic pressing condition,” *Computational Materials Science,* pp. 209-219, 2017.

[42] k. Rafi, N. V. Karthik, T. . L. Starr and B. E. Stucker, “Defect formation in EBM parts built in horizontal orientation,” University of Louisville, Louisville, 2012.

[43] Y.-S. Chou, and K. Cooper, “Systems and methods for designing and fabricating contact-free support structures for overhang geometries of parts in powder-bed metal additive manuafcaturing”. United States of America Patent 14/276,345, 12 may 2014.

[44] H. P. Tang, M. Qian, N. Liu, X. Zhang and J. Wang, “Effect of Powder Reuse Times on Additive Manufacturing of Ti-6Al-4V by Selective Electron Beam Melting,” *The Journal of The Minerals, Metals & Materials Society (TMS),* 2015.

[45] M. Svensson, “EBM-manufactured Ti6AL4v & Ti6AL4V ELI under raw and HIP conditions,” Arcam AB, Sweden, 2009.

[46] A. M. Venter, “Non-destructive characterization of materials and components with neutron and and X-ray diffraction methods,” *The Journal of The Southern African Institute of Mining and Metallurgy,* vol. 115, no. 10, p. 925, 2015.

[47] J. Bruno, A. Rochman, and A. Cassar, “Effect of Build Orientation of Electron Beam Melting on Microstructure and Mechanical Properties of Ti-6Al-4V,” *Journal of Materials Engineering and Performance*, 2017.

[48] I. Elfström, “Additive Manufacturing with EBM,” Arcam, Mölndal, Sweden, 2013.

[49] N. Hrabe and T. Quinn, “Effects of processing on microstructure and mechanical properties of a titanium alloy (Ti–6Al–4V) fabricated using electron beam melting (EBM), part 1: Distance from build plate and part size,” *Materials Science and Engineering: A*, vol. 573, pp. 264-270, 2013.

[50] D. Brintz, “Electron Beam Melting of Ti 6-Al 4-V case study,” Univeristy of Birmingham, Birmingham, 2015.

[51] X. Tan, Y. Kok, W. Q. Toh, Y. J. Tan, M. Descoins, D. Mangelinck, S. B. Tor, K. F. Leong and C. K. Chua, “Revealing martensitic transformation and α/β interface evolution in electron beam melting three-dimensional-printed Ti-6Al-4V,” *Scientific Reports*, vol. 6, no. 1, p. August, 2016.

[52] E. Hernández-Nava, C. J. Smith, F. Derguti, S. Tammas-Williams, F. Leonard, P. J. Withers, I. Todd and R. Goodall, “The effect of defects on the mechanical response of Ti-6Al-4V cubic lattice structures fabricated by electron beam melting,” *Acta Materialia*, vol. 108, pp. 279-292, 2015.

[53] John J. Lewandowski and Mohsen Seifi, “A Review of Mechanical Properties,” *Metal Additive Manufacturing*, 2016.

[54] H. Z. F. L. F. D. I. T. P. P. S. Tammas-Williams, “XCT analysis of the influence of melt strategies on defect population in Ti–6Al–4V components manufactured by Selective Electron Beam Melting,” *Materials Characterization,* vol. 102, pp. 47-61, 2015.

[55] R. Cunningham, S. P. Narra, T. Ozturk, J. Beuth and A. D. Rollett, “Evaluating the Effect of Processing Parameters on Porosity in Electron Beam Melted Ti-6Al-4V via Synchrotron X-ray Microtomography,” *JOM,* pp. 765-771, 2016.

[56] N. Hrabe, R. Kircher and T. Quinn, “Effects of Processing on Microstructure and Mechanical Properties of Ti-6Al-4V Fabricated using Electron Beam Melting (EBM): Orientation and Location,” National Institute of Standards and Technology (NIST), Golden, 2012.

[57] R. I. Jaffee and H. M. Burte, “Critical review. In Titanium science and technology,” 1973, pp. 1665-1693.

[58] J. M. Oh, B. G. Lee, S. W. Lee, S. W. Cho, G. S. Choi and J. W. Liam, “Oxygen effects on the mechanical properties and lattice strain of Ti and Ti-6Al-4V,” *Metals and Materials International,* vol. 15, no. 5, pp. 733-7396, 2011.

[59] J. Mireles, “LayerwiseMonitoring and Control in Metallic Powder Bed Fusion Additive Manufacturing,” The Univerisity of Texas, El Pase, 2015.

[60] A. Kirchner, T. Weissgaerber, B. Kloeden and S. Bagehorn, “Effect of heat treatments on the mechanical properties of Ti-6Al-4v additevely manufactured by electron beam melting,” Fraunhofer, Nurnberg, 2016.

[61] A. Kirchner, B. Klöden, J. Luft,, T. Weißgärber and B. Kieback, “Process window for electron beam melting of Ti-6Al-4V,” *Powder Metallurgy,* pp. 246-249, 2015.

[62] S. Hou, E. Muzangaza, M. Bombardiere, A. Okioga and D. Bracket, "Optimising the Dynamic Process Parameters in Electron Beam Melting (EBM) to Achieve Internal Defect Quality Control," in *European Powder Metallurgy Association*, Milan, 2017.

[63] A. Triantaphyllou, C. L. Giusca, G. D. Macaulay, M. Hoebel, R. Leach, B. Tomita, K. Milne and R. Leach, "Surface texture measurement for additive manufacturing," Surface Topography: Metrology and Properties, 2015.

[64] L. Roy, "Variation in mechanical behaviour due to dfferent build directions of Ti6Al4V fabricated by Electron Beam Melting additive manufacturing technology," The University of Alabama, Tuscaloosa, 2013.

[65] H. Rafi, N. Karthik, H. Gong, T. L. Starr and B. Stucker, "Microstructures and Mechanical Properties of Ti6Al4V Parts Fabricated by Selective Laser Melting and Electron Beam Melting," *Journal of Materials Engineering and Performance,* vol. 22, no. 12, pp. 3872-3883, 2013.

[66] D. Greitemeier, F. Palm, F. Syassen and T. Melz, "Fatigue performance of additive manufactured TiAl6V4 using electron and laser beam melting," *International Journal of Fatigue*, vol. 94, pp. 211-217, 2017.

[67] M. Kahlin, H. Ansell and J. J. Moverare, "Fatigue behaviour of notched additive manufactured Ti6Al4V with as-built surfaces," *internation Journal of fatigue,* pp. 51-60, 2017.

[68] N. Hrabe, T. Gnäupel-Herold and T. Quinn, "Fatigue properties of a titanium alloy (Ti–6Al–4V) fabricated via electron beam melting (EBM): Effects of internal defects and residual stress," *International Journal of Fatigue,* pp. 202-210, 2015.

[69] Y. Pan, Y. Chen and C. Zhou, "Fabrication of Smooth Surfaces based on Mask Projection Stereolithography," Epstein Department of Industrial and Systems Engineering. University of Southern California, Los Angeles, 2011.

[70] H. Gong, K. Rafi, N. Karthik, T. Starr and B. Stucker, "Defect Morphology in Ti-6Al-4V Parts Fabricated by Selective Laser Melting," Department of Chemical Engineering, University of Louisville, Louisville, 2013.

[71] R. Cunningham, A. Nicolas, J. Madsen, E. Fodran, E. Anagnostou, M. D. Sangid and . A. D. Rollett, "Analyzing the effects of powder and postprocessing on porosity and properties of electron Beam melted Ti-Al-4V," *Materials Research Letters,* pp. 516-525, 2017.

[72] S. Bagehorn, J. Wehr, S. Nixon, A. Balastrier, T. Mertens and H. J. Maier, "Electrochemical enhancement of the surface morphology and the fatigue performance of ti-6al-4v parts manufactured by laser beam melting," *Solid Freeform Fabrication.*

[73] P. O. Hara, "Superfinihsing and shot peening of surfaces to optimise roughness and stress," *Transanctions of Engineering Sciences* , 1999.

[74] A. Lassell, "The electropolishing of electron beam melting, additively manufactured TI6AL4V titanium : relevance, process parameters and surface finish.," 1 May 2016. [Online]. Available: https://ir.library.louisville.edu/etd/2369/. [Accessed 22 April 2018].

[75] A. Triantaphyllou, C. L. Giusca, G. Macaulay, F. Roerig, M. Hoebel, R. Leach, B. Tomita and K. A. Milne, "Surface texture measruement for additive manufacturing," *Surface Topography: Metrology and Properties,* vol. 3, no. 2, 2015.

[76] A. Townsend, L. Blunt and P. Bills, "Investigating the capability of microfocus X-ray computed tomography for areal surface analysis of additively manufactured parts," 2016.

[77] A. Townsend, N. Senin, L. Blunt, R. Leach and J. Taylor, "Surface texture metrology for metal additive manufacturing: a review," *Precision Engineering,* vol. 46, pp. 34-47, 2016.

[78] E. Todorov, R. Spencer, S. Gleeson, M. Jamshidinia and S. M. Kelly, "America Makes: National Additive Manufacturing Innovation Institute (Namii) Project 1: Nondestructive Evaluation (Nde) Of Complex Metallic Additive Manufactured (Am) Structures," Air Force Research Laboratory, United States, 2014.

[79] A. Thompson, I. Maskery and R. Leach, " X-ray computed tomography for additive manufacturing: a review," Measurement Science and Technology, Nottingham, 20116.

[80] Vibrant NDT, "Process Compensated Resonance Testing," Accessed 2016. [Online]. Available: http://www.vibrantndt.com/wp-content/uploads/Intro-to-PCRT.pdf. [Accessed 2016].

[81] Y. Zheng, R. G. Maev and I. Y. Solodov, "Nonlinear acoustic applications for material characterization: A review," *Canadian Journal of Physics,* vol. 77, pp. 927-967, 1999.

[82] A. Lopez, R. Bacelara, I. Pires, T. G. Santos, J. PedroSousa and L. Quintinoa, "Non-destructive testing application of radiography and ultrasound for wire and arc additive manufacturing," *Additive Manufacturing,* vol. 21, pp. 298-306, 2018.

[83] P. J. d. S. Bartolo, A. C. S. d. Lemos, A. M. H. Pereira, A. J. D. S. Mateus, C. Ramos, C. D. Santos, D. Oliveira, E. Pinto and F. Craveiro, "High Value Manufacturing: Advanced Research in Virtual and Rapid Prototyping," Leiria, 2013.

[84] J. M. Waller, B. H. Parker, K. L. Hodges, E. R. Burke and J. L. Walker, “Nondestructive Evaluation of Additive Manufacturing,” NASA, Langley Resarch Center, Hampton, Virginia, 2014.

[85] S. K. Everton , M. Hirscha, P. Stravroulakisa, R. K. Leacha and A. T. Clarea, “Review of in-situ process monitoring and in-situ metrology for metal additive manufacturing,” *Elsevier,* vol. 95, p. 431–445, 2016.

[86] S. Price, . J. Lydon, K. Cooper and K. Chou, “Experimental temperature analsusis of powder based election beam additive manufacturing,” Marshall Space Flight Center, Huntsville, 2013.

[87] ArcamAB, “Arcam Q20plus XQam,” Gothenberg, 2016.

[88] Spener wright, “First EBM prints,” 4 July 2015. [Online]. Available: http://pencerw.com/feed/2015/7/4/first-ebm-prints.

[89] M. M. Attallah, R. Jennings, X. Wang and L. N. Carter, “Additive manufacturing of Ni-based superalloys: The outstanding issues,” *MRS Bulletin,* pp. 758-764, 2016.

[90] P. A. Kobryn, E. H. Moore and L. S. Semiatin, “Effect of laser power and traverse speed on microstructure, porosity, and build height in laser-deposited Ti-6Al-4V,” *Scripta Materialia,* vol. 43, no. 4, pp. 299-305, 2000.

[91] ASTM International, “Standard Specification for Additive Manufacturing Titanium-6 Aluminum-4 Vanadium with Powder Bed Fusion,” [Online]. Available: https://compass.astm.org/download/F2924.17405.pdf. [Accessed 22 April 2018].

[92] . E. W. Weisstein, “Fraunhofer Diffraction -- from Eric Weisstein's World of Physics,” Scienceworld wolfram, [Online]. Available:

http://scienceworld.wolfram.com/physics/FraunhoferDiffraction.html. [Accessed 22 April 2018].

[93] M. Naito, O. Hayakawa and K. Nakahira, "Effect of particle shape on the particle size distributions measured with commercial equipment," *Powder Technology,* vol. 100, pp. 52-60, 1998.

[94] ASTM International, "Standard Test Method for Particle Size Distribution of Metal Powders and Related Compounds by Light Scattering (B822-10)," 2010.

[95] Malvern Instruments Ltd., "Mastersizer 3000 User Manual (MAN0474-2.1)," 2013.

[96] Innopharmalabs, " Particle Size Monitoring," Innopharma technology, [Online]. Available: https://www.innopharmalabs.com/tech/applications-and-processes/particle-size-monitoring. [Accessed 25 November 2017].

[97] freemantech, "Powder Testing with the FT4 Powder Rheometer," freemantech, [Online]. Available: http://www.freemantech.co.uk/_powders/ft4-powder-rheometer-universal-powder-tester. [Accessed 22 April 2018].

[98] ASTM International, "Standard Test Method for Apparent Density of Free-Flowing Metal Powders Using the Hall Flowmeter Funnel," [Online]. Available: https://compass.astm.org/download/B212-12.8063.pdf. [Accessed 22 April 2018].

[99] ASTM International, "Standard Test Method for Determination of Oxygen and Nitrogen in Titanium and Titanium Alloys by Inert Gas Fusion (E1409-13)," 2013.

[100] ASTM International, "Standard Test Method for Determination of Hydrogen in Titanium and Titanium Alloys by Inert Gas Fusion (B1447-09)," ASTM International, 2009.

[101] ASTM International, “Standard Test Method for Analysis of Titanium by Direct Current Plasma and Inductively Coupled Plasma Atomic Emission Spectrometry (E2371-13),” 2013.

[102] Exova, “Exova tensile testing,” 2016. [Online]. Available: http://www.exova.com/capabilities/tensile-testing/.

[103] ASTM International, “Standard Practice for microetching metal and alloys,” ASTM International, 1 January 2016. [Online]. Available: https://compass.astm.org/download/E407.21719.pdf. [Accessed 22 April 2018].

[104] ASTM international, “Standard Test Method for Brinell Hardness of Metallic Materials,” ASTM international, [Online]. Available: https://compass.astm.org/download/E10.24213.pdf. [Accessed 22 April 2018].

[105] American Society of Mechanical Engineers., “Surface texture : surface roughness, waviness and lay,” American Society of Mechanical Engineers, 2009. [Online]. Available: https://www.asme.org/products/codes-standards/b461-2009-surface-texture-surface-roughness. [Accessed 22 April 2018].

[106] ISO 25178-3, “Geometrical product specifications (GPS) -- Surface texture: Areal -- Part 3: Specification operators,” International Organisation of Standardisation, 2012.

[107] L. E. Murr, S. M. Gaytan,, F. Medina, E. Martinez, D. H. Hernandez, L. Martinez, M. I. Lopez, R. B. Wicker and S. Collins, “Effect of build parameters and build geometries on residual microstructures and mechanical properties of Ti-6Al-4V components built by Electron Beam Melting (EBM),” The University of Texas, El Paso, 2009.

[108] A. Safdar, “Microstructures and surface roughness of EBM,” Malmö University, Sweden, 2010.

[109] tekna, “www.tekna.com,” 2015. [Online]. Available: http://tekna.com/equipment-spheroidization-nanosynthesis-deposition/deposition-equipment/.

[110] SpecialTesing, “Special tesling ltd,” 2016. [Online]. Available: http://www.specialtesting.co.uk/mechanical-test-list/.

[111] I. Gibson, D. W. Rosen and B. Stucker, Additive Manufacturing Technologies: Rapid Prototyping to Direct Digital Manufacturing, New York: Springer, 2010.

[112] C. Hauser, “Laser Additive Manufacturing as a Key Enabler for the Manufacture of Next Generation Jet Engine Components - Technology Push,” TWI, 2012.

[113] B. Josso, D. Burton and M. Lalor, “Wavelet strategy for surface roughness analysis and characterisation,” *Computer methods in applied mechanics and engineering,* pp. 1-14, 2000.

[114] C. Giusca, R. Leach, F. Helery and T. Gutauskas, “Calibration of the geometrical characteristics of areal surface topography measuring instruments,” Journal of Physics: Conference Series 311, 2011.

[115] ISO 25178-2, “Geometrical product specifications (GPS) -- Surface texture: Areal -- Part 2: Terms, definitions and surface texture parameters,” International Organisation of Standardisation, 2012.

[116] genmed.info, “Treatment Revolutionized The Use Of Titanium Rod,” 19 july 2016. [Online]. Available: http://genmed.info/treatment-revolutionized-the-use-of-titanium-rod/.

[117] S. Saadi, “An investigation into microstructure and microstructural control of additive layer manufactured Ti-6Al-4V by electron beam melting,” *University of Sheffield,* 2016.

[118] Sir Authur Russel, Bart, “discoverer of titanium,” *The Mineralogical Magazine and Journal of the Mineralogical Society,* pp. 617-624, 1955.

[119] Yuwei Zhai, Haize Galarraga, Diana A. Lados, “ Microstructure Evolution, Tensile Properties, and Fatigue Damage Mechanisms in Ti-6Al-4V Alloys Fabricated by Two Additive Manufacturing Techniques. Procedia Engineering, 114„” *Procedia Engineering,* pp. 658-666, 2015.

[120] Qian, “Thermal history and microstructure of direct laser fabricated,” *Material Science and Technology, Vol21, ,*2005..

[121] Dutta B and Froes FHS, “Additive manufacturing of titanium alloys,” *Adv. Mater. Res. 1019(Oct.),* pp. 19-25, 2014.

[122] J. Karlsson, A. Snis, H. Engqvistc and J. Lausmaa, “Characterization and comparison of materials produced by ElectronBeam Melting (EBM) of two different Ti–6Al–4V powder fractions,” *Journal of Materials Processing Technology,* 2013.

[123] E. Martin, “Surface roughness modification of bone tissue engineering scaffolds by electrochemical etching: optimisation and quantitative characterisation,” MSc Thesis, Catholic University Leuven, 2011.

[124] AIAG, “Advanced Product Quality Planning and Control Plan,” 2008.

[125] A. S. S. S. J. L. Mohsen Seifi, “Defect distribution and microstructure heterogeneity effects on fracture,” *International Journal of Fatigue,* 2016.

[126] N. Brierley, “A11108: Simulation Enhanced Inspection: Deliverable 3. Final Report on Proof-of-Concept Demonstration,” The Manufacturing Techology Centre, Coventry, 2016.

[127] A. Muhammad, A. M. Alahmari, M. K. Mohammed, R. K. Renganayagalu, and K. Moiduddin, “Effect of Energy Input on Microstructure and Mechanical Properties of Titanium Aluminide Alloy Fabricated by the Additive Manufacturing Process of Electron Beam Melting,” *material,* 2017.

[129] S. L. Lu, Y. P. Ning, N. Liu, D. H. StJohn and M. Qian, “Microstructure and Mechanical Properties of Long Ti-6Al-4V Rods Additively Manufactured by Selective Electron Beam Melting Out of a Deep Powder Bed and the Effect of Subsequent Hot Isostatic Pressing,” *Metallurgical and Materials Transactions A,* pp. 3824-3834, 2015.

[130] Roland Berger, “Additive Manufacturing,” November 2013. [Online]. Available: http://www.rolandberger.co.uk/expertise/publications/2013-11-29-Additive_manufacturing.html.

[131] Additive Manufacturing SIG, “Shaping Our National Competency in Additive Manufacturing,” Technology Strategy Board, UK, 2012.

[132] Lloyds Register Energy, “The Opportunities for Additive Manufacturing in the Energy Industry,” Lloyds Register Energy, 2014.

[133] I. Gibson, D. W. Rosen and B. Stucker, Additive Manufacturing Technologies: Rapid Prototyping to Direct Digital Manufacturing., New York: Springer, 2010.

[134] United States Government Accountability Office, "3D Printing: Opportunities, Challenges, and Policy Implications of Additive Manufacturing," 2015.

[135] Energetics Incorporated, "Measurement Science Roadmap for Metal-Based Additive Manufacturing," National Institute of Standards and Technology, 2013.

[136] NIST, "Measurement Science Roadmap for Metal-Based Additive Manufacturing," 2013.

[137] "Arcam A2 Specification," 2010. [Online]. Available: http://www.arcam.com/wp-content/uploads/Arcam-A2.pdf. [Accessed April 2016].

[138] K. A. Mumtaz and N. Hopkinson, "Selective Laser Melting of thin wall parts using pulse shaping," *Journal of Materials Processing Technology,* vol. 210, pp. 279-287, 2010.

[139] K. Cooper, P. Steele, B. Cheng and K. Chou, "Contact-Free Support Structures for Part Overhangs in Powder-Bed Metal Additive Manufacturing," The University of Alabama, Tuscaloosa, 2016.

[141] M. Suard, "Characterization and Optimization of Lattice Structures made by Electron Beam Melting," Université Grenoble Alpes, Grenoble, 2015.

[142] A. T. Sidambe, I. Todd and P. V. hatton, "Effects of build orientation induced surface modifications on the in vitro biocompatibility of electron beam melted Ti6Al4V," *Powder Metallurgy* , vol. 59, no. 1, pp. 57-65, 2015.

[143] anom, "U.S pharmacopeia," pharmacopeia, [Online]. Available: http://www.pharmacopeia.cn/v29240/usp29nf24s0_c1174.html. [Accessed 02 June 2016].

[144] G. K. Lewis and . E. Schlienger, “Practical considerations and capabilities,” *Mater. Des,* vol. 21, pp. 417-423, 200.

[145] P. A. Kobryn and S. L. Semiatin:, “Mechanical properties of laserdeposited,” *Solid freeform fabrication proceedings,* 2001.

[146] ASTM International, “Standard Test Method for Determination of Tap Density of Metallic Powders and Compounds,” [Online]. Available: https://compass.astm.org/download/B527-06.37980.pdf. [Accessed 22 April 2018].

[147] Finecs ltd, “Barrel Finishing,” finecs, [Online]. Available: http://www.finecs.co.jp/en/manufacturing/barrel-polishing.html. [Accessed 22 Apri 2018].